Regional-scale forward modeling and inversion of 3D wave propagation and dynamic rupture processes with nonlinear mechanical models of rocks and soils

Zihua Niu

München 2025

Regional-scale forward modeling and inversion of 3D wave propagation and dynamic rupture processes with nonlinear mechanical models of rocks and soils

Zihua Niu

Dissertation
an der Fakultät für Geowissenschaften
der Ludwig–Maximilians–Universität
München

vorgelegt von
Zihua Niu

München, den 18. Februar 2025

Erstgutachter: Prof. Dr. Heiner Igel
Zweitgutachter: Prof. Dr. Alice-Agnes Gabriel
Tag der mündlichen Prüfung: 05. Juni 2025

Acknowledgements

First and foremost, I extend my deepest gratitude to Prof. Dr. Alice-Agnes Gabriel and Prof. Dr. Heiner Igel for guiding me on this incredible journey of doctoral research. I am deeply grateful for the intellectual freedom you provided, allowing me to pursue directions that resonate with my passions. Your unwavering encouragement in my progress, coupled with your constructive criticism, has helped me grow both as a researcher and as a person. Your dedication to science and mentorship not only has inspired me to overcome challenges but has also brought immense joy to my academic and personal life. Heiner, thank you for teaching me skiing and for the music that we play together. Alice, thank you for inviting me to Scripps, where I had the unforgettable opportunity to witness breathtaking sunsets.

I also wish to express my sincere appreciation to my friends and colleagues at LMU and TUM. A special thanks goes to Dr. Sebastian Wolf for guiding me through the early days of working with SeisSol, making my transition into this large project much smoother. I am equally grateful to Dr. Linus Seelinger, Dr. Shihao Yuan, Dr. Duo Li, Dr. Andreas Brotzer, Dr. Thomas Ulrich, David Schneller, Dr. Jorge Nicolas Hayek Valencia, Nico Schliwa, Dr. Le Tang, Yunong Wei, Yuchen Chi, Roman Freissler, and Vikas Kurapati for the engaging scientific discussions, shared lunches and dinners, and for making my PhD experience so much more colorful, both in academia and in life.

I would also like to acknowledge the SPIN-ITN network for their invaluable support. A heartfelt thank you to Dr. Christoph Sens-Schönfelder, Prof. Dr. Céline Hadziioannou, and Dr. Ernst Niederleithinger for organizing the network and for hosting me during my stays in Potsdam and Berlin. I also thank Marco Antonio Dominguez Bureos, Manuel Asnar, and Sergio Diaz-Meza for making my time within the network and in Berlin so enjoyable.

My deepest gratitude goes to my parents, whose unwavering support and understanding have been my bedrock throughout this journey. Thank you for trusting my decisions unconditionally and for standing by me, even when my busy schedule left little time to stay in touch. If there is one thing I could change, it would be to spend more time with you, at the very least, through more frequent phone calls.

Finally, I would like to express my heartfelt thanks to my girlfriend, Jiawei Zhou. Thank you for bringing joy and adventure into my life, for always proposing fun things for us to experience together, and for being such an important part of my journey. Meeting you has truly completed a significant part of my life.

This dissertation would not have been possible without the support, encouragement, and companionship of all those mentioned above. Thank you!

Abstract

Earthquakes are catastrophic geohazards with severe impacts on life and property. Emerging evidence suggests that linear mechanical models are inadequate for fully explaining the origins and consequences of devastating earthquakes. There is a critical need for adequate physics-based rock models and efficient numerical algorithms to explore how nonlinearities affect our understanding of earthquake mechanisms, in-situ rock conditions along seismic paths, and the resulting ground motions. In this dissertation, I focus on enhancing the representation and simulation of nonlinear rock behaviors under dynamic loading across multiple scales, i.e., from laboratory rock samples to regional-scale earthquakes. The advancement incorporates physics-based nonlinear rock models derived from laboratory experiments, scalable software for physics-based earthquakes simulation from source to site on supercomputers, and innovative inversion algorithms aimed at accurately determining nonlinear parameters of both laboratory and in-situ rocks.

The first part of the dissertation introduces two continuum damage models that aligns with observations of nonlinear behaviors in rock samples from two commonly utilized laboratory experiment setups. In the second part, I propose an algorithm based on the discontinuous Galerkin method to model wave propagation through nonlinear rock rheologies in 3D. This algorithm is designed for regional-scale simulations that involve complex geometries. I verify the algorithm against three sets of analytical solutions and confirm that the algorithm scales effectively on supercomputers. I demonstrate the applicability of the framework to simulating co-seismic wave speed changes and ground motions during the 2015 M_w 7.8 Ghorka earthquake in Kathmandu valley. In the third part, the numerical solver is extended to incorporate 3D dynamic rupture modeling. This extension allows us to illustrate the off-fault co-seismic damage patterns and the high-frequency seismic radiation. In addition, I demonstrate that in the tensile step-over configuration, localized damage zones extending from one fault can induce heterogeneous stress perturbations on a neighboring fault, thereby triggering nucleation. This capability enables detailed simulations of dynamic rupture processes, including off-fault co-seismic moduli reduction at regional scales.

Based on the earthquake simulation software developed in this dissertation, I propose two Markov chain Monte Carlo (MCMC) sampling methods to perform Bayesian inversion of nonlinear material parameters. At the laboratory scale, the forward simulations are computationally inexpensive. I demonstrate, in the first part of the dissertation, that the Adaptive Metropolis MCMC algorithm can be utilized to illustrate the precision with which material parameters can be constrained from the existing experiment setups. At the regional scale, each forward simulation takes thousands of core hours on modern compute clusters. To accelerate the inversion, I propose, in the fourth part of this work, a more effective sampling algorithm, i.e., the Multi-level Delayed Acceptance (MLDA) MCMC algorithm. In the fifth part of this work, I then show how the MLDA algorithm can be optimized for nonlinear inversion of parameters in dynamic rupture models, specifically for the 2019 M_w 7.1 Ridgecrest earthquake, leveraging geological, seismic, and geodetic observations.

Contents

List of Tables

List of Figures

Chapter 1

Introduction

Earthquakes are profoundly destructive natural events that can cause significant loss of life, property damage, and disruption to society (Ben-Zion et al., 2022). To mitigate these adverse effects, it is crucial to forecast when an earthquake will occur and to understand the expected ground motions associated with it. Furthermore, knowledge of expected ground motions helps to design buildings and infrastructure that can withstand seismic forces, reducing the potential for catastrophic damage and improving the resilience of communities against such unpredictable natural disasters. Accurate hazard quantification enables timely evacuations and the implementation of safety measures. In this work, we focus on realistic physics-based modeling of earthquakes, with the aim of providing new tools to better assess the effects of earthquakes on Earth.

Earthquakes feature abrupt failure of rocks that propagate through weak zones in 3D subsurface. They are typically hosted by the Earth's lithosphere, consisting of the crust and the upper layer of the mantle (White, 1988). Many evidence points to the fact that the lithosphere is divided into tectonic plates. The basic hypothesis for the tectonic plates is given by Morgan (1968). Driven by the convective motion of the lower mantle, the plates move against each other, loading or unloading the rocks in the lithosphere (Iaffaldano and Bunge, 2009).

The relative motion at plate boundaries, convergent, divergent, or parallel, leads to various styles of faulting: thrust, normal, strike-slip, or mixed faulting (Lowrie and Fichtner, 2020). The fault zones are mechanically weak and host the majority of significant earthquakes on Earth. Due to their chemical composition, pressure, and temperature conditions, the rocks in the lithosphere are mainly brittle (Zoback et al., 2007; Robbiano et al., 2024). Once the brittle rocks reach their failure condition under tectonic loading, the rapid dynamic motion in the lithosphere is initiated mostly from 0 to 70 km at depths (Maggi et al., 2000; Scholz, 2019) and generates seismic (mechanical) waves. The wave travels through different geological structures (crust, mantle, or core, depending on the distance between the epicenter and the location where the motion is recorded). Before reaching our infrastructure, the dynamic motion is further modulated by the unconsolidated materials in sedimentary basins and/or by the surface topography.

Over decades of investigation, physical models have been proposed to describe the onset of earthquakes on natural faults (source) and how seismic waves travel through different geological structures, such as crust, mantle, or core, depending on the distance between the epicenter and the location where the motion is recorded (path) and reach the ground surface with sedimentary basins or topography (site). A successful model that describes the physical processes during the onset and development of an earthquake in a system of faults is the dynamic rupture (DR) model. The key components of a DR model are summarized

in Fig. 1.1a. They consist of curved fault structures that represent the geological plate boundaries, host rocks next to the fault surfaces whose mechanical properties vary in the 3D subsurface, and a ground surface with zero load on its top.

In DR models, an earthquake initiates from the fault structures. The basic assumption is that the two sides of the fault contact each other through a frictional interaction (e.g., Scholz, 2019). The relative movement of the tectonic plates drives a temporal variation in the loading conditions on the fault. When loads exceed the local frictional strength within a certain region of the fault (Rubin and Ampuero, 2005), a dynamic relative motion of the plates (at a speed much higher than that of the tectonic plate motion, typically a few centimeters per year) can begin from that region. The region with a dynamic relative motion can expand until the expansion front reaches certain barriers, such as areas with high frictional strength (Molina-Ormazabal et al., 2023), geometric discontinuities of fault surfaces (King, 1986; Okuwaki and Yagi, 2018), or the brittle-ductile transition zone (Molnar, 2020).

Such DR models account for different factors that affect the sources of earthquakes, including the roughness (Power et al., 1987; Morad et al., 2022), the stress state (Ripperger et al., 2007; Brodsky et al., 2020), the temperature (Bizzarri and Cocco, 2006), and the fluid pressure conditions (Vyas et al., 2023) on the fault. Under the above control factors, the DR models describe the rupturing process on the fault by quantifying the stress drop (Gallovič and Valentová, 2020), rupture speed (Gabriel et al., 2013), and the slip history on the fault. The model also resolves vastly different amounts of energy release (earthquake magnitude), source frequency contents (Taufiqurrahman et al., 2022), radiation pattern (Palgunadi et al., 2024b; Mia, 2024), and directivity (Yen et al., 2025).

After the dynamic relative motion of the tectonic plates is triggered, the radiated seismic energy from the source can be transferred to the host rocks and propagate inside the Earth. A first-order approximation of such energy radiation is the linear visco-elastic wave equation (Brennan and Smylie, 1981). The equation can account for geometrical spreading (Chapman and Godbee, 2012), viscous attenuation (Chapman, 2004), heterogeneity of the geological structures (Kumagai et al., 2011), anisotropy (Igel et al., 1995; Wolf et al., 2020a), etc. After reaching the unconsolidated part of the lithosphere (shallow subsurface above $\sim$1 km), the equation can also capture the amplification of the strain and velocity field in soft materials (van Ginkel et al., 2022). Local structures, for example, sedimentary basins (Semblat et al., 2005) and surface topography (Poursartip et al., 2017), can further modulate the frequency content of the surface ground motion.

1.1 Observed nonlinearity in rocks and soils

Notwithstanding the success of linear visco-elastic model in addressing many aspects of earthquake-induced dynamic motion of the Earth, there is increasing evidence that a linear rock model is not sufficient to quantify the ground motions in earthquakes for hazard assessment. Figs. 1.1b to 1.1g summarize the evidence of nonlinear response of rocks and soils to dynamic mechanical perturbations from source, path to site, including both laboratory experiments and earthquake measurements.

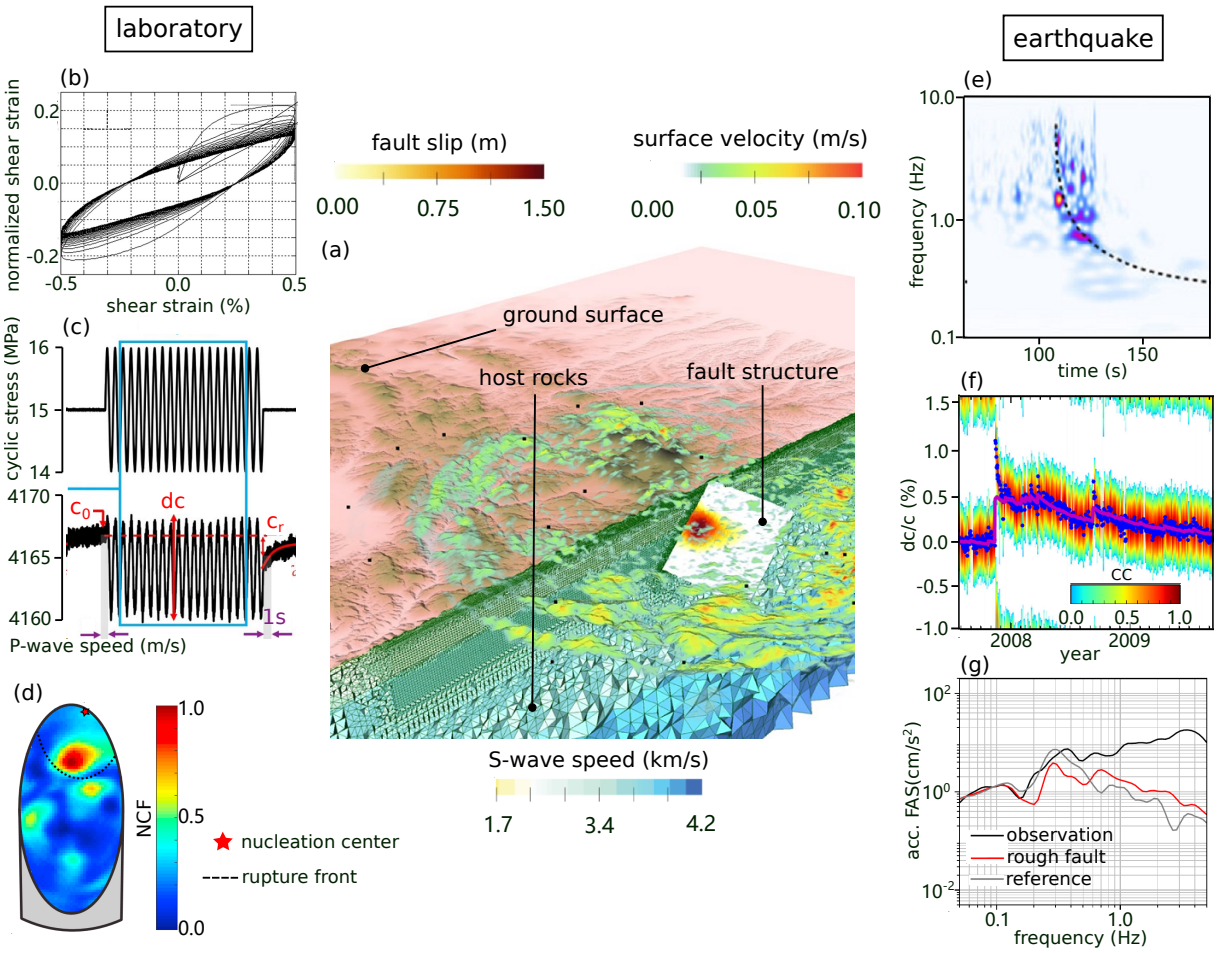

Figure 1.1: Summary of the key components in a dynamic rupture model (a) and the observed nonlinear responses of rocks and soils in laboratory experiments (b-d) and in earthquake observations (e-g). The dynamic rupture model setup in (a) is adapted from Taufiqurrahman et al. (2022). Evidence of rock nonlinearity close to the fault surface is shown in (d) for laboratory adapted from Marty et al. (2019b) and in (g) for earthquake adapted from Taufiqurrahman et al. (2022). The sawcut rock sample in (d) shows spatial distribution of the normalized coherence function (NCF) of the back-projected energy between 400 and 800 kHz on the rupture surface 4-6 μs after the nucleation of the rupture from the red star. The dashed black curve marks the location of the rupture front. The frequency amplitude spectra for the acceleration time series recorded during the 2016 Amatrice earthquake show a comparison among the observation (the black curve), the reference model with a planar fault surface (the gray curve), and the model with a rough fault surface (the red curve). Evidence of rock nonlinearity in the host rocks is shown in (c) for laboratory adapted from Manogharan et al. (2022) and in (f) for earthquake adapted from Gassenmeier et al. (2016). The top panel in (c) shows the cyclic loading in stress, while the bottom panel shows the induced changes in P wave speed. We show the wave speed changes dc/c from ambient noise cross-correlation before and after the Tocopilla earthquake in Chile on 2007 November 14th. The color code shows the cross-correlation coeffcient for a given change in dc/c. The positive dc/c means decrease in wave speed here. Evidence of nonlinearity in soft sediments is shown in (b) for laboratory adapted from Vucetic and Mortezaie (2015) and in (e) for earthquake adapted from Bonilla et al. (2011). The hysteresis loops of the stress-strain relationship for a soil sample under cyclic loading is shown in (b). It also shows the gradual rotation of the hysteresis loop closer to x-axis during the loading. The panel (e) shows the frequency spectrogram of the ground motion recorded above a soft sediments in Japan after the 2011 Tohoku earthquake.The blue to purple regions mark how the frequency components with high energy transit from ∼2 Hz to ∼0.3 Hz.

Within the fault zone, the non-linearities of the rock are evidenced by the complex fracture networks in field observations (e.g. Sibson, 1977; Chester et al., 1993; Mitchell and Faulkner, 2009). The fractures indicate that the materials surrounding the fault cores are subjected to co-seismic damage. Marty et al. (2019a) performed laboratory experiments on dynamic ruptures with sawcut rock samples and found enhanced high-frequency radiation behind the rupture front, as shown in the red region in Fig. 1.1d. From 2D dynamic rupture simulations, one hypothesis that explains the high-frequency radiation is the co-seismic triggering of off-fault fractures (Thomas and Bhat, 2018; Okubo et al., 2019; Idini and Ampuero, 2020). As shown in Fig. 1.1g, the additional high-frequency energy from off-fault damage may potentially fill the gap between the numerical modeling and observations which cannot be explained with the fault roughness and surface topography (Taufiqurrahman et al., 2022). In addition to high-frequency radiation, co-seismically developed off-fault damage zones change how much of the released energy from the unlocked rebound of the tectonic plate is transferred into seismic radiation (kinetic energy, Kanamori and Rivera, 2006; Okubo et al., 2019). The off-fault damage also results in a more heterogeneous stress distribution around the fault and influences the earthquake interactions in the fault system (Sammis et al., 2010; Xu et al., 2015; Mia et al., 2024).

Outside the fault zone, over the past few decades, nonlinear mechanical responses of rocks to seismic waves have also been widely observed at distances from a few kilometers to more than 100 kilometers away from the activated faults. Researchers managed to monitor temporal variations of seismic wave speeds in rocks during and after earthquakes with various monitoring techniques, such as repeating earthquakes (Poupinet et al., 1984; Bokelmann and Harjes, 2000; Niu et al., 2003; Schaff and Beroza, 2004), controlled sources (Yamaoka et al., 2001), and cross- or auto-correlation of ambient noises or aftershock recordings among seismic stations (Sens-Schönfelder and Wegler, 2006; Brenguier et al., 2008b; Bonilla and Ben-Zion, 2021; Qin et al., 2020). As shown in Fig. 1.1f, the typical behaviors of rocks consist of a rapid co-seismic reduction of seismic wave speeds during the earthquake followed by a long-term recovery process. Ranging from 0.01% to $\geq$10%, the measured amplitudes of the co-seismic wave speed reductions depend on rock types, distances from the source, depths of interest, temporal resolution of the monitoring techniques, etc.

Similarly to the co-seismic reduction of wave speeds in the field, such reductions are also measured on laboratory rock samples. The well-controlled environment and accurate laboratory measurement techniques offer a chance to connect changes in seismic wave speeds with the rheological and physical conditions of rocks. Renaud et al. (2012) make it possible to quantitatively investigate how rock moduli change during dynamic perturbations using Dynamic Acousto-elastic Testing (DAET) experiments. As shown in Fig. 1.1c, in response to dynamic cyclic stress perturbations, the wave speed evolves through a process similar to that during earthquakes: (1) As the loading starts, the wave speed of the sample experiences an overall reduction of the wave speed, which gradually stabilizes and reaches a new quasi-steady state (inside the blue rectangle); (2) After removing the cyclic loading, the wave speed c_r recovers over an extended period of time, illustrated by the solid red curve. We refer to such responses of rock samples to dynamic perturbations as "non-classical nonlinearity". Since then, researchers have investigated the dynamic nonlinear response of different types of sandstones and granites as well (Rivière et al., 2015, 2016; Manogharan et al., 2021). It has been found that the co-seismic wave speed changes under dynamic per-

turbation are sensitive to rheology, ambient stress, and thermal and hydraulic conditions (Manogharan et al., 2022; Lu and Ben-Zion, 2022). This is potentially a new observable that we can extract from seismic waves to probe subsurface rheology and physical conditions.

Close to the ground surface, nonlinear site effects in earthquakes have also been observed in numerous studies, particularly in regions where soft sediments amplify the strain field. These nonlinear behaviors are typically marked by a reduction in the seismic wave speed and an increase in damping as the ground shake intensifies (Darendeli, 2001). One key observation of site nonlinearity is the strain-dependent behavior of soils, where larger strains and cyclic loading lead to a decrease in the shear modulus and an increase in damping, as shown in Fig. 1.1b adapted from Vucetic and Mortezaie (2015). They affect both the amplitude and the frequency content of ground motions. This phenomenon was first documented in the aftermath of strong earthquakes like the 1994 Northridge earthquake, where nonlinear site responses were observed in soft sedimentary basins (Beresnev and Wen, 1998). Another important finding came from the study of the 1985 Michoacán earthquake in Mexico City, where significant amplification of ground motions was observed due to local site effects, with clear signs of nonlinear soil response (Seed et al., 1989).

Recent advances in instrumentation and data collection have further clarified these effects. For example, recordings from borehole arrays, such as those in Japan (Okada et al., 2004; Oth et al., 2011) and California (Bonilla et al., 2002), have provided direct evidence of nonlinear soil behavior during strong earthquakes. Researchers have observed reductions in shear wave velocity during strong shaking, followed by partial recovery after the seismic event, a key signature of soil nonlinearity (Wang et al., 2021). A related effect on ground motion is the enhancement of low-frequency components as shown in Fig. 1.1e during the 2011 Tohoku Earthquake (Bonilla et al., 2011). These findings highlight the importance of incorporating nonlinear site effects into seismic hazard assessments, as they can significantly alter the expected ground motion, especially in urban areas built on soft soils.

The evidence presented above confirms that the mechanical responses of rocks are inherently nonlinear, a fact with significant implications for understanding earthquake sources, the radiated seismic wave field, and their impact on modern civilization. For instance, co-seismic off-fault damage can generate additional high-frequency ground motions, which, when recorded above soft sediments, may be modulated to lower frequencies. This alters the frequency-dependent behavior of seismic ground motions, a key factor in designing earthquake-resistant structures (Yang et al., 2024). In addition, source nonlinearity influences fault interactions within complex fault systems, affecting earthquake magnitudes and the interplay between mainshocks and foreshocks (Hauksson et al., 1993; Ulrich et al., 2019; Taufiqurrahman et al., 2023; Gabriel et al., 2023). Understanding these dynamics is essential for earthquake preparedness and risk mitigation.

1.2 Nonlinear physical models for rocks and soils

To quantify the nonlinear responses of rocks and soils discussed in Section 1.1, numerous nonlinear mechanical models have been proposed. However, providing a comprehensive

review of all existing models would be beyond the scope of this section. Instead, this section focuses on summarizing representative models that are particularly relevant to the earthquake observations presented in Section 1.1. These models contribute to a more precise quantification of earthquake sources and the resulting ground motions, thereby enhancing seismic hazard assessment.

Models used to quantify co-seismically generated off-fault damage can be broadly categorized into two types: (1) discrete models, which incorporate geometrically predefined discrete structures, and (2) continuum models, which employ a continuous geometry representation. Discrete models include the finite discrete element method (FDEM, Munjiza, 1992, 2004; Gao et al., 2018; Okubo et al., 2019; McBeck et al., 2022) and the discontinuous Galerkin finite element method (DG-FEM, Palgunadi et al., 2024a; Gabriel et al., 2024; Palgunadi et al., 2024b). These models offer a conceptually intuitive way to represent material deficiencies within or near fault cores (Mitchell and Faulkner, 2009). However, they present challenges, such as complex mesh generation across multiple scales (Palgunadi et al., 2024a) and increased computational costs due to geometrical discontinuities (Gao et al., 2018). Additionally, it is necessary to assess the extent to which the modeling results are influenced by predefined deficiency structures.

In contrast, continuum models typically do not require a detailed geometric representation of small-scale material deficiencies, making them more flexible in handling variations in element size. Instead of explicitly defining geometrical structures, these models represent material deficiencies through one or more state variables (Kachanov, 1986), which capture the influence of defects on the material's mechanical response. These state variables evolve according to thermodynamic principles in response to external loading. Representative continuum models include the phase-field model (Fei et al., 2023; Hayek et al., 2023), the Godunov–Peshkov–Romenski model (Resnyansky et al., 2003; Romenski et al., 2007; Gabriel et al., 2021), the fracture-based damage model (Thomas and Bhat, 2018), and the continuum damage breakage model (Lyakhovsky and Ben-Zion, 2014; Lyakhovsky et al., 2016). Aside from these emerging models for the earthquake source nonlinearity, a more widely applied simple model for fault zone rocks is the Drucker-Prager plasticity (Andrews, 2005; Wollherr et al., 2018). While this model accounts for off-fault energy dissipation, it simplifies the damage process by neglecting the potential high-frequency radiation (Thomas and Bhat, 2018; Okubo et al., 2020; Lyakhovsky et al., 2023) and the perturbations in the fault-adjacent stress field, which will be further examined in Chapter 4.

As summarized in Section 1.1 and illustrated in Figures 1.1c and 1.1f, rocks exhibit non-classical nonlinearity. This is distinct from the classical rock nonlinearity, which ignores the temporal evolution of rock moduli under dynamic perturbations. Several existing models have proposed hypotheses for this phenomenon based on micro-physical processes (Delsanto and Scalerandi, 2003; Aleshin and Van Den Abeele, 2007; Lebedev and Ostrovsky, 2014). However, these models involve a large number of variables, making experimental validation extremely challenging and their application to earthquakes even more intractable. Addressing these challenges will be a key focus in Chapter 2.

When modeling the mechanical response of soils in soft sediments during earthquakes, it is essential to account for energy dissipation resulting from the hysteresis curves shown in Figure 1.1b. The mechanical responses also include a gradual degradation of moduli under

cyclic loading (Vucetic and Mortezaie, 2015), which is similar to the previously discussed non-classical nonlinearity. In existing models that have been applied for regional-scale earthquake modeling, the IWAN model (Iwan, 1967; Roten et al., 2023) in 3D can quite successfully resolve the hysteresis curve.

However, the mechanical behaviors of soils are more complicated than hysteresis curves and can be quite different between sands and clays. For example, loosely packed sandy or silty soils lose their strength and stiffness due to increased pore water pressure, usually under cyclic loading. This is also known as the liquefaction effect (Terzaghi et al., 1996; Castro, 1975). With the liquefaction front model of Iai et al. (1990), Oral et al. (2019) investigate the effect of liquefaction on ground motion on a small scale inside 2D sedimentary basins. Many more advanced models have been proposed for different types of soils and have been applied to small-scale simulations to study site effects. I refer to Powrie (2018) for a systematic overview of the more advanced models.

1.3 Methods for numerical simulation of earthquakes

To apply these advanced nonlinear physical models in actual earthquakes, we need the physics-based simulation. This essentially requires solving systems of partial differential equations (PDEs). Several factors make the solutions to the PDEs in the field more complicated than those in laboratory experiments: (1) While the sizes of the samples in the laboratory are usually a few tens of meters, earthquakes with magnitudes greater than M_w 7 can impact regions beyond 100 km. (2) Unlike the controlled, simple geometries in laboratory settings, the field exhibits greater geometric complexity. (3) Natural materials in the field are inherently more heterogeneous than those used in laboratory experiments. These complexities necessitate numerical solutions to the PDEs. Additionally, the large spatial scales involved in field simulations pose significant challenges to both computational efficiency and the implementation of numerical algorithms.

Earthquake modeling includes simulation of the rupture dynamics at the source and of radiated seismic waves until they reach the ground surface. Dynamic rupture simulations have been a key area of study to better understand the earthquake rupture process, with pioneering work by Rice (1980) who integrated the principles of fracture mechanics to describe the rupture behavior along faults. His contributions laid the groundwork for understanding the physics of earthquake sources as akin to crack propagation in solid mechanics. Analytical models, often based on simple geometries and homogeneous material properties, offer valuable first-order approximations of the rupture process (Madariaga, 1976; Andrews, 1976; Das and Aki, 1977). These models help to capture the general principles of stress transfer, energy release, and rupture velocity. However, natural fault systems exhibit highly complex behaviors that involve irregular geometries, heterogeneous material properties, and variable stress conditions that cannot be fully captured by analytical approaches.

As a result, numerical simulations have become indispensable for studying the intricacies of earthquake ruptures (Oglesby et al., 1998). These simulations allow the incorporation of more realistic fault geometries, heterogeneous material distributions, and complex bound-

ary conditions that are observed in nature. To model dynamic ruptures with higher fidelity, researchers have developed a variety of numerical algorithms that account for the frictional behavior along the fault interface, which represents the core mechanism driving the rupture process. These frictional interfaces are often modeled to capture rate- and state-dependent friction laws that control the evolution of slip during an earthquake (Dieterich, 1979; Lapusta et al., 2000).

A range of numerical methods have been employed to simulate dynamic ruptures, each with its strengths and limitations. Among the most widely used are boundary integral methods, which are effective in modeling rupture in infinite or semi-infinite domains, reducing the dimensionality of the problem (Geubelle and Rice, 1995; Lapusta and Liu, 2009). The finite difference method (FDM) has also been applied to simulate dynamic ruptures with the summation-by-part operator (Day et al., 2005; Kozdon et al., 2013), offering simplicity in implementation and the ability to model wave propagation efficiently in heterogeneous media. Other techniques include the split-node finite element method (FEM, Barall, 2009), which allows discontinuous displacements across the fault plane compared to the more classical Galerkin FEM (Thomée, 2007). For the same purpose of representing the rupture boundary, the discontinuous Galerkin (DG) method is another approach that has been particularly useful. It can also handle complex fault geometries with high-order accuracy (de la Puente et al., 2009). Due to its element-local operators, the DG method is also highly scalable and can be efficiently parallelized on supercomputers for large-scale simulations (Uphoff et al., 2017; Krenz et al., 2021).

These numerical approaches are crucial for capturing the second-order effects that are often neglected in analytical models, such as the influence of off-fault yielding (Wollherr et al., 2018), fault roughness (Shi and Day, 2013; Taufiqurrahman et al., 2022), and near-field ground motion. As computational power continues to increase, these numerical models are also evolving to account for multi-physics problems, such as fluid flow in fault zones (Wolf et al., 2022; Mosconi et al., 2024; Wolf et al., 2024) and thermal processes that occur during slip (Bizzarri and Cocco, 2006; Herrera et al., 2024).

In the numerical simulation of the radiated seismic wave outside fault zones, many of the numerical methods overlap with those used for dynamic rupture simulations, including FDM, FEM and DG methods. FDM is a straightforward method that approximates spatial and temporal derivatives using finite difference discretizations, which makes it efficient and easy to implement on structured grids. However, it struggles with complex geometries and sharp material discontinuities, which can introduce numerical artifacts (Virieux, 1986; Graves, 1996). One of the most advanced FDM codes for 3D seismic simulations is AWP-ODC (Anelastic Wave Propagation - Olsen, Day, Cui), developed by Olsen et al. (2008) and Roten et al. (2023). FEM solves the wave equation with higher-order accuracy employing more sophisticated basis functions. It is highly versatile, capable of handling complex geometries and heterogeneous media, but it comes with a higher computational cost (Komatitsch and Tromp, 1999). A specialized variant of FEM is the Spectral Element Method (SEM), which combines the geometrical flexibility of FEM with orthogonal basis functions for efficient matrix inversion. SEM is widely used for large-scale 3D seismic simulations because it offers a good balance between accuracy and computational cost (Komatitsch and Vilotte, 1998; Carrington et al., 2008). Lastly, DG allows for discontinuities between elements and ensures the numerical stability at the element interfaces with numer-

ical fluxes (Dumbser and Käser, 2006). It has also been mathematically proven to be stable for handling nonlinear wave equations even with strong nonlinearity (Cockburn et al., 2012) with high-order accuracy (Dumbser et al., 2008; Reinarz et al., 2020). I take advantage of this very useful feature of DG and extend it for modeling regional-scale 3D nonlinear wave propagation in Chapter 3 and for modeling 3D dynamic rupture with co-seismic off-fault damage in Chapter 4.

1.4 Inversion of nonlinear parameters in rupture dynamics

Recent advances in numerical modeling methods have significantly improved our understanding of the parameters governing nonlinear on-fault and off-fault physical processes during earthquakes. These advances enable a more accurate interpretation of earthquake recordings, which are themselves enriched by the continuous development of measurement techniques. Modern innovations such as large node arrays (Mellors et al., 2018; Arrowsmith et al., 2022), ocean bottom stations (Stähler et al., 2016; Marra et al., 2018), and distributed acoustic sensing (DAS, Parker et al., 2014; Zhan, 2020) have dramatically improved the spatial and temporal resolution of seismic data. In addition, specialized laboratories, such as the Bedretto Underground Laboratory (Ma et al., 2022; Mosconi et al., 2024), provide unique opportunities to observe seismic processes in controlled environments, offering valuable insight into fault mechanics.

The availability of richer data sets has already facilitated substantial progress in the inversion of heterogeneous velocity structures of the Earth. Full waveform inversion (FWI, Virieux and Operto, 2009; Fichtner et al., 2013) methods, for instance, have evolved to integrate high-resolution data, enabling a more accurate construction of regional velocity models. Several studies have highlighted the potential of FWI to resolve complex subsurface structures by incorporating diverse datasets, such as DAS (Egorov et al., 2018; Fichtner et al., 2025) and ocean-bottom recordings (Plessix and Perkins, 2010; Operto et al., 2015), into their analysis.

Beyond velocity models, richer datasets also offer the potential to constrain nonlinear parameters associated with dynamic rupture processes at the earthquake sources. Dynamic rupture inversion techniques aim to retrieve detailed information about fault slip evolution, stress changes, and other physical parameters from earthquake observations. One of the first attempts on dynamic rupture inversion dates back to Mikumo et al. (1987), which simplify the rupturing mechanism with a locking fracture criterion. Since then, Peyrat and Olsen (2004) and Twardzik et al. (2014) employ the fully spontaneous dynamic rupture model and the neighborhood inversion algorithm (Sambridge, 1999), a nonlinear derivative-free technique to estimate the best-fit model without sufficient information about uncertainties in the inversion. For the uncertainty analysis, Gallovič et al. (2019) establish and apply a Bayesian dynamic source inversion framework to regional-scale earthquakes (Gallovič et al., 2019; Gallovič and Valentová, 2020). Premus et al. (2020) accelerate the Bayesian inversion for dynamic rupture inversion by more efficient numerical modeling of the dynamic rupturing process. Their inversion scheme increase the resolution of the inversion (Premus et al.,

2022; Schliwa et al., 2024a). However, the acceleration sacrifices the complexities in the geometric complexity of the fault structure, as well as the off-fault nonlinear mechanical processes (Fig. 1.1d and g), which is the core of this dissertation.

Without compromising the accuracy of forward simulations, the parametric derivative information provided by the adjoint-based solver can significantly reduce the number of dynamic rupture simulations required for uncertainty quantification (Gebraad et al., 2020; Zhang et al., 2023). Adjoint-based inversion serves as a cornerstone for achieving high-resolution FWI of the Earth's velocity structure. However, applying the adjoint method to the governing equations of dynamic rupture simulations remains a challenge (Stiernström et al., 2024). These limitations highlight a fundamental challenge in inverting nonlinear parameters in dynamic rupture simulations: minimizing the number of computationally expensive yet accurate simulations while ensuring precise uncertainty quantification of the nonlinear parameters. This challenge motivates my work in Chapters 5 and 6.

1.5 Implementation of nonlinear models in SeisSol

The foundation of this dissertation lies in the implementation of advanced nonlinear models (Section 1.2) within a numerical solver that fully leverages the computational power of modern supercomputing infrastructure. Accurate and efficient numerical solvers are essential both for analyzing the effects of nonlinear rock models on earthquake source mechanisms and ground motions (Section 1.1) and for inverting nonlinear model parameters using an expanding modern dataset (Section 1.4). As highlighted in Section 1.3, the DG algorithm emerges as a particularly robust candidate, offering the flexibility and computational efficiency required to integrate a wide range of nonlinear rock and soil models effectively.

I build on the highly efficient, parallelized numerical solver SeisSol for dynamic rupture and wave propagation simulations (de la Puente et al., 2009; Uphoff et al., 2024). SeisSol applies the Arbitrary-accuracy DERivative (ADER) discretization in time (Titarev and Toro, 2002; Dumbser et al., 2008; Gassner et al., 2011), and the DG discretization in space. The ADER method leverages a one-step prediction-correction and explicit time-stepping scheme. This maintains a high-order convergence rate as the element size decreases (Käser et al., 2008). In earthquake simulations, a convergence rate of order six is commonly used. SeisSol also incorporates a hybrid MPI-OpenMP parallelization strategy, where MPI manages inter-node communication, while OpenMP handles multi-threaded parallelization within each node (Uphoff et al., 2017). Compared to the Runge-Kutta time-stepping (Butcher, 2007), the one-step ADER scheme reduces communication operations between neighboring MPI ranks, enhancing its scalability on a large number of compute nodes.

With more than 15 years of development, SeisSol has already incorporated efficient implementation of a wide range of linear physical models, including linear elasticity and viscoelasticity (Pelties et al., 2012; Uphoff et al., 2017), acousto-elasticity (Krenz et al., 2021), anisotropic elasticity (de la Puente et al., 2007; Wolf et al., 2020a), and poroelasticity (de la Puente et al., 2008; Wolf et al., 2022, 2024). To account for the degradation of off-fault materials under high stress levels during earthquakes, an elasto-plastic model with the

Drucker Prager yielding criterion has been implemented by Wollherr et al. (2018). This is an inelastic nonlinear model that assumes no strain-hardening effect after the stress state touches the yielding surface. However, the return mapping algorithm (Andrews, 2005) allows one to maintain the linear wave propagation solver while accumulating plastic strain. The algorithm also restricts the increase in stress levels within the defined yielding surface.

However, the existing elasto-plastic model is not sufficient to explain most of the nonlinear responses of rocks and soils summarized in Fig. 1.1. Additionally, most models in Section 1.2 require explicit nonlinear stress-strain functions. These two factors motivate the requirement to completely move away from the linear hyperbolic form of the linear wave equations:

$$\frac{\partial u_p^\sigma}{\partial t} + A_{pq}^d \frac{\partial u_q^\varepsilon}{\partial x_d} = E_{pq} u_q^\varepsilon, \tag{1.1}$$

where $\boldsymbol{u}^\sigma = u_p^\sigma = (\sigma_{xx}, \sigma_{yy}, \sigma_{zz}, \sigma_{xy}, \sigma_{yz}, \sigma_{zx}, v_x, v_y, v_z)^T$ is a vector of the conservative variables. σ_{xx}, σ_{yy}, σ_{zz}, σ_{xy}, σ_{yz}, and σ_{zx} are six components of the stress tenser $\boldsymbol{\sigma} = \sigma_{ij}$; v_x, v_y and v_z are the three components of the particle velocity vector $\boldsymbol{v}$. A_{pq}^d are the coefficient matrices where the index d runs from 1 to 3 for waves propagating in three-dimensional space. They consist of the constant material parameters in the linear wave equations, containing the information of wave speed at which the conservative variable u_p gets transferred through a unit area in the direction x_d (LeVeque, 2002). The source $E_{pq} u_q^\sigma$ is a linear function of $\boldsymbol{u}^\sigma$, with E_{pq} being a constant matrix that contains the linear material properties. I refer to Uphoff (2020) for the extended definitions of A_{pq}^d and E_{pq}.

Instead, we need to express the wave equations in the following nonlinear hyperbolic form:

$$\frac{\partial u_p^\varepsilon}{\partial t} + \frac{\partial F_p^d(\boldsymbol{v}, \boldsymbol{\varepsilon}, \boldsymbol{\alpha})}{\partial x_d} = s_p(\boldsymbol{v}, \boldsymbol{\varepsilon}, \boldsymbol{\alpha}), \tag{1.2}$$

where $\boldsymbol{u}^\varepsilon = u_p^\varepsilon = (\varepsilon_{xx}, \varepsilon_{yy}, \varepsilon_{zz}, \varepsilon_{xy}, \varepsilon_{yz}, \varepsilon_{zx}, v_x, v_y, v_z, \boldsymbol{\alpha})^T$ is a vector of the conservative variables. ε_{xx}, ε_{yy}, ε_{zz}, ε_{xy}, ε_{yz}, and ε_{zx} are six components of the strain tenser $\boldsymbol{\varepsilon} = \varepsilon_{ij}$. $\boldsymbol{\alpha}$ is a vector that collects all the physical state variables in the nonlinear stress-strain relationships, which can vary between different models. The flux term F_p^d represents the rates at which the conservative variable q_p gets transferred through a unit area in the direction x_d (LeVeque, 2002). The source vector $\boldsymbol{s} = s_p$ is a vector that consists of nonlinear functions of $\boldsymbol{v}$, $\boldsymbol{\varepsilon}$ and $\boldsymbol{\alpha}$. I refer to Chapter 3 and 4 for the definitions of F_p^d and s_p for four different nonlinear models that show the generic applicability of the nonlinear DG algorithm and its implementation in SeisSol that I develop in this dissertation.

Here, I summarize the key differences in the implementation of nonlinear rock models in SeisSol, compared to the existing linear models:

- SeisSol originally employs the stress-velocity formulations in Eq. (1.1) for the linear seismic wave equations (Uphoff et al., 2024). This works equivalently well as the strain-velocity scheme (Wilcox et al., 2010) for the linear case. However, the majority of the nonlinear models mentioned in Section 1.2 can only express the stress tensor

$\boldsymbol{\sigma}$ as the explicit function of the strain tensor $\boldsymbol{\varepsilon}$. Therefore, it is more convenient in my implementation in this work to re-formulate the wave equations with the strain-velocity scheme, in addition to the change in expression of the flux term from linear to nonlinear.

- The second difference is the way to estimate the discretization coefficient in space and time during the prediction step. Instead of the linear Cauchy-Kovalevskaya approach (Kovalevskaja, 1874). I employ a linearization procedure in the nonlinear models to maintain the HPC-optimized data structure of SeisSol (Uphoff et al., 2024). I release this restriction in the subsequent correction step described later. This assumption preserves the convergence of the algorithm for nonlinear hyperbolic PDEs but can have an effect on the convergence rate with strong nonlinearity, as we will discuss in Chapter 3.

- The third major difference lies in the data to be communicated between neighboring MPI ranks for the correction step of the DG algorithm. As explained by Uphoff (2020), as long as the entire mesh uses a globally uniform time step size, the only information that needs to be passed on to elements in the neighboring ranks is the integrated conservative variable $I_p = \int_{t_n}^{t_{n+1}} u_p^\sigma \mathrm{d}t$ within the current time step $[t_n, t_{n+1}]$. However, for the nonlinear case, the complete set of coefficients for space and time discretization needs to communicated, whose data size can be 1 to 7 times larger depending on the polynomial degrees of the basis functions in DG.

1.6 Scope and outline of this work

This work contains two major objectives: (1) to constrain nonlinear rock models from laboratory and earthquake data and (2) to investigate the impact of nonlinear rock models on the earthquake source mechanism and the ground motions. The advances in these two aspects are achieved based on my adaptation and implementation of the nonlinear DG algorithm in SeisSol with its justified scalability on thousands of compute nodes on supercomputers and its adequate flexibility with the different nonlinear models that can be solved.

Chapter 2 slightly modifies two nonlinear rock models in accordance with the two types of laboratory experiments on quantifying the co-seismic wave speed changes under dynamic stress perturbations. I implement both models in ExaHyPE (Reinarz et al., 2020) for 2D wave propagation and integrate it with a classical Bayesian inversion algorithm to quantify how well the nonlinear model parameters can be constrained from the data in the laboratory experiments. This study justifies the validity of these two physical models in explaining the observed co-seismic wave speed changes.

Chapter 3 extends these two justified nonlinear models to 3D regional-scale modeling of seismic wave propagation during earthquakes. I introduce a nonlinear DG algorithm that is flexible for solving different nonlinear models, demonstrated with three examples, including the two in Chapter 2. With these models, I verify the numerical solutions against existing analytical solutions and apply one of the constrained models in Chapter 2 to the 2015

M_w 7.8 Ghorka earthquake in the Kathmandu valley. The unique merit of this work is its capability of generating the spatial distribution of the co-seismic wave speed changes after earthquakes using physics-based simulations. We also compare the modeled ground motions within the sedimentary Kathmandu basin of this nonlinear model with those of linear elastic, visco-elastic, and elasto-plastic models.

Chapter 4 further demonstrates the adaptability of the proposed DG algorithm in this work by implementing an additional nonlinear rock model that is well suited for investigating earthquake source mechanisms with co-seismic off-fault moduli reduction. In this work, I couple the wave propagation algorithm with the frictional boundaries at fault surfaces for 3D dynamic rupture simulations. This work enables the investigation of the impacts of co-seismic off-fault moduli reduction on the earthquake energy budgets, source frequency components of the seismic radiation, and interactions among different fault segments.

Chapters 5 and 6 focus on how to constrain the nonlinear model parameters in dynamic rupture simulations from data in earthquakes. Chapter 5 integrates an efficient and scalable Bayesian inversion algorithm with SeisSol for parallel execution of ensembles of dynamic rupture models for inversion using supercomputer clusters. This work shows how the new inversion algorithm reduces the number of dynamic rupture simulations required for the inversion. The other aspect of this work is to show how the additional levels of parallelization from the inversion algorithm contribute to the efficient execution of SeisSol simulations on the full machine of supercomputers.

Finally, Chapter 6 shows the application of the above integrated configurations on supercomputers to the inversion of nonlinear on-fault and off-fault parameters from multidisciplinary ground motion recordings during the 2019 M_w 7.1 Ridgecrest earthquake. The dynamic rupture model in this inversion consists of surface topography of the ground, curved sub-parallel and conjugate fault structures, nonlinear on-fault friction laws, as well as off-fault inelastic deformation, which is for the first time integrated in the dynamic rupture inversion. The inversion quantifies the uncertainties in the fault slip distribution, which are also constrained by laws of physics, in contrast to the kinematic source inversion. The geometric and physical complexity involved in the dynamic rupture model in this chapter also highlights the applicability of the inversion scheme to other earthquakes.

Chapter 2 has been published in the Journal of Geophysical Research: Solid Earth as

- Niu, Z., Gabriel, A. A., Seelinger, L., & Igel, H. (2024). Modeling and quantifying parameter uncertainty of co-seismic non-classical nonlinearity in rocks. Journal of Geophysical Research: Solid Earth, 129(1), e2023JB027149, DOI 10.1029/2023JB027149.

Chapter 3 has received the Outstanding Student Presentation Award (OSPA) at the American Geophysical Union's (AGU) annual meeting, 2023, and has been submitted in a slightly altered form to the Journal of Geophysical Research: Solid Earth as

- Niu, Z., Gabriel, A. A., Wolf, S., Ulrich, T., Lyakhovsky, V., & Igel, H. (2025). A discontinuous Galerkin method for simulating 3D seismic wave propagation in nonlinear rock models: verification and application to the 2015 M_w 7.8 Gorkha earthquake,

submitted to Journal of Geophysical Research: Solid Earth.

Chapter 4 will be submitted for publication shortly as

- Niu, Z., Gabriel, A. A., Ben-Zion, Y., & Igel, H. (2025). Amplified seismic radiation and delayed dynamic triggering: brittle rock damage as a catalyst for 3D cascading earthquake dynamics, in preparation for submission to Geophysical Research Letters.

Chapter 5 has been accepted in a slightly altered form with minor revision as

- Kruse, M., Niu, Z., Seelinger, L., Wolf, S., Lykkegaard, M., Bader, M., Gabriel, A. A., Bader, M., Seelinger, L. Scalable Bayesian inference of large simulations via asynchronous prefetching multilevel delayed acceptance. Proceedings of the Platform for Advanced Scientific Computing Conference, Windisch, Switzerland, 2025, Association for Computing Machinery.

Chapter 6 will also be submitted for publication as

- Niu, Z., Kruse, M., Seelinger, L., Schliwa, N., Igel, H., Bader, M., Gabriel, A. A. (2025). Bayesian inversion of on-fault friction and off-fault plastic deformation in the 2019 M_w 7.1 Ridgecrest earthquake with dynamic rupture simulations, in preparation.

Chapter 2

Bayesian-inversion constrained nonlinear rock models from laboratory data

Dynamic perturbations reveal unconventional nonlinear behavior in rocks, as evidenced by field and laboratory studies. During the passage of seismic waves, rocks exhibit a decrease in elastic moduli, slowly recovering after. Yet, comprehensive physical models describing these moduli alterations remain sparse and insufficiently validated against observations. Here, we demonstrate the applicability of two physical damage models - the internal variable model (IVM) and the continuum damage model (CDM) - to provide quantitative descriptions of nonlinear co-seismic elastic wave propagation observations. While the IVM uses one internal variable to describe the evolution of elastic material moduli, the CDM damage variable is a mathematical representation of microscopic defects. We recast the IVM and CDM models as nonlinear hyperbolic partial differential equations and implement 1D and 2D numerical simulations using an arbitrary high-order discontinuous Galerkin method. We verify the modeling results with co-propagating acousto-elastic experimental measurements. Subsequently, we infer the parameters for these nonlinear models from laboratory experiments using probabilistic Bayesian inversion and 2D simulations. By adopting the Adaptive Metropolis Markov chain Monte Carlo method, we quantify the uncertainties of inferred parameters for both physical models, investigating their interplay in 70,000 simulations. We find that the damage variables can trade off with the stress-strain nonlinearity in discernible ways. We discuss physical interpretations of both damage models and that our CDM quantitatively captures an observed damage increase with perturbation frequency. Our results contribute to a more holistic understanding of co-seismic damage and post-seismic recovery after earthquakes bridging the worlds of theoretical analysis and laboratory findings.

2.1 Introduction

Materials with micro- and mesoscale heterogeneities, such as rocks and cementitious materials, have been widely observed to exhibit non-classical nonlinearity (Guyer and Johnson, 1999; Van Den Abeele et al., 2000; Johnson and Sutin, 2005). In classical nonlinearity, researchers formulate stress as a nonlinear function of strain (e.g., the second order stress-strain models of Murnaghan (1937) and Hamiel et al. (2011); the third order stress-strain models in Landau et al. (1986)). Classical nonlinearity can describe how the speeds of elastic waves depend on the stress state of the material (Pao and Gamer, 1985),

This chapter has been published as Niu, Z., Gabriel, A. A., Seelinger, L., & Igel, H. (2024). Modeling and quantifying parameter uncertainty of co-seismic non-classical nonlinearity in rocks. Journal of Geophysical Research: Solid Earth, 129(1), e2023JB027149, DOI 10.1029/2023JB027149.

as well as the different stress-strain relationships between compression and extension. Recent examples are the "bi-linear" models suggested by Pecorari and Solodov (2006) and Panteleev et al. (2021). However, they are proposed to account for neither the different stress-strain relationships during loading and unloading nor the time-dependent mechanical behavior of materials like rocks (Van Den Abeele et al., 2000). In this work, we define non-classical nonlinearity as the behavior of rocks that cannot be explained by formulating stress as a nonlinear function of strain. One type of such non-classical nonlinearity can be characterized by hysteresis models (Preisach, 1935; Mayergoyz, 1985; McCall and Guyer, 1996). Hysteresis models describe stress as a function of not only the current strain state, but of the strain history as well. Aside from hysteresis, researchers noticed that, under continuous dynamic external loads, the mechanical responses of rocks may change over time. Experimental observations of such non-classical nonlinearity were first reported in Ten Cate and Shankland (1996) from Nonlinear Resonance Ultrasound Spectroscopy (NRUS) experiments. In their NRUS, the sample's dynamic response to the excitation at the same frequency is unexpectedly different depending on whether it is measured during the upward or downward sweep across different frequencies. We refer to TenCate (2011) and references therein for a comprehensive summary of the NRUS observations of the latter type of non-classical nonlinearity.

Details on how rock moduli change during dynamic perturbations were first reported by Renaud et al. (2012) who performed Dynamic Acousto-elastic Testing (DAET) experiments on Barea sandstone. Since then, DAET experiments have been developed and conducted on different types of rock samples (e.g., Rivière et al., 2013, 2015; Jin et al., 2018). Fig. 2.1 shows a recent DAET measurement by Shokouhi et al. (2017) on Berea sandstone samples. We will refer to all three phases illustrated in Figs. 2.1b and c as "slow dynamics" (following e.g., Johnson and Sutin, 2005; Rivière et al., 2015; Shokouhi et al., 2017; Manogharan et al., 2021).

Similar observations have also been reported from the field since the pioneering work of Sens-Schönfelder and Wegler (2006) and Brenguier et al. (2008a). Gassenmeier et al. (2016) monitor the change of seismic velocity around the station PATCX from the Integrated Plate Boundary Observatory Chile Network (IPOC, 2006). During the occurrence of the M_w 7.7 Tocopilla earthquake in Chile on November 14th, 2007, Gassenmeier et al. (2016) observe a drop and subsequent recovery of seismic velocity within a radius of $\approx$ 2.3 km surrounding a station that is about 100 km away from the fault using coda wave interferometry in the frequency range of 4-6 Hz. Similar co-seismic velocity drops are reported to occur not only during large earthquakes but also due to intermediate earthquakes with magnitudes between M_w 5 and M_w 7. Brenguier et al. (2014) map the co-seismic velocity drop in Japan after the 2011 Tohoku-Oki earthquake (see Fig. 2.1d) using data from the high sensitivity seismograph network (Hi-net) in Japan (Takanami et al., 2003). While it is commonly assumed that transient fluid effects are key to the observed velocity drop (Brenguier et al., 2014; Illien et al., 2022), Manogharan et al. (2021, 2022) find that a velocity drop during dynamic perturbations of fractured fluid-saturated rocks is not more significant than that of fractured dry rocks.

Despite phenomenologically comparable observations, it is currently unclear how relevant the non-classical nonlinearity observed in laboratory experiments is to the observed co-seismic velocity drops in the field and if an overarching theoretical physical framework

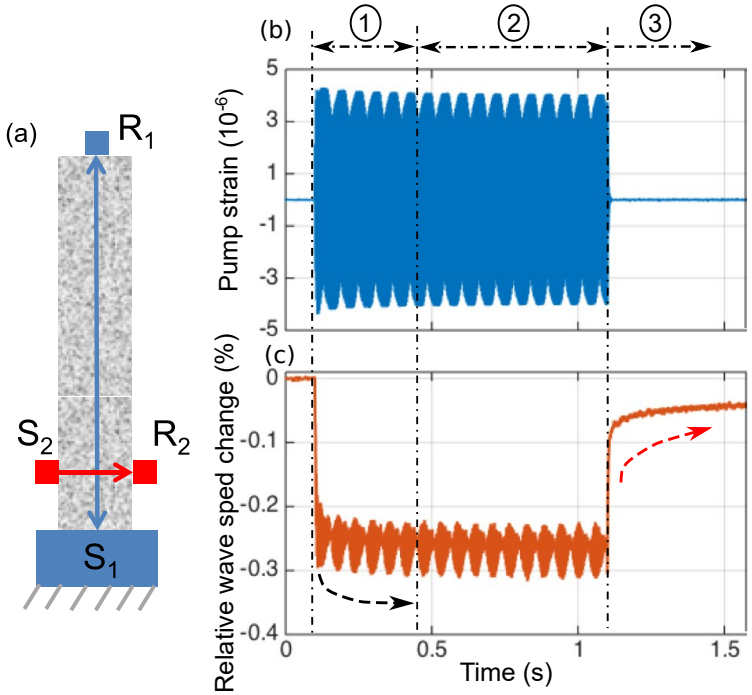

Figure 2.1: Dynamic acousto-elastic testing (DAET) by Shokouhi et al. (2017) on Berea sandstone samples. (a) The pump-probe system in DAET. S1-R1 is the pumping sensor pair. S1 is a piezoelectric ceramic disk glued to the sample. S1 generates a dynamic strain field (the pump field) with an amplitude of around 4×10^{-6} and a frequency of around 4.5 kHz. R1 is a miniature accelerometer that measures the dynamic strain field (the pump field) generated by S1. The probing ultrasonic transducer pair S2-R2 measures the change of the P-wave speed Δc_p due to the pump field. (b) The pump field measured with R1. (c) The measured relative change in P-wave speed $\Delta c_p/c_{p0}$, due to the pump field, with S2-R2. Here, c_{p0} is the initial P-wave speed of the sample. In response to the dynamic strain field from S1, the wave speed evolves in three consecutive phases: (1) As loading starts, the wave velocity of the sample reaches a non-equilibrium state and experiences an overall drop aside from fluctuations with the cyclic loading. This phase is referred to as the conditioning of the material and is marked by a dashed black curve with an arrow; (2) The overall drop of wave velocity stabilizes and reaches a new steady state; (3) After removing the cyclic loading, the velocity recovers over an extended period of time, illustrated by the dashed red curve with an arrow.

can be established. Furthermore, despite the relatively low velocity drops (usually smaller than 1%) using ambient noises and coda wave Interferometry (e.g., Brenguier et al., 2014; Gassenmeier et al., 2016; Illien et al., 2022), more recent measurements based on auto-correlation of a single station (Lu and Ben-Zion, 2022) or the combination of surface and borehole stations (Qin et al., 2020; Wang et al., 2021), observed velocity drop can be higher than 10%. Unifying laboratory and field observations is challenged by the vastly different scales and sparsity of high-resolution observations. We need an appropriate physical model that can be employed at both scales.

At the field scale, a range of models has been proposed to explain or predict source and site effects of nonlinearity on earthquake nucleation, rupture dynamics, and ground motions. The Masing-Prager-Ishlinski-Iwan (MPII) model (Iwan, 1967) has been implemented to study local non-linear site effects due to soft sediments (Roten et al., 2013, 2018; Oral et al., 2019, 2022). The MPII model reproduces the hysteretic stress-strain relations and can be extended to explain the excess pore pressure in liquefiable soils (Oral et al., 2019). The nonlinearity of fault zone deformation has been modeled as co-seismic off-fault brittle continuum damage (e.g., Xu et al., 2015; Thomas and Bhat, 2018) or non-associative Drucker-Prager off-fault plasticity (e.g., Andrews, 2005; Wollherr et al., 2018), explicit secondary tensile and shear fracturing (Okubo et al., 2020; Yamashita, 2000; Gabriel et al., 2021), using a volumetric representation of fault zones governed by reformulated rate-and-state friction laws (Preuss et al., 2019, 2020; Pranger et al., 2022) or phase-field inspired methods (e.g., Fei et al., 2023). However, a physical model that can be used to explain the co-seismic drop of wave speeds and subsequent recovery is missing. This paper focuses on identifying appropriate theoretical model(s) that can be informed and verified by laboratory experiments and are applicable for future large-scale numerical simulations (e.g., Roten et al., 2023) of seismological observations on the field scale.

Over the past two decades, researchers have proposed different models to explain non-classical nonlinearity with physical processes at the microscopic scale. Delsanto and Scalerandi (2003) proposed a model that includes thermally activated random transitions between two different interstitial states. Since then, many studies have used the framework of adhesive contacts at rough crack surfaces to explain slow dynamics (Pecorari, 2004; Aleshin and Van Den Abeele, 2007; Lebedev and Ostrovsky, 2014; Wang et al., 2021). We briefly summarize the basic ideas of the adhesive contact theory in Appendix 2.E.

While the above physical models are firmly rooted in processes at the microscopic scale, they introduce a significant number of parameters. Many of these parameters are hard to constrain directly from observations. Also, the proposed models are restricted to 0D (oscillation) or 1D analysis, and extension to 2D and 3D would require a substantial effort although it is crucial for the verification and interpretation of field observations. There also exist phenomenological models, with fewer parameters, that have been developed over the last two decades, such as the soft ratchet model of Vakhnenko et al. (2004, 2005). Their model includes a fast subsystem of displacement and a slow subsystem of ruptured intergrain cohesive bonds. The concentration of the ruptured bonds is represented by an internal (damage) variable that evolves to a stress-dependent equilibrium. Later, Favrie et al. (2015) fully couple these two subsystems.

Berjamin et al. (2017) extend the description of Favrie et al. (2015) by using one internal

variable to describe the evolution of elastic material moduli. This model will be herein referred to as the internal variable model (IVM) in the following. IVM ensures that the kinematics of the internal variable complies with the laws of thermodynamics. The model can reproduce the conditioning and recovery phases of nonclassical nonlinear elasticity with only two additional parameters than those used in classical nonlinearity. However, their expression for the internal energy of the material contains a term that is not clearly linked to physical processes.

In this work, we offer a physics-based understanding of the origin of such a phenomenological term. To this end, we resort to continuum damage mechanics (CDM) (Kachanov, 1958, 1986). We show that the internal variable in Berjamin et al. (2017) is very similar to a scalar damage variable in typical CDM approaches (Chaboche, 1988). The scalar damage variable approach is popular in diffuse interface approaches, e.g., to 'smear out' sharp discontinuous cracks via a smooth but rapid transition between intact and fully damaged material states (Borst et al., 2004; Tavelli et al., 2020). In the CDM context, the damage variable is a mathematical representation of defects, e.g. intergranular cavities or microcracks density, which are distributed in a solid. Different CDM models are characterized by different assumptions on the distribution of microscopic defects and by the various mathematical operations of homogenization. Budiansky and O'connell (1976) derive the elastic moduli as a function of the damage variable with the homogenization of cracks whose directions are uniformly and omnidirectionally distributed. The Godunov–Peshkov–Romenski (GPR) model (Resnyansky et al., 2003; Romenski et al., 2007; Tavelli et al., 2020; Gabriel et al., 2021) uses a different homogenization scheme, continuum mixture theory (Romenski and Toro, 2004), to define a material that is a mixture of a "totally-damaged" and an "undamaged" constituents. It is also possible to account for different elastic behaviors during extension and compression within the framework of CDM, for example, the "unilateral" damage model from Chaboche (1992), Lemaitre and Desmorat (2006), and Desmorat (2016).

However, the above CDM-based damage models do not allow healing. The continuum damage healing model (CDHM) introduces an additional healing variable aside from the damage variable (Darabi et al., 2012; Oucif and Mauludin, 2018). A potentially simpler framework that can allow healing is the damage model proposed by Lyakhovsky et al. (1997a). It is based on homogenizing micro-cracks oriented perpendicular to the maximum tension (or compression). This is different from other damage models based on the homogenization of cracks oriented uniformly and omnidirectionally (e.g., Budiansky and O'connell, 1976; Chaboche, 1988; Borst et al., 2004). The internal energy of this model is not unconditionally decreasing with the increase of the damage variable. However, it has not yet been investigated how this model can be related to observed slow dynamics. We summarize these and other representative damage models with respect to non-classical nonlinearity in Table 2.E.1.

From the above overview of models, we notice that the models of Berjamin et al. (2017) and Lyakhovsky et al. (1997a) both have the potential to reproduce all three phases of slow dynamics with a small number of model parameters. In the following, we will focus on two models, IVM by Berjamin et al. (2017) and CDM by Lyakhovsky et al. (1997a), and will refer to them as "model B" and "model L", respectively, for brevity. We hope to answer the following questions about the two models in this work. However, it has not been explored, if they can quantitatively reproduce the modulus changes, of rocks observed in laboratory

experiments, or how well laboratory findings may constrain theoretical model parameters.

To investigate these questions, we implement both models in the arbitrary high-order discontinuous Galerkin (ADER-DG) solver ExaHyPE (Reinarz et al., 2020) and verify the numerical simulation results with experimental observations. We infer model parameters from laboratory measurements using a Markov chain Monte Carlo (MCMC, Metropolis et al. (1953)) algorithm. This takes uncertainties due to measurement errors into account and allows us to investigate model parameters' relative importance and their interactions. Lastly, we discuss that the CDM model by Lyakhovsky et al. (1997a) may be a preferred model for large-scale wave propagation simulations capable of linking observations of coseismic damage in the field with laboratory findings and continuum damage mechanics theory.

In Section 2.2, the two models of Lyakhovsky et al. (1997a) and Berjamin et al. (2017) (model L and model B hereafter) are summarized within the framework of thermodynamics. We propose a way to explain the origin of the phenomenological term in the model of Berjamin et al. (2017). We then describe the numerical simulation of the nonlinear wave propagation with the two models. This is followed by a description of the experiment that we will compare to the Bayesian problem used for parameter inference and the Adaptive Metropolis Markov chain Monte Carlo (AM-MCMC) method solving it. In Section 2.3, we compare the two models regarding the damage evolution during dynamic acousto-elastic testing and measured amplitude- and frequency-dependent damage. The inversion results of the model parameters are also shown. Finally, the performance and restrictions of the two models will be discussed in Section 2.4.

2.2 Methods

We separate this section into two parts. We first detail the derivation of the nonlinear damage models based on the laws of thermodynamics. This approach ensures that the model parameterization we derive has a clear physical meaning. Based on our thermodynamically motivated derivation, we aim to infer physical constraints on slow dynamics that are beyond phenomenological descriptions. We then describe the experiment and the Adaptive Metropolis Markov chain Monte Carlo (AM-MCMC) method that we use to evaluate the model parameters.

2.2.1 The thermodynamic formulation of nonlinear damage models

In the framework of continuum damage mechanics (see Chapter 3 of Zhang and Cai, 2010), a scalar variable can describe the changes in elastic moduli with damage. We start with the 1st law of thermodynamics,

$$\dot{e} = \dot{w} + \dot{q}, \tag{2.1}$$

where $\dot{(\cdot)}$ denotes the time derivative, e is the specific internal energy of the system normalized by volume, w is the external work per unit volume of the system and q is the absorbed heat from the environment per unit volume of the system. At the time scale of elastodynamic processes, the heat transfer and any possible heat sources are assumed to be negligible, i.e. we assume an adiabatic process where $\dot{q} = 0$. In case of only considering mechanical work, it is $\dot{w} = \underset{=}{\sigma} : \dot{\underset{=}{\epsilon}} = \sigma_{ij}\dot{\epsilon}_{ij}$ and $\underset{=}{(\cdot)}$ denotes a tensor of rank two.

The expression of the internal energy depends on the choice of state variables that are used to describe the system. For an elastic material, we chose the strain $\underset{=}{\varepsilon}$ and the specific entropy s as state variables. In addition, to incorporate the damage to the material, we include another scalar state variable α. This means $e \equiv e(s, \underset{=}{\varepsilon}, \alpha)$.

With the above definitions of state variables, the Gibbs identity can be written as

$$\dot{e} = T\dot{s} + \frac{\partial e}{\partial \underset{=}{\varepsilon}} : \dot{\underset{=}{\varepsilon}} + \frac{\partial e}{\partial \alpha}\dot{\alpha}, \tag{2.2}$$

where $T = \dfrac{\partial e}{\partial s} > 0$ is the absolute temperature.

Different nonlinear or damage models have different ways of defining the internal energy as a function of $\underset{=}{\varepsilon}$ and α. The combination of Eqs. (2.1) and (2.2), together with the earlier defined assumptions of $\dot{q} = 0$ and $\dot{w} = \underset{=}{\sigma} : \dot{\underset{=}{\varepsilon}}$, yields

$$T\dot{s} = (\underset{=}{\sigma} - \frac{\partial e}{\partial \underset{=}{\varepsilon}}) : \dot{\underset{=}{\epsilon}} - \frac{\partial e}{\partial \alpha}\dot{\alpha}. \tag{2.3}$$

For a spontaneous process in an adiabatic system, $\mathrm{d}s \geq 0$ for any given $\dot{\varepsilon}$ and $\dot{\alpha}$, which is known as the Clausius–Duhem inequality (Truesdell, 1952). Assuming $\underset{=}{\sigma}$ is independent of $\dot{\varepsilon}$, we derive that

$$\underset{=}{\sigma} = \frac{\partial e}{\partial \underset{=}{\varepsilon}}, \tag{2.4}$$

and

$$\frac{\partial e}{\partial \alpha}\dot{\alpha} \leq 0, \tag{2.5}$$

where $\dfrac{\partial e}{\partial \alpha}$ can be any function of the state variables. Eq. (2.5) describes the evolution of the damage variable α. A simple and non-trivial (non-zero) expression can be

$$\frac{\partial e}{\partial \alpha} = -\tau\dot{\alpha}, \tag{2.6}$$

where τ can be any non-negative constant or non-negative function of the state variables. In Eq. (2.6), we see that damaged material will only heal ($\dot{\alpha} < 0$) when $\tau > 0$ and $\frac{\partial e}{\partial \alpha} > 0$; otherwise damage will steadily accumulate. More specifically, our derivation indicates that the system's internal energy shall not always decrease with an increase of damage, when the healing of the material follows a physically meaningful model. Such interpretation is possible since we use the framework of a continuum damage model. Substituting Eq. (2.6) and (2.4) into Eq. (2.3) yields the energy dissipation rate of the system,

$$\mathscr{D} = T\dot{s} = \begin{cases} 0 & \text{if } \tau = 0 \\ \frac{1}{\tau}(\frac{\partial e}{\partial \alpha})^2 & \text{if } \tau > 0 \end{cases}. \tag{2.7}$$

Both model L (Lyakhovsky et al., 1997a) and model B (Berjamin et al., 2017) describe the mechanisms of damage and recovery. But they are introduced under different assumptions regarding the form of the internal energy as a function of strain $\underline{\underline{\varepsilon}}$ and the damage variable α. The internal variable of Berjamin et al. (2017) is defined as

$$e = (1-\alpha)\mathcal{E}(\underline{\underline{\varepsilon}}) + \phi(\alpha), \tag{2.8}$$

where $\phi(\alpha)$ is called the storage energy and increases with the development of damage. In the 1D case where only $\varepsilon_{xx} = \varepsilon$ is non-zero, Berjamin et al. (2017) express the elastic energy term in the internal energy as $\mathcal{E} = (\frac{1}{2} - \frac{\beta}{3}\varepsilon - \frac{\delta}{4}\varepsilon^2)M\varepsilon^2$ based on Landau's law (Landau et al., 1986), where $M = \lambda + 2\mu$ is acoustic modulus while λ and μ are the two Lamé parameters. In the 2D plane-strain case, Berjamin et al. (2019) use the Murnaghan's law $\mathcal{E} = \frac{\lambda+2\mu}{2}E_I^2 - 2\mu E_{II} + \frac{l+2m}{3}E_I^3 - 2mE_IE_{II} + nE_{III}$ (Murnaghan, 1937). l, m, and n are the three Murnaghan coefficients (third-order elastic constants), while $E_I = \epsilon_{kk}$, $E_{II} = 1/2((\epsilon_{kk})^2 - \epsilon_{ij}\epsilon_{ij})$ and $E_{III} = \delta_{ijk}\epsilon_{i1}\epsilon_{j2}\epsilon_{k3}$ are three stress invariants that are defined in Berjamin et al. (2019). δ_{ijk} denotes Levi-Civita permutation symbol.

According to Eq. (2.6), the damage evolution then reads

$$\dot{\alpha} = \frac{1}{\tau}(\mathcal{E}(\underline{\underline{\varepsilon}}) - \phi'(\alpha)), \tag{2.9}$$

where Berjamin et al. (2017) proposed two possible expressions of ϕ: $\phi'(\alpha) = \gamma_b\frac{\alpha}{1-\alpha^2}$ or $\phi'(\alpha) = \gamma_b\alpha$. The scaling factor τ is formulated as $\tau = \gamma_b\tau_b$, where γ_b is the scale of storage energy $\phi(\alpha)$ and τ_b is the time scale of damage evolution.

In the model L proposed by Lyakhovsky et al. (1997a) internal energy is defined as

$$e = \mathcal{E}(\underline{\underline{\varepsilon}}, \alpha) - \gamma I_1\sqrt{I_2}, \tag{2.10}$$

where, in the linear elastic case, $\mathcal{E}(\underline{\underline{\varepsilon}}, \alpha) = \frac{\lambda}{2}I_1^2 + \mu I_2$, $I_1 = \varepsilon_{kk}$ and $I_2 = \varepsilon_{ij}\varepsilon_{ij}$ are the

first and the second strain invariant, and γ is a third modulus that originates from the homogenization of parallel cracks (Lyakhovsky et al., 1997b). It is assumed that $\lambda = \lambda_0$, $\mu = \mu_0 - \alpha\mu_r$ and $\gamma = \alpha\gamma_r$. The corresponding damage kinematics is then derived by inserting Eq. (2.10) into Eq. (2.6).

$$\begin{aligned}\dot{\alpha} &= C_d\gamma_r(I_1\sqrt{I_2} - \xi_0 I_2) \\ &= C_d\gamma_r I_2(\xi - \xi_0),\end{aligned} \tag{2.11}$$

where $\xi_0 = -\dfrac{\mu_r}{\lambda_r}$ and is a negative parameter for solid materials; $\xi = I_1/\sqrt{I_2}$ and C_d can be any non-negative function of the state variables $\underset{=}{\epsilon}$ and α. We note that the material heals ($\dot{\alpha} < 0$) when $\xi - \xi_0 < 0$ and is damaged ($\dot{\alpha} > 0$) when $\xi - \xi_0 > 0$.

A comparison of Eqs. (2.9) and (2.11) shows that both models in principle include the mechanics of healing. However, the crucial term ϕ for explaining slow dynamics in model B in Eq.(2.8) has only limited physical meaning, which challenges the interpretation of the physical mechanisms driving the observed slow dynamics (Fig. 2.1c). On the other hand, conditioning and healing were not yet explored using the model L of Lyakhovsky et al. (1997a).

So far we have summarized model L and model B in the same thermodynamics framework. Next, we explain why, based on model L, it may be physically plausible to include a term in the internal energy W that can increase with damage and how this term can result in both the conditioning during dynamic perturbations and the recovery after removing the perturbations. We here propose that the steady state (phase 2 in Fig. 2.1c) during perturbations can be recovered by assuming the following form of damage kinematics in Eq.(2.12) for the model L that differentiates the evolution laws during the recovery from that during the damage. A recovery phase after dynamic perturbations can occur if an initial strain that satisfies $\xi - \xi_0 < 0$ exists. This strain level does not need to be large since ξ is only related to the relative magnitude of each strain component (i.e., the shape of the strain tensor).

$$\dot{\alpha} = \begin{cases} C_d(\alpha)\gamma_r I_2(\xi - \xi_0) & \text{if } \xi - \xi_0 > 0 \text{ and } \alpha \geq 0 \\ C_r(\alpha)\gamma_r I_2(\xi - \xi_0) & \text{if } \xi - \xi_0 \leq 0 \text{ and } \alpha \geq 0 \\ 0 & \text{if } \alpha < 0 \end{cases}. \tag{2.12}$$

The evolution laws during 'damage' ($C_d(\alpha)$, the conditioning during dynamic perturbations) and recovery ($C_r(\alpha)$) are treated separately. The steady state (phase 2 in Fig. 2.1c) requires the increase of $C_d(\alpha)$, the decrease of $C_r(\alpha)$ or both. At the same time, $C_d(\alpha)$ and $C_r(\alpha)$ are required to remain non-negative to preserve a non-decreasing entropy of the system according to Eq. (2.7). With the above considerations, we choose $C_d(\alpha) = c_d \exp(-\dfrac{\alpha}{\alpha_d})$ and $C_r(\alpha) = c_r\alpha$ to represent, respectively, the decrease of damage coefficient C_d and the increase of recovery coefficient C_r with the increase of the damage variable.

Our proposed damage evolution still follows the laws of thermodynamics. We show in

Section 2.3 that the combination of Eq. (2.12) and the existence of a well-defined initial strain level recovers many aspects of the observed slow dynamics.

2.2.2 Verification, validation and parameter constraints using laboratory observations

We implement both models in ExaHyPE (Reinarz et al., 2020), an engine built for solving nonlinear hyperbolic partial differential equations (PDEs) with the arbitrary high-order derivative discontinuous Galerkin (ADER-DG) method. In Appendix 2.B, we verify the implementation by comparing our numerical solutions with those given by Berjamin et al. (2019), who implemented model B in 2D under plain-strain conditions using the finite volume method with flux limiters. We provide the comparison of our simulation with those from Berjamin et al. (2019) in Fig. 2.B.1. In the following, we focus on validating the performance of model B and model L against laboratory observations.

We generate ensembles of our numerical simulations using the two models and compare to laboratory measurements. One of the main advantages of model B (IVM) and model L (CDM) is that they have fewer parameters and, therefore may be easier to constrain than models that are established on detailed physical processes at microscopic scales. We apply Bayesian inversion to quantify how well the model parameters can be constrained from laboratory experiments. Most laboratory experiments of slow dynamics are based on 1D setups. Feng et al. (2018) proposed an experimental setup (copropagating acousto-elastic testing, Fig. 2.2) that enables the observation of acoustic modulus change during the propagation of waves in a rock sample. In the following, we first describe the experimental setup. Next, we formulate a Bayesian inversion problem that we apply for quantitative characterization of the theoretical model parameters and their associated uncertainties with respect to reproducing laboratory results. The Bayesian inversion problem is solved with a Markov chain Monte Carlo (MCMC, Metropolis et al. (1953)) type method.

Laboratory verification experiment measuring slow dynamics in 2D

The experiment is conducted using a sample of Crab Orchard sandstone of size 15 cm × 15 cm × 5 cm. Feng et al. (2018) attached two ultrasound transducers and one receiver to the rock sample as shown in Fig. 2.2a. T1 is a low-energy high-frequency (HF) transmission ultrasound (US) transducer, the probe, and R1 is a HF reception US transducer. T2 is a high-energy low frequency (LF) transmission US transducer, the pump, and R2 is the laser vibrometer. In the experiment, T2 generates a pumping signal with a frequency of 74 kHz. The particle velocity field excited by T2 is measured with the vibrometer R2 and the particle velocity is converted to the strain (ε_{xx}) along the ray path A between T1 and R1. The P-wave speed along the ray path A is probed with a 620 kHz signal from T1. The amplitude of the perturbation by T1 is of much lower amplitude than that by T2 and is therefore assumed to not perturb the strain field. Once T2 is triggered at t_0, T1 will send signals every 1 μs to measure the P-wave speed along the ray path A. The time difference between the signal from T1 and t_0 is called "trigger delay". The strain field at the wavefront

of each trigger delay along the ray path A is averaged and shown in Fig. 2.2b. The acoustic modulus change $\Delta M/M_0$ is computed from the change in P-wave speed of each trigger delay in Fig. 2.2c.

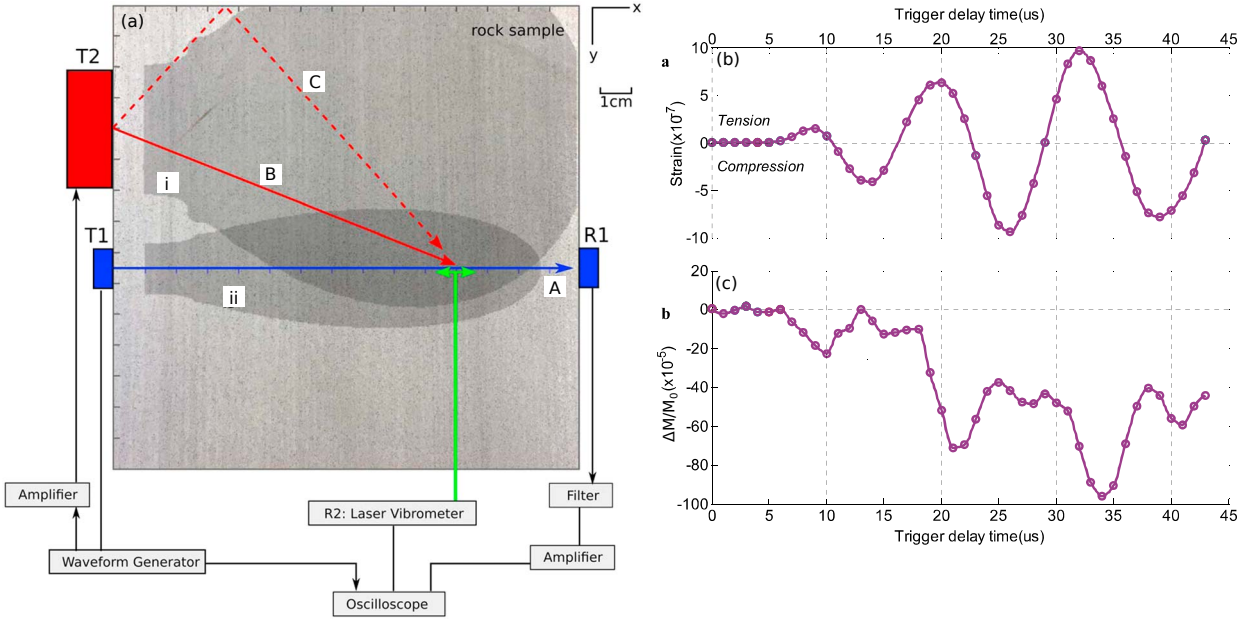

Figure 2.2: (a) Experimental setup to perform copropagating acousto-elastic testing (Figure adapted from Feng et al., 2018). T1 is a low-energy high-frequency (HF) transmission ultrasound (US) transducer, the probe, and R1 is the receiver of T1. T2 is a high-energy low frequency (LF) transmission US transducer. The induced velocity field is recorded by the laser vibrometer R2. The velocity field is converted to the strain field with the method described by Feng et al. (2018). The shadowed areas indicate the radiation pattern (amplitude as a function of angle) of (i) T2 and (ii) T1. Line A is the direct ray path from T1 to R1, line B is the direct ray path from T2 to a point of wave interaction at (8.5, 11.0) cm, and the dashed line C shows the ray path for the wave from T2 reflected at the top boundary of the sample that arrives at that same point of interaction at (8.5, 11.0) cm. (b) The strain (ε_{xx}) measured at the wavefront of the waves that are excited from T1 at different trigger time delays. Each data point is the averaged strain at the wavefront during its propagation from T1 to R1. (c) The estimated relative change in acoustic modulus, based on the travel time difference between T1 and R1, as a function of the trigger time delays. Acoustic modulus $M = \lambda + 2\mu$. M_0 is the M without the pumping signals, while ΔM is the change in M during the propagation of the pumping signals.

Feng et al. (2018) explain the relation between the strain field and the acoustic modulus change with the nonlinear visco-elastic relationship. They observe a time shift of around 2 μs between the peak in the acoustic modulus change and in strain, which is fit by imposing a "delay time" Δt in the visco-elastic relationship. We show in this work that the data may also be explained with the proposed damage models, without having to impose a "delay time" for explaining the time shift.

Probabilistic inversion and uncertainty quantification with a Markov chain Monte Carlo approach

We begin by defining configurations of our two competing deterministic models, matching the experimental setup. Next, we augment the deterministic models by embedding them in a Bayesian inversion problem. This allows us to infer model parameters from data and discover their interactions, taking into account possible ambiguities and the effect of uncertainties in experimental measurements.

Deterministic models

We model the 2D slow dynamics experimental setup with both the L and the B models. The perturbation from T2 is simulated as a Dirichlet boundary condition distributed in the area where T2 is in contact with the sample. The remaining boundaries are treated as free surfaces with zero traction. As in the experiment, the strain ε_{xx} and the acoustic modulus change are averaged over the path of the wavefront between T1 and R1 for each trigger delay (every 1 μs between 0 and 39 μs).

In Eq. (2.8) of model B, the first order nonlinearity in 2D Murnaghan's law already involves three parameters (l, m and n). The laboratory data are not sufficient to constrain all three parameters. Similar to the simplification made in the original paper of Feng et al. (2018), the change in $M = \lambda + 2\mu$, which is related to the speed of the P-wave, is simplified as a function of the damage parameters computed from the 2D simulation and the 1D first and second order nonlinearity parameters as in Eq. (2.13).

$$M = M_0(1 - g)(1 - \beta\varepsilon_{xx} - \delta\varepsilon_{xx}^2), \tag{2.13}$$

where M_0 is the initial acoustic modulus of the undamaged rock sample before the perturbations. Such a relationship is also used by Berjamin et al. (2017) in the 1D formulation of their model. For model L, we derive the variations in speed of the P-wave with the strain tensor and the damage parameter in Appendix 2.A.

In model B, the two parameters that control the damage evolution are γ_b and τ_b. Combining these with the two nonlinear parameters in Eq.(2.13), the parameters to be inverted are β, δ, γ_b and τ_b.

In model L, it is

$$\dot{\alpha} = \begin{cases} c_d\gamma_r I_2(\xi - \xi_0) & \text{if } \xi - \xi_0 > 0 \text{ and } \alpha \geq 0 \\ c_r\alpha\gamma_r I_2(\xi - \xi_0) & \text{if } \xi - \xi_0 \leq 0 \text{ and } \alpha \geq 0 \\ 0 & \text{if } \alpha < 0 \end{cases} \tag{2.14}$$

where $C_d(\alpha) = c_d$ and $C_r(\alpha) = c_r\alpha$ in Eq. (2.12). This preserves the necessary components for describing the observed slow dynamics while reducing the number of parameters that need to be constrained. In this case, five parameters are related to the damage, i.e. ξ_0,

γ, c_d, c_r, and the initial strain tensor. It is difficult to constrain all five parameters from the observations by Feng et al. (2018). We choose the parameters following Lyakhovsky et al. (1997b, 2016). We assume that $\xi_0 = -0.79$ and that the initial strain tensor in 2D is $\varepsilon_{xx0} = -\varepsilon_0$, $\varepsilon_{yy0} = -\varepsilon_0$ and $\varepsilon_{xy0} = \varepsilon_{yx0} = 1.46\varepsilon_0$ such that ξ at the initial strain state satisfies $\xi - \xi_0 < 0$. This enables the damaged rock to heal after removing dynamic perturbations. With the above simplifications, the parameters to be inverted in model L are γ_r, c_d, c_r, and ε_0.

Bayesian inversion and uncertainty quantification (UQ)

In order to quantify the relative importance of the theoretical model parameters in explaining the evolution of the observed slow dynamics, we apply Bayesian inversion. We first define the required terms to describe the probabilistic distributions of parameters of both models. The model parameters $\underline{m}$ and experimental observations $\underline{d}^{obs}$ are viewed as random variables in $\mathbb{M} \subset \mathbb{R}^{n_m}$ and $\mathbb{D} \subset \mathbb{R}^{n_d}$, where n_m and n_d are the number of model parameters and the number of observed data points.

We then aim to find the posterior, namely the conditional distribution of $\underline{m}$ for a given observation $\underline{d}^{obs}$. We denote the corresponding probability density function (PDF) by $\rho(\underline{m}|\underline{d}^{obs})$. We refer to Appendix 2.C for a more detailed description of the Bayesian inversion method that we employ.

To compute an approximation to the posterior distribution, we use the Markov chain Monte Carlo (MCMC) approach. Based on the amount of a priori information about the PDEs and the cost of each forward simulation, different types of MCMC sampling algorithms may be chosen. In this work, we choose the AM-MCMC (Haario et al., 2001) algorithm since the forward model simulated with ExaHyPE does not provide the derivatives of the solution with respect to the model parameters. AM-MCMC learns an approximate variance of the posterior on the fly, automatically improving its efficiency during the run by tuning its proposals. While more complex UQ algorithms may achieve higher efficiency, AM-MCMC readily meets our accuracy and computational cost requirements.

We use the AM-MCMC implementation provided by the open-source MIT Uncertainty Quantification Library ((MUQ) Parno et al., 2021). To couple MUQ to the forward model in the ExaHyPE simulation framework, we use the universal UQ / model interface UM-Bridge (Seelinger et al., 2023), which is fully supported by MUQ. For reproducibility, we provide, in the open research section, the forward model as a ready-to-run container image, that any UM-Bridge supporting UQ software can connect to.

In order to ensure that the MCMC method gives a sufficiently good approximation of the inversion results, we compute the Monte Carlo standard error (MCSE) as an indicator (Vehtari et al., 2021). It is defined as

$$\text{MCSE} = \sqrt{\frac{\text{Var}(\rho^{MC}(\underline{m}|\underline{d}^{obs}))}{S}}, \tag{2.15}$$

where $\rho^{MC}(\underline{m}|\underline{d}^{obs})$ is the estimated posterior, $\text{Var}(\cdot)$ is the variance of a random variable and S is the number of independent samples drawn from the posterior. MCMC necessarily produces correlated samples, so the effective sample size (ESS) is applied instead of S. The ESS is not immediately available, but can in turn be estimated from the chain's correlated samples (Vehtari et al., 2021). The MCSE estimates are provided by the ArviZ tool (Kumar et al., 2019).

2.3 Results

In Section 3.1, we show that model B and model L can reproduce the three phases of slow dynamics (Fig. 2.1c). In Section 3.2, we analyze the dependence of the simulated damage on both the frequency and amplitude of perturbations. In Section 3.3, we quantify the uncertainty of each model parameter based on experimental data.

2.3.1 The three phases of slow dynamics

As shown in Fig. 2.1c, the change of modulus under cyclic loading experiences three phases from conditioning to recovery. In this section, we explain how models B and L can reproduce the three phases of slow dynamics observed in laboratory experiments. To demonstrate the conditioning and recovery of the damage under dynamic perturbations, we treat the sample in the DAET experiment as an oscillator. We justify the validity of this assumption in Appendix 2.D. As in Berjamin et al. (2017), we assume that only one strain component ε_{xx} is perturbed. The damage evolution equations for model B are simplified to Eqs. (2.16a), and those for model L to Eqs. (2.16b), as

$$\dot{\alpha} = \frac{1}{\tau_b \gamma_b}(W - \gamma_b g), \tag{2.16a}$$

$$\dot{\alpha} = \begin{cases} c_d \exp\left(-\dfrac{\alpha}{\alpha_d}\right)\gamma_r I_2(\xi - \xi_0) & \text{if } \xi - \xi_0 > 0 \text{ and } \alpha \geq 0 \\ c_r \alpha \gamma_r I_2(\xi - \xi_0) & \text{if } \xi - \xi_0 \leq 0 \text{ and } \alpha \geq 0 \\ 0 & \text{if } \alpha < 0 \end{cases}, \tag{2.16b}$$

where $W = (\frac{1}{2} - \frac{\beta}{3}\varepsilon_{load} - \frac{\delta}{4}\varepsilon_{load}^2)M\varepsilon_{load}^2$ in Eq. (2.16a), ε_{load} is the perturbation on ε_{xx} and all other strain components are assumed to be zero. This implies that ε_{load} is $A_0 sin(2\pi f_c t)$ when $t \leq 10$ s and becomes 0 when $t > 10$ s. In Eq. (2.16b), ξ is computed, using Eq. (2.11), from 2D initial strain with three components ε_{xx0}, ε_{yy0}, and ε_{xy0} plus the perturbation in $\varepsilon_{xx} = \varepsilon_{xx0} + \varepsilon_{load}$ and the remaining strain components are assumed to be zero.

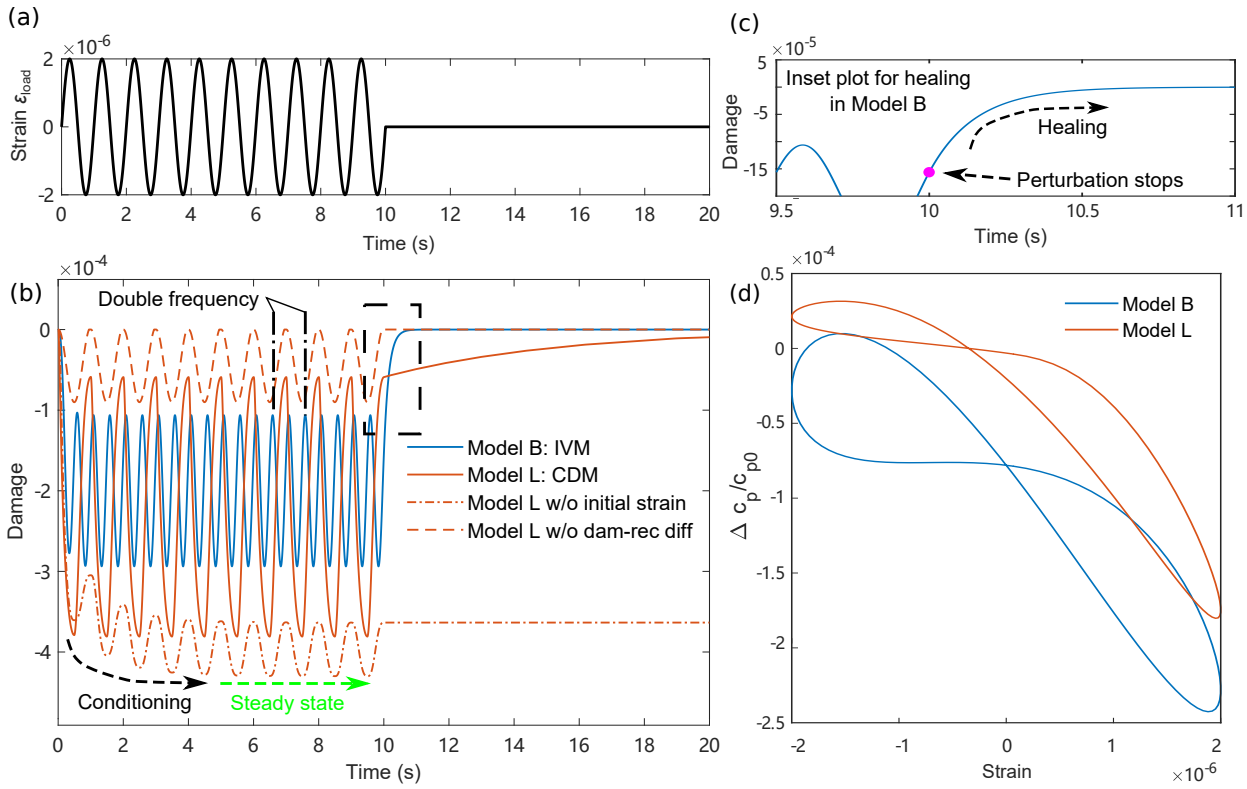

Figure 2.3: Evolution of the damage variables in model B and model L under a dynamic perturbation that resembles a DAET experiment. (a) The strain perturbation ε_{load} added to the system. (b) Comparison of the damage conditioning and recovery of model B (blue curve), model L (solid red curve), model L without initial strain (dashed red curve), and model L without different damaging and healing evolution (dash-dotted red curve), i.e. $C_d(\alpha) = C_r(\alpha)$ in Eq. (2.12). model B (Berjamin et al., 2017) is described in Eq.(2.16a), while model L (Lyakhovsky et al., 1997a) is described in Eq.(2.16b). The conditioning phase of the models is illustrated with a dashed black curve with an arrow. The steady state evolution phase of the models is illustrated with a dashed green curve with an arrow. The region inside the dashed black rectangle is enlarged in (c) to highlight the healing phase of model B after the perturbation stops (marked with a pink dot). The two dashed-dotted lines highlight the doubled frequency during the evolution of damage variable α in model B. (d) Comparison of the change in P-wave speed during one cycle of perturbation after reaching the steady state. $\Delta c_p/c_{p0}$ is the change of P-wave speed Δc_p over the P-wave speed before perturbations c_{p0}.

Table 2.1: Summary of model parameters for the comparison of model B and model L, with A_0 being the amplitude of the sinusoidal strain perturbation, f_c the frequency of the strain perturbation, β the first order nonlinearity, δ the second-order nonlinearity, γ_b the damage energy, τ_b the evolution time scale, γ_r the nonlinear modulus, c_d the damage coefficient, c_r the healing coefficient, ξ_0 the modulus ratio as defined in Eq. (2.11), c_r is the healing coefficient, ε_{ij0} the different components of initial strains and α_d the normalization factor as defined in Eq. (2.16b).

	Parameters	Values	Units	Parameters	Values	Units
Perturbation	A_0	2×10^{-6}	1	f_c	~~100~~	~~kHz~~Hz
model B	β	1.0×10^{2}	1	δ	3.0×10^{6}	1
	γ_b	5.0×10^{1}	Pa	τ_b	1.5×10^{-1}	s
model L	c_d	1.2×10^{-1}	$(\text{Pa}\cdot\text{s})^{-1}$	ε_{xx0}	-1.00×10^{-6}	1
	c_r	5.0×10^{1}	$(\text{Pa}\cdot\text{s})^{-1}$	ε_{yy0}	-1.00×10^{-6}	1
	γ_r	1.6×10^{10}	Pa	ε_{xy0}	1.46×10^{-6}	1
	ξ_0	-0.79	1	α_d	1.0×10^{-4}	1

We show the evolution of the damage variables in both models in Fig. 2.3b and c. We note that the conditioning phase of model L (marked with dashed black curve with an arrow) is subtle in Fig. 2.3b but will be more pronounced if we set c_d to a smaller value in Eq. (2.16b). The parameters are detailed in Table 2.1. We choose initial strains that satisfy $\xi(\varepsilon_{xx0}, \varepsilon_{yy0}, \varepsilon_{xy0}) - \xi_0 \approx -0.01 < 0$. Both model B and model L (the red solid curve) gradually reach the steady state during perturbations and recover after $\varepsilon_{load} = 0$. In Fig. 2.3b, we also show how the damage will evolve differently when not adding the initial strain or without differentiating the evolution laws for damaging and healing in model L, i.e. Eq. (2.16b). Without the initial strain (the red dashed curve), the steady state is reached at a later stage, and larger damage will be induced. More importantly, the accumulated damage does not heal after removing the perturbations. In the case that $\dot{\alpha} = C_d \gamma_r I_2(\xi - \xi_0)$ irrespective of the sign of $\xi - \xi_0$ (the red dash-dotted curve), we observe that no damage accumulates at the end of each cycle. In this case, all damage that accumulated during the damaging phase of a cycle is recovered during the healing phase due to the identical evolution equations.

Fig. 2.3d shows how the change in P-wave velocity relates to the strain perturbations during the stationary phase. We note here that while only the damage evolution of model B doubles the perturbation frequency (highlighted with the two dash-dotted black lines in Fig. 2.3b), both model B and model L generate the "bow-tie" loop that is reported in DAET experiments (Renaud et al., 2012; Rivière et al., 2015, 2016). We will discuss how the "bow-tie" loops form with different mechanisms in Section 2.4.2.

2.3.2 Amplitude- and frequency-dependent damage

Both, amplitude- and frequency-dependence of damage have been observed in DAET. Many observations show that the damage at the steady state (marked by the dashed green line with

an arrow in Fig. 2.3b) grows with the magnitude and frequency of dynamic perturbations. The amplitude-dependence of damage can be resolved by various models (Aleshin and Van Den Abeele, 2007; Vakhnenko et al., 2005; Favrie et al., 2015); however, modeling the frequency dependence of damage remains challenging. The following discussion will focus on the capabilities to also model the frequency-dependent damage in laboratory experiments using models B and L.

We show in Figs. 2.4a-ee how the damage variable α, under two perturbation frequencies (0.1 and 1 Hz), evolves in our numerical simulation using the two models. In model L, both the start of recovery (SOR, annotated in Fig. 2.4b) and the average damage (AD, Fig. 2.4b) during the steady state (phase 2 in Fig. 2.1c) increase with f_c, which is consistent with the observations from Rivière et al. (2016) and Manogharan et al. (2021, 2022). In model B, SOR follows a similar trend as that in model L. But it shows a frequency independent AD. The difference between SOR and AD damage is usually not explicitly pointed out in the observations regarding the metrics for describing the damage. However, as shown in Fig. 2.4e, they can behave very differently when quantifying the frequency-dependent damage. While AD follows different trends between models B and L, SOR consistently increases with the perturbation frequency in both models.

We note here that the above frequency-dependent behavior of both models results are obtained even when assuming that all nonlinear parameters,i.e. β, δ, γ_b and τ_b in Eq. (2.16a) and γ_r, ξ_0, c_d and c_r in Eq. (2.16b), are frequency-independent. A qualitative explanation of the frequency-dependent of SOR can be the following. Under our assumption that the recovery rate increases with the value of the damage variable, stationarity requires a certain level of averaged damage. For higher frequencies, the amplitude of the oscillations of damage in each cycle becomes smaller. This may imply that from the same level of averaged damage, the damage value that the material reaches after one cycle (c.f., the minimum damage) will increase with frequency.

In Fig. 2.4f, we compare the frequency-dependent AD in model L with the measurements by Manogharan et al. (2021) using the model parameters in Table 2.D.1. The rectangles show the AD measured by Manogharan et al. (2021) in their Fig. 8g for 5 different amplitudes and 3 frequencies (0.1 Hz in purple, 1 Hz in red, and 10 Hz in yellow). The colored dots with error bars show the results from model L with parameters shown in Table 2.D.1. The model parameters are varied within certain ranges. The dots represent the mean values of the model results with parameter variations; while the length of error bars is the standard deviation of the model results. We find that most of the measured data points fall within the model predictions and their uncertainties are computed by varying the model parameter as in Table 2.D.1. AD increases almost linearly with the amplitude of perturbations (Johnson and Sutin, 2005; Manogharan et al., 2021). The trend of rising damage with higher perturbation frequencies is also captured by model L. We will present a mathematical derivation to explain how model L resolves such frequency-dependent damage in Section 4.1.

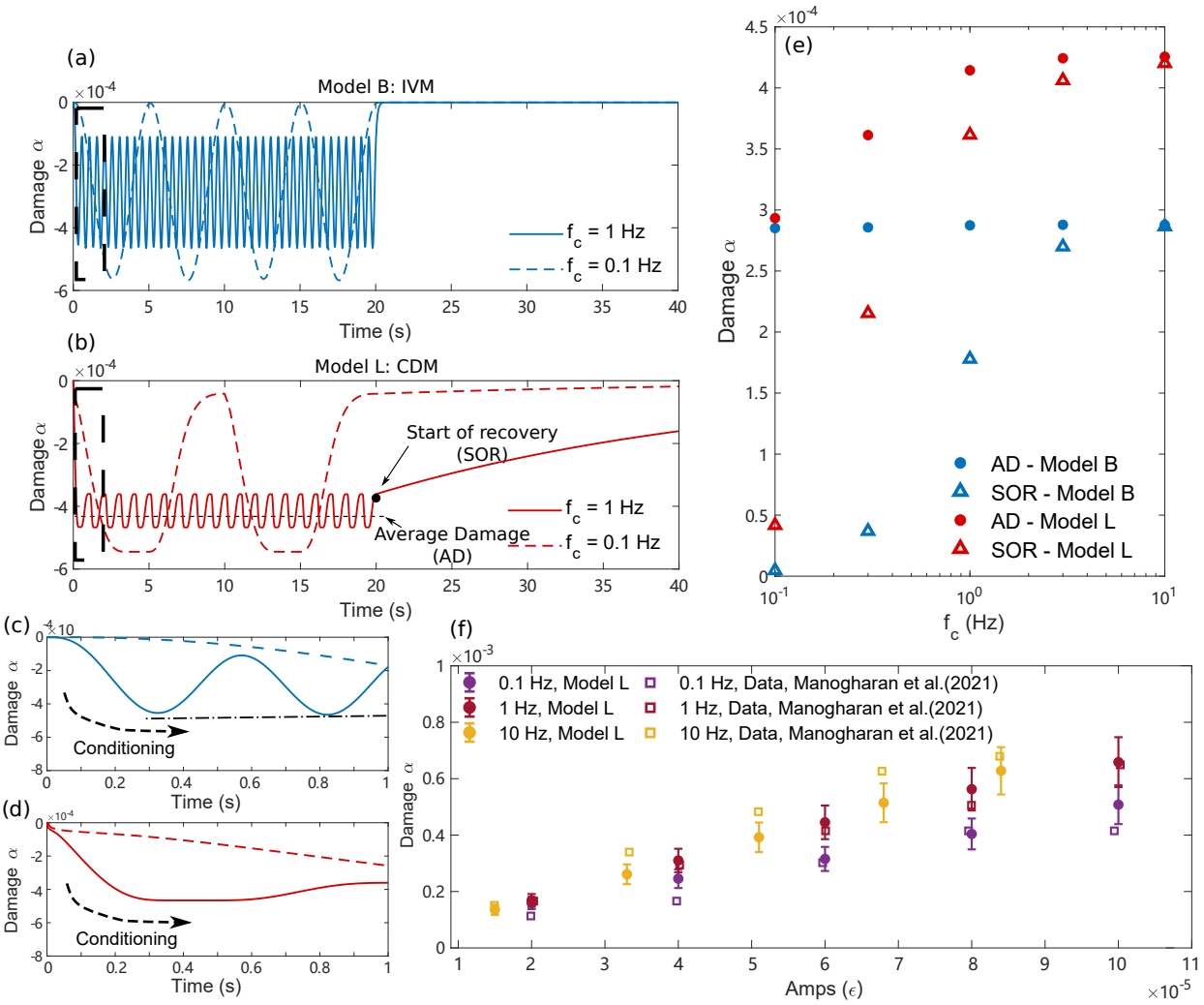

Figure 2.4: (a) Evolution of the damage variables in model B during dynamic perturbations of a 0.1 Hz (blue dashed curve) and 1 Hz (blue solid curve) source signal. model B (Berjamin et al., 2017) is described in Eq.(2.16a). The damage evolution at the beginning of perturbations (the region inside the black dashed rectangle) is enlarged in (c) to highlight the conditioning phase. (c) The zoomed-in plot of the region inside the black dashed rectangle in (a). The dash-dotted line shows the peak damage is not reached during the first cycle of perturbations. This indicates that the damage evolution is still in the conditioning phase until ∼0.8 s. (b) Evolution of the damage variables in model L during dynamic perturbations of a 0.1 Hz (red dashed curve) and 1 Hz (red solid curve) source. model L (Lyakhovsky et al., 1997a) is described in Eq.(2.16b). The start of recovery (SOR) refers to the damage value at the end of the perturbation and the average damage (AD) refers to the average value of the damage variable at the stationary phase. The damage evolution at the beginning of perturbations (the region inside the black dashed rectangle) is enlarged in (d) to highlight the conditioning phase. (d) The zoomed-in plot of the region inside the black dashed rectangle in (b). (e) Change of AD and SOR at the end of the perturbations under different dynamic perturbation frequencies. The blue dots indicate our results for model B while the green dots are for model L. (f) The change of AD during the stationary phase with the amplitude and the frequency of the perturbations. The rectangles show the AD measured by Manogharan et al. (2021) in their Fig. 8g for 5 different amplitudes and 3 frequencies (0.1 Hz in purple, 1 Hz in red and 10 Hz in yellow). The colored dots with error bars show our results from model L with the model parameter α_d varying between 0.4 and 0.9 in Table 2.D.1. The dots represent the mean values of the model results with varying parameters; while the length of the error bars is the standard deviation of the model results.

2.3.3 Bayesian inversion of damage model parameters from laboratory observations

In this section, we constrain the behaviors of models B and L with another laboratory experimental set-up - copropagating acousto-elastic testing (Feng et al., 2018). We not only explore the capability of the models in explaining observations but also quantify how well (or badly) model parameters can be constrained from this experiment with the AM-MCMC method introduced in Section 2.2. The values of the parameters to be inverted are of vastly different magnitudes. Thus, normalization is required for the joint sensitivity analysis of all parameters. We assume that the values of σ_M in Eq. (2.C.2) are 6×10^{-7} and 1×10^{-6}, respectively, for the inversion of model B and model L. The inversion parameters are listed in Table 2.2.

Table 2.2: Summary of all model parameters considered in the MCMC inversion, with β being the first-order nonlinearity, δ the second-order nonlinearity, γ_b the damage energy, τ_b the evolution time scale, γ_r the nonlinear modulus, c_d the damage coefficient, c_r the healing coefficient, ξ_0 the modulus ratio as defined in Eq. (2.11), c_r the healing coefficient and ε_{ij0} the different components of initial strains.

	Param.	Values	Units	Param.	Values	Units
model B	β	$1.8 \times 10^2 \times$ [0,4]	1	δ	$3.0 \times 10^8 \times$ [0,4]	1
	γ_b	$1.0 \times 10^{[0,2]}$	Pa	τ_b	$1.0 \times 10^{-6} \times 10^{[0,3]}$	s
model L	γ_r	$4.5 \times 10^9 \times$ [0,4]	Pa	ε_{xx0}	$-\varepsilon_0$	1
	c_d	$1.0 \times 10^5 \times$ [0,4]	$(\text{Pa}\cdot\text{s})^{-1}$	ε_{yy0}	$-\varepsilon_0$	1
	c_r	$5.0 \times 10^6 \times 10^{[0,2]}$	$(\text{Pa}\cdot\text{s})^{-1}$	ε_{xy0}	$1.46\varepsilon_0$	1
	ε_0	$5.0 \times 10^{-8} \times 10^{[0,3]}$	1	ξ_0	-0.79	1

In the MCMC runs of model B and model L, 70,000 simulations with different model parameters are sampled from the posterior. In this process, 13,826 and 10,444 proposals are accepted, respectively. The Monte Carlo standard errors (MCSE) of each parameter in models B and L are given in Figs 2.6a, f, k, and p. The inversion for each of model B and model L on a single core of the Intel i7-1165G7 processor takes around 10 hours.

We compare the simulation results and the observations from the experiment in Fig. 2.5. We show the raw data of measured modulus changes with dashed red curves. The solid blue curve in Fig. 2.5a and the solid green curve in Fig. 2.5b are, respectively, predictions of model B and model L with the best-fit parameter set in MCMC. Model B (the solid blue curve) and model L (the solid green curve) match the observations with correlation coefficients of 0.91 (model B) and 0.83 (model L). While model B has a higher correlation coefficient, the variation of modulus is delayed compared to the data (the dashed red curve). This time shift is also applied in the visco-elastic formulation proposed by Feng et al. (2018). However, since we here directly simulate the wave propagation and the variation of modulus, needing to add a delay is unexpected.

Unlike model B, if we compare model L and the data in the time interval between 30 μs and 40 μs, the delay is better resolved. Model L overestimates the modulus increase during

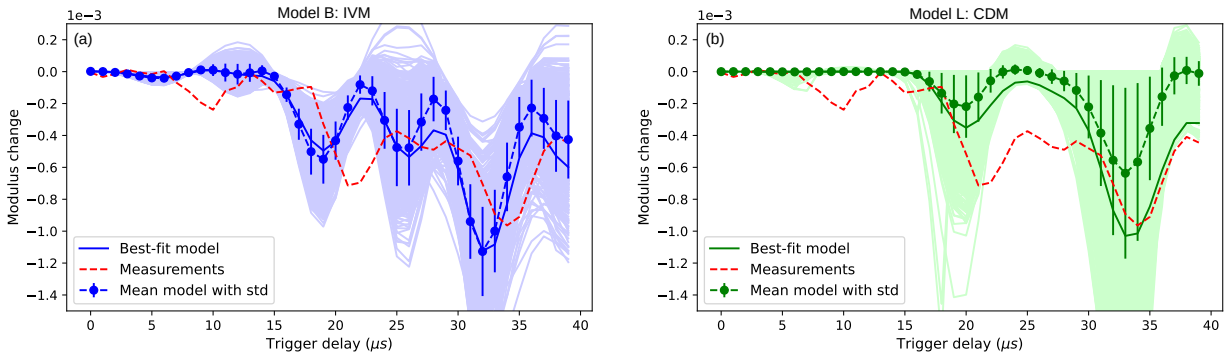

Figure 2.5: Comparison between the observations from experiments by Feng et al. (2018) and model predictions corresponding to 70,000 MCMC samples of the respective model's Bayesian posterior. The data from the experiment is shown with the red dashed line. (a) Inversion results of model B, Eqs.(2.13) and (2.16a). The model prediction with the highest posterior probability is shown in the solid blue curve. The dashed line shows the mean prediction with error bars indicating the standard deviation. All samples' model predictions are plotted as a blue-shaded area. (b) Inversion results of model L, Eq.(2.14). The model prediction with the highest posterior probability is shown in the solid green curve. The dashed line shows the mean prediction with error bars indicating the standard deviation. All samples' model predictions are shown in a green shade.

the compression of the sample between 20 μs and 30 μs. The MCMC ensembles of model B (the blue-shaded area) and model L (the green-shaded area) partially account for modulus variation in the early period between 5 μs and 15 μs. While Feng et al. (2018) achieved a better fit to that earlier part of the signal, their discrepancies between data and model predictions in the later time range, e.g., between 30 μs and 40 μs, were large. We refer to Appendix 2.D for a further discussion about the agreement between the model predictions and the experimental data.

The marginal probability distributions of the laboratory-constrained model parameters of models B and L are shown in Fig. 2.6. The histograms in blue on the diagonal of Fig. 2.6 show the one-dimensional marginal distribution of the model parameters in model B. The values with the highest marginal probability for the normalized β, δ, γ_b and τ_b are 1.10, 3.21, 0.88, and 1.75. The two-dimensional marginal distribution of each pair of two parameters is shown on the upper triangle of Fig. 2.6. The first-order nonlinearity parameter β remains relatively independent of other parameters. In distinction, the correlations among the other three parameters are significantly stronger. We can infer that with higher damage energy (γ_b), the second-order nonlinearity will more likely be larger whereas the time scale for damage evolution τ_b be smaller.

Similarly, the histograms in green on the diagonal of Fig. 2.6 show the one-dimension marginal distribution of the model parameters in model L. The values with the highest marginal probability for the normalized γ_r, c_d, and ε_0 are 1.30, 0.50, and 1.80. We find that the healing coefficient c_r is not well constrained by the laboratory observations. The two-dimensional marginal distribution of each pair of two parameters is shown on the lower triangle of Fig. 2.6. We observe a negative correlation between the nonlinear modulus γ_r and the damage coefficient c_d. We relate this effect to the lack of resolution in constraining the healing coefficient. According to Figs. 2.6e and j, the trend of damage increase due

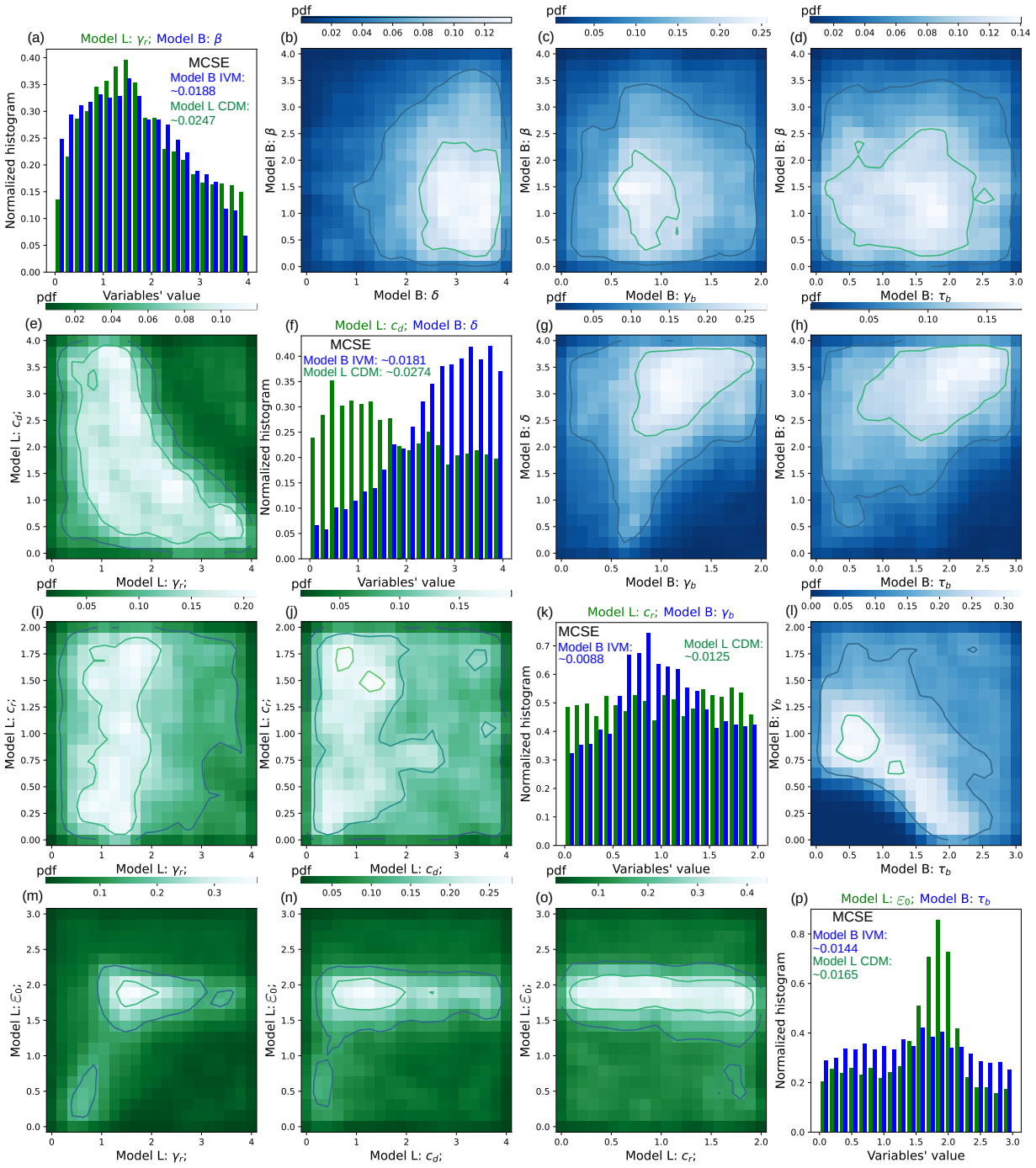

Figure 2.6: Sensitivity of different parameters in model B and in model L based on MCMC inversion. We show the one-dimension marginal probability density of the four parameters in model B (in blue) and model L (in green) on the diagonal of the plot matrix. The four parameters in model B from left to right and top to bottom are the first-order nonlinearity (β), the second-order nonlinearity (δ), the damage energy (γ_b), and the evolution time scale (τ_b). The four parameters in model L from left to right and top to bottom are the nonlinear modulus (γ), the damage coefficient (c_d), the healing coefficient (c_r) and the initial strain level (ε_0). The two-dimension marginal probability density of all pairs of two parameters in model B is shown in the upper triangle subplots of the plot matrix. The density is shown with the color map from dark blue to white. The brighter the color, the higher the density. Similarly, the two-dimension marginal probability density of all pairs of two parameters in model L is shown in the lower triangle subplots of the plot matrix. The density is shown with the color map from dark green to white. The brighter the color, the higher the density. MCSE stands for Monte Carlo standard errors of each model parameter.

to larger damage coefficient c_d is better compensated for by the decrease of the nonlinear modulus γ_r than by the increase of the healing coefficient c_r.

We here summarize the information gained from this section. We can estimate the following parameters from the data in co-propagating acousto-elastic testing: the first-order nonlinearity (β), the second-order nonlinearity (δ), and the damage energy (γ_b) in model B, as well as the nonlinear modulus (γ), the damage coefficient (c_d), and the initial strain level (ε_0) in model L. Among them, the initial strain level (ε_0) is an important parameter that we introduce in this paper to explain slow dynamics as shown by the dash-dotted red curve in Fig. 2.3b. We will discuss the physical implications of this parameter in Section 4.3. Two model parameters are poorly constrained - the evolution time scale (τ_b) in model B, and the healing coefficient (c_r) in model L. We will discuss possible reasons and suggest feasible ways to better constrain these parameters in Section 4.4.

2.4 Discussion

In this paper, we analyse the behavior of two physical models to simulate nonlinear elastic wave propagation and compare them with laboratory observations. Several interesting aspects are worth further discussing here: (1) We find that model L can reproduce the increase of average damage (AD) with the frequency of strain perturbations during the steady state of damage. We will here revisit this main advantage and interpret it from both mathematical and physical points of view. (2) We will also discuss how the influence of the damage variable on the wave speeds can be similar to second-order nonlinearity. (3) In model L, one of the key assumptions required for recovery after removing perturbations is the existence of initial strain. We will discuss the validity of this assumption. (4) Most importantly, we will revisit the major goal of proposing a model(s) whose parameters can be constrained. This enables the model(s) to be applied to connect the observed non-classical nonlinearity in the laboratory and in the field.

2.4.1 The frequency-dependence of damage

Recent studies find a general trend of increasing average damage with the excitation frequency during the stationary phase (Rivière et al., 2016; Manogharan et al., 2022, 2021). However, the underlying mechanism is not well understood. While Rivière et al. (2016) favors models with rate/time dependencies, not every such model also results in frequency-dependent damage during the steady state. In model B, the average damage is $\frac{E}{4\gamma_b}A^2 + \mathcal{O}(A^4)$ (Berjamin et al., 2017), where A is the strain amplitude of perturbations and is not related to the frequency (see also Fig. 2.4). In model L, frequency-dependent average damage is observed and follows the same trend as the measurements (c.f., the red dots in Fig. 2.4e).

We here interpret these findings analytically (see Appendix 2.A). We show that in model L, the decrease of the damage coefficient and the increase of the healing coefficient with damage

contribute differently to the frequency-dependent AD. We can also show that damage at the steady state can increase with the frequency of the dynamic perturbation. Specifically, with increasing healing coefficient ($C_r(\alpha) = c_r\alpha$), the average damage tends to decrease with frequency, i.e. Eq. (2.A.2); while with decreasing damage coefficient ($C_d(\alpha) = c_d \exp(\alpha/\alpha_d)$), AD becomes larger as the frequency increases, i.e. Eq. (2.A.6).

2.4.2 Damage vs. second-order nonlinearity contributions to coseismic changes in wave speed

Forming a "bow-tie" loop relation between the wave speed variation and the strain perturbation requires that the time series of the modulus change contain a frequency component that doubles the frequency of strain oscillation. In model B, there are two sources of such double frequency. The first mechanism is second-order nonlinearity, as has been recognized in previous analysis (Sens-Schönfelder et al., 2019). The second mechanism contributing to the double frequency is related to damage and healing within a cycle. The rock is damaged when the absolute value of the strain increases while it heals otherwise. This leads to two cycles of damage and healing inside one cycle of strain perturbation.

In model L, neither the second-order nonlinearity (δ) nor the double damage-healing cycles exist. The rock damages when the tensile strain is large enough that $\xi - \xi_0 > 0$ and it heals otherwise. This implies that the oscillation of the damage variable has the same frequency as the strain perturbations, as highlighted with the two dash-dotted black lines in Fig. 2.3b. Instead, the mechanism in model L that adds the double frequency to the damage evolution is the change of wave speed with the amplitude of the strain, coming from the third non-quadratic term in Eq. (2.10).

We caution that damage effects may be confused with the effects of second-order nonlinearity in observations of "bow-tie" loops. In the framework of this paper, we introduce a damage variable to explain the conditioning and the recovery of the wave speed. However, in addition to slow dynamics, the damage variable can also influence the measured wave speed in a similar way as classical nonlinearity. Such confusion may also appear in comparisons of modulus variation as in Fig. 2.6. The third parameter (the damage energy γ_b) in model B determines the magnitude of damage: the smaller the damage energy, the larger the magnitude of the damage. We conclude that the positive correlation between γ_b and the second-order nonlinearity (δ) implies that the effect of the damage evolution on the modulus is comparable to that of the second-order nonlinearity. However, it is possible to discern the fundamental difference in the effects of the damage variable versus second-order (classical) nonlinearity. The latter will lead to the same strain-dependent modulus change, irrespective of the loading rate. However, the change of modulus due to the damage variable will always be rate-dependent, as given in Eq. (2.6).

2.4.3 Physical interpretation of both damage models

Whether damage evolution discriminates between compression and extension can lead to different interpretation of the physical mechanisms underlying the evolution of the damage variables. Different hypotheses have been proposed relating damage to friction (Aleshin and Van Den Abeele, 2007) or to adhesion (Lebedev and Ostrovsky, 2014). Since the sign of $\gamma_b g$ in Eq. (2.8) is not related to compression or extension of strain, the healing and damage terms of model B are clearly separated. The healing term becomes larger than zero once damage occurs irrespective of the strain state. The healing term is simultaneously increasing with the accumulation of damage. Once the healing term becomes large enough, damage accumulation reaches a quasi-static state.

In contrast, the damage evolution of the material in model L differentiates between compressive and extensive deformation. Here, rock only heals when the material is sufficiently compressed ($\xi - \xi_0 < 0$). The quasi-static state is reached due to increasing healing speed. Lebedev and Ostrovsky (2014) proposed a possible explanation of slow dynamics being related to the thermal processes due to adhesion at the contacts of rock grains. The adhesion potential (Jacob and Israelachvili, 1992) is non-symmetric for compression and extension. The mechanism of adhesion therefore also favors a model that considers different effects of damage and healing under compression and extension.

While both models explain the slow dynamics mathematically, the physical interpretation of the L model has richer physical implications. First, each term in the internal energy of the L model has a physical meaning, and the formulation strictly follows the laws of thermodynamics. The healing is related to $\gamma I_1 \sqrt{I_2}$, a term that comes from the opening and closing of micro-cracks (Lyakhovsky et al., 1997a). At the microscopic scale, this may be interpreted as a re-attachment of asperities at contact surfaces. Second, as shown in Fig. 2.6, the initial strain is relatively well resolved to be around 3×10^{-6}. The existence of this non-negligible initial strain may be related to the cohesive contact or to the thermal deformation of rocks. The typical thermal expansion coefficient of rock is of the order of $10^{-5} K^{-1}$ (Kirk and Williamson, 2012), where K is the unit of the absolute temperature. This means a change of less than 1 K may equate to the here-constrained magnitude of the initial strain. Although more observations are required to confirm this interpretation, the existence of initial strain possibly explains why slow dynamics typically become prominent when the dynamic strain is larger than 10^{-6} but not for smaller values (Remillieux et al., 2017). Gajst (2020) and Lyakhovsky et al. (2022) add a storage energy term in model L that is similar to the second term in Eq. (2.8). This new term also prevents the growth of damage until the perturbation is larger than a certain threshold. Whether introducing an initial strain as in our work or adding an additional storage energy term is more suitable for explaining the observed non-classical nonlinearity discussed in this paper is an interesting topic for future work.

We also note that the steady state is reached due to the increasing speed of healing under compression with higher accumulated damage. This increase is not necessarily linear. It is here in Eq. (2.14) only assumed to be linear for simplicity and demonstration purposes. A physically motivated expression requires specific experiments to constrain this behavior.

2.4.4 Model complexities and data availability

In the following, we discuss current limitations and future avenues for constraining parameters in models B and L from experiments. We will argue for the potential of conducting DAET and copropagating acousto-elastic testing experiments on the same sample to more accurately invert the model parameters.

β and δ in Eq. (2.13) of model B, and γ_r and ε_0 in Eq. (2.14) of model L are related to the simultaneous oscillation of modulus with the cyclic loading in phase 2 of slow dynamics in Fig. 2.1. In the copropagating acousto-elastic testing experiments, the wavefront of the probing wave is propagating simultaneously with the wavefront of the pump wave. Thus, we can use this experiment to constrain β and δ in model B and γ_r, ε_0 in model L, see Figs. 2.6a, f, and p.

However, since the duration of perturbation in the copropagating acousto-elastic testing experiments is not long enough, τ_b in Eq. (2.13) of model B, Cd and Cr in Eq. (2.14) of model L are less well constrained in Figs. 2.6f, k, and p. As explained in Section 3.1, τ_b and γ_b of model B, as well as C_d and C_r of model L, describe how the models reproduce the mechanical response of rock samples at a longer time scale. In this work, we use DAET experiments to estimate these model parameters in Fig. 2.4f. However, for the same sample, no co-propagating acousto-elastic testing experiments are available. Longer time scale damage model parameters may be better constrained using DAET and copropagating acousto-elastic testing experiments on the same sample.

2.4.5 Limitations

The damage variable capsulizes changes in material stress-strain relations due to the physical processes, such as adhesion (Lebedev and Ostrovsky, 2014), plastic deformation at grain contacts (Lieou et al., 2017) or friction (Aleshin and Van Den Abeele, 2007), at meso- and microscopic scales. Compared to the explanation of Lebedev and Ostrovsky (2014), the accumulation of damage during the extension of material might be related to the detachment at the contacts of asperities; whereas the recovery (decrease of the damage variable value) might be associated with re-attachment and with asperities that gradually shift from the secondary stationary state to the main stationary state. However, developing a stringent mathematical framework connecting the damage variable at the macroscopic scale with microscopic physical processes is challenging and currently elusive.

Model L does not match the modulus change equally well as model B, especially during rock compression. In model L, the increase in wave speed due to the third term $\gamma I_1\sqrt{I_2}$ during compression cancels out the wave-speed drop from damage. Future modification of the L model may mitigate the influence of its third term on the change in wave speed while preserving differentiating between tensile and compressive strains.

In this work, we analyze the behaviors of two damage models. To compare our 2D simulation results with laboratory observations, we simplify some of the model parameters acknowledging the limited amount of available observational data. One aspect that will require

further investigation for modeling slow dynamics in 2D and 3D is the full response of material damage from strain perturbations including different components of the strain/stress tensor. Lott et al. (2017) proposed a formulation that connects a scalar damage variable to the stiffness tensor. The resulting changes in P- and S-wave speed in response to different modes of perturbations qualitatively match observations. In future work, this relationship may be combined into the internal energy formulation in Eq.(2.2) to potentially refine our dynamic understanding of how the steady state in DAET (phase 2 in Fig. 2.1) is reached.

The achieved quantitative match of our modeling results and laboratory observations demonstrate the potential of both proposed models to capture natural co-seismic damage of rocks. The amplitudes of the changes in moduli modeled here and observed in laboratory experiments are small under small strain perturbations ($\sim 10^{-4}$, see Tables 2.1 and 2.2, and Fig. 2.4f). At the field scale, the observed magnitudes of moduli changes vary between 10^{-4} and 10^{-1} depending on the depth, rock/soil types, and level of the dynamic strain (e.g., Gassenmeier et al., 2016; Qin et al., 2020; Wang et al., 2021). As a next step, the nonlinear models can be implemented in large-scale 3D wave solvers, e.g., SeisSol (https://seissol.org) or ExaHyPE (Reinarz et al., 2020). The associated major challenges stem from the nature of nonlinear hyperbolic partial differential equations. Solutions can become discontinuous during the propagation of waves even when the initial conditions are smooth (LeVeque, 2002). There are numerical methods that may resolve such dynamic discontinuities by introducing numerical diffusion. This comes with different criteria for numerical stability and typically requires higher spatial and temporal resolution. It leads to computationally more expensive schemes. However, to simulate co-seismic damage and post-seismic recovery as observed in the field, 3D simulations will be indispensable to help bridge the gap between the laboratory and the field scales.

2.5 Conclusions

We demonstrate the applicability and compare two models that explain the observed nonclassical nonlinear behaviors of rocks, an internal variable model (IVM) and a continuum damage model (CDM). The analyzed IVM, model B, is proposed by Berjamin et al. (2017), while the CDM, model L, is adapted from Lyakhovsky et al. (1997a). Using both physical models, we numerically simulate nonlinear wave propagation in rocks with fast and slow dynamics with the discontinuous Galerkin (DG) method in 2D.

- We compare the simulation results with two sets of experiments. In dynamic acousto-elastic testing, the model that we adapted from Lyakhovsky et al. (1997a). can quantitatively explain both amplitude- and frequency-dependent damage of rock samples.

- In co-propagating acousto-elastic testing, the change of modulus in laboratory observation has a higher correlation coefficient with simulation results using the model by Berjamin et al. (2017) than those of the model that we adapted from Lyakhovsky et al. (1997a). However, only the latter model explains the observed delay of modulus variation relative to strain.

- From the joint posterior distribution of the model's parameter space using Adaptive Metropolis Markov chain Monte Carlo (AM-MCMC), we demonstrate that nonlinear parameters can be resolved but that the associated uncertainties vary. We find that the effects on wave-speed changes from the second-order nonlinearity and from the damage variable can be very similar.
- The evolution time scale (τ_b) in the model of Berjamin et al. (2017) and the healing coefficients c_r in the adapted model from Lyakhovsky et al. (1997a) are particularly challenging to resolve from co-propagating acousto-elastic testing. We suggest that the model parameters can be better constrained if we can conduct dynamic acousto-elastic testing and copropagating acousto-elastic testing on the same sample.

We conclude that the quantitative match between both models and the laboratory observations justify the applicability of these models in describing the phenomena of slow dynamics. Future nonlinear damage modeling using either physical model in a 3D highly-scalable software for seismic wave propagation simulations will allow comparison to field-scale observations and account for natural complexities such as complex surface topography and subsurface heterogeneities.

Acknowledgments

The authors are grateful for helpful and inspiring discussions with Christoph Sens-Schönfelder, Harold Berjamin, Vladimir Lyakhovsky, Dave A. May, Anne Reinarz, Michael Dumbser, Evgeniy Romenskiy, Yehuda Ben-Zion, Sebastian Wolf and Parisa Shokouhi. We would also like to acknowledge comments from the reviewer Vladimir Lyakhovsky and an anonymous reviewer.

This project has received funding from the European Union's Horizon 2020 research and innovation programme under the Marie Skłodowska-Curie grant agreement No 955515 – SPIN ITN (www.spin-itn.eu). AAG acknowledges additional support from European Union's Horizon 2020 Research and Innovation Programme (TEAR grant No. 852992) and Horizon Europe (ChEESE-2P grant No. 101093038, DT-GEO grant No. 101058129 and Geo-INQUIRE grant No.101058518), the National Science Foundation (grant No. EAR-2121666), the National Aeronautics and Space Administration (80NSSC20K0495) and the Southern California Earthquake Center (SCEC award 22135).

Open research

The combination of the AM-MCMC algorithm of MUQ (Parno et al., 2021) and the forward modeling in ExaHyPE (Reinarz et al., 2020) is implemented with UM-Bridge (Seelinger et al., 2023). The detailed description of these packages, the algorithms therein, as well as the code of our implementation are provided in the following repository:
https://zenodo.org/badge/latestdoi/551506661.

Appendices

Appendix 2.A Analytical analysis of model L

A1 Analytical interpretation of the frequency dependence of model L

Here we derive analytical solutions to the frequency-dependent damage of the model of Lyakhovsky et al. (1997a). We make the following simplifying assumptions: First, we assume that only ε_{xx} is perturbed by $\varepsilon_{load} = \varepsilon_0 sin(\omega_c t)$, as in Fig. 2.3. As in Table 2.1, $\xi(\varepsilon_0)+\xi \approx 0.01$ and is assumed to be zero at the initial strain level. Further, we approximate $I_2(\xi - \xi_0) = R_0\varepsilon_{load} + \mathcal{O}(\varepsilon_{load}^2) \approx R_0\varepsilon_{load}$.

- **Increasing healing coefficient with damage**

In the case when the healing coefficient linearly increases with the damage variable, Eq. (2.12) is simplified as

$$\dot{\alpha} = \begin{cases} C_d\gamma_r R_0\varepsilon_{load} = \dfrac{c_1}{\varepsilon_0}\varepsilon_{load} & \text{if } \varepsilon_{load} > 0 \text{ and } \alpha \geq 0 \\ C_r\alpha\gamma_r R_0\varepsilon_{load} = \dfrac{k_1}{\varepsilon_0}\alpha\varepsilon_{load} & \text{if } e\varepsilon_{load} \leq 0 \text{ and } \alpha \geq 0 \\ 0 & \text{if } \alpha < 0 \end{cases} \cdot \tag{2.A.1}$$

Consider one cycle of perturbation where $t \in [0, 2\pi/\omega_c]$ and the damage variable at the beginning of the cycle is α_0. We then derive that the maximum damage at $t = \pi/\omega_c$ is $\alpha_{max} = \alpha_0 + 2c_1/\omega_c$ at the end of the cycle, $\alpha_t = \alpha_{max}\exp(-2k_1/\omega_c)$. At the dynamically steady state, $\alpha_t = \alpha_0$. The average of the damage variable in a cycle is approximated by

$$< \alpha > \approx 0.5(\alpha_0 + \alpha_{max}) = \frac{c_1}{\omega_c}\frac{1 + \varepsilon_{load}^{-2k_1/\omega_c}}{1 - \varepsilon_{load}^{-2k_1/\omega_c}}, \tag{2.A.2}$$

which is monotonously decreasing with frequency.

- **Decreasing damaging coefficient with damage**

In the case when the damage coefficient exponentially decreases with the damage variable, Eq.(2.12) is simplified as

$$\dot{\alpha} = \begin{cases} C_d\gamma_r R_0 \exp\left(-\alpha/\alpha_d\right)\varepsilon_{load} = \dfrac{c_1}{\varepsilon_0}\exp\left(-\alpha/\alpha_d\right)\varepsilon_{load} & \text{if } \varepsilon_{load} > 0 \text{ and } \alpha \geq 0 \\ C_r\gamma_r R_0\varepsilon_{load} = \dfrac{c_2}{\varepsilon_0}\varepsilon_{load} & \text{if } \varepsilon_{load} \leq 0 \text{ and } \alpha \geq 0 \\ 0 & \text{if } \alpha < 0 \end{cases}. \tag{2.A.3}$$

Following a similar consideration as above, we derive

$$\exp\left(\alpha_0/\alpha_d\right) = \frac{K}{1-K}\frac{2c_1}{\omega_c\alpha_d}, \tag{2.A.4}$$

$$\exp\left(\alpha_{max}/\alpha_d\right) = \exp\left(\alpha_0/\alpha_d\right) + \frac{2c_1}{\alpha_d\omega_c}, \tag{2.A.5}$$

where $K = \exp\left(-\dfrac{2c_2}{\alpha_d\omega_c}\right)$. Multiplying Eq. (2.A.4) and (2.A.5), it is derived that

$$\exp\left(\frac{\alpha_0+\alpha_{max}}{\alpha_d}\right) = \frac{K}{(1-K)^2}\left(\frac{2c_1}{\omega_c\alpha_d}\right)^2. \tag{2.A.6}$$

with the right-hand side monotonously increasing with frequency.

Analytical analysis of the combination of the two cases in Eq. (2.A.1) and (2.A.3) is challenging. But within the parameter space used in Fig. 2.4, we can show that the damage at the steady state can increase with the frequency of the dynamic perturbation.

A2 Model L in 2D

The model of Lyakhovsky et al. (1997a), with plane strain assumption, can be written in 2D as a set of hyperbolic PDEs as

$$\frac{\partial \underline{q}}{\partial t} = \frac{\partial \underline{F}}{\partial x} + \frac{\partial \underline{G}}{\partial y} + \underline{s}, \tag{2.A.7}$$

where

$$\begin{aligned} \underline{q} &= (\varepsilon_{xx}, \varepsilon_{yy}, \varepsilon_{xy}, v_x, v_y, \alpha)^T, \\ \underline{F} &= (v_x, 0, \frac{1}{2}v_y, \sigma_{xx}/\rho, \sigma_{xy}/\rho, 0)^T, \\ \underline{G} &= (0, v_y, \frac{1}{2}v_x, \sigma_{xy}/\rho, \sigma_{yy}/\rho, 0)^T, \\ \underline{s} &= (0, 0, 0, 0, 0, \dot{\alpha}), \end{aligned}$$

and $\dot{\alpha}$ is given in Eq. (2.12). The stress-strain relationship is $\sigma_{ij} = (\lambda I_1 - \gamma\sqrt{I_2})\delta_{ij} + (2\mu - \gamma\frac{I_1}{\sqrt{I_2}})\varepsilon_{ij}$. It is therefore derived that

$$\frac{\partial \underline{F}}{\partial \underline{q}} = \begin{bmatrix} 0 & 0 & 0 & 0 & 1 & 0 & 0 \\ 0 & 0 & 0 & 0 & 0 & 0 & 0 \\ 0 & 0 & 0 & 0 & 0 & 1/2 & 0 \\ Q_{11} & Q_{12} & Q_{13} & 0 & 0 & 0 & D_1 \\ Q_{21} & Q_{22} & Q_{23} & 0 & 0 & 0 & D_2 \\ 0 & 0 & 0 & 0 & 0 & 0 & 0 \end{bmatrix}, \tag{2.A.8}$$

where

$$\begin{aligned}
\rho Q_{11} &= (\lambda + 2\mu) - \gamma(2\frac{\varepsilon_{xx}}{\sqrt{I_2}} + \frac{I_1(\varepsilon_{yy}^2 + 2\varepsilon_{xy}^2)}{I_2\sqrt{I_2}}), \\
\rho Q_{12} &= \lambda - \gamma(\frac{I_1}{\sqrt{I_2}} - \frac{I_1\varepsilon_{xx}\varepsilon_{yy}}{I_2\sqrt{I_2}}), \\
\rho Q_{13} &= -\gamma(\frac{2\varepsilon_{xy}}{\sqrt{I_2}} - \frac{2I_1\varepsilon_{xx}\varepsilon_{xy}}{I_2\sqrt{I_2}}), \\
\rho Q_{21} &= -\gamma(\frac{\varepsilon_{xy}}{\sqrt{I_2}} - \frac{I_1\varepsilon_{xx}\varepsilon_{xy}}{I_2\sqrt{I_2}}), \\
\rho Q_{22} &= -\gamma(\frac{\varepsilon_{xy}}{\sqrt{I_2}} - \frac{I_1\varepsilon_{yy}\varepsilon_{xy}}{I_2\sqrt{I_2}}), \\
\rho Q_{23} &= 2\mu - \gamma I_1 \frac{\varepsilon_{xx}^2 + \varepsilon_{yy}^2}{I_2\sqrt{I_2}}.
\end{aligned}$$

With the same method as in Berjamin et al. (2019), the P-wave velocity in the x direction reads

$$c_p = \frac{1}{2}\sqrt{2Q_{11} + Q_{23} + \sqrt{(2Q_{11} - Q_{23})^2 + 8Q_{13}Q_{21}}}, \tag{2.A.9}$$

Appendix 2.B Numerical implementation and verification in ExaHyPE

We implement both models in ExaHyPE (Reinarz et al., 2020), an engine built for solving nonlinear hyperbolic partial differential equations (PDEs) with the arbitrary high-order derivative discontinuous Galerkin (ADER-DG) method. We verify the implementation by means of comparison of our numerical solutions with those given by Berjamin et al. (2019), who implemented the IVM B model in 2D under plain-strain conditions using the finite volume method with flux limiters.

In this verification benchmark, the simulation domain is [0.0, 0.4] m × [0.0, 0.4] m. A point force radiates seismic waves and is defined as $f_x = A \sin 2\pi f_c t \delta(x - x_s)\delta(y - y_s)$, where δ is

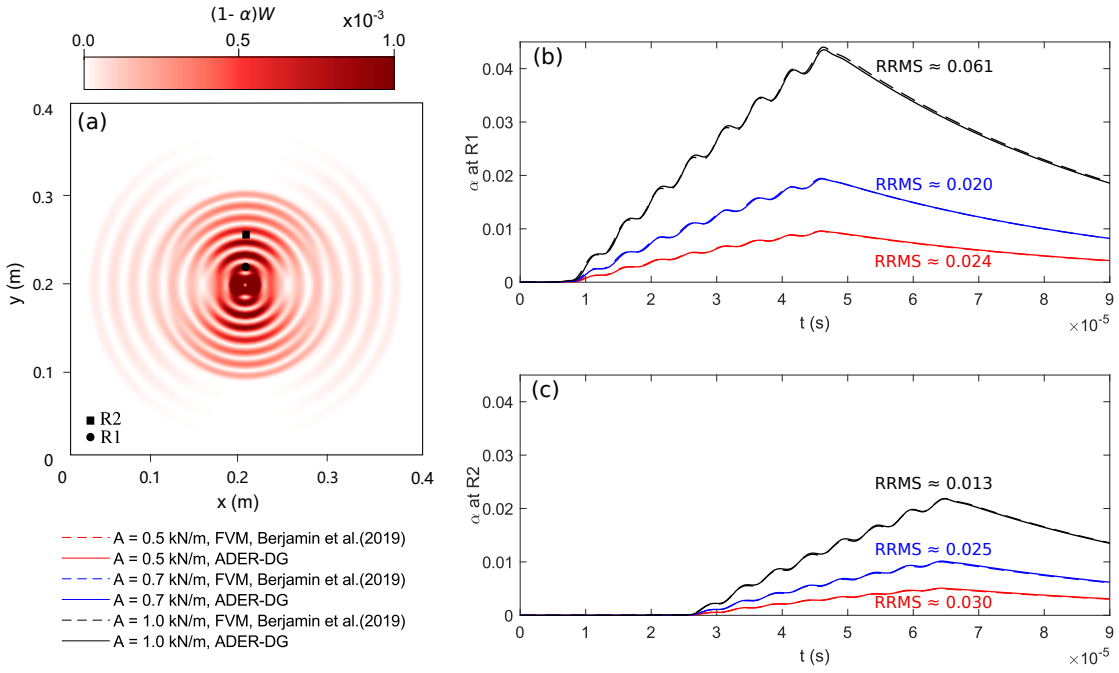

Figure 2.B.1: (a) Snapshot of the elastic strain energy field $(1-\alpha)W$ in J/m^3 at $t = 0.04$ ms by Berjamin et al. (2019) simulated using the Finite Volume Method (FVM). R1 at (0.2, 0.22) m and R2 at (0.2, 0.27) m are the locations of two receivers where the recorded time series of the damage variable α is shown in (b) and (c), respectively. The solutions from Berjamin et al. (2019) with FVM are plotted as dashed curves and the ExaHyPE solutions of our implementation with the arbitrary high-order discontinuous Galerkin (ADER-DG) method are plotted in solid curves for R1 in (b) and R2 in (c). Different source amplitudes with $A = 0.5$, 0.7, and 1.0 kN/m are plotted in red, blue, and black, respectively. The relative root mean square (RRMS) errors $= \sqrt{(\boldsymbol{\alpha_1} - \boldsymbol{\alpha_2})^2/(\boldsymbol{\alpha_2} - \bar{\boldsymbol{\alpha_2}})^2}$, derived from the solution vectors of ADER-DG $\boldsymbol{\alpha_1}$ and FVM $\boldsymbol{\alpha_2}$ respectively are denoted and $\bar{\boldsymbol{\alpha_2}}$ is the average of $\boldsymbol{\alpha_2}$.

the Dirac delta function injected at (0.2, 0.2) m in x-direction and $f_c = 100$ Hz. Following the implementation of Berjamin et al. (2019), the Dirac delta function is approximated as

$$\delta(x - x_s)\delta(y - y_s) = \frac{\exp\left(-(d/\sigma_c)^2\right)}{\pi\sigma_c^2(1 - \exp\left(-(R/\sigma_c)^2\right))}\mathbf{1}_{d\leq R}, \tag{2.B.1}$$

where $d = \sqrt{(x - x_s)^2 + (y - y_s)^2}$; $\mathbf{1}_{d\leq R}$ is the indicator function whose support is a disk space with a radius of $R = c_p/(7.5f_c)$; $c_p = \sqrt{(\lambda + 2\mu)/rho_0}$ is the speed of the P-wave in the undamaged material and the width parameter of the Gaussian function is $\sigma_c = R/2$. In the simulation using the ADER-DG method in ExaHyPE, a structured quadrilateral computational mesh is used to discretise space with an element edge length of around 1.66 mm, which means that 27 cells resolve one wavelength of P waves and 16 cells resolve one wavelength of S waves. We choose the 1st order Lagrange basis with Gauss-Legendre quadrature nodes. The achieved excellent agreement is shown in Fig. 2.B.1a. shows the map of elastic strain energy at $t = 0.04$ ms from Berjamin et al. (2019). Solutions to the damage (α) evolution at the two receivers, R1 at (0.2, 0.22) m and R2 at (0.2, 0.27) m are compared between the Finite Volume solutions of Berjamin et al. (2019) and our implementation in ExaHyPE in Figs. 2.B.1b and c.

Appendix 2.C Theoretical background for Bayesian inversion

In order to quantitatively investigate the relative importance of the theoretical model parameters that explain the evolution of the observed slow dynamics, we apply Bayesian inversion to both models.

The model parameters $\underline{m}$ and experimental observations $\underline{d}^{obs}$ are viewed as random variables in $\mathbb{M} \subset \mathbb{R}^{n_m}$ and $\mathbb{D} \subset \mathbb{R}^{n_d}$, where n_m and n_d are the number of model parameters and the number of observed data points. Let $G : \mathbb{R}^{n_m} \to \mathbb{R}^{n_d}$ denote the model map taking a parameter onto a model prediction.

We then aim to find the posterior, namely the conditional distribution of $\underline{m}$ for a given observation $\underline{d}^{obs}$. We denote the corresponding probability density function (PDF) by $\rho(\underline{m}|\underline{d}^{obs})$. To directly compute underlying parameters from observed data, we would have to apply the inverse of the model map G^{-1}. However, that inverse is not available for our models. Employing Bayes' theorem, we can reformulate the posterior in a way that, as will be detailed below, only involves the forward map G:

$$\rho(\underline{m}|\underline{d}^{obs}) = \frac{\rho(\underline{d}^{obs}|\underline{m})\rho(\underline{m})}{\rho(\underline{d}^{obs})} \propto \rho(\underline{d}^{obs}|\underline{m})\rho(\underline{m}). \tag{2.C.1}$$

We call $\rho(\underline{m})$ the prior density, $\rho(\underline{d}^{obs}|\underline{m})$ is the likelihood that describes the probability

density of measuring the observed data when $\underline{m}$ is given, and $\rho(\underline{d}^{obs})$ is the unconditional PDF of measuring the observed data. Broadly speaking, the posterior considers a model parameter to be likely if the parameter is plausible and its corresponding model prediction is close to observed data.

In practice, $\rho(\underline{d}^{obs})$ is not available. A way to circumvent an analytical derivation is to sample the posterior with the Markov chain Monte Carlo (MCMC) method, where $\rho(\underline{d}^{obs})$ cancels out due to being independent of $\underline{m}$.

The prior encodes expert knowledge about what parameters might be generally plausible, not considering our specific observation. Considering the physical constraint that all model parameters are non-negative, it is $\mathbb{M} = \{\underline{m} \in \mathbb{R}^{n_m} | 0 \leq m_i \leq b_i, i = 1, 2, \ldots, n_m\}$. b_i is the assumed upper bounds of each model parameter. Another constraint on the model parameters is $\int_{\mathbb{M}} \rho(\underline{m})\, d\underline{m} = 1$. With the above two constraints and based on the maximum entropy principle of designing the prior (Good, 1963), the data is assumed to be uniformly distributed in $\mathbb{M}$.

Since we assume measurement errors to be Gaussian, we choose the likelihood as a Gaussian distribution centered around the model prediction $G(\underline{m})$:

$$\rho(\underline{d}^{obs}|\underline{m}) = \frac{1}{\sqrt{(2\pi)^n \det \underline{\underline{C}}}} e^{-\frac{1}{2}(\underline{d}^{obs} - G(\underline{m}))^T \underline{\underline{C}}^{-1} (\underline{d}^{obs} - G(\underline{m}))}. \tag{2.C.2}$$

The covariance matrix $\underline{\underline{C}} \in \mathbb{R}^{n_d \times n_d}$ captures the assumed variances of and the correlation between data points, encoding our knowledge about measurement accuracy. With the additional assumption that the measurements of data points are independent of each other and all have the same variance σ_m^2, we set $\underline{\underline{C}} = \mathrm{diag}(\sigma_m^2, \ldots, \sigma_m^2)$.

From Eq. (2.C.1) and Eq. (2.C.2) it is clear that the posterior density can, up to an unknown constant factor, be computed point-wise. Every evaluation then requires a corresponding evaluation of the model map, i.e. one simulation run.

Appendix 2.D Details about the comparison with the DAET experiments

D1 The validity of treating a DAET sample as a 0D oscillator

Manogharan et al. (2021) conduct DAET measurements on Westerly granite rock samples under triaxial loading conditions. They load the sample with 20 cycles of sinusoidal stress perturbations in one direction. The loading frequencies are 0.1, 1, and 10 Hz. For each

frequency, they load the sample with 5 different amplitudes. They monitor the change of P-wave speeds during the oscillations and also after the oscillation stops.

Before looking into details of the results, we first justify the validity of assuming the sample in DAET as an oscillator under the used loading frequencies. The shortest wavelength of P-wave in their rock sample is around 4165 m/s / 10 Hz ≈ 416.5 m (Manogharan et al., 2021). This is still much larger than the length of the sample, which is 26 mm in the direction of loading. If we further assume the material is homogeneous, the strain field induced by the pumping signals is then uniform. This also means we can ignore the propagation of the pumping waves. In other words, we treat the sample as an oscillator.

D2 Agreement between the model predictions and the experimental data in Fig. 2.5

We here extend the discussion in Section 3.3 of the main text. We first give an explanation to how model L explains the delay. In Eq. (11), when the tensile strain reaches its peak, damage development will not cease ($\xi - \xi_0 > 0$). It only stops upon the strain becoming sufficiently compressive, i.e., once ξ is much smaller than zero such that $\xi - \xi_0 < 0$. This further damage that lasts for around 1/4 of the cycle leads to a larger modulus drop after peak tensile stress as is observed in the laboratory data. However, between 20 μs and 30 μs, there is a discrepancy between the solid green curve and the dashed red curve. The strain within this time range is negative (compressive). This indicates that model L overestimates the modulus increase during the compression of the sample.

Between 5 μs and 15 μs, both model B (the solid blue curve) and model L (the solid green curve) do not vary as much as the data. However, the MCMC ensembles of model B (the blue-shaded area) and model L (the green-shaded area) account for modulus variation at that early period. The early modulus drops are compromised in our inversion to fit the later part of the data better. Feng et al. (2018) made a better fit to the earlier part of the signal, whereas their discrepancies between data and model predictions in the later time range, e.g. between 30 μs and 40 μs, were then too large.

D3 Model parameters used to compare with the observed amplitude-frequency dependence

The evolution of damage follows Eq. (2.12) with $C_d(\alpha) = c_d \exp\left(-\frac{\alpha}{\alpha_d\sqrt{I_2}}\right)$ and $C_r(\alpha) = c_r\alpha$. We adopt a slight change in $C_d(\alpha)$ for a better fit of the data. Our adapted damage evolution is still subject to the restrictions from the laws of thermodynamics in Eq. (2.5), i.e., ensuring that the entropy is increasing in a closed system.

Table 2.D.1: Summary of parameters for the comparison of model B and L, with A_0 being the amplitude of the sinusoidal strain perturbation, f_c the frequency of the strain perturbation, β the first order nonlinearity, δ the second-order nonlinearity, γ_b the damage energy, τ_b the evolution time scale, γ_r the nonlinear modulus, c_d the damage coefficient, c_r the healing coefficient, ξ_0 the modulus ratio as defined in Eq. (2.11), c_r the healing coefficient, ε_{ij0} the different components of initial strains and α_d the normalization factor as defined in Appendix 2.D.

	Para.	Values	Units	Para.	Values	Units
Perturbation	A_0	6×10^{-5}	1	f_c	0.1, 1 or 10	Hz
model B	β	1×10^{2}	1	δ	3×10^{7}	1
	γ_b	3×10^{4}	Pa	τ_b	1×10^{-1}	s
model L	c_d	5.0×10^{0}	$(\text{Pa}\cdot\text{s})^{-1}$	ε_{xx0}	-2.00×10^{-6}	1
	c_r	5.0×10^{-2}	$(\text{Pa}\cdot\text{s})^{-1}$	ε_{yy0}	-2.00×10^{-6}	1
	γ_r	8.0×10^{9}	Pa	ε_{xy0}	6.78×10^{-6}	1
	ξ_0	-0.39	1	α_d	$[0.4, 0.9]$	1

Appendix 2.E A short review of theories for slow dynamics and damage mechanics

We provide a list of continuum damage models in terms of how they behave with respect to non-classical nonlinearity in Table 2.E.1. We compare these models in terms of four characteristics: (1) Stress-strain relation under zero damage; (2) Whether the model differentiates between extension and compression in damage kinematics; (3) Linear or nonlinear relationship between the damage variable and the moduli; (4) Whether they contain the mechanism of healing.

Table 2.E.1: Summary of chosen representative damage models (see text for details). The two models that we focus on in this work are highlighted in bold.

models	stress-strain relationship before damage	damage kinematics in compression and extension	relationship between damage variable and moduli	healing mechanisms
IVM[1]	Nonlinear	Same	Linear	Yes
CDM[2]	Linear	Different	Linear	Yes
CDM[3]	Linear	Same	Nonlinear	No
GPR[4]	Linear	Same	Nonlinear	No
CDHM[5]	Linear	Same	Nonlinear	Yes

[1] model B, Berjamin et al. (2017)
[2] model L, Lyakhovsky et al. (1997a)
[3] Budiansky and O'connell (1976)
[4] Resnyansky et al. (2003); Romenski et al. (2007); Tavelli et al. (2020); Gabriel et al. (2021)
[5] Darabi et al. (2012)

As mentioned in the main text, many studies have used the framework of adhesive contacts at rough crack surfaces to explain slow dynamics. The adhesion potential at the contact of the grain boundary, as a function of the displacement of one surface relative to the

other interacting surface, can have two local stationary points. This is different from the linear elastic case where the elastic energy of the material, as a function of strain, only has one global minimum, which is the vertex of the quadratic curve. Lebedev and Ostrovsky (2014) argue that, under a certain level of external forcing, the energy input from smaller asperities can be large enough to cause the system to leave the first local minimum and reach a secondary local minimum during the perturbation. Compared to the displacement at the first local minimum, the second one has larger values. This means at the same level of external forcing, the displacement at the interface becomes larger. This corresponds to a softening of the material. Such contacts may gradually return to the initial state of equilibrium due to thermal fluctuations and may be responsible for the slow dynamics.

The apparent logarithmic recovery of material moduli with time in slow dynamics may be explained by a superposition of exponential evolution processes at different time scales. This idea is supported both mathematically (Snieder et al., 2017; Sens-Schönfelder et al., 2019) and from experimental observations (Shokouhi et al., 2017). The anisotropic elastic moduli drop can be explained to the first order by introducing a scalar conditioning variable (Lott et al., 2017) to the stiffness tensor as defined by Hughes and Kelly (1953).

Chapter 3

Nonlinear wave propagation in 3D with kinematic source models

The nonlinear mechanical responses of rocks and soils to seismic waves play an important role in earthquake physics, influencing ground motion from source to site. Continuous geophysical monitoring, such as ambient noise interferometry, has revealed co-seismic wave speed reductions extending tens of kilometers from earthquake sources. However, the mechanisms governing these changes remain challenging to model, especially at regional scales. Using a nonlinear damage model constrained by laboratory experiments, we develop and apply an open-source 3D discontinuous Galerkin method to simulate regional co-seismic wave speed changes during the 2015 M_w7.8 Gorkha earthquake. We find pronounced spatial variations of co-seismic wave speed reduction, ranging from <0.01% to >50%, particularly close to the source and within the Kathmandu Basin. The most significant reduction occurs within the sedimentary basin and varies with basin depths, while wave speed reductions correlate with the fault slip distribution near the source. By comparing ground motions from simulations with elastic, viscoelastic, elastoplastic, and nonlinear damage rheologies, we demonstrate that the nonlinear damage model effectively captures low-frequency ground motion amplification due to strain-dependent wave speed reductions in soft sediments. We verify the accuracy of our approach through comparisons with analytical solutions and assess its scalability on high-performance computing systems. The model shows near-linear strong and weak scaling up to 2048 nodes, enabling efficient large-scale simulations. Our findings provide a physics-based framework to quantify nonlinear earthquake effects and emphasize the importance of damage-induced wave speed variations for seismic hazard assessment and ground motion predictions.

3.1 Introduction

Large earthquakes generate strong ground motions that pose a significant threat to civil structures and human life (Ben-Zion et al., 2022). Physics-based models of rocks and soils are essential for simulating potential ground motions from earthquakes in numerical simulations that can account for the spatial heterogeneity and complex surface topography of the Earth's lithosphere (Cui et al., 2010; Taufiqurrahman et al., 2022; Roten et al., 2023). Linear models have successfully explained key phenomena in seismic wave propagation, such as wave field amplification in soft sediments (Moczo and Bard, 1993; van Ginkel et al., 2022), directivity effects of large earthquakes (Boatwright and Boore, 1982; Roten et al., 2014; Wollherr et al., 2019), and resonance in near-surface structures, including surface topography (Lee et al., 2009; Hartzell et al., 2014) and sedimentary basins (Castellaro and

Musinu, 2023).

In recent decades, nonlinear mechanical responses of rocks to seismic waves have been widely observed, covering distances from a few kilometers to over one hundred kilometers from the source (Sens-Schönfelder and Wegler, 2006; Gassenmeier et al., 2016; Lu and Ben-Zion, 2022). Temporal variations in seismic wave speeds during and after earthquakes have been observed using techniques such as repeating earthquakes (Poupinet et al., 1984; Bokelmann and Harjes, 2000; Schaff and Beroza, 2004), cross-correlation of the ambient noise or aftershock recordings between seismic station pairs (Sens-Schönfelder and Wegler, 2006; Brenguier et al., 2008b; Qiu et al., 2020a), and auto-correlation of data at individual stations (Bonilla et al., 2019; Qin et al., 2020; Li and Ben-Zion, 2023). In these observations, rocks typically exhibit a rapid co-seismic reduction in seismic wave speeds, followed by long-term recovery (Gassenmeier et al., 2016). Measured magnitudes of such co-seismic wave speed reduction range from less than 1% up to over 10%, depending on factors such as rock type, distance from the source, depth of interests, and the temporal resolution of the monitoring technique (Brenguier et al., 2014; Wang et al., 2021). Notably, auto-correlation analyses at single stations reveal that co-seismic reductions in wave speed up to 8% are possible at depths between 1 km and 3 km within 20 minutes after an earthquake (Bonilla and Ben-Zion, 2021). Co-seismic wave speed changes under dynamic perturbation are sensitive to rheology, ambient stress, and thermal and hydraulic conditions (Manogharan et al., 2022; Lu and Ben-Zion, 2022). Such changes are potentially new observables that can be extracted from seismic waves to probe subsurface structure and rheology. However, observations of co-seismic wave speed changes may not be adequately captured by linear elastic or visco-elastic models (Johnson and Sutin, 2005; Rivière et al., 2015; Manogharan et al., 2022), indicating the need for more advanced physics-based frameworks.

The nonlinear mechanical responses become most prominent when seismic waves propagate through soft sediments, typically located a few hundred meters below the ground surface (Wang et al., 2021). Soft sediments typically exhibit low seismic wave speeds, amplifying the strain field to values exceeding 10^{-3} and reducing the shear modulus by more than 50% (Roten et al., 2012; van Ginkel et al., 2022). This behavior is accompanied by the damping of ground motion amplitudes (Rajaure et al., 2017) and a change in the frequency components of seismograms toward lower values (Bonilla et al., 2011; Castro-Cruz et al., 2020). Accounting for such nonlinear mechanical responses is crucial for modeling ground motions at both low frequencies ($\leq$1 Hz, Roten et al., 2014) and high frequencies (Roten et al., 2016).

Capturing co-seismic wave speed changes relies on adequate nonlinear rock models. Some of such nonlinear models originate from thermodynamic processes at the microscopic scale (Iwan, 1967; Delsanto and Scalerandi, 2003; Lebedev and Ostrovsky, 2014). These models usually introduce more parameters than those constrained by observations (Wang et al., 2021). As a practical compromise, continuum damage mechanics (CDM) models are based on simplified assumptions about microscopic material deficiencies and describe macroscopic stress-strain relationships using fewer parameters (Kachanov, 1986; Desmorat, 2016; Gabriel et al., 2021). Within this framework, the CDM model by Lyakhovsky et al. (1997a) and the internal variable model (IVM) by (Berjamin et al., 2017) have been shown to reproduce laboratory measurements of co-seismic wave speed changes in rocks (Renaud et al., 2012; Feng et al., 2018; Manogharan et al., 2022; Niu et al., 2024). For unconsolidated sediments,

such as soil, the loss of stiffness under cyclic loading is effectively described by a hyperbolic shear modulus reduction curve (Kramer and Stewart, 2024; Vardanega and Bolton, 2013).

Previous studies have developed numerical methods for modeling co-seismic wave speed changes in 1D (Remillieux et al., 2017; Berjamin et al., 2017) and 2D (Berjamin et al., 2019; Niu et al., 2024), which have been validated through laboratory experiments. The fourth-order staggered-grid finite difference method, implemented in the software AWP-ODC, resolves shear modulus reduction using the IWAN model (Iwan, 1967) in 3D, with a focus on capturing nonlinear effects in soft sediments for ground motion simulations (Cui et al., 2010; Roten et al., 2023). Consolidated rocks, such as granite, also experience co-seismic wave speed reductions (Shokouhi et al., 2017), which remain mostly smaller than 1%. Resolving such small changes is computationally expensive using the IWAN model (Roten et al., 2023). Leveraging this phenomenon as a probe for rock types and subsurface physical conditions (Rivière et al., 2015; Manogharan et al., 2022) requires the development of a numerical framework capable of resolving 3D co-seismic wave speed changes in consolidated rocks. Such a framework would act as a critical bridge, enabling realistic regional-scale modeling of co-seismic wave speed changes directly informed by laboratory data. However, to the best of the authors' knowledge, this approach remains unrealized to date.

To fill this gap, we here propose and validate a novel algorithm based on the discontinuous Galerkin method (Cockburn and Shu, 1989; Dumbser and Käser, 2006; Dumbser et al., 2008) for modeling seismic wave propagation in 3D nonlinear rock rheologies. We implement this algorithm in the open-source software SeisSol (Heinecke et al., 2014; Uphoff et al., 2017; Krenz et al., 2021; Uphoff et al., 2024), which is specifically suited for field-scale seismic wave propagation simulations involving heterogeneous velocity models and complex geometries. We verify the implementation by comparison against analytical solutions and present scaling tests on the Frontera supercomputer (Stanzione et al., 2020).

Using this framework, we simulate co-seismic wave speed changes and ground motions during the 2015 M_W 7.8 Gorkha earthquake in the Kathmandu Valley. This earthquake occurred directly beneath the Kathmandu Valley (Fan and Shearer, 2015), causing over 9,000 fatalities, extensive property damage, and significant loss of life in Nepal. Ground motion records reveal that the Kathmandu basin experienced unexpectedly weak high-frequency motions but larger low-frequency motions compared to empirical predictions (Takai et al., 2016). This behavior has been attributed to nonlinear site response (Castro-Cruz et al., 2020). To evaluate this hypothesis, we utilize an experimentally constrained nonlinear model, IVM, to simulate the co-seismic wave speed changes in rocks (Niu et al., 2024). We also adapt IVM such that it captures the hyperbolic shear modulus reduction curve in soft sediments. By integrating laboratory data, our simulation results quantify the spatial variability of field-scale co-seismic wave speed changes and their impact on peak ground motions, offering important insights for seismic hazard assessment.

3.2 Method

When nonlinear rock rheology is incorporated into seismic wave propagation simulations, the governing wave equations are classified as nonlinear hyperbolic partial differential equations (PDE, Lax, 2005). A key characteristic of these equations is their potential for solutions to develop spatial discontinuities, even if the initial conditions are smooth (LeVeque, 2002). Solving these equations requires an algorithm that can adequately resolve discontinuities while maintaining numerical stability. Additionally, to allow realistic large-scale earthquake simulations and energy efficiency, the implementation must scale efficiently across a large number of compute ranks (Carrington et al., 2008; Cui et al., 2010; Heinecke et al., 2014; Uphoff, 2020; Krenz et al., 2021).

This section describes how we formulate the two nonlinear damage rock models employed in this work as a system of nonlinear hyperbolic PDEs. We then outline the spatial and temporal discretization of these PDEs using the discontinuous Galerkin method (Hesthaven and Warburton, 2007; Cockburn et al., 2012).

3.2.1 Mathematical framework for nonlinear wave propagation in damaged rocks

To model co-seismic wave speed changes and their impact on ground motions, we adopt the recent mathematical framework by Niu et al. (2024) that utilizes a continuum damage model (CDM, Lyakhovsky et al., 1997a) and an internal variable model (IVM, Berjamin et al., 2017). Both models have been shown to quantitatively match laboratory data (Manogharan et al., 2022; Feng et al., 2018; Niu et al., 2024). 2D solutions for co-seismic wave speed changes modeled with the IVM implemented in the DG method have been validated against the results of the finite volume method (Niu et al., 2024).

In the following, we present a unified DG algorithm for nonlinear wave propagation, designed to accommodate any nonlinear rock model explicitly formulated as a system of hyperbolic equations, including IVM and CDM. This approach extends our previous 2D implementation of IVM to 3D and applies our 3D discontinuous Galerkin (DG) method to model wave propagation using the CDM nonlinear rock model.

Hyperbolic PDEs are required for implementation in SeisSol (Uphoff et al., 2024). Previous work implemented linear visco-elasticity (Käser et al., 2007; Uphoff, 2020) and Drucker-Prager elasto-plasticity (Wollherr et al., 2018) using the DG algorithm for linear hyperbolic equations. In contrast, CDM and IVM introduce nonlinear hyperbolic PDEs, which we summarize as follows:

$$\begin{cases} \dfrac{\partial \varepsilon_{ij}}{\partial t} &= \dfrac{1}{2}\left(\dfrac{\partial v_i}{\partial x_j} + \dfrac{\partial v_j}{\partial x_i}\right) \\ \rho \dfrac{\partial v_i}{\partial t} &= \dfrac{\partial \sigma_{ij}(\underline{\underline{\varepsilon}}, \alpha)}{\partial x_j} \\ \dfrac{\partial \alpha}{\partial t} &= r_\alpha(\underline{\underline{\varepsilon}}, \alpha) \end{cases}, \tag{3.1}$$

where $\underline{\underline{\varepsilon}} = \varepsilon_{ij}$ and σ_{ij} denote, respectively, the total strain and stress tensors, v_i is the vector for particle velocity, and ρ is the material mass density. α is a damage variable, which is 0 for intact rock and 1 for fully damaged rock. r_α defines the evolution rate of the damage variable α as a function of the strain tensor and the damage variable itself.

IVM and CDM are both extensions of the classical linear elastic stress-strain relationship that is parameterized with two Lamé parameters, i.e., λ_0 and μ_0 (Landau et al., 1986). The differences between the two models lie in how they are extended to include nonlinear functions of the stress tensor $\sigma_{ij}(\underline{\underline{\varepsilon}}, \alpha)$, and how the source term $r_\alpha(\underline{\underline{\varepsilon}}, \alpha)$ is defined.

For the IVM (Berjamin et al., 2017), we write

$$\begin{cases} \sigma_{ij}(\underline{\underline{\varepsilon}}, \alpha) = (1-\alpha)(\lambda_0 I_1 \delta_{ij} + 2\mu_0 \varepsilon_{ij} + \sigma_{ij}^{\text{mur}}) \\ r_\alpha(\underline{\underline{\varepsilon}}, \alpha) = \dfrac{1}{\gamma_b \tau_b}[\dfrac{1}{2}\lambda_0 I_1^2 + \mu_0 I_2 + W^{\text{mur}} - \phi(\alpha)] \end{cases}, \tag{3.2}$$

where $\phi(\alpha) = \gamma_b[\alpha/(1-\alpha)]^2$ is the storage energy, γ_b is the scale of $\phi(\alpha)$ with units in pascals (Pa), and τ_b is the time scale of damage evolution. $I_1 = \varepsilon_{kk}$ and $I_2 = \varepsilon_{ij}\varepsilon_{ij}$ are two strain invariants.

The original IVM framework can incorporate the classical Murnaghan nonlinear elasticity (Murnaghan, 1937) with three additional material parameters l_0, m_0, and n_0 to account for third-order terms in the non-quadratic components of the elastic energy function $W^{\text{mur}} = (l-m)/3I_1^3 + mI_1I_2 + nI_3$, where $I_3 = \delta_{ijk}\varepsilon_{i1}\varepsilon_{j2}\varepsilon_{k3}$. This leads to the additional stress component $\sigma_{ij}^{\text{mur}} = a_0\delta_{ij} + a_1\varepsilon_{ij} + a_2\varepsilon_{ik}\varepsilon_{kj}$, where the coefficients $a_0 = l_0 I_1^2 - (m_0 - 1/2n_0)(I_1^2 - I_2)$, $a_1 = (2m_0 - n_0)I_1$, and $a_2 = n$. δ_{ijk} denotes the Levi-Civita permutation symbol.

While Murnaghan nonlinear elasticity is useful for modeling some instances of stress-induced anisotropy (Sharma, 2010), it may not adequately explain the observed co-seismic wave speed reductions under dynamic stress fields (Gassenmeier et al., 2016; Berjamin et al., 2017; Niu et al., 2024). Therefore, in the following, we choose to set $l_0 = m_0 = n_0 = 0$ to exclude the additional terms of Murnaghan nonlinear elasticity in our proposed algorithm. This also ensures that $\sigma_{ij}^{\text{mur}} = W^{\text{mur}} = 0$ in Eq. (3.2). However, in Sections 3.3.1 and 3.3.2, we demonstrate that our proposed algorithm remains generic and can accurately resolve nonlinear effects resulting from a simplified Murnaghan nonlinear elasticity in 1D.

For the CDM (Lyakhovsky et al., 1997a, 2016), we write

$$\begin{cases} \sigma_{ij}(\underline{\underline{\varepsilon}}, \alpha) = \lambda_0 I_1 \delta_{ij} - \alpha\gamma_r\sqrt{I_2}\delta_{ij} + [2(\mu_0 + \alpha\xi_0\gamma_r) - \alpha\gamma_r\xi]\varepsilon_{ij} \\ r_\alpha(\underline{\underline{\varepsilon}}, \alpha) = \begin{cases} C_d\gamma_r I_2(\xi - \xi_0) & \text{, if } \xi - \xi_0 > 0 \\ 0 & \text{, if } \xi - \xi_0 \le 0 \end{cases} \end{cases}, \tag{3.3}$$

where γ_r is a third modulus originating from the homogenization of parallel cracks (Lyakhovsky et al., 1997b), and C_d is a damage evolution coefficient. $\xi = I_1/\sqrt{I_2}$ is derived from the two strain invariants. It grows from $-\sqrt{3}$ for isotropic compression to $\sqrt{3}$ for isotropic extension. The damage α starts to accumulate as the strain state deviates farther enough from the isotropic compression. This is expressed as $\xi - \xi_0 > 0$, where ξ_0 is a material parameter that is usually negative for rocks (Lyakhovsky et al., 2016).

In this work, we propose a generic algorithm that can be used for either IVM or CDM. Both models can generally be formulated as a nonlinear hyperbolic system of conservation laws with an additional source term following Dumbser et al. (2008):

$$\frac{\partial u_p}{\partial t} + \frac{\partial F_p^d(\underline{v}, \underline{\underline{\varepsilon}}, \alpha)}{\partial x_d} = s_p(\underline{v}, \underline{\underline{\varepsilon}}, \alpha), \tag{3.4}$$

where $u_p = (\varepsilon_{xx}, \varepsilon_{yy}, \varepsilon_{zz}, \varepsilon_{xy}, \varepsilon_{yz}, \varepsilon_{zx}, v_x, v_y, v_z, \alpha)^T$ is a vector of the conservative variables. ε_{xx}, ε_{yy}, ε_{zz}, ε_{xy}, ε_{yz}, and ε_{zx} are six components of the strain tensor $\underline{\underline{\varepsilon}} = \varepsilon_{ij}$; v_x, v_y and v_z are the three components of the particle velocity vector $\underline{v}$. The flux term F_p^d represents the rates at which the conservative variable u_p gets transferred through a unit area in the direction x_d (LeVeque, 2002). The source vector $s_p = (0, 0, 0, 0, 0, 0, 0, 0, 0, r_\alpha)^T$ with only one non-zero element r_α defined in Eq. (3.2) for IVM or Eq. (3.3) for CDM.

3.2.2 Numerical discretization of the nonlinear wave equations

Our implementation adopts the Arbitrary-accuracy DERivative (ADER) discretization in time (Titarev and Toro, 2002; Dumbser et al., 2008; Gassner et al., 2011), and the discontinuous Galerkin (DG) discretization in space (Cockburn and Shu, 1989; Dumbser et al., 2008). Here, we apply a linearization to the nonlinear hyperbolic PDEs to simplify the adaptation of the algorithm to both damage models, as outlined in Section 3.2.1. This linearization also minimizes the necessary changes to the existing data structure in SeisSol (Uphoff, 2020; Uphoff et al., 2024). We provide a detailed description of the method in this section and Appendix 3.A and will demonstrate in Section 3.3.1 that the algorithm still converges using linearization.

We subdivide the computational domain into tetrahedral elements. Within each element $\mathcal{T}_m$, we use a modal discontinuous Galerkin approach to approximate the conservative variables as $\underline{u} \approx \underline{u}^h$, employing Dubiner's orthogonal polynomial basis functions, $\phi_l(\underline{x})$ (Cockburn et al., 2012). The temporal evolution of the solution is captured using time-dependent coefficients $Q_{lp}(t)$ defined as:

$$u_k^h(\underline{x}, t) = \sum_{l=1}^{L} U_{lk}(t)\phi_l(\underline{x}),\ k = 1, 2, ..., K, \tag{3.5}$$

where the index l runs from 1 to $L = (p+1)(p+2)(p+3)/6$ for a polynomial degree p. The index k runs from 1 to K, the number of elements in the conservative variables u_p in Eq.

(3.4). We discretize the time-dependent coefficients using the ADER scheme with a Taylor series as

$$U_{lp}(t) = \sum_{i=0}^{N} \frac{(t-t_n)^i}{i!} \mathcal{D}_{lp}^i, \tag{3.6}$$

where $\mathcal{D}_{lp}^0 = U_{lp}(t_n)$, and $\mathcal{D}_{lp}^i = \left.\frac{\partial^i U_{lp}}{\partial t^i}\right|_{t=t_n}$ for $i \geq 1$.

This discretized system is solved in two steps. First, we linearize the nonlinear hyperbolic system and estimate $\mathcal{D}_{lp}^i$ using the Cauchy-Kovalevskaya approach (Kovalevskaja, 1874). In the following, we refer to this step as the "prediction step". It allows us to obtain the estimated $U_{lp}(t)$ within one stage, as opposed to the Runge-Kutta method (Butcher, 2007; Gassner et al., 2011). In the second step, we use the predicted $U_{lp}(t)$ to integrate the conservative variables over time while adequately addressing spatial discontinuities at element interfaces, which we refer to as the "correction step". In Appendix 3.A, we detail the algorithm to solve these discretized nonlinear wave equations proposed in this work, including how we implement free-surface and absorbing boundary conditions.

3.3 Verification against analytical solutions

In this section, we verify the proposed numerical algorithm by solving three problems with known analytical solutions. It is essential to confirm that the proposed numerical scheme converges to the correct solutions before applying it to large-scale seismological applications, for which it is impossible to derive analytical solutions for nonlinear wave equations in 3D.

We first compare our numerical solutions for plane waves in 3D with two existing analytical solutions in 1D: (1) the nonlinear Riemann problem and (2) the generation of high-frequency harmonics from a single-frequency source. For 3D analysis, we show that the proposed algorithm can accurately resolve stress-induced anisotropy of CDM, in agreement with the analytical solutions from Hamiel et al. (2009).

3.3.1 The nonlinear 1D Riemann problem

The Riemann problem is a canonical benchmark with analytical solutions for nonlinear hyperbolic PDEs in one dimension (LeVeque, 2002). It is defined by initial conditions with a single discontinuous interface, where the variables have one set of uniform values on one side of the interface while having another set of different uniform values on the other side. The Riemann problem is widely used to assess whether numerical algorithms can accurately resolve discontinuities in solutions, which is an important feature of nonlinear hyperbolic PDEs.

We use a plane shear wave in 3D to configure the 1D Riemann problem. The plane shear wave comprises ε_{xy} and v_y. We set the remaining components to zero. We define the

wavefront as parallel to the $y-z$ plane, such that the domain only varies in the x direction, which simplifies Eqs. (3.1) to:

$$\begin{cases} \dfrac{\partial \varepsilon_{xy}}{\partial t} & = \dfrac{1}{2}\left(\dfrac{\partial v_y}{\partial x}\right) \\ \rho \dfrac{\partial v_y}{\partial t} & = \dfrac{\partial \sigma_{xy}(\varepsilon_{xy})}{\partial x} \end{cases}, \tag{3.7}$$

where we define $\sigma_{xy} = 2\mu(1-\beta\varepsilon_{xy})\varepsilon_{xy}$ as a nonlinear function of ε_{xy} with β being the first order nonlinear coefficient (Landau et al., 1986).

This formulation is comparable to a 1D reduction of Murnaghan nonlinear elasticity, as described after Eq. (3.2). Meurer et al. (2002) provide analytical solutions to the Riemann problem for Eqs. (3.7), incorporating the simplified 1D nonlinear stress-strain relationship.

We choose material parameters and initial conditions to show the accuracy of our proposed algorithm for materials with strong nonlinearity. Therefore, we set the following initial conditions for the Riemann problem.

$$[\varepsilon_{xy}, v_y]^T = \begin{cases} [0.1, -0.5]^T \text{ for } x < 0 \\ [0.2, -1.0]^T \text{ for } x \geq 0 \end{cases} . \tag{3.8}$$

These initial conditions are also shown as dashed curves in Fig. 3.1. We set $\rho = 1.0$, $\mu = 1.0$ and $\beta = 10.0$. The black curves shown in Fig. 3.1 are the corresponding analytical solutions evaluated after 4 ms. The solutions feature one shock wave (interface with sharp discontinuities, marked with red dashed rectangles) and one rarefaction wave (a smooth transition from one state on the left to another state on the right, highlighted by purple rectangles).

We compare this analytical solution to several numerical results obtained with a polynomial order $p = 3$ on three mesh sizes: $h = 2.5$ mm (dashed blue curves), $h = 0.5$ mm (dash-dotted blue curves) and $h = 0.1$ mm (solid blue curves). Figs. 3.1c and 3.1d focus on the numerical solutions at the shock wavefront and at the rarefaction wavefront. The shock wave exhibits stronger spatial oscillations than the rarefaction wave, primarily due to solution variations within each element. The amplitude and wavelength of these oscillations both decrease as the mesh is refined, indicating that oscillations can be effectively suppressed with mesh refinement.

We analyze the convergence rates for different orders of polynomial basis functions and present the results in Fig. 3.1b. We quantify the L_2 errors in our numerical simulations at $t = 4$ ms using the L_2 norms of the differences between the analytical solution u^{ana} and the numerical solutions u^{num}. We determine the convergence rate by analyzing the reduction of L_2 errors with mesh size h on a logarithmic scale. The observed convergence rate remains first order across all polynomial degrees tested (1 to 5), indicating that this algorithm does not achieve arbitrarily high-order accuracy at discontinuities. Nonetheless, we still observe lower L_2 errors with higher-order basis functions on the same mesh (p-convergence, Wollherr et al., 2018). We will discuss the underlying causes and potential improvements in Section

3.5.1.

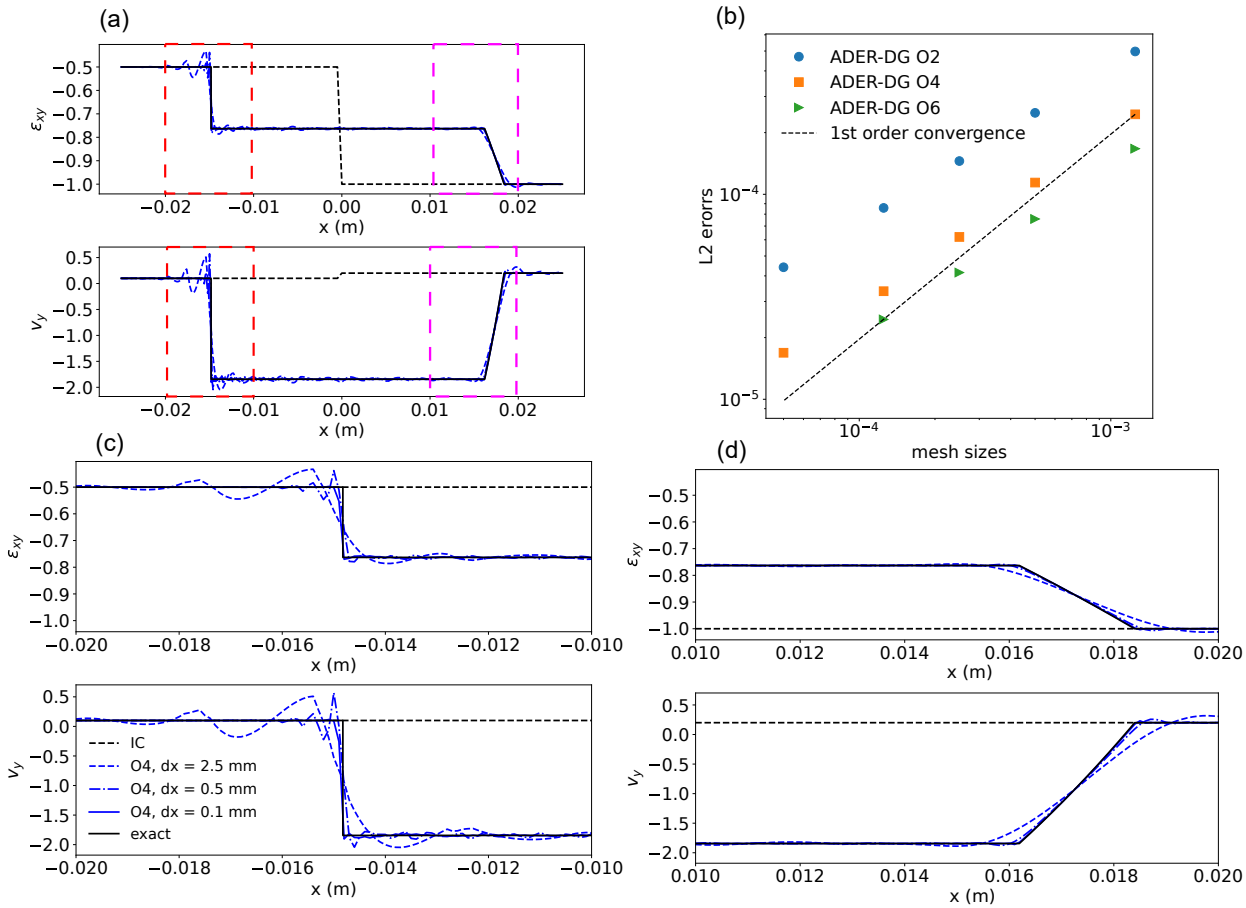

Figure 3.1: Comparison of the analytical and the numerical solutions with varying mesh resolution h and polynomial degrees p for the Riemann problem. (a) Comparison of numerical and analytical solutions of v_y and ε_{xy} using shape functions of polynomial degree 3 (O4, representing convergence rate of order 4). We show solutions for three mesh sizes: $h = 2.5$ mm (dashed blue curves), $h = 0.5$ mm (dash-dotted blue curves) and $h = 0.1$ mm (solid blue curves). The initial conditions (IC) are illustrated as dashed black curves, and the analytical solutions are given in solid black curves. (b) Convergence analysis showing the error decay with decreasing mesh size h, for simulations using basis functions of polynomial degrees 1 (O2, blue dots), 3 (O4, orange rectangles), and 5 (O6, green triangles). The dashed black line indicates first-order convergence as a reference. Panels (c) and (d) highlight specific features of (a): the shock wavefront (inside the dashed red rectangles) in (c) and the rarefaction wavefront (inside the dashed pink rectangles) in (d).

3.3.2 1D frequency modulation by nonlinear materials

The generation of harmonics from a single-frequency source is a mathematically intriguing problem in nonlinear wave propagation. It is widely used to quantify material nonlinearity in acoustic testing and non-destructive evaluation (Shah and Ribakov, 2009; Matlack et al., 2015; Jiao et al., 2025). This behavior is a distinctive and general feature of wave propagation in nonlinear materials, existing in both the Murnaghan nonlinear elasticity and the nonlinear stress-strain relationship in Eq. (3.3) of CDM.

For the 1D Murnaghan nonlinear elasticity defined in Eq. (3.7), we use the 1D analytical asymptotic solutions from McCall (1994) derived using perturbation theory, which describes how the amplitudes of generated harmonics depend on the nonlinear parameters of the material, the propagation distance, and the source amplitude. We use this analytical reference solution in the following to show that our proposed algorithm can accurately resolve the generation of harmonics in 1D nonlinear numerical simulations, exemplarily for 1D Murnaghan nonlinear elasticity.

We adopt the same plane shear wave description as in Section 3.3.1 for the single-frequency source setup and solve the same nonlinear wave equations as in Eqs. (3.7). The simulation is carried out in a cubic domain [-0.025, 0.025] m × [-0.025, 0.025] m × [-0.025, 0.025] m, with periodic boundary conditions on all faces. We define the initial conditions for the plane wave such that the wavelength is 0.05 m, matching the length of the simulation domain:

$$[\varepsilon_{xy}, v_y]^T = [V_0/c_s, V_0]^T \times \sin(2\pi k x), \tag{3.9}$$

where $k = 20\ \mathrm{m}^{-1}$ and $c_s = \sqrt{\mu/\rho}$ is the shear wave speed. We set $\mu = 82.7$ GPa, $\rho = 2473$ kg/m^3, and vary the wave amplitude V_0 and the nonlinear coefficient β to assess whether the simulation results can quantitatively match the analytical asymptotic solutions at a small propagation distance in Eq. (34) of McCall (1994). We note that the shear modulus defined here is unrealistically high for rocks; however, these parameters are chosen solely to verify that the numerical solutions are mathematically consistent with the asymptotic solutions. Additionally, the asymptotic solution from McCall (1994) indicates that the amplitude of the second-order harmonics does not depend on μ.

The single-frequency waveform is modulated by the nonlinear parameter β during propagation. Fig. 3.2a shows the modeled time series at distances of 0.0, 0.5, and 1.0 m from the source. While the peak amplitude and period remain unchanged, the shape of the waveform changes within one period due to the high-order harmonic generation.

We show the generated harmonics 1.0 m away from the source in Fig. 3.2b. McCall (1994) derived an asymptotic solution for the amplitude of the second-order harmonics at small distances away from the source. This analytical asymptotic solution is no longer valid at larger distances. As shown in Fig. 3.2c, these analytical solutions (dashed curves) serve as exact asymptotes to the numerical solutions (solid curves) at small distances. We present results for three sets of parameters, demonstrating the robustness of the match between the analytical asymptotic and our numerical solutions.

3.3.3 3D stress- and damage-induced anisotropy

Rocks exhibit various types and levels of anisotropy (Nur and Simmons, 1969; Nur, 1971; Browning et al., 2017). This anisotropy arises from various internal flaws, such as cracks, joints, and fabric development due to differential stress and strain during tectonic processes (Panteleev et al., 2024). The anisotropy of seismic wave propagation in such rocks can depend on the stress state and accumulated damage, a phenomenon referred to as stress- and damage-induced anisotropy. This dependence leads to nonlinear stress-strain relation-

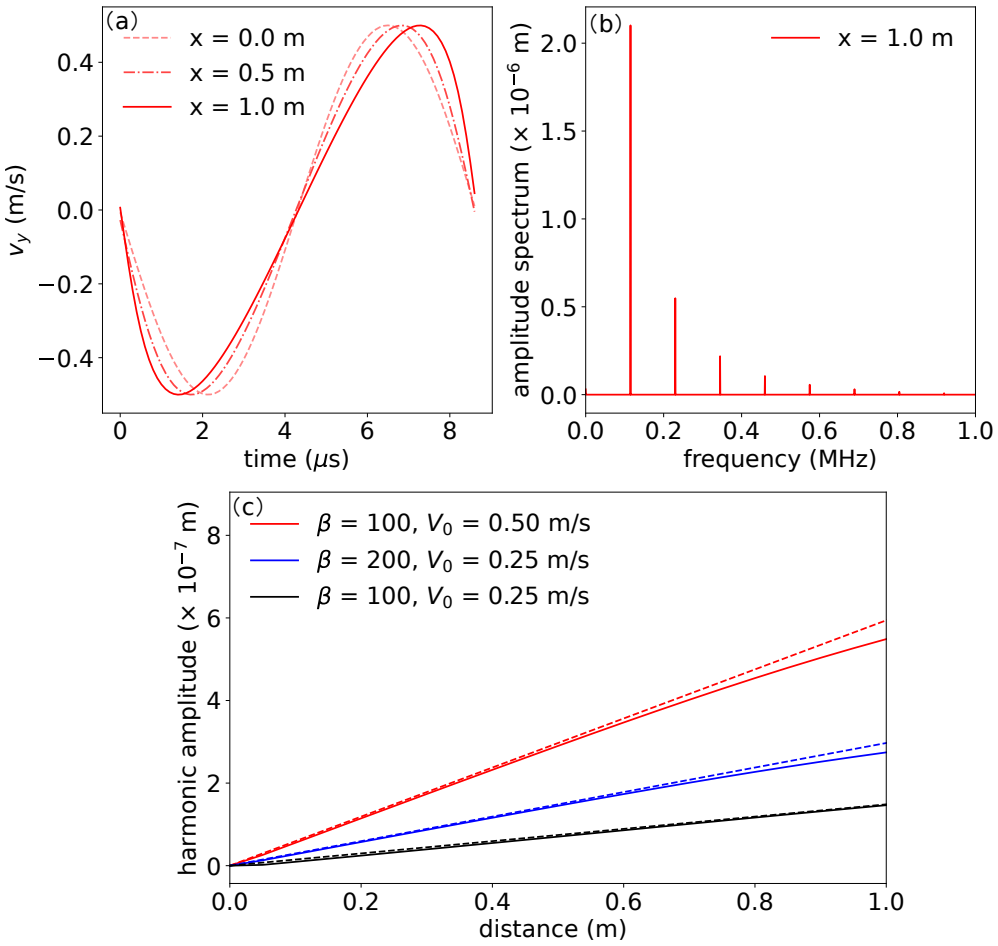

Figure 3.2: Comparison between numerical and analytical asymptotic solutions for wave propagation from a single-frequency source. (a) Recorded time series of v_y at the source (dashed red curve) and at distances of 0.5 m (dash-dotted red curve) and 1.0 m (solid red curve) from the source. (b) The frequency amplitude spectrum of the time series of v_y at 1.0 m from the source shows the generation of high-order harmonics, which are multiples of the fundamental frequency. (c) Comparison between the analytical asymptotic solutions (dashed curve) and the numerical (solid curves) solutions. We show three sets of parameters, with variations in the nonlinear modulus β and the amplitude of the source V_0. We note that the analytical asymptotic solutions are known to be only valid at short distances from the source.

ships, which are important for capturing path and site effects in earthquake simulations. Accurately resolving these effects is essential to advance numerical simulations of ground motions.

Both Murnaghan nonlinear elasticity and CDM describe stress-induced anisotropy (Johnson and Rasolofosaon, 1993; Hamiel et al., 2009). However, while Murnaghan nonlinear elasticity may require unrealistically high values for l_0, m_0, and n_0 in Eq. (3.2), CDM provides a physical framework that can describe stress- and damage-induced anisotropy and has been experimentally validated (Hamiel et al., 2009). Here, we demonstrate that our proposed generic algorithm is suitable for implementing CDM by verifying its ability to resolve stress- and damage-induced anisotropy in 3D. We compare the numerical results with the analytical solutions derived by Hamiel et al. (2009).

We set up several plane-wave initial value problems to investigate how the P, S, and qS wave speeds depend on the orientation of the initial stress with respect to the normal vector of the initial wavefront and the damage level α. The qS wave speed is the additional wave speed resulting from anisotropy (Harris et al., 2009). Without loss of generality, we fix the normal vector of the wavefront to (1,0,0) and vary only the initial stress field and α. Since CDM represents the seismic wave field using the total strain tensor $\underline{\underline{\varepsilon}} = \underline{\underline{\varepsilon}}^{\text{pre}} + \underline{\underline{\varepsilon}}^{\text{dyn}}$, we pragmatically apply initial stress by prescribing initial strain values.

The initial strain field consists of two parts: (i) a uniform strain field $\underline{\underline{\varepsilon}}^{\text{pre}}$, that represents the stress (strain) state of the rocks before dynamic perturbations from seismic waves; and (ii) the perturbation field $u_i^{\text{dyn}} = (\varepsilon_{xx}^{\text{dyn}}, \varepsilon_{yy}^{\text{dyn}}, \varepsilon_{zz}^{\text{dyn}}, \varepsilon_{xy}^{\text{dyn}}, \varepsilon_{yz}^{\text{dyn}}, \varepsilon_{zx}^{\text{dyn}}, v_x, v_y, v_z, \alpha)^T$, substituted into Eq. (3.4). The expression for u_i^{dyn} depends on the wave type and is given as

$$\begin{cases} u_i^{\text{dyn}} = A_0 r_i^1 \sin(2\pi k x) & \text{, for P wave} \\ u_i^{\text{dyn}} = A_0 r_i^2 \sin(2\pi k x) & \text{, for S or qS wave} \\ u_i^{\text{dyn}} = A_0 r_i^3 \sin(2\pi k x) & \text{, for S or qS wave} \end{cases}, \tag{3.10}$$

where the three vectors r_i^1, r_i^2 and r_i^3 are defined in Eq. (3.A.21). The classification of r_i^2 or r_i^3 is either S or qS waves depending on the orientation of the uniform strain field $\underline{\underline{\varepsilon}}^{\text{pre}}$.

We list the material properties of the CDM model and the initial values of the PDEs in Table 3.1. The corresponding mathematical formulation is provided in Eq. (3.3). We adopt the same cubic geometry as in Section 3.3.2.

Table 3.1: Summary of the perturbation field and the model parameters of the continuum damage model.

	Parameters	Values	Units	Parameters	Values	Units
perturbations	A_0	2.5×10^{-6}	1	k	20	m^{-1}
model para.	λ_0	32	GPa	γ_r	37	GPa
	μ_0	32	GPa	ξ_0	-0.75	1
	ρ	2760	kg/m^3	C_d	0.0	$(\text{Pa·s})^{-1}$

We set the initial damage variable α to 0.5. We define $\underline{\underline{\varepsilon}}^{\text{pre}}$ in its principal coordinate

system as $(\varepsilon_{xx}^{\text{pre}}, \varepsilon_{yy}^{\text{pre}}, \varepsilon_{zz}^{\text{pre}}, \varepsilon_{xy}^{\text{pre}}, \varepsilon_{yz}^{\text{pre}}, \varepsilon_{zx}^{\text{pre}})^T = (1 \times 10^{-3}, 0, 0, 0, 0, 0)^T$. Following Hamiel et al. (2009), we initially align the global coordinate system in the numerical simulation with the principal coordinate system of $\underline{\underline{\varepsilon}}^{\text{pre}}$. We then rotate $\underline{\underline{\varepsilon}}^{\text{pre}}$ counterclockwise around the z-axis by an angle ϕ^{ani}, which ranges from 0 to 180 degrees.

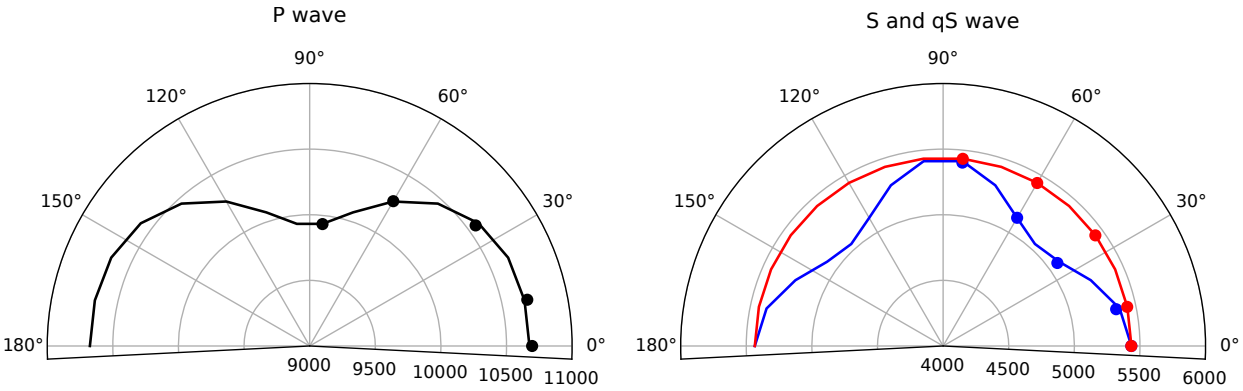

Figure 3.3: Comparison between analytical and numerical wave speeds of different phases for damage- and stress-induced anisotropy. (a) P-wave speed comparison, where black dots represent numerical simulation results and the black curve corresponds to the analytical solution. (b) S-wave (red curve and dots) and qS-wave (blue curve and dots) comparisons, showing numerical results alongside analytical predictions.

Figs. 3.3a and 3.3b compare analytical and numerical solutions for P waves and for S and qS waves, respectively.

3.4 Modeling co-seismic wave speed changes during the 2015 Gorkha earthquake

We apply our verified numerical framework to model co-seismic wave speed changes during the April 25, 2015, M_w 7.8 Gorkha earthquake in the Kathmandu Valley. We set up a geometrically complex 3D simulation of nonlinear seismic wave propagation from a finite source model of the 2015 M_w 7.8 Gorkha earthquake. Our setup captures key features relevant for modeling earthquake-related ground motions: a geometrically complex low-velocity sedimentary basin, layered subsurface geometry that represents different geological units, and a finite source model accounting for the directivity effect of a large earthquake.

3.4.1 Numerical setup, nonlinear parameters and source model

As shown in Fig. 3.4b, the 3D computational domain has a size of 440×380×200 km^3. The velocity model includes five geological units (Table 3.2). The first unit accounts for the surface topography and bathymetry of the shallow sediments within the Kathmandu basin with a low S-wave velocity of 200 m/s (Bohara and Ghimire, 2015). The second unit captures the strong topographical variation outside of the sedimentary basin within the

Kathmandu Valley. We sample the surface topography with a resolution of 5 km. Units 3 through 5 are derived from a regional 1D velocity model (McNamara et al., 2017).

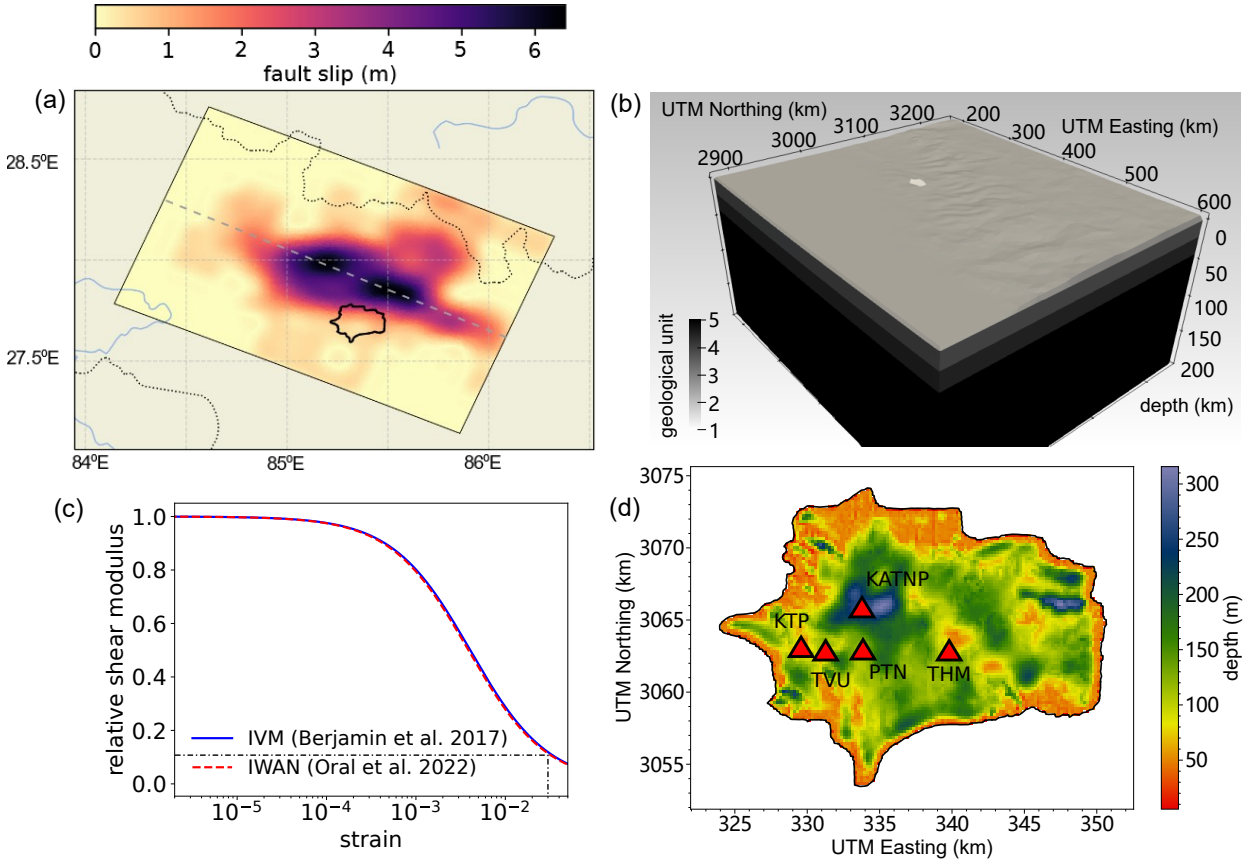

Figure 3.4: Model setup for the non-linear kinematic simulation of the 2015, M_W 7.8 Gorkha earthquake. (a) Fault slip distribution interpolated from Wei et al. (2018)'s kinematic source model. The dashed gray line indicates the 12-km depth slice shown in Fig. 3.5a. (b) Computational domain, consisting of five geological units. We incorporate topography, as well as the bathymetry of the sedimentary basin (white region at the upper boundary of the domain). (c) Shear modulus reduction with strain amplitude of the IVM model (blue curve) within the basin that has been parameterized to match the IWAN model (dashed red curve, Iwan, 1967). (d) Map view of sedimentary basin depth variation, with five strong motion stations (Takai et al., 2016) marked by red triangles.

We will compare the effects of three inelastic rheologies and elastic behavior using otherwise the same model setup: (i) visco-elastic, (ii) elasto-plastic, and (iii) internal variable model (IVM). In the visco-elastic case, we adopt the Zener model (Carcione et al., 1988) to describe viscous attenuation in SeisSol (Uphoff and Bader, 2016a; Uphoff et al., 2024). We list the visco-elastic quality factors for the P-wave (Q_P) and the S-wave (Q_S) inside each layer in Table 3.2. The effective quality factors approximate the target quality factors well within the frequency range of 0.03 to 3 Hz. They increase asymptotically to infinity outside this frequency range, yielding close to linear elastic behavior. We set the quality factors as $Q_P = 0.1V_S$ and $Q_S = 0.05V_S$ for V_S measured in m/s following Olsen et al. (2003). In the elasto-plastic setup, the inelastic behavior is only effective inside the sedimentary basin (unit 1). We adopt the Drucker-Prager plasticity (Wollherr et al., 2018) and provide the material parameters in the footnote of Table 3.2.

We employ the IVM (Berjamin et al., 2017) to investigate nonlinear co-seismic wave speed changes outside the fault core and extending over 100 kilometers from the fault. The model has been validated in Niu et al. (2024) against two sets of laboratory experiments, which demonstrates its ability to quantify nonlinear co-seismic wave speed changes in granite samples (Manogharan et al., 2022) and sandstone samples (Feng et al., 2018). The mathematical description of IVM nonlinearity is summarized in Eq. (3.2). We refer to Berjamin et al. (2017) and Niu et al. (2024) for more details. The chosen model parameters of the IVM within each region are given in Table 3.2. The nonlinear parameters inside the sedimentary basin (unit 1) are calibrated to match the modulus reduction curve from a 2D analysis presented in Oral et al. (2022), constrained by the shift in resonance frequencies observed during significant events with magnitudes exceeding M_W 6.5 within the Kathmandu Valley (Rajaure et al., 2017). For the layered bedrocks (units 2 to 5), we constrain the nonlinear IVM parameters from experiments by Manogharan et al. (2022) investigating nonlinear co-seismic wave speed changes of Westerly granite samples. As discussed in Niu et al. (2024), the parameter γ_b, which determines the amplitude of stationary wave speed reductions under dynamic perturbations, can be constrained from experiments. However, the time scale τ_b, which governs how quickly rocks reach the stationary state, remains highly uncertain. Here, we assume $\tau_b = 10$ s in units 1 to 5, which is consistent with the time scale at which the changes in wave speed stabilize, as observed in experiments on Westerly granite samples (Manogharan et al., 2021).

Table 3.2: Material parameters for each geological unit of the computational domain.

region	depth	c_p	c_s	ρ	Q_p	Q_s	γ_b	τ_b
unit	km	m/s	m/s	kg/m^3	1	1	kPa	s
1*	variable	300	200	1400	20	10	0.5	10
2	variable - 3	5500	3250	2700	325	162.5	356	10
3	3 - 23	5502	3600	2700	360	180	437	10
4	23 - 45	6100	3600	2900	360	180	437	10
5	45 - 200	8100	4500	3300	450	225	550	10

* Plasticity is only effective inside the sedimentary basin in the elasto-plastic simulation. The yielding strength is 224 kPa, with an internal friction angle of 26 degrees and a visco-plastic relaxation time T_v of 0.05 s (Wollherr et al., 2018).

We employ a polynomial degree of five and SeisSol's velocity-aware meshing capabilities to adapt the element size h for each of the five geological units, ensuring at least three elements per S-wave wavelength of a maximum target frequency. In this way, our simulations resolve up to 0.5 Hz of the seismic wavefield everywhere in the domain, including in the complex geometry, low-velocity basin. We refine this mesh around the finite fault plane, which is embedded in units 1 to 3, to $h = 800$ m for a higher resolution of the kinematic rupture evolution. As a result of the velocity-aware meshing, the sedimentary basin (unit 1) is resolved with a higher mesh resolution of $h \approx 133$ m. In units 2 and 3, mesh resolution gradually decreases, and h increases from 800 m near the finite fault plane to ≈2000 m away from the source region.

In this example, we implement the finite source model of Wei et al. (2018) on a meshed finite fault plane to represent the M_W 7.8 Gorkha earthquake. We do not model the spontaneous dynamic rupture process on the fault. The relatively coarse kinematic source

model is interpolated using 2D polynomial functions of degree three over a 186 km × 121 km rectangular fault plane, which results in 22,506 square sub-faults of size 1 km × 1 km. We infer a variable slip rate on each of these sub-faults from the finite source model. Next, we interpolate the imposed slip rates onto SeisSol's triangular fault mesh as an internal boundary condition. This implementation is based on the approach of Tinti et al. (2005); Causse et al. (2014). We use a Gaussian source time function to describe the slip rate function on each fault element (Bouchon, 1997).

3.4.2 Large-scale nonlinear co-seismic wave speed changes

Our nonlinear simulations reveal a significant reduction of co-seismic wave speed changes following the Gorkha earthquake across a vast region (Fig. 3.5). Fig. 3.5a shows wave speed changes 80 s after the rupture onset at 12 km depth. Nonlinear co-seismic wave speed reductions near the source range between 1% and 10% and are particularly pronounced close to the fault plane. For example, in the 12-km depth slice shown in Fig. 3.5a), the dashed black line marks the fault plane, which hosts a high slip at this depth.

The spatial distribution of the near-fault wave speed changes correlates with the fault slip distribution (Fig. 3.4a), with larger reductions in areas of large fault slip. Within the range of 70 km from the fault intersection, the wave speed reductions all exceed 0.01%. This level of damage is still measurable with coda-wave- or ambient-noise-based interferometry (e.g., Brenguier et al., 2014; Gassenmeier et al., 2016; Lu and Ben-Zion, 2022).

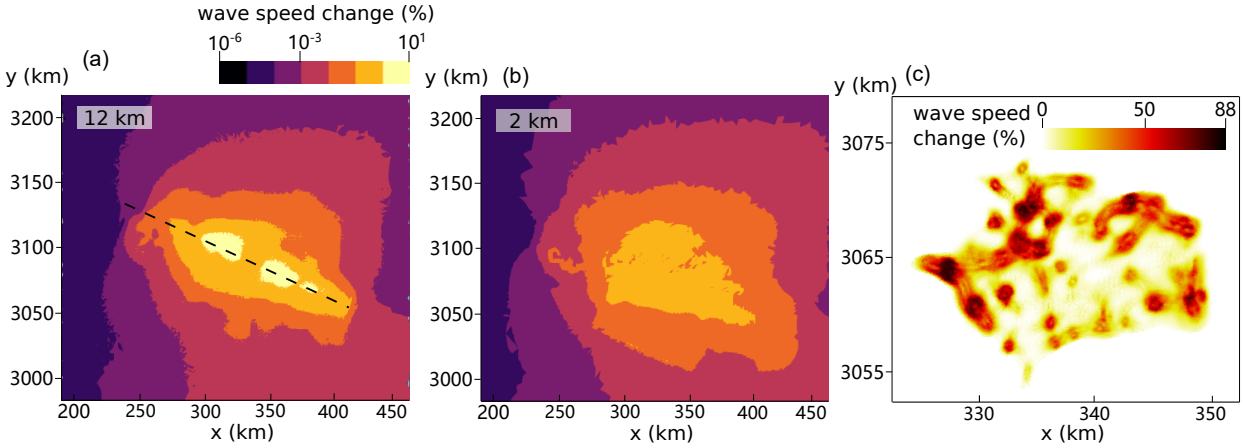

Figure 3.5: Map views of co-seismic wave speed changes and fault slip distribution. (a) Co-seismic wave speed changes at 12 km depth, illustrating spatial variations in velocity reduction. The dashed black line marks the fault plane location at this depth. (b) Co-seismic wave speed changes at 2 km depth, highlighting near-surface variations in wave speed reduction. (c) Co-seismic wave speed changes within the sedimentary basin, showing localized effects of nonlinearity in low-modulus materials.

We show simulated co-seismic wave speed changes at 2 km depth in Fig. 3.5b, which are lower compared with the changes at 12 km depth in Fig. 3.5a. However, the affected region is larger. At 2 km depth, wave speed reductions exceed 0.01% within a 100 km radius.

Within the sedimentary basin, nonlinear co-seismic wave speed changes are much larger

(Fig. 3.5c), and peak changes reach 88%, corresponding to local peak strains up to 3×10^{-2} as can be seen in the shear modulus reduction curve (Fig. 3.4c). The spatial distribution of these changes correlates with the depth variations of the sedimentary basin (Fig. 3.4 d), with greater reductions in wave speed located in regions with larger basin depths. These findings align with field observations of nonlinear site effects, which report significant wave speed reductions in soft sediments during strong shaking (Bonilla et al., 2011). We will further compare the wave speed changes modeled here with observations in Section 3.5.

3.4.3 Nonlinear site effects and sedimentary basin effects

In conjunction with co-seismic wave speed changes, we observe clear effects of the nonlinear rheology on ground motions. Such effects are exemplified in synthetic seismograms comparing linear elastic, visco-elastic, perfect elasto-plastic, and nonlinear damage model simulations (Fig. 3.6a) at station KTP (Fig. 3.4d). Compared to the linear elastic case, all three other models show different levels of ground motion damping at station KTP. The nonlinear damage model exhibits the strongest wave attenuation due to progressive modulus degradation, the accumulation of damage leading to the reduction of moduli.

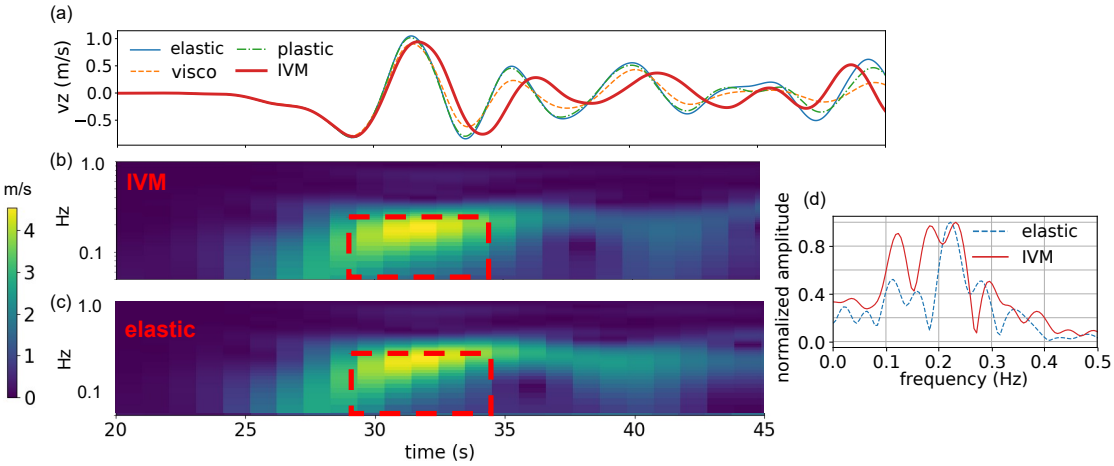

Figure 3.6: Time series and frequency analysis at station KTP. (a) Time series recorded at station KTP (marked in Fig. 3.4b) for different rheological models: elastic (solid blue curve), elasto-plastic (dash-dotted green curve), visco-elastic (dashed orange curve), and the IVM (solid red curve). (b) and (c) are spectrograms of the IVM and elastic cases, respectively, showing the frequency content of the recorded waveforms. The dashed red rectangles highlight the amplification of lower-frequency components in the IVM simulation. (d) Normalized frequency spectra of the time series recorded between 20 s and 50 s, comparing elastic (dashed blue curve) and IVM (solid red curve) models, illustrating the enhanced low-frequency content in the IVM simulation. In Fig. 3.B.1, we show the frequency spectra of time series recorded at four other stations marked in Fig. 3.4d.

Our simulations suggest that co-seismic degradation of rock moduli may be an important mechanism contributing to the observed low-frequency amplification in soft sediments (Bonilla et al., 2011). We capture this effect in the spectrograms of nonlinear damage vs. linear elastic models (Figs. 3.6b, c). In the amplitude-frequency spectra of the modeled ground motion recorded between 20 s and 50 s after rupture onset(Fig. 3.6d), we observe a systematic enhancement of low-frequency components (0.1–0.2 Hz). In our simulation,

this low-frequency amplification is not unique to station KTP. As shown in Fig. 3.B.1, low-frequency amplification is a general feature of the modeled ground motions at stations with high PGV values. High PGVs are correlated with significant ground deformation, leading to strong moduli reduction, consistent with the IVM shear modulus reduction curve (Fig. 3.4c). Such low-frequency amplification is expected during wave propagation through materials with co-propagating wave speed reduction. For example, a laboratory acoustic experiment on rock samples illustrates this phenomenon (Remillieux et al., 2017), where wave speed reduction delays the arrival time of later phases, elongating the period and consequently shifting the energy to a lower frequency.

3.4.4 Nonlinear rheology and ground motions (<0.5 Hz)

We compare modeled shake maps of peak ground velocity (PGV) across models with varying rheologies in Fig. 3.7. Linear elastic simulations show a strong correlation between the PGV in Fig. 3.7a and the depth of the sedimentary basin in Fig. 3.4d. Visco-elastic and elasto-plastic models reduce PGVs inside the Kathmandu basin, consistent with previous regional-scale studies (Narayan and Sahar, 2014; Taborda and Roten, 2015; Esmaeilzadeh et al., 2019). Extending Southern California ShakeOut simulations to include IWAN plasticity also led to a reduction in ground motion amplitudes (e.g., Roten et al., 2023).

The nonlinear damage model attenuates PGVs across both high- and low-shaking intensity regions, unlike the elasto-plastic model, which primarily reduces high PGVs (Fig. 3.7b). The elasto-plastic model attenuates regions of high PGVs, such as in the pink dash-dotted rectangles in Fig. 3.7b. However, elasto-plastic effects are negligible in regions with relatively low PGVs, such as those marked with blue dashed rectangles in Fig. 3.7b, which is expected from previous theoretical work and numerical simulations (e.g., Roten et al., 2014; Kojima and Takewaki, 2016; Seylabi et al., 2021). The plastic yielding surface is only reached when stress reaches a certain threshold. Below this threshold, the mechanical behavior of the material is the same as that of the linear elastic model. In contrast, the nonlinear damage model continuously degrades moduli with increasing strain amplitude (Fig. 3.4c).

3.5 Discussion

3.5.1 Accuracy and performance of the nonlinear implementation

In Section 3.4, we applied the proposed algorithm to model regional-scale nonlinear coseismic wave speed changes in 3D. Nonlinear seismic wave propagation simulations are computationally demanding, necessitating efficient algorithms and optimized implementations for execution on large-scale high-performance computing (HPC) systems (e.g., Reinarz et al., 2020; Roten et al., 2023). To illustrate the efficiency of our nonlinear PDE solver, we analyze its convergence rate with reduced element size h in Section 3.3.1. We also analyze p convergence in Fig. 3.1, where the L_2 errors in numerical solutions decrease with element

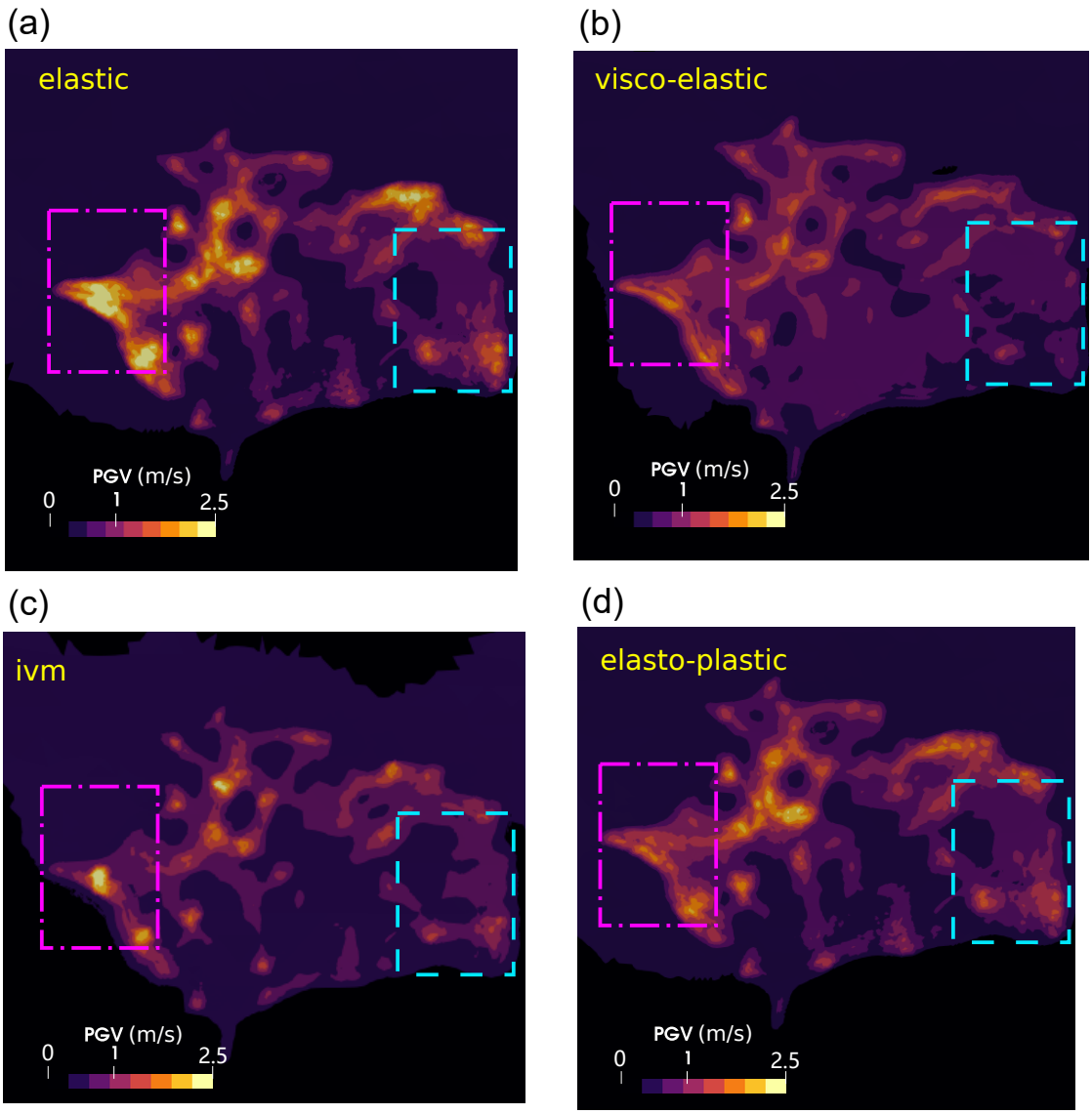

Figure 3.7: Maps of peak ground velocity (PGV) for different rheologies: (a) elastic, (b) visco-elastic, (c) IVM and (d) elasto-plastic. The dashed blue rectangles highlight the region where the elasto-plastic model exhibits minimal attenuation, while the dash-dotted pink rectangles indicate areas where attenuation is more pronounced.

shape functions of higher polynomial degree p.

Fig. 3.1 shows a first-order convergence rate for simulations using basis functions of polynomial degrees 1 to 5. This low order of convergence results from the linearized Cauchy-Kovalevskaya procedure used in the prediction step, c.f. Eq. (3.A.2). The prediction step approximates the time-dependent coefficients $U_{lp}(t)$ within a single time step using a Taylor series expansion (Toro et al., 2001). In this step, to compute high-order time derivatives, we linearize the nonlinear hyperbolic equations in Eq. (3.A.2) and apply the Cauchy–Kovalevskaya procedure to the linearized system, as detailed in Dumbser and Käser (2006). This linearization ensures algorithmic generality across various nonlinear rock models but limits the accuracy of $U_{lp}(t)$ at higher orders, thus constraining the overall convergence rate.

A low-order convergence rate observed at solution discontinuities, such as shock waves, is consistent with Godunov's theorem (Godunov and Bohachevsky, 1959). This theorem establishes that high-order linear solvers have non-monotonic behavior near steep solution gradients. In addition, spectral convergence properties might be reduced to low-order accuracy due to the manifestation of the well-known Gibbs phenomena in the vicinity of strong discontinuities (e.g., Hesthaven and Warburton, 2007, Chapter 5.6). Local low-order convergence is also evident in SeisSol's dynamic rupture implementation (Sec. 6.3 Wollherr et al., 2018).

A potentially promising extension of our work is the incorporation of a discrete Picard iteration scheme (Lindelöf, 1894; Youssef and El-Arabawy, 2007; Dumbser et al., 2008; Gassner et al., 2011; Reinarz et al., 2020). The Picard iteration can substitute our linearized Cauchy-Kovalevskaya procedure in the prediction step to estimate $\mathcal{D}^i_{lp}$ in Eq. (3.3). This approach has been shown to help preserve high-order convergence up to 7 in ADER-DG solvers (Dumbser et al., 2008).

We analyze the performance of our SeisSol implementation on the supercomputer Frontera at TACC (Stanzione et al., 2020). Additionally, we suggest potential improvements to enhance the current algorithm, including future large-scale hardware architectures.

We evaluate the scalability and speed-up of the nonlinear SeisSol implementation using the 2015 Kathmandu earthquake model shown in Fig. 3.4b. We here discretize the simulation domain with three different meshes containing approximately 17, 40, and 100 million elements, respectively. In the discontinuous Galerkin (DG) method, the degrees of freedom (DOFs) are directly proportional to the number of tetrahedral elements. We use a polynomial degree $p = 3$ (Eq. 3.5) for performance analysis, resulting in 200 DOFs per element.

The scaling tests consist of simulations using all three meshes and various numbers of compute nodes, running for 3 s of physical simulation time with the same time step size. SeisSol employs a hybrid MPI-OpenMP parallelization scheme, utilizing MPI for inter-node communication and OpenMP for multi-threaded parallelization within each node (Uphoff et al., 2017).

We evaluate the performance in terms of speed-up, which is defined as t_s/t_0 with t_s being

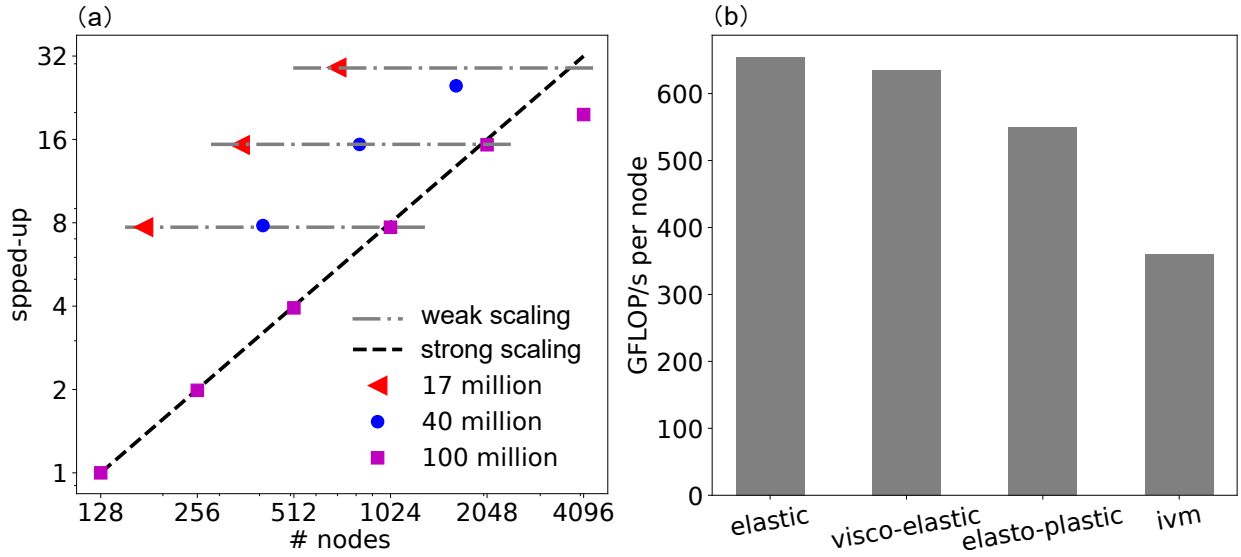

Figure 3.8: Scalability and performance. (a) Speed-up of simulations as a function of the number of compute nodes, scaling up to 4096 nodes on Frontera (Stanzione et al., 2020). The dashed black curve represents the ideal strong-scaling regime, where doubling the number of nodes halves the time to solution. The dash-dotted gray curves illustrate the ideal weak-scaling regime, where proportionally increasing the number of nodes with the number of mesh elements results in the same speed-up. Different mesh sizes are represented by red triangles (17 million elements), blue circles (40 million elements), and purple rectangles (100 million elements). Both axes use a logarithmic scale. (b) Hardware performance analysis during simulations of the 2015 M_W 7.8 Ghorka earthquake (Section 3.4) for different rock models, shown as a bar plot. The mesh used here contains ≈2.3 million elements, and the simulation ran on 32 nodes of SuperMUC-NG (Phase 1).

the time to solution for a given combination of mesh size and number of compute nodes, t_0 is the time to solution of the baseline simulation which uses a 100-million-element mesh on 128 nodes. Fig. 3.8 illustrates the scalability on the Frontera supercomputer at TACC (Stanzione et al., 2020). Frontera employs Intel Xeon Platinum 8280 ("Cascade Lake") processors, each offering 56 cores per node and operating at 2.7 GHz. The total number of available compute nodes is 8,368.

We analyze how speed-up depends on mesh sizes and the number of compute nodes in Fig. 3.8a. To facilitate direct comparison across different mesh sizes for both strong and weak scaling, we normalize the speed-up by nodes per million elements in the following discussions. The results indicate that for fewer than 20 nodes per million elements, strong scaling is nearly linear using the 100 million element mesh, meaning that speed-up increases almost proportionally with node count.

To analyze weak scaling behavior, we compare different mesh sizes using the same number of nodes per million elements. The speed-up across the three different mesh sizes remains nearly identical as long as the number of nodes per million elements remains below 20. However, at 40 nodes per million elements, performance deviates significantly from ideal scaling in both strong and weak scaling tests. Performance degradation becomes more pronounced as the number of elements increases, corresponding to a larger number of compute nodes. One possible explanation is that the communication time between MPI ranks occupies a larger proportion of the overall computation time. Optimizing SeisSol's performance at those higher node counts is beyond the scope of this study and requires further development efforts.

We compare the performance of our implementation using nonlinear space-time interpolation kernels with that of existing SeisSol models. Since our implementation in this work for nonlinear hyperbolic equations only supports a uniform time step size across the entire simulation domain (global time stepping, GTS), we constrain our comparison with the other existing models in SeisSol to the GTS scheme. Uphoff et al. (2017) demonstrate the strong scaling behavior of SeisSol for dynamic rupture earthquake simulations using a linear elastic model. With a mesh containing approximately 51 million elements, the parallel efficiency remained ∼95% on 512 nodes compared to a performance of ∼660 GFLOP/s on 16 nodes. The simulation on 512 nodes corresponds to ∼10 nodes per million elements, which is within the range of our scaling analysis in Fig. 3.8a.

In terms of strong scaling, our nonlinear implementation reaches a speed-up of ∼15.3 when increasing the number of nodes from 128 to 2048 for a mesh with ∼100 million elements. This result is comparable to the elastic model above, with a parallel efficiency of 95.7% up to ∼20 nodes per million elements. However, when the number of nodes is further increased to 4,096, the parallel efficiency drops to 61.5%, indicating the need for further optimization of our current implementation for handling nonlinear wave propagation at extreme scales. For example, Wolf et al. (2022) recently optimized the implementation of computationally intensive poro-elastic rheologies in SeisSol, achieving performance degradation of less than 10%, even at more than 40 nodes per million elements.

The strong scaling behavior does not fully capture the absolute performance of the code in terms of floating point operations per second (FLOP/s). To provide a more precise

assessment, we compare FLOP/s among simulations using the four material models described in Section 3.4. For a 2.3 million element mesh, performance measurements are taken from results running on 16 nodes of SuperMUC-NG (Phase 1) with shape functions of polynomial degree 3. SuperMUC-NG employs Intel Xeon Platinum 8174 processors, each equipped with 48 cores per node, operating at 2.7 GHz. As shown in Fig. 3.8b, simulations with elastic, visco-elastic, and elasto-plastic materials achieve a node-average performance of 654 GFLOP/s, 636 GFLOP/s, and 550 GFLOP/s, respectively, using double-precision floating-point arithmetic. In contrast, the nonlinear implementation with IVM achieves 360 GFLOP/s, which represents a 45% reduction in computational performance compared to the elastic model.

The current implementation does not yet support local time stepping (LTS, Breuer et al., 2016; Uphoff, 2020), which is crucial for efficiently handling non-uniform element sizes due to mesh refinement near faults, complex fault geometries, or highly-varying surface topography. Thus, on the same mesh, the time-to-solution for the nonlinear IVM implementation is approximately 5.56 times longer than the linear elastic material in our simulations presented in Section 3.4. Therefore, future implementation of LTS for nonlinear models is a promising avenue for improving computational efficiency while maintaining accuracy.

3.5.2 Linking co-seismic wave speed changes of rocks from laboratory measurements to regional scale field observations

In this section, we discuss what the simulations of the 2015 Ghorka earthquake reveal about co-seismic wave speed changes in linking measurements of co-seismic wave speed changes from the laboratory with field-scale observations. Under well-controlled environments and boundary conditions in the laboratory, the dynamic responses of rocks to seismic wave fields can be better constrained. In this work, we employ an experimentally constrained continuum mechanics model, the IVM (Berjamin et al., 2017; Niu et al., 2024). However, the amplitudes of the modeled regional wave speed changes may not be comparable to observations during the 2015 Ghorka earthquake. In the following, we discuss reasons that may contribute to the amplitude difference between the simulated regional co-seismic wave speed changes and those in field observations.

Lu and Ben-Zion (2022) show that the average wave speed changes within a depth range from 0 to ≈3 km can exceed 1% within 90 km from the fault. These changes are two orders of magnitude larger than our simulated wave speed changes at depths of 2 km within 100 km from the fault, which is likely due to large perturbations within soft sediments across the upper few hundred meters below the surface. Such significant perturbations inside the sediments are not reflected in our analysis of a depth slice at 2 km. Fig. 3.5c shows that wave speed changes within the sedimentary basin reach 88%. Similarly, using seismic observations from the KiK-net network, Bonilla et al. (2019) observe wave speed reductions greater than 60% in shallow soft sediments within 150 s after the occurrence of the 2011 M_W 9.0 Tohoku-oki earthquake in Japan. These results suggest that incorporating the shallowest sedimentary layers may increase the average wave speed changes, potentially enabling a more quantitative comparison between numerical simulations and field observations.

Although this study demonstrates how to adapt laboratory-derived nonlinear models to regional-scale numerical simulations of co-seismic wave speed changes, the nonlinear IVM material properties used in our simulations were not constrained with rock samples from the Kathmandu Valley. However, the spatial variation patterns of co-seismic wave speed changes modeled here may be transferable across similar lithologies. For example, our simulations reveal that the amplitude of co-seismic wave speed changes correlates strongly with fault slip close to the source (Figs. 3.5a and 3.4a). At increasing distances from the fault, the dynamic strain amplitude is modulated by the layered Earth model, shown in Fig. 3.4. With slightly softer rocks (lower c_s in Table 3.2) at a depth of 2 km, the region where the changes in wave speed are greater than 0.01% is broader than that at a depth of 12 km (Fig. 3.5a and 3.5b). This effect is particularly prominent within the sedimentary basin, where low-moduli unconsolidated materials experience greater strain amplification. We find that the basin depth distribution is an additional factor that adds to the spatial variability of changes in nonlinear wave speed. Our results (Fig. 3.5c) indicate that larger sedimentary basin depths lead to greater co-seismic wave speed reductions. Other factors that might contribute to the variation, for example, the direction of incoming waves (Oral et al., 2022), require further investigation as a next step.

A limitation of our approach is that the nonlinear damage model (IVM) remains isotropic even as damage accumulates. However, material anisotropy may develop under high damage levels (Fig. 3.3), further influencing directivity effects and path and site effects. Accounting for non-linear anisotropy will introduce additional challenges in accurately implementing free-surface boundary conditions. Although the method outlined in Appendix 3.A is suitable for isotropic models only, it can serve as a first-order approximation for damage- and stress-induced moduli changes at the free-surface boundary by only accounting for the induced changes in the effective Lamé parameters in Eq. (3.A.17).

3.5.3 Incorporating background stress effects on co-seismic nonlinear wave speed changes

In Section 3.4, we use the IVM with experimentally constrained parameters (Niu et al., 2024) on Westerly granite to quantify the spatial distribution of co-seismic wave speed reductions following the 2015 M_W 7.8 Ghorka earthquake. This model assumes a universal co-seismic wave speed reduction, irrespective of the initial stress state. Similar universal reductions in wave speed under dynamic perturbations have been observed in laboratory rock samples under unconfined stress conditions Remillieux et al. (2017); Feng et al. (2018) and under uniaxial compression of up to 20 MPa (Rivière et al., 2015; Manogharan et al., 2021). However, Manogharan et al. (2022) show that the level of uniaxial compression exerts a second-order influence on the amplitude of co-seismic wave speed reductions, indicating that a more advanced model is needed to incorporate the dependence of wave speed changes on the background stress state.

The CDM (Lyakhovsky et al., 1997a), described in Eq. (3.3), explicitly accounts for the background stress state. In this model, the amplitude of damage accumulation depends on how close the current stress state is to a critical stress threshold, defined by ξ_0 in Eq. (3.3). In Section 3.3.3, we demonstrate that our proposed algorithm can quantify stress- and

damage-induced anisotropy in wave propagation using CDM. However, applying CDM to co-seismic wave speed changes requires sufficient knowledge of the pre-existing background stress state.

Properly configuring the background stress state is especially important when modeling layered geological structures, particularly when accounting for spatially varying bathymetry in sedimentary basins (unit 1 in Fig. 3.4). Using CDM, the background stress state is imposed by specifying the initial strain tensor. To prevent spurious wave generation at the beginning of the simulation, it is necessary to ensure the stress continuity condition at layer boundaries. This is challenging when incorporating geometrically complex basin bathymetry, where the strain tensor must be reoriented according to the basin geometry. A potential solution to this challenge in future work may be first to solve the static strain field resulting from the overburden of rocks and soils. This balanced strain field may then be applied as the initial strain state for wave simulations, ensuring a physically consistent background stress distribution.

3.6 Conclusions

To develop a seismic wave propagation method capable of modeling observed co-seismic wave speed changes, we propose a generic numerical algorithm based on the discontinuous Galerkin (DG) method that can be applied to a wide range of nonlinear rock models. We verify the numerical solutions obtained using our new approach implemented in the open-source software SeisSol against three sets of analytical solutions and confirm the convergence of the algorithm. Using the Riemann problem setup, we demonstrate that the proposed method accurately resolves discontinuities in nonlinear hyperbolic equations. We find a 1st order convergence rate at solution discontinuities with basis functions of polynomial degrees 1 to 5. On the same mesh, using higher-degree basis functions leads to lower numerical errors. We show that the method can accurately resolve the amplitude of high-frequency harmonics generated by wave propagation in the Murnaghan nonlinear elasticity model. The proposed method can also properly quantify the stress- and damage-induced mechanical anisotropic behaviors of rocks.

We evaluate the parallel performance of our implementation on Frontera and find that both weak and strong scaling remain close to linear up to 20 nodes per million elements, allowing efficient simulations on meshes with up to 100 million elements and scalability up to 2048 nodes. However, despite the good parallel scalability, node-level performance remains non-optimal, indicating the need for further optimizations to improve computational efficiency and reduce runtime for handling future nonlinear wave propagation simulations at extreme scales.

We apply our algorithm to regional-scale earthquake simulations, including non-linear wave propagation effects from source to site. We use the experimentally constrained nonlinear model IVM to capture co-seismic wave speed changes during the 2015 M_w 7.8 Gorkha earthquake in the Kathmandu Valley, incorporating a free surface with topography, a sedimentary basin with low wave speeds and complex bathymetry, a layered geological structure, and a

finite source model that accounts for rupture directivity effects. The simulation results show that co-seismic wave speed reductions depend on the fault slip distribution near the source and are modulated by basin depth tens of kilometers away from the fault. Co-seismic wave speed changes also enhance low-frequency components in soft sedimentary layers, affecting ground motions. This study demonstrates, using a physics-based framework to quantify nonlinear earthquake effects at a regional scale, the importance of damage-induced wave speed variations for seismic hazard assessment, ground motion predictions, and as an observable to better constrain earthquake physics and rock mechanics.

Open Research

The source code of SeisSol with nonlinear IVM implementation is available as open-source software from Uphoff et al. (2024) under the branch `damaged-material-nonlinear-drB`. The model setup, simulation outputs, and post-processing scripts to reproduce all figures are available from Niu et al. (2025).

Appendices

Appendix 3.A DG algorithm for nonlinear wave equations

In this section, we provide the details on three components of the DG algorithm proposed in this work: prediction step, correction step, and boundary conditions.

Prediction step: linearization and temporal approximation

In the prediction step, we retain only the conservative term of Eq. (3.4) assuming weak nonlinearity ($\partial\sigma_{ij}/\partial\varepsilon_{mn}$ and $\partial\sigma_{ij}/\partial\alpha \rightarrow$ constant) and employ a linearization procedure. Our main motivation for this linearization in the prediction step is to maintain the HPC-optimized data structure of SeisSol (Uphoff et al., 2024). We will release this restriction in the subsequent correction step described later. This assumption preserves the convergence of the algorithm for nonlinear hyperbolic PDEs but can have an effect on the convergence rate, as we will discuss in Section 3.3.1.

We write for the linearized prediction step:

$$\begin{aligned}\frac{\partial u_p}{\partial t} &= -\frac{\partial F_p^d}{\partial x_d} \\ &= -\frac{\partial F_p^d}{\partial u_q}\frac{\partial u_q}{\partial x_d},\end{aligned} \tag{3.A.1}$$

where $F_p^d = F_p^d(\underline{u})$ is a nonlinear function of the conservative variables u_p, with $\dfrac{\partial F_p^d}{\partial u_q}$ corresponding to its Jacobian matrix. Taking a time derivative on both sides of Eq. (3.A.1), we approximate the second time derivative of u_p as:

$$\begin{aligned}\frac{\partial^2 u_p}{\partial t^2} &= -\frac{\partial}{\partial t}\left(\frac{\partial F_p^d}{\partial u_q}\frac{\partial u_q}{\partial x_d}\right) \\ &= -\frac{\partial}{\partial t}\left(\frac{\partial F_p^d}{\partial u_q}\right)\frac{\partial u_q}{\partial x_d} - \frac{\partial F_p^d}{\partial u_q}\frac{\partial}{\partial x_d}\left(\frac{\partial u_q}{\partial t}\right) \\ &\approx -\frac{\partial F_p^d}{\partial u_q}\frac{\partial}{\partial x_d}\left(\frac{\partial u_q}{\partial t}\right).\end{aligned} \tag{3.A.2}$$

This condition is satisfied if $\frac{\partial}{\partial t}\left(\frac{\partial F_p^d}{\partial u_q}\right)\frac{\partial u_q}{\partial x_d} \ll \frac{\partial F_p^d}{\partial u_q}\frac{\partial}{\partial x_d}\left(\frac{\partial u_q}{\partial t}\right)$, which requires $\frac{\partial F_p^d}{\partial u_q}$ to vary slowly in time compared to the temporal variation of u_q.

From Eqs. (3.1) and (3.4), F_p^d incorporates the nonlinear stress-strain relationships. Consequently, $\frac{\partial F_p^d}{\partial u_q}$ changes gradually under weak nonlinearity. The weak nonlinearity makes Eq. (3.A.2) a more accurate approximation for the second-order time derivative of u_p. We reiterate that this assumption only pertains in the prediction step.

Following Uphoff (2020), the arbitrary order (i) derivative of q_p in time ($\mathcal{D}_{lp}^i$) is computed as follows:

$$\mathcal{D}_{lp}^i \int_{\mathcal{T}_m} \phi_k \phi_l \mathrm{d}V = -\int_{\mathcal{T}_m} \phi_k B_{pq}^d(\underline{u}^{t_n}) \mathcal{D}_{lq}^{(i-1)} \frac{\partial \phi_l}{\partial x_d} \mathrm{d}V, \tag{3.A.3}$$

where $\mathcal{D}_{lq}^i \phi_l = \frac{\partial^i u_q}{\partial t^i}$.

For linear wave equations, we derive $B_{pq}^d = \frac{\partial F_p^d}{\partial u_q}$ as a cell-wise constant that keeps its value along the simulation (Uphoff, 2020). In our nonlinear case, we need to re-compute the cell-wise averaged B_{pq}^d from $u_p^{t_n}$ at the beginning of each time step t_n, i.e. $B_{pq}^{d,t_n} = B_{pq}^d(\underline{u}^{t_n}) = \int_{\mathcal{T}_m} B_{pq}^d(\underline{u}^{t_n})\mathrm{d}V/V_e$ and V_e is the volume of the tetrahedral element.

If we substitute B_{pq}^{d,t_n} in Eq. (3.A.3), the integration in a reference cell $\mathcal{E}_3$, which is defined in a reference Cartesian coordinate system where the position vector of a point is ξ_i, will be

$$\mathcal{D}_{lp}^i |J| \int_{\mathcal{E}_3} \phi_k \phi_l \mathrm{d}V = -|J| \Theta_{ed}^{-1} \mathcal{D}_{lp}^{(i-1)} B_{pq}^{d,t_n} \int_{\mathcal{E}_3} \phi_k \frac{\partial \phi_l}{\partial \xi_e} \mathrm{d}V, \tag{3.A.4}$$

where $\Theta_{ed}^{-1} = \partial \xi_e / \partial x_d$. We refer to Chapter 3.1 of Uphoff (2020) for the detailed definition of the reference Cartesian coordinate system. Defining $M_{kl} = \int_{\mathcal{E}_3} \phi_k \phi_l \mathrm{d}V$ and $K_{lk}^e = \int_{\mathcal{E}_3} \phi_k \frac{\partial \phi_l}{\partial \xi_e} \mathrm{d}V$, we derive

$$\mathcal{D}_{lp}^i |J| M_{kl} = -|J| \Theta_{ed}^{-1} \mathcal{D}_{lq}^{(i-1)} B_{pq}^{d,t_n} K_{lk}^e, \tag{3.A.5}$$

which is directly comparable to Eq.(3.31) in Uphoff (2020).

If the nonlinear source term is considered, we simplify and add the nonlinear source term only when $i = 1$ in Eq. (3.A.5).

$$\mathcal{D}_{lp}^1 |J| M_{kl} = -|J| \Theta_{ed}^{-1} \mathcal{D}_{lq}^0 B_{pq}^{d,t_n} K_{lk}^e + |J| \int_{\mathcal{E}_3} s_p(\underline{q}^{t_n}) \phi_k \mathrm{d}V, \tag{3.A.6}$$

where $u_q^{t_n} = \mathcal{D}_{lq}^0 \phi_l$, with the same definition of Θ_{ed}^{-1} as Eq. (3.A.4). The nonlinear source function $s_p(\underline{u}^{t_n})$ is evaluated on a nodal basis of $u_q^{t_n}$ projected from the modal basis coefficients $\mathcal{D}_{lq}^0$ as presented by Wollherr et al. (2018).

Correction step: time integration and discontinuity handling

The weak form of Eq. (3.4) with integration by part looks like

$$\frac{\partial}{\partial t}\int_{\mathcal{T}_m} \phi_k U_{lp}(t)\phi_l \mathrm{d}V + \int_{\partial\mathcal{T}_m} \phi_k (F_p^d n_d)^* \mathrm{d}S - \int_{\mathcal{T}_m} \frac{\partial \phi_k}{\partial x_d} F_p^d \mathrm{d}V = \int_{\mathcal{T}_m} s_p(U_{lp}\phi_l)\phi_k \mathrm{d}V, \quad (3.A.7)$$

where $s_p(U_{lp}\phi_l) = (0,0,0,0,0,0,0,0,0,r_\alpha)^T$ as in Eq. (3.4). n_d is the normal vector of the interface $\partial\mathcal{T}_m$. Integrating both sides of the Eq. (3.A.7) in one time step $[t_n,\, t_{n+1}]$ yields

$$\int_{\mathcal{T}_m} \phi_k\phi_l[Q_{lp}^{n+1} - U_{lp}^n]\mathrm{d}V + \int_{\partial\mathcal{T}_m} \phi_k \int_{t_n}^{t_{n+1}} (F_p^d n_d)^* \mathrm{d}\tau \mathrm{d}S - \int_{\mathcal{T}_m} \frac{\partial \phi_k}{\partial x_d} \int_{t_n}^{t_{n+1}} F_p^d \mathrm{d}\tau \mathrm{d}V$$
$$= \int_{\mathcal{T}_m} \phi_k \int_{t_n}^{t_{n+1}} s_p(U_{lp}\phi_l)\mathrm{d}\tau \mathrm{d}V. \quad (3.A.8)$$

According to Eqs. (3.5) and (3.6), we estimate the space-time integration in each term of Eq. (3.A.8) with $\mathcal{D}_{lp}^i$ derived from the prediction step.

We expand on the space-time integration term by term in the following. We start from the second term on the left-hand-side of Eq. (3.A.8) when $\partial\mathcal{T}_m$ is on the element surfaces that are not on the boundaries of the computation domain. The latter case will be addressed in Appendix 3.A. The interface flux within the computational domain $(F_p^d n_d)^*$ must account for the solution discontinuities on each side of the interface. Strictly speaking, this requires solving the Riemann problem for a nonlinear hyperbolic system (LeVeque, 2002). Here we use the local Lax-Friedrich flux F_p^{LF} which has a simple form while preserving numerical stability. Its expression is

$$\begin{aligned} F_p^{LF} &= (F_p^d n_d)_p^* \\ &= \frac{1}{2}(F_p^d(u_p^+) + F_p^d(u_p^-))n_d + \frac{1}{2}C(u_p^- - u_p^+), \end{aligned} \quad (3.A.9)$$

where C is the largest eigenvalues of the matrix $B_{pq}^d((\underline{u}^+ + \underline{u}^-)/2)$ in Eq. (3.A.3). As defined in Eq. (3.A.9), F_p^{LF} is a nonlinear function of u_p on both sides of u_p^+ and u_p^-. For the numerical integration, we evaluate F_p^{LF} at the quadrature points in space and time following Uphoff (2020) and expand the second term on the left-hand-side of Eq. (3.A.8) as

$$\int_{\partial\mathcal{T}_m} \phi_k \int_{t_n}^{t_{n+1}} (F_p^d n_d)^* \mathrm{d}\tau \mathrm{d}S$$
$$= \sum_{i=1}^{N^s} \beta_i \phi_{k,i} \sum_{z=1}^{N^t} \gamma_z F_{lp,z,s}^{LF} |S_f| \Delta t, \tag{3.A.10}$$

where β_i and γ_z are weights, respectively, for surface and time integration.

For the third term on the left-hand-side of Eq. (3.A.8), we also discretize $F_p^d = \mathcal{F}_{lp}^d(t)\phi_l(\boldsymbol{x})$ with the same modal basis functions as u_p. We briefly summarize the procedures here and refer to Wollherr et al. (2018) for the detailed formulae. The evaluation of $\mathcal{F}_{lp}^d(t)$ follows 3 steps: (1) Project $U_{lp}(t)$ into a nodal basis and obtain the $U_{lp}^{Node}(t)$ coefficients in the nodal basis; (2) Evaluate the coefficients $\mathcal{F}_{lp}^{d,Node}$ in nodal space by substituting $U_{lp}^{Node}(t)$ into the nonlinear function $\mathcal{F}_p^d(U_{lp}^{Node})$ based on Eq. (3.1) to Eq. (3.3); (3) Obtain the coefficients $\mathcal{F}_{lp}^d(t)$ in modal space by projecting back from the nodal space coefficients $\mathcal{F}_p^d(U_{lp}^{Node})$. The third term on the left-hand-side of Eq. (3.A.8) then becomes

$$\int_{\mathcal{T}_m} \frac{\partial \phi_k}{\partial x_d} \int_{t_n}^{t_{n+1}} F_p^d \mathrm{d}\tau \mathrm{d}V$$
$$= \int_{t_n}^{t_{n+1}} \mathcal{F}_{lp}^d(\tau) \mathrm{d}\tau \int_{\mathcal{T}_m} \frac{\partial \phi_k}{\partial x_d} \phi_l \mathrm{d}V. \tag{3.A.11}$$

We employ a similar procedure for the right-hand-side of Eq. (3.A.8). We discretize $s_p(t) = S_{lp}(t)\phi_l$ and yield

$$\int_{\mathcal{T}_m} \phi_k \int_{t_n}^{t_{n+1}} s_p(U_{lp}\phi_l) \mathrm{d}\tau \mathrm{d}V$$
$$= \int_{t_n}^{t_{n+1}} S_{lp}(\tau) \mathrm{d}\tau \int_{\mathcal{T}_m} \phi_k \phi_l \mathrm{d}V. \tag{3.A.12}$$

Free surface and absorbing boundary conditions

We need to take care of the numerical flux $(F_p^d n_d)^*$ in the second term of Eq. (3.A.8) when $\partial\mathcal{T}_m$ is defined on two types of boundaries that are important for earthquake simulations: the absorbing boundary and the free-surface boundary. While IVM in Eq. (3.2) remains isotropic with damage accumulation, CDM in Eq. (3.3) can introduce stress-induced anisotropic mechanical responses in rocks (Hamiel et al., 2009). Such anisotropy inside the bulk materials can be resolved using the local Lax-Friedrich flux in Eq. (3.A.9) (de la Puente et al., 2007). In defining the boundary conditions of the simulation domain, we simplify by only considering the nonlinear effects on the isotropic moduli, i.e., the two Lamé parameters. To achieve this, we retain only the components of $\underline{\underline{B}}^d = B_{pq}^d$ that correspond to the isotropic effective Lamé parameters, denoting an approximated matrix as

$\underline{\underline{B}}^{d,eff}$. The expressions for $\underline{\underline{B}}^{d,eff}$ are (Wilcox et al., 2010):

$$\underline{\underline{B}}^{1,eff} = \begin{bmatrix} 0 & 0 & 0 & 0 & 0 & 0 & -1 & 0 & 0 & 0 \\ 0 & 0 & 0 & 0 & 0 & 0 & 0 & 0 & 0 & 0 \\ 0 & 0 & 0 & 0 & 0 & 0 & 0 & 0 & 0 & 0 \\ 0 & 0 & 0 & 0 & 0 & 0 & 0 & -\frac{1}{2} & 0 & 0 \\ 0 & 0 & 0 & 0 & 0 & 0 & 0 & 0 & 0 & 0 \\ 0 & 0 & 0 & 0 & 0 & 0 & 0 & 0 & -\frac{1}{2} & 0 \\ -\frac{\lambda^{eff}+2\mu^{eff}}{\rho} & -\frac{\lambda^{eff}}{\rho} & -\frac{\lambda^{eff}}{\rho} & 0 & 0 & 0 & 0 & 0 & 0 & 0 \\ 0 & 0 & 0 & -\frac{2\mu^{eff}}{\rho} & 0 & 0 & 0 & 0 & 0 & 0 \\ 0 & 0 & 0 & 0 & 0 & -\frac{2\mu^{eff}}{\rho} & 0 & 0 & 0 & 0 \\ 0 & 0 & 0 & 0 & 0 & 0 & 0 & 0 & 0 & 1 \end{bmatrix}, \tag{3.A.13}$$

$$\underline{\underline{B}}^{2,eff} = \begin{bmatrix} 0 & 0 & 0 & 0 & 0 & 0 & 0 & 0 & 0 & 0 \\ 0 & 0 & 0 & 0 & 0 & 0 & 0 & -1 & 0 & 0 \\ 0 & 0 & 0 & 0 & 0 & 0 & 0 & 0 & 0 & 0 \\ 0 & 0 & 0 & 0 & 0 & 0 & -\frac{1}{2} & 0 & 0 & 0 \\ 0 & 0 & 0 & 0 & 0 & 0 & 0 & 0 & -\frac{1}{2} & 0 \\ 0 & 0 & 0 & 0 & 0 & 0 & 0 & 0 & 0 & 0 \\ 0 & 0 & 0 & -\frac{2\mu^{eff}}{\rho} & 0 & 0 & 0 & 0 & 0 & 0 \\ -\frac{\lambda^{eff}+2\mu^{eff}}{\rho} & -\frac{\lambda^{eff}}{\rho} & -\frac{\lambda^{eff}}{\rho} & 0 & 0 & 0 & 0 & 0 & 0 & 0 \\ 0 & 0 & 0 & 0 & -\frac{2\mu^{eff}}{\rho} & 0 & 0 & 0 & 0 & 0 \\ 0 & 0 & 0 & 0 & 0 & 0 & 0 & 0 & 0 & 1 \end{bmatrix}, \tag{3.A.14}$$

$$\underline{\underline{B}}^{3,eff} = \begin{bmatrix} 0 & 0 & 0 & 0 & 0 & 0 & 0 & 0 & 0 & 0 \\ 0 & 0 & 0 & 0 & 0 & 0 & 0 & 0 & 0 & 0 \\ 0 & 0 & 0 & 0 & 0 & 0 & 0 & 0 & -1 & \\ 0 & 0 & 0 & 0 & 0 & 0 & 0 & 0 & 0 & 0 \\ 0 & 0 & 0 & 0 & 0 & 0 & 0 & -\frac{1}{2} & 0 & 0 \\ 0 & 0 & 0 & 0 & 0 & 0 & -\frac{1}{2} & 0 & 0 & 0 \\ 0 & 0 & 0 & 0 & 0 & -\frac{2\mu^{eff}}{\rho} & 0 & 0 & 0 & 0 \\ 0 & 0 & 0 & 0 & -\frac{2\mu^{eff}}{\rho} & 0 & 0 & 0 & 0 & 0 \\ -\frac{\lambda^{eff}}{\rho} & -\frac{\lambda^{eff}+2\mu^{eff}}{\rho} & -\frac{\lambda^{eff}}{\rho} & 0 & 0 & 0 & 0 & 0 & 0 & 0 \\ 0 & 0 & 0 & 0 & 0 & 0 & 0 & 0 & 0 & 1 \end{bmatrix}. \tag{3.A.15}$$

The effective Lamé parameters for IVM are

$$\begin{cases} \lambda^{eff} = (1-\alpha)\lambda_0 \\ \mu^{eff} = (1-\alpha)\mu_0 \end{cases}. \tag{3.A.16}$$

The effective Lamé parameters for CDM are

$$\begin{cases} \lambda^{eff} = \lambda_0 - \alpha\gamma_r\epsilon/\sqrt{I_2} \\ \mu^{eff} = \mu_0 - \alpha\xi_0\gamma_r - 0.5\alpha\gamma_r\xi \end{cases}, \tag{3.A.17}$$

where $\epsilon = (\varepsilon_{xx} + \varepsilon_{yy} + \varepsilon_{zz})/3$.

We compute the numerical fluxes $(F_p^d n_d)^*$ on both the absorbing boundary and the free-surface boundary based on the solutions of the Riemann problem with an upwind method using the approximate effective matrix $\underline{\underline{B}}^{d,eff}$ defined in Eq. (3.A.13) to (3.A.15). We assume that the outgoing waves at the element interface are only influenced by the state in the element that the interface belongs to; the incoming waves at the element interface are only influenced by the state in the neighboring element.

To compute the upwind flux, we diagonalize matrix $\underline{\underline{B}}^{1,eff} = \underline{\underline{\underline{R}}}\,\underline{\underline{\Lambda}}\,\underline{\underline{\underline{R}}}^{-1}$, where $\underline{\underline{\Lambda}} = \mathrm{diag}(-c_p^{eff}, -c_s^{eff}, -c_s^{eff}, 0, 0, 0, c_s^{eff}, c_s^{eff}, c_p^{eff}, 0)$, $c_p^{eff} = \sqrt{(\lambda_{eff} + 2\mu_{eff})/\rho}$, $c_p^{eff} = \sqrt{\mu_{eff}/\rho}$,

and

$$\underline{\underline{R}} = \begin{bmatrix} 1 & 0 & 0 & -\frac{\lambda^{eff}}{\lambda^{eff}+2\mu^{eff}} & 0 & -\frac{\lambda^{eff}}{\lambda^{eff}+2\mu^{eff}} & 0 & 0 & -1 & 0 \\ 0 & 0 & 0 & 0 & 0 & 1 & 0 & 0 & 0 & 0 \\ 0 & 0 & 0 & 1 & 0 & 0 & 0 & 0 & 0 & 0 \\ 0 & \frac{1}{2} & 0 & 0 & 0 & 0 & 0 & -\frac{1}{2} & 0 & 0 \\ 0 & 0 & 0 & 0 & 1 & 0 & 0 & 0 & 0 & 0 \\ 0 & 0 & \frac{1}{2} & 0 & 0 & 0 & -\frac{1}{2} & 0 & 0 & 0 \\ c_p^{eff} & 0 & 0 & 0 & 0 & 0 & 0 & 0 & c_p^{eff} & 0 \\ 0 & c_s^{eff} & 0 & 0 & 0 & 0 & 0 & c_s^{eff} & 0 & 0 \\ 0 & 0 & c_s^{eff} & 0 & 0 & 0 & c_s^{eff} & 0 & 0 & 0 \\ 0 & 0 & 0 & 0 & 0 & 0 & 0 & 0 & 0 & 1 \end{bmatrix}, \tag{3.A.18}$$

where the last column results from the extra zero eigenvalues due to the introduction of the damage variable.

For the absorbing boundaries, we use the same method as Dumbser and Käser (2006).

$$\begin{aligned} F_p^{abs} &= (F_p^d n_d)_p^* \\ &= T_{pq} B_{qr}^{1,eff,+} T_{rs}^{-1} q_s, \end{aligned} \tag{3.A.19}$$

where $\underline{\underline{B}}^{1,eff,+} = \underline{\underline{R}}\,\underline{\underline{\Lambda}}^{+}\underline{\underline{R}}^{-1}$. $\underline{\underline{\Lambda}}^{+} = \mathrm{diag}(0,0,0,0,0,0,c_s^{eff},c_s^{eff},c_p^{eff},0)$ only keeps the positive terms in $\underline{\underline{\Lambda}}$. T_{pq}^{-1} is the rotation matrix that operates on the vector of the conservative variables u_s, rotating the quantities to the face-aligned coordinate system.

$$\underline{\underline{T}} = \begin{bmatrix} n_x^2 & s_x^2 & t_x^2 & 2n_x s_x & 2s_x t_x & 2t_x n_x & 0 & 0 & 0 & 0 \\ n_y^2 & s_y^2 & t_y^2 & 2n_y s_y & 2s_y t_y & 2t_y n_y & 0 & 0 & 0 & 0 \\ n_z^2 & s_z^2 & t_z^2 & 2n_z s_z & 2s_z t_z & 2t_z n_z & 0 & 0 & 0 & 0 \\ n_x n_y & s_x s_y & t_x t_y & n_x s_y + n_y s_x & t_x s_y + t_y s_x & n_x t_y + n_y t_x & 0 & 0 & 0 & 0 \\ n_z n_y & s_z s_y & t_z t_y & n_z s_y + n_y s_z & t_z s_y + t_y s_z & n_z t_y + n_y t_z & 0 & 0 & 0 & 0 \\ n_x n_z & s_x s_z & t_x t_z & n_x s_z + n_z s_x & t_x s_z + t_z s_x & n_x t_z + n_z t_x & 0 & 0 & 0 & 0 \\ 0 & 0 & 0 & 0 & 0 & 0 & n_x & s_x & t_x & 0 \\ 0 & 0 & 0 & 0 & 0 & 0 & n_y & s_y & t_y & 0 \\ 0 & 0 & 0 & 0 & 0 & 0 & n_z & s_z & t_z & 0 \\ 0 & 0 & 0 & 0 & 0 & 0 & 0 & 0 & 0 & 1 \end{bmatrix}. \tag{3.A.20}$$

For the free-surface boundaries, we first rotate u_q to the face-aligned coordinate system as $u_p^n = T_{rs}^{-1} u_s$. We then derive the constraints to the conservative variables u_q^b on the boundary face from an upwind flux below in a similar way as Uphoff (2020).

$$
\begin{aligned}
\underline{u}^b &= \underline{u}^- + \omega_1 \underline{r}^1 + \omega_2 \underline{r}^2 + \omega_3 \underline{r}^3 \\
&= \underline{u}^- + \omega_1 \begin{pmatrix} 1 \\ 0 \\ 0 \\ 0 \\ 0 \\ 0 \\ c_p^{eff} \\ 0 \\ 0 \\ 0 \end{pmatrix} + \omega_2 \begin{pmatrix} 0 \\ 0 \\ 0 \\ 1/2 \\ 0 \\ 0 \\ 0 \\ c_s^{eff} \\ 0 \\ 0 \end{pmatrix} + \omega_3 \begin{pmatrix} 0 \\ 0 \\ 0 \\ 0 \\ 0 \\ 1/2 \\ 0 \\ 0 \\ c_s^{eff} \\ 0 \end{pmatrix},
\end{aligned} \tag{3.A.21}
$$

where $\underline{u}^-$ is the projection of solutions in the local element on the free surface; $\underline{r}^1$ is the column in $\underline{\underline{R}}$ that corresponds to -c_p^{eff} in $\underline{\underline{\Lambda}}$; $\underline{r}^2$ and $\underline{r}^3$ are the two columns in $\underline{\underline{R}}$ that correspond to -c_s^{eff} in $\underline{\underline{\Lambda}}$. ω_1, ω_2 and ω_3 are unknowns to be constrained from the free-surface boundary conditions, which we will further define below.

We derive from u_p^b the face-aligned boundary stress $u_p^{\sigma,b} = (\sigma_{xx}, \sigma_{yy}, \sigma_{zz}, \sigma_{xy}, \sigma_{yz}, \sigma_{zx}, v_x, v_y, v_z, \alpha)^T$, where

$$
\begin{aligned}
u_p^{\sigma,b} &= C_{pq} u_q^b \\
&= \begin{bmatrix}
\lambda^{eff}+2\mu^{eff} & \lambda^{eff} & \lambda^{eff} & & 0 & 0 & \\
\lambda^{eff} & \lambda^{eff}+2\mu^{eff} & \lambda^{eff} & 0 & 0 & 1 & \\
\lambda^{eff} & \lambda^{eff} & \lambda^{eff}+2\mu^{eff} & 0 & 0 & 0 & \underline{\underline{0}} \\
0 & 0 & 0 & 2\mu^{eff} & 0 & 0 & \\
0 & 0 & 0 & 0 & 2\mu^{eff} & 0 & \\
0 & 0 & 0 & 0 & 0 & 2\mu^{eff} & \\
 & & \underline{0} & & & & \underline{\underline{I}}
\end{bmatrix} \underline{u}^b,
\end{aligned} \tag{3.A.22}
$$

where $\underline{\underline{I}}$ is a 4 by 4 identity matrix, while $\underline{\underline{0}}$ and $\underline{0}$ are, respectively, the zero matrix and zero vector that complete the matrix C_{pq}.

On the free surface, σ_{xx}, σ_{xy} and σ_{zx} in $u_p^{\sigma,b}$ should be zero. With these three more constraints, we solve the unknowns ω_1, ω_2 and ω_3 in Eq. (3.A.21). We can substitute these unknowns back in Eq. (3.A.21) to obtain u_q^b in the face-aligned coordinate system. We finally compute the boundary flux with u_q^b as below.

$$
\begin{aligned}
F_p^{free} &= (F_p^d n_d)_p^* \\
&= T_{pq} B_{qr}^{1,eff} u_r^b.
\end{aligned} \tag{3.A.23}
$$

Appendix 3.B DG algorithm for nonlinear wave equations

This section provides supporting information for reproducing the low-frequency enhancement observed in ground motions from our simulations using the nonlinear damage model, IVM. We present comparisons between the frequency components of the velocity time series predicted by the elastic model and the IVM at four additional strong motion stations within the Kathmandu Valley, as shown in Fig. 3.B.1. Among the four listed stations, we find a prominent low-frequency enhancement in the simulations with IVM between 0.2 Hz and 0.35 Hz at station TVU and between 0.3 Hz and 0.45 Hz at station KATNP. In contrast, the frequency spectra at stations THM and PTN show negligible differences between simulations using the linear elastic model and those with IVM. peak ground velocity (PGV) is strongly correlated with the prominence of the low-frequency enhancement. Specifically, the PGV at station TVU and KATNP is approximately twice and four times higher, respectively, than at station THM. The PGV at the station PTN is approximately 60% larger than that at station THM. With such an intermediate PGV value, only a minor low-frequency enhancement between 0.25 Hz and 0.4 Hz is observed at station PTN. The more prominent low-frequency enhancement associated with larger PGV is attributed to the stronger reduction in co-seismic moduli in regions with high PGV values.

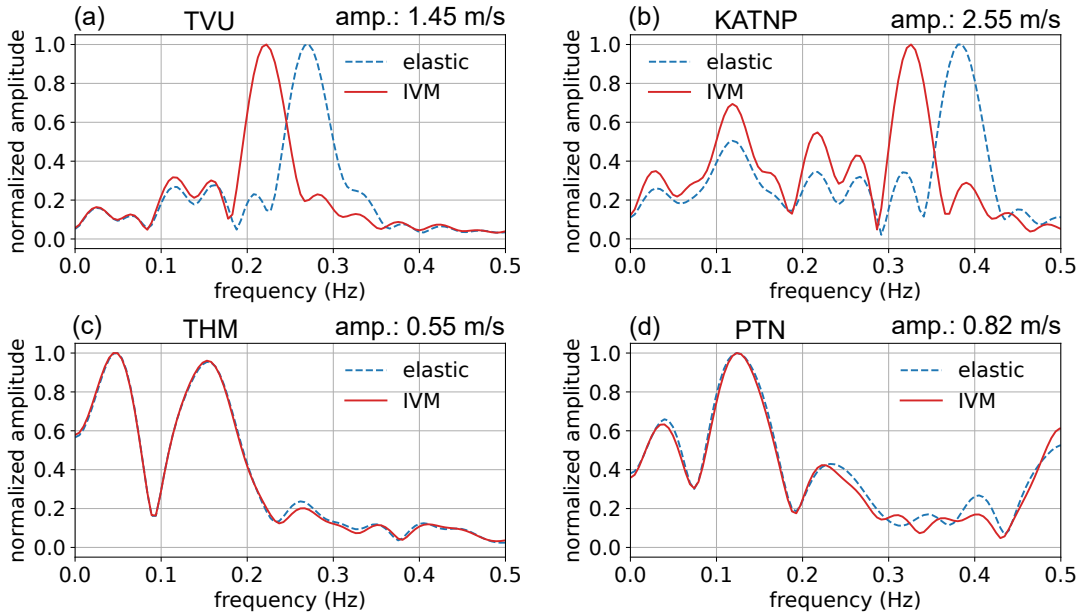

Figure 3.B.1: Normalized frequency spectra of the upward-downward velocity time series recorded between 20 s and 50 s for simulations employing elastic model (the dashed blue curve) and IVM (the solid red curve) at 4 stations: (a) TVU, (b) KATNP, (c) THM, and (d) PTN. We provide peak magnitudes of the velocity vector at the four stations on the top right of each subfigure.

Chapter 4

Dynamic rupture simulations in 3D with co-seismic off-fault damage

Understanding the nonlinear mechanical response of rocks and soils to seismic waves is crucial for understanding earthquake rupture dynamics and ground shaking across source, path, and site. However, the critical reduction in elastic moduli during earthquakes is often ignored. Using a novel 3D high-performance computing implementation of the nonlinear Continuum Damage Breakage model, we show that the earthquake energy budget differs significantly between elastic and damage-inclusive scenarios. Nonlinear off-fault damage leads to increased high-frequency radiation and off-fault shear band formation. The nonlinear seismic wave field includes frequency modulation, damage- and stress-induced anisotropy, and additional inelastic energy dissipation. We identify a new mechanism of delayed dynamic triggering, driven by damage-induced stress heterogeneity and rock moduli reduction in tensile stepover fault systems. Nonlinear damage facilitates rupture cascading across multi-fault systems, with varying delay times linked to damage rheology and geometric fault zone evolution, suggesting potential for new observational constraints.

4.1 Introduction

Geological and geophysical evidence shows ubiquitously that crustal faults are surrounded by hierarchical zones of rock damage with reduced elastic moduli (e.g., Sibson, 1977; Chester et al., 1993; Ben-Zion and Sammis, 2003; Mitchell and Faulkner, 2009). These damage zones are generated, maintained, and grow by recurring earthquake ruptures (e.g., Mitchell and Faulkner, 2009; Rockwell and Ben-Zion, 2007). Such damage contributes to off-fault energy dissipation as well as to a stronger heterogeneity in the off-fault materials. This heterogeneity can lead to significant differences in rupture processes compared to scenarios where it is not considered. These variations may manifest in several ways, including altered energy partitioning, distinct seismic radiation patterns, and modified fault interactions. (Passelègue et al., 2016; Okubo et al., 2019; Johnson et al., 2021; Kurzon et al., 2022).

The energy partition during the occurrence of earthquakes is important for understanding how much energy stored in the bulk rock materials can be released and how much of the released energy is converted to seismic motions (kinetic energy, Rice et al., 2005; Kanamori and Rivera, 2006). It is also one of the first-order constraints for validating analytical and numerical models for dynamic rupture against field or laboratory observations (Kanamori and Rivera, 2006). Okubo et al. (2019) adopted 2D Finite-discrete Element Method to model the dynamic rupture processes on the main fault and the off-fault fractures at the

same time. Off-fault fractures are represented as the loss of cohesion at the interfaces of elements. They find that the off-fault fracture energy can take up 4% to 34% of the total energy released, depending on the rupture distance and the initial background stress field. This represents a significant amount of energy, while the exact value varies between the 2D and 3D configurations of the rupture dynamics, particularly at shallow depths (Ma, 2008).

Aside from the total radiated kinetic energy, the frequency components of the seismic radiation can also be qualitatively alternated by the off-fault co-seismic damage. Taufiqurrahman et al. (2022) find deficits in the high-frequency components of seismograms in simulations compared to the recorded ground motions. The origin of high-frequency radiation has been studied over decades (e.g., Madariaga, 1977; Hanks and McGuire, 1981; Hanks, 1982; Dunham et al., 2011; Castro and Ben-Zion, 2013; Passelègue et al., 2016; Ben-Zion et al., 2024). There are multiple factors that affect high-frequency radiation, such as sudden nucleation and arrest of rupture, complex fault geometry, roughness of the fault surface, and the nonlinear response in subsurface sedimentary rock. Marty et al. (2019b) shed light on the additional high-frequency acoustic waves during stick-slip events. Okubo et al. (2019) show that secondary fractures can promote high-frequency radiation in 2D. Kurzon et al. (2022); Lyakhovsky et al. (2023) enable the "quasi-static" simulation of dynamic rupture in a diffused fault zone and the off-fault damage in 3D to investigate the radiated high-frequency seismic energy in a heterogeneous fault core. Thomas and Bhat (2018) adopted a damage model that writes the Gibbs energy of the material as the summation of the elastic energy in the bulk and the fracture surface energy of all crack fronts. In all of the above simulations, they find that the off-fault damage comes with high-frequency radiation during the dynamic rupture. However, quantifying the enhanced high-frequency radiation for realistic regional-scale earthquakes remains difficult due to limitations in computational power.

Beyond the influence of off-fault damage on the dynamic rupture process of a single fault, the reduction of moduli during the damage process and the resulting stress heterogeneities can also have a significant impact on fault interactions in fault systems (Sammis et al., 2010; Xu et al., 2015; Mia et al., 2024). To investigate the first-order factors that influence fault interactions, the fault system is simplified as two parallel fault planes that are separated by a few kilometers from each other. Finzi and Langer (2012) investigate the fault interaction with a zone with pre-defined lower shear modulus. They find that this enables the rupture to jump over a larger distance. Liu and Duan (2014) compare the elastic case with the Drucker-Prager plasticity and with the existence of off-fault pore pressure. But Drucker-Prager plasticity does not account for the moduli reduction before reaching the yielding strength of rocks. It also ignores the temporal evolution of the damage, as evidenced by the experiment of Hamiel et al. (2006) on granitic rocks. To accurately quantify the heterogeneous off-fault moduli reduction and the perturbed stress field, which is critical for determining the activation of neighboring faults in realistic fault zones, a numerical algorithm and its efficient implementation are essential but are still missing for 3D dynamic rupture simulations.

We propose an algorithm based on discontinuous Galerkin method to combine dynamic rupture simulation with wave propagation in different nonlinear rock rheologies in 3D. We prove in an earlier work that the algorithm is stable and converging for nonlinear wave equations in 3D. Chapter 3 describes how experimentally-constrained nonlinear damage rock models

can be formulated as a system of nonlinear hyperbolic PDEs. The algorithm can adequately address frequency modulation and the damage- and stress-induced anisotropy in nonlinear wave propagation. In this work, we employ this algorithm to solve the nonlinear continuum damage breakage (CDB) model by Lyakhovsky and Ben-Zion (2014) and Lyakhovsky et al. (2016). We further extend the algorithm to include dynamic rupture modeling. With the extension, we illustrate the incurred off-fault damage and the its impact on earthquake interaction. We parallelized the numerical framework using MPI and OpenMP to enable efficient execution on modern high-performance computing systems. This enables the simulation of dynamic rupture and the related co-seismic off-fault damage, as well as co-seismic wave speed changes far away from the source, for realistic regional-scale earthquakes.

Utilizing the comprehensively verified algorithm in this work, we unleash the possibility of quantitatively modeling how the heterogeneous off-fault moduli reduction can facilitate the triggering of earthquakes on neighboring faults in 3D. We also show the distributed mesh-independent mathematical representation of the rock damage can localize into shear bands. The shear band angles quantitatively match the theories and are stable features that can be resolved consistently better with mesh refinement. Such localized co-seismic moduli reduction also generates additional high-frequency radiation between 1 and 10 Hz. This might compensate for the high-frequency deficit in many dynamic rupture simulations compared to observations.

4.2 Integrate dynamic rupture into nonlinear wave simulations in 3D

We build on the method described in Chapter 3 by implementing the continuum damage-breakage (CDB) model from Lyakhovsky and Ben-Zion (2014). In this study, we integrate nonlinear wave propagation with 3D dynamic rupture simulations.

We first summarize the CDB model that we implemented in this work and show how it fits into the numerical algorithms described in Chapter 3. CDB model is proposed within the framework of continuum mechanics. The mechanical response of rocks from their intact states to their failure is mathematically described with a scalar damage variable (α) that represents the density of distributed micro-cracks and a scalar breakage variable (B) describing the grain size distribution in the post-failure stage of rocks (Einav, 2007a,b). In CDB, the latter stage is named the granular phase (Lyakhovsky et al., 2016). Both α and B are defined in the range of [0,1].

The generic formula for the system of equations that are suitable for the numerical algorithms proposed in Chapter 3 is the following nonlinear hyperbolic system of conservation laws with a source term (Dumbser et al., 2008) in Eq. (4.1).

$$\begin{cases} \dfrac{\partial \varepsilon_{ij}}{\partial t} & = \dfrac{1}{2}\left(\dfrac{\partial v_i}{\partial x_j} + \dfrac{\partial v_j}{\partial x_i}\right) \\ \rho \dfrac{\partial v_i}{\partial t} & = \dfrac{\partial \sigma_{ij}(\underline{\underline{\varepsilon}}, \alpha, B)}{\partial x_j} \\ \dfrac{\partial \alpha}{\partial t} & = r_\alpha(\underline{\underline{\varepsilon}}, \alpha, B) \\ \dfrac{\partial B}{\partial t} & = r_B(\underline{\underline{\varepsilon}}, \alpha, B) \end{cases}, \tag{4.1}$$

where $\underline{\underline{\varepsilon}} = \varepsilon_{ij}$ and σ_{ij} denote strain and stress tensor, v_i is the vector for particle velocity, and ρ is material mass density. α is a damage variable and B is a breakage variable. r_α and r_B are two functions of the strain tensor, the damage variable and the breakage variable.

For CDB model, we substitute the expressions for σ_{ij}, r_α and r_B with the ones listed in Eq. (4.2).

$$\begin{cases} \sigma_{ij}(\underline{\underline{\varepsilon}}, \alpha, B) = (1-B)\sigma^s_{ij} + B\sigma^b_{ij} \\ r_\alpha(\underline{\underline{\varepsilon}}, \alpha, B) = \begin{cases} C_d(1-B)\gamma_r I_2(\xi - \xi_0) & \text{, if } \xi - \xi_0 > 0 \\ 0 & \text{, if } \xi - \xi_0 \le 0 \end{cases} \\ r_B(\underline{\underline{\varepsilon}}, \alpha, B) = \begin{cases} C_B(1-B)P(\alpha)\gamma_r I_2(\xi - \xi_0) & \text{, if } \xi - \xi_0 > 0 \\ 0 & \text{, if } \xi - \xi_0 \le 0 \end{cases} \end{cases}, \tag{4.2}$$

where γ_r is the nonlinear modulus. $I_1 = \varepsilon_{kk}$ and $I_2 = \varepsilon_{ij}\varepsilon_{ij}$ are the first and the second strain invariant. $\xi = I_1/\sqrt{I_2}$ is derived from the two strain invariants. It grows from $-\sqrt{3}$ for isotropic compression to $\sqrt{3}$ for isotropic extension. The damage α starts to accumulate as the strain state deviates farther enough from the isotropic compression. This is formulated as $\xi - \xi_0 > 0$, where ξ_0 is a material parameter that is usually negative for rocks (Lyakhovsky et al., 2016). C_d and C_B are, respectively, the damage and the breakage evolution coefficient, $P(\alpha) = \dfrac{1}{\exp\left(\dfrac{\alpha_{cr} - \alpha}{\beta}\right) + 1}$ is the probability of the material to be in the granular phase (Lyakhovsky and Ben-Zion, 2014). Such mathematical expression makes sure that the probability of transition $P(\alpha) \approx 0$ when $\alpha \ll \alpha_{cr}$, whereas $P(\alpha) \approx 1$ when $\alpha \gg \alpha_{cr}$. With this definition of $P(\alpha)$, the breakage accumulation rate $\dfrac{\partial B}{\partial t}$ in Eq. (4.1) is very small when the damage variable is well below its critical transition value ($\alpha \ll \alpha_{cr}$). The breakage accumulation rate becomes significant when $\alpha \to \alpha_{cr}$. This represents the rapid transition from the solid to the granular phase (Lyakhovsky and Ben-Zion, 2014). $\sigma^s_{ij} = \lambda_0 I_1 \delta_{ij} - \alpha\gamma_r\sqrt{I_2}\delta_{ij} + [2(\mu_0 + \alpha\gamma_r\xi_0) - \alpha\gamma_r\xi]\varepsilon_{ij}$ is the stress-strain relationship for solid state of the material and $\sigma^b_{ij} = (2a_2 + 3a_3\xi)I_1\delta_{ij} + a_1\sqrt{I_2}\delta_{ij} + (2a_0 + a_1\xi - a_3\xi^3)\varepsilon_{ij}$ is the stress-strain relationship for granular state of the material (Lyakhovsky et al., 2016). The granular phase moduli from a_0 to a_3 ensure the mechanical stability of the material during the transition from the solid phase to the granular phase (Lyakhovsky and Ben-Zion, 2014).

The system of equations in Eq. (4.1) can be more generally formulated in the following form for the nonlinear hyperbolic system of conservation laws with a source term (Dumbser et al., 2008).

$$\frac{\partial q_p}{\partial t} + \frac{\partial F_p^d(\underline{v}, \underline{\underline{\varepsilon}}, \alpha, B)}{\partial x_d} = s_p(\underline{v}, \underline{\underline{\varepsilon}}, \alpha, B), \tag{4.3}$$

where $\boldsymbol{q} = (\varepsilon_{xx}, \varepsilon_{yy}, \varepsilon_{zz}, \varepsilon_{xy}, \varepsilon_{yz}, \varepsilon_{zx}, v_x, v_y, v_z, \alpha, B)^T$ is a vector of the conservative variables. ε_{xx}, ε_{yy}, ε_{zz}, ε_{xy}, ε_{yz}, and ε_{zx} are six components of the strain tenser $\underline{\underline{\varepsilon}} = \varepsilon_{ij}$; v_x, v_y, and v_z are the three components of the particle velocity vector $\underline{v}$. The flux term F_p^d represents the rates at which the conservative variable q_p gets transferred through a unit area in the direction x_d (LeVeque, 2002). The source vector $s_p = (0, 0, 0, 0, 0, 0, 0, 0, 0, r_\alpha, r_B)^T$ with only two non-zero components r_α and r_B defined in Eq. (4.2).

We then take care of the numerical flux on the frictional interface for dynamic rupture simulation. We first rotate q_q to the face-aligned coordinate system as $q_p^n = T_{rs}^{-1} q_s$, with the rotation matrix T_{rs} given in Chapter 3. For a more accurate estimation of the stress on the fault, we derive the face-aligned conservative variables $q_p^{\sigma,b} = (\sigma_{xx}, \sigma_{yy}, \sigma_{zz}, \sigma_{xy}, \sigma_{yz}, \sigma_{zx}, v_x, v_y, v_z, \alpha, B)^T$ for the stress-velocity form of the wave equations according to Pelties et al. (2012) with the nonlinear stress-strain relationships in Eq. (4.2). Using $q_p^{\sigma,b}$, we solve the stress on the interface with various types of friction laws (Uphoff, 2020) on the fault interface. We follow the same procedures as described in earlier publications related to SeisSol from Pelties et al. (2012) and refer to them for more detailed descriptions of the formula.

4.3 Off-fault damage patterns, high-frequency radiation, and energy dissipation from damage evolution

In this section, we systematically examine the effects of co-seismically evolving off-fault damage on the dynamic rupture process in 3D. We focus on three aspects: (1) Different off-fault damage patterns below and beyond the solid-granular phase transition of rocks; (2) Generation of high-frequency seismic (kinetic) energy during the rapid transition between solid and granular state; (3) Partitioning of on-fault and off-fault energy partitioning accounting for the thermodynamical irreversibility of the rock damage process.

To investigate the above problems, we employ the setup according to the community benchmark problem TPV3 (Harris et al., 2009). It features a right-lateral vertical strike-slip fault in a half-space that nucleates from the center of the fault. In our 3D simulation, the domain is 120 km, 120 km, and 60 km long, respectively, in the x, y, and z directions. The fault is 30 km along the strike (x-dir) and 15 km deep (z-dir). The fault slip behaviors are governed by the linear slip weakening law (Rice, 1985; Harris et al., 2009). We list the material properties that are not defined in the benchmark and the initial background stress hosted in the rocks in Table 4.1.

We first investigate the patterns of off-fault damage according to the CDB model. We show results in two end-member cases: (1) small damage, where the material does not reach the solid-granular phase transition; (2) large damage, where the material transits into the granular phase within ∼0.01 s.

Table 4.1: Summary of model parameters for tpv3. The nonlinear modulus γ_r and the granular phase moduli from a_0 to a_3 are computed according to Lyakhovsky and Ben-Zion (2014), with a strain invariants ratio for onset of breakage decrease ξ_d = -0.9 defined therein. The stress component pair $(\sigma_{xx}, \sigma_{zz})$ = (-71, -71) MPa and (-45, -118) MPa correspond to the maximum compressive stress oriented, respectively, 59.1 and 54.6 degrees from x-axis.

	Parameters	Values	Units	Parameters	Values	Units
fault	σ_{xx}	-71, -45	MPa	D_c	0.3	m
	σ_{yy}	-120	MPa	μ_s	0.667	1
	σ_{zz}	-71, -118	MPa	μ_d	0.425	1
	σ_{xy}	70	MPa	σ_{yz}, σ_{zx}	0	MPa
bulk material	λ_0	32	GPa	a_0	7.43	GPa
	μ_0	32	GPa	a_1	-22.14	GPa
	γ_r	37	GPa	a_2	20.93	GPa
	ξ_0	-0.75	1	a_3	-8.56	GPa
	C_d	6.0×10^{-5}	$(\text{Pa·s})^{-1}$	C_B	$100C_d$	$(\text{Pa·s})^{-1}$
	β_{cr}	0.05	1	ρ	2760	kg/m^3

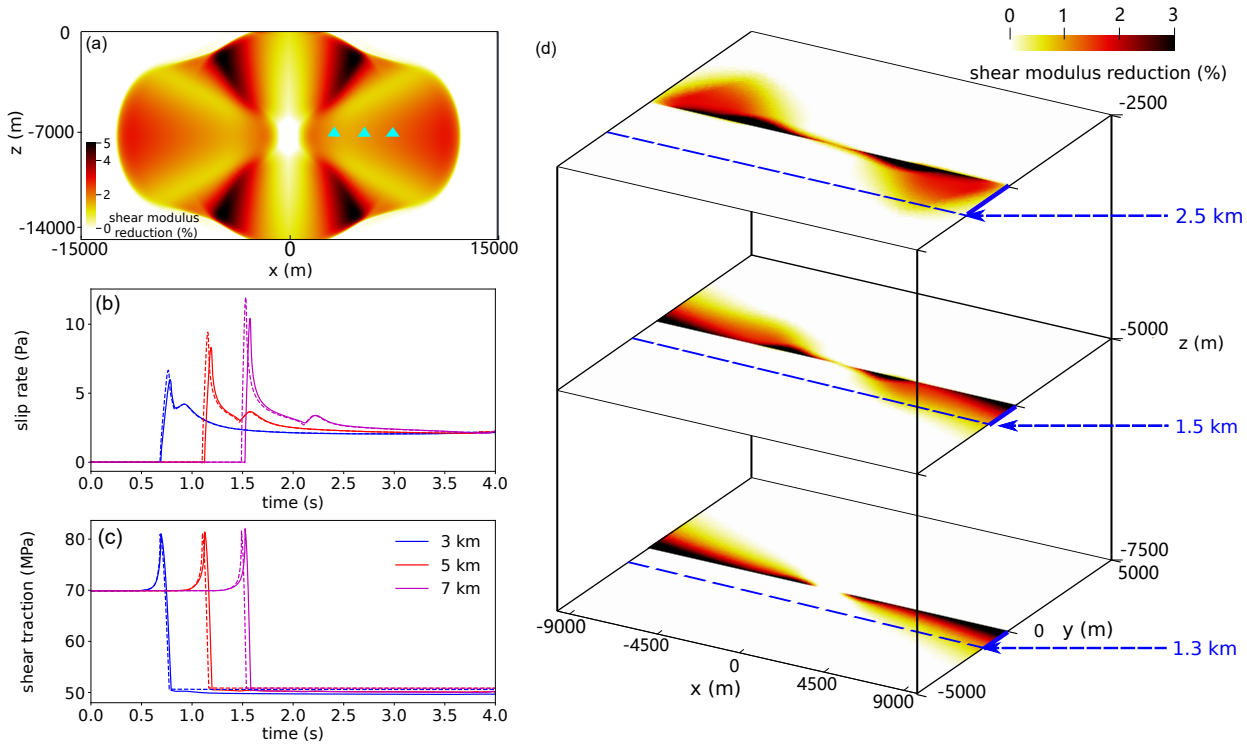

Figure 4.1: Dynamic rupture when the damage level is below the solid-granular phase transition. The damage distributions across the fault at the depths of 7.5, 5.0 and 2.5 km are shown in (d). The damage distribution on the fault plane is shown in (a). The recorded time series of slip rate (b) and shear traction (c) at the three on-fault receivers, i.e. the green rectangles in (a), are also shown. In (b) and (c), the dashed curves are from reference simulations where the off-fault materials are elastic; while the solid curves are from simulations where the CDB model is implemented.

We show in Fig. 4.1 the distribution of off-fault damage and how it influences the dynamic rupture processes in the small damage case. The region of on-fault damage is larger at depths that are farther away from the depth of nucleation. When comparing the off-fault damage among depths of 2.5, 5.0 and 7.5 km, we find that the damage also extends the farthest away from the fault plane at 2.5 km; whereas it is constrained closest to the fault plane at 7.5 km, as shown in Fig. 4.1d.

We then show how the time series of the slip rate and the fault traction in the strike direction are different from the linear elastic case in Fig. 4.1b and 4.1c. The rupture speed becomes smaller. This results from the energy released during the rupturing being partially consumed by the off-fault damage. It also leads to a lower peak in slip rate. After the passage of the rupture front, the shear traction also falls back to a slightly lower value, compared to the case with elastic off-fault materials (the dashed curves in Fig. 4.1c).

When the damage level reaches the solid-granular transition conditions in the CDB model, the stress-strain relationship will rapidly change from the solid type, that is, $B \to 0$ in Eq. (4.2), to the granular type, i.e. $B \to 1$ in Eq. (4.2). This transition leads to significant differences in the off-fault damage distribution. In Fig. 4.2f, we show the off-fault damage distribution at 7.5 km depth. We can see localized damage structures that extend from the fault plane into the bulk material at an angle of around 35.6 degrees. The theory of CDB describes the internal friction angle of the material in analogy to Byerlee (1978). The equivalent internal friction angle in the CDB model is determined from the nonlinear material properties ξ_0 in Eq. (4.2). As listed in Table 4.1, ξ_0 is -0.75 (Lyakhovsky et al., 1997a). This corresponds to an internal friction angle of 43 degrees. In the simulation of Fig. 4.2f, the angle between the maximum compressive principal stress and the fault plane is 59.1 degrees. The two conjugate weak planes should take an angle of 45 - 43/2 = 23.5 degrees from the maximum compressive principal stress. This corresponds to angles of 59.1 - 23.5 = 35.6 degrees or 59.1 + 23.5 = 82.6 degrees between the weak plane and the fault plane. We find the theoretical angle of 35.6 degrees from the fault plane in Fig. 4.2f (red dashed line) agrees with our numerical simulation results. The same angles are kept as the depth changes from 7.5 to 2.5 km in Fig. 4.2d and Fig. 4.2e. We further verify the consistency by varying the angle between the maximum compressive principal stress and the fault plane from 59.1 degrees to 54.6 degrees in Fig. 4.2c. This time, the weak plane from numerical simulation also takes a smaller angle from the fault plane, which is around 31.1 degrees. The damage pattern is also stable when refining mesh sizes from 100 m to 25 m. We show the mesh-independency in Appendix 4.C.

Aside from changes in off-fault damage patterns, the sudden transition from solid to granular states also generates high-frequency seismic waves. We show a snapshot of the velocity field at 3.5 s after the nucleation of the fault in Fig. 4.2b. We can see the secondary wave field generated from the regions where the solid-granular transition takes place. We put two receivers at (1.0, -0.1, -7.5) km (the red triangle) and at (1.0, -3.0, -7.5) km (the blue triangle). We illustrate how the frequency components of the seismograms are different from the linear elastic case in Fig. 4.2a. We see that at both locations, frequencies between 2 and 10 Hz are enhanced by the secondary wave field. The high-frequency waves generated behind the rupture front are also observed in laboratory experiments by Marty et al. (2019b). This is an indication that including the off-fault damage may compensate for the high-frequency deficiency between the observations and simulations by Taufiqurrahman

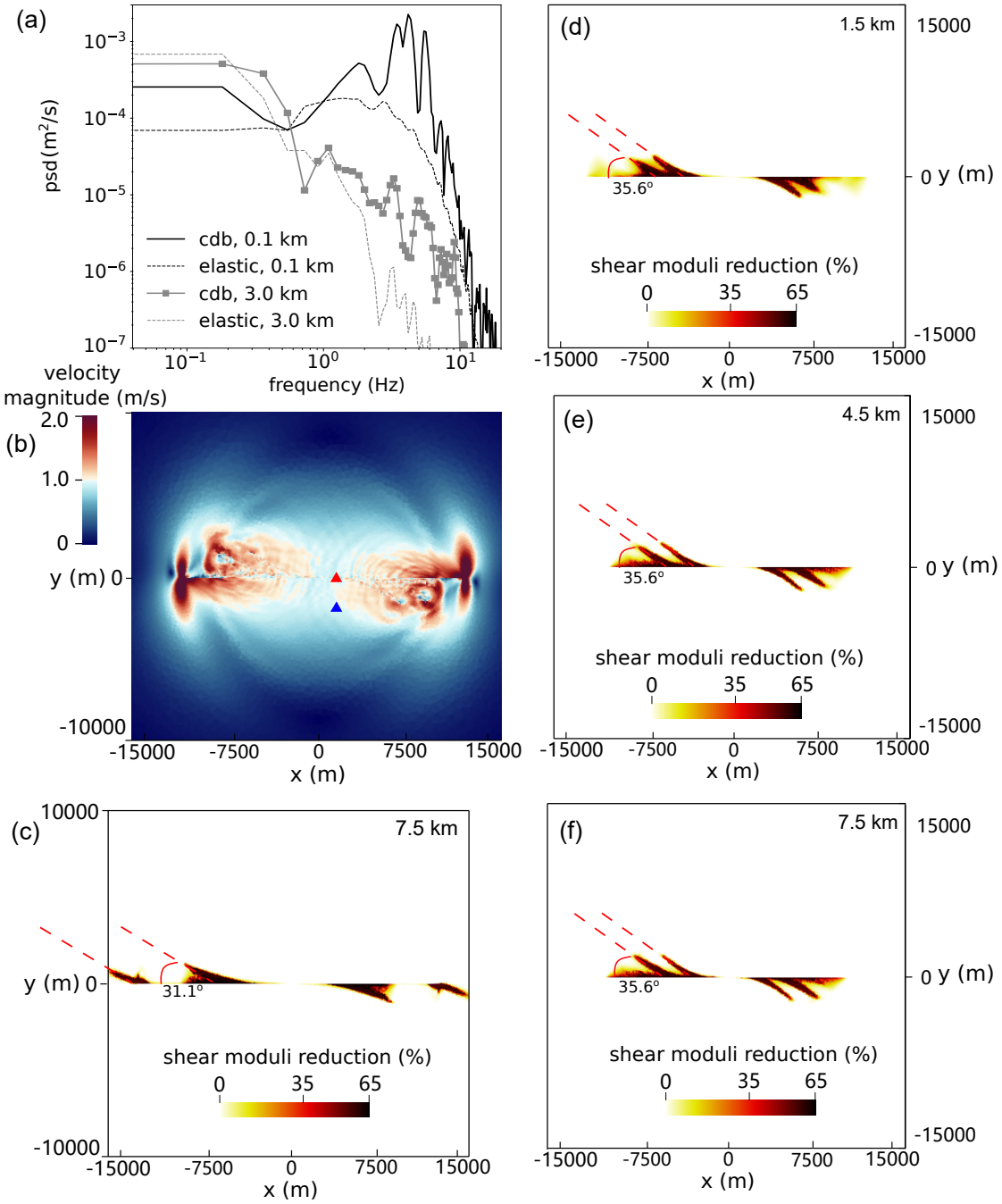

Figure 4.2: Dynamic rupture when the damage level reaches the solid-granular phase transition. The damage distributions for maximum compressive stress oriented 59.1 and 54.6 degrees from the x-axis at the depth of 7.5 km are, respectively, shown in (c) and (f). For the case when the orientation angle is 54.6 degrees, the damage distribution at 2.5 km and 5.0 km are given in (d) and (e). The distribution of the magnitude of the velocity vector at the depth of 7.5 km for background stress orientation angle of 59.1 degrees is given in (b). We put two receivers at (1.0, -0.1) km (the red rectangle) and (1.0, -3.0) km (the blue rectangle) in (b). The solid black (R1) and gray (R2) curves are the power spectral density (psd) of the recorded seismograms in (a). The dashed black (R1) and grey (R2) curves are the power spectral density of the seismograms for the linear elastic off-fault material.

et al. (2022) for actual earthquake events.

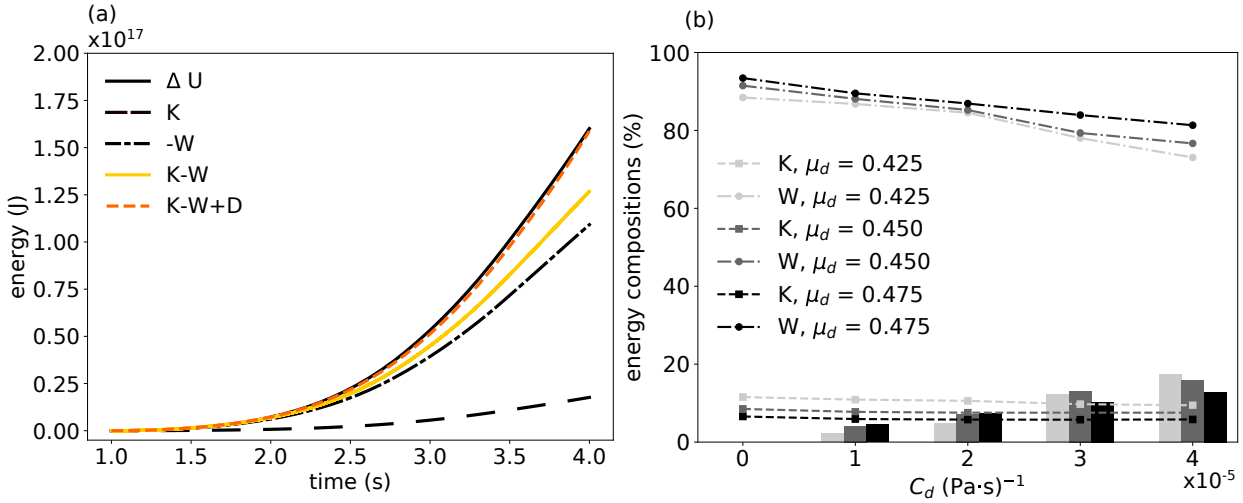

Figure 4.3: Energy budget during the dynamic rupture process. (a) Accumulation of different energy components during the dynamic rupture process in time. (b) The dashed curves represent are kinetic energy; the dash-dotted curves represent the absolute values of the frictional work on the fault; and the bar plots represent the percentage of the off-fault energy dissipation. The initial stress conditions are the same as in Fig. 4.2f. And the undefined parameters are the same as in Table 4.1.

As shown in Fig. 4.2b, the rapid transition of the off-fault material from solid to granular phase generates additional kinetic energy. In addition to this, the thermodynamically irreversible damage evolution process also contributes to off-fault energy dissipation. This is important for evaluating how much of the stored energy in locked faults can be released as kinetic energy when they are unlocked.

We first show the different components of energy in our simulations are consistent with the energy conservation laws. This is an important basis for later energy analysis. We provide the mathematical definition of each energy component in Appendix 4.B. The component that releases energy and drives the dynamic rupturing process is the drop in the stored mechanical potential energy ΔE in the bulk rock material, i.e. Eq. (B7). Similarly to the elastic case, the energy released is consumed by the breakdown work W_b, the friction work W_f on the fault after the friction coefficient reaches its dynamic value μ_d, and the radiated kinetic energy K. In the CDB model, an additional member that consumes energy is the dissipation (increase of entropy of the system) during the evolution of damage. The energy dissipation rate $T\dot{s}$ can be derived as in Eq. (4.B.6). In our simulation, we compute each energy component independently and show how they accumulate in time in Fig. 4.3a. We can see that $K - W_f - W_b + D$ matches the released mechanical potential energy $-\Delta E$.

We then compare the proportion of different energy components by the time the entire fault is ruptured. Higher ratio of kinetic energy is generated from the dynamic rupture process for lower μ_d. This ratio does not change significantly as the off-fault damage becomes larger (larger C_d). As shown in the dash-dotted curves in Fig. 4.3b, in the linear elastic case (zero C_d), the energy dissipated by the fault friction takes the largest proportion when $\mu_d = 0.475$ (the black dash-dotted curve). Such on-fault energy dissipation drops systematically with the increase of the damage evolution coefficient C_d for all the tested dynamic coefficient

μ_d. In particular, the on-fault dissipation drops faster for lower μ_d. At $C_d = 4 \times 10^{-5}$, in contrast to $C_d = 1 \times 10^{-5}$, the off-fault dissipation (the bar plots) takes the smallest proportion when $\mu_d = 0.475$ is the highest.

Off-fault energy dissipation has several impacts on dynamic rupture processes. First, it slows down the rupture speed and therefore makes the cohesive zone size drop slower in the along-strike direction, i.e. Fig. 4.D.2. Such larger cohesive zone size also exists for off-fault plasticity that dissipates energy off-fault (Wollherr et al., 2018). The lower rupture speed also reduces shear traction ahead of the rupture front to a lower value and impedes the transition from the sub-Rayleigh rupture speed to an intersonic speed (supershear) (Dunham, 2007). This is also observed with discrete off-fault fracture networks by Okubo et al. (2019). We show in Fig. 4.D.1 how the supershear transition systematically takes longer propagation distance to develop with increasing damage evolution coefficient C_d.

4.4 Facilitated but delayed trigger by the evolving damage

We show in Fig. 4.2c that the damage extends in the direction of the weak plane predicted by the CDB model. We also demonstrate in Fig. 4.3 that the total energy released from the bulk materials matches the sum of the radiated kinematic energy, the negative frictional work on the fault, and the energy dissipation during the thermodynamically irreversible rock damage process. These results confirm that the numerical simulations properly solve the physics of the CDB model.

Table 4.2: Summary of model parameters for tpv23. The nonlinear modulus γ_r and the granular phase moduli from a_0 to a_3 are computed according to Lyakhovsky and Ben-Zion (2014), with a strain invariants ratio for onset of breakage decrease $\xi_d = -0.9$ defined therein.

	Parameters	Values	Units	Parameters	Values	Units
fault	σ_{xx}	-25	MPa	D_c	0.3	m
	σ_{yy}	-60	MPa	μ_s	0.548	1
	σ_{zz}	-25	MPa	μ_d	0.433	1
	σ_{xy}	29.38	MPa	σ_{yz}, σ_{zx}	0	MPa
bulk material	λ_0	32	GPa	a_0	7.43	GPa
	μ_0	32	GPa	a_1	-22.14	GPa
	γ_r	37	GPa	a_2	20.93	GPa
	ξ_0	-0.75	1	a_3	-8.56	GPa
	C_d	5.0×10^{-6}	$(\text{Pa}\cdot\text{s})^{-1}$	C_B	$100C_d$	$(\text{Pa}\cdot\text{s})^{-1}$
	β_{cr}	0.05	1	ρ	2760	kg/m^3

With the above assertion on the correctness of the solutions, we employ the numerical simulations to analyze how the off-fault damage influences the rupture triggering on neighboring fault segments that are geometrically disconnected in 3D. We choose the configuration as described in the TPV23 community benchmark (Harris et al., 2018). It features two right-lateral vertical strike-slip fault planes in a half-space. The earthquake nucleation starts from

fault A. In our 3D simulation, the domain is 120 km, 120 km, and 60 km long, respectively, in the x, y and z directions. Both faults are 30 km along-strike (x-dir) and 20 km deep (z-dir). They are aligned parallel to each other and are separated by 3 km in y-dir. In the along-strike direction, their projection in the x-z plane overlap for 10 km. The fault slip behaviors are governed by the linear slip weakening law (Rice, 1985; Harris et al., 2018). We list the material properties and the initial stress on the fault in Table 4.2. In the rock experiment, we see that the rock modulus drops at a higher level of loading during damage (Hamiel et al., 2009). This is not fully accounted for with perfect plasticity. Here we show the mechanisms of how such modulus reduction can facilitate earthquake triggering between two adjacent faults.

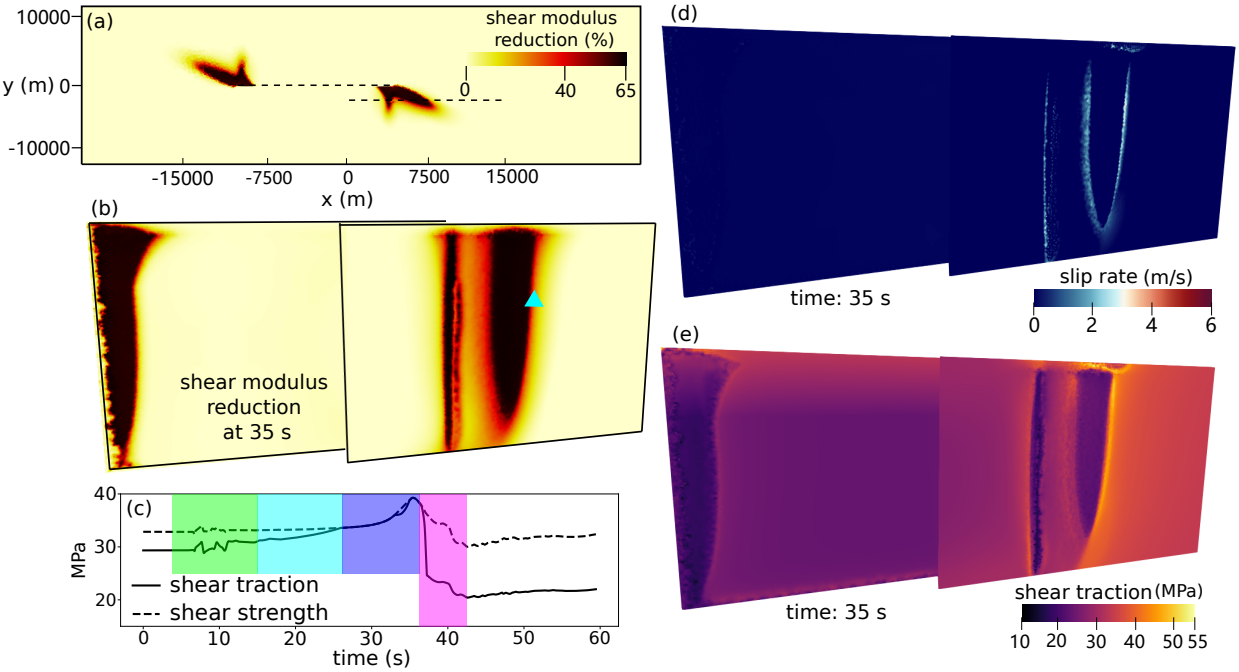

Figure 4.4: Jump across a stepover with off-fault moduli reduction. The slip rate distributions and the shear traction distributions on both faults are shown in Fig. 4.E.1. We plot the distribution of shear modulus reduction (b), slip rate (d) and shear traction (e) on both faults at 35 s; while the distribution of shear modulus reduction across the faults at 35 s is given in (a). The comparison between the shear traction (the solid curve) and the shear strength (the dashed curve) at the receiver (the blue triangle) in (b) is given in (c).

The dynamic rupture process initiates from one of the fault planes. As shown in the slip rate distribution at 4 s and 7 s after nucleation in Figs. 4.E.1a-1 and 4.E.1a-2, the rupturing process is similar to that in the linear elastic case. The instantaneous dynamic stress perturbations on the second fault, that is, the green region in Fig. 4.4c, is not sufficient to make the shear traction larger than the shear strength. After the rupture front reaches the edge of the first fault plane, large localized damage begins to accumulate from the left and right edges of the first fault (the light blue regions in Fig. 4.4c). The damage then starts to expand in 3D and slowly reaches the second fault plane (the dark red patches in Fig. 4.4b). Such damage leads to a drop in the rock moduli and, as a result, to a drop in the shear traction (as shown in the dark patch in the right column in Fig. 4.4e). The local drop in shear traction results in an increase in shear traction in its neighboring regions, e.g. the bright yellow curved strip surrounding the dark purple patch at 35 s in Fig. 4.4e and

the blue region in Fig. 4.4c. This leads to a creeping front that migrates with the high shear traction region. This process corresponds to the dark blue region in Fig. 4.4c. Then the nucleation of spontaneous dynamic rupturing processes initiates from these high shear traction regions and starts to propagate, as shown in the pink region in Fig. 4.4e. The second fault eventually breaks off as in Fig. 4.E.1a-4.

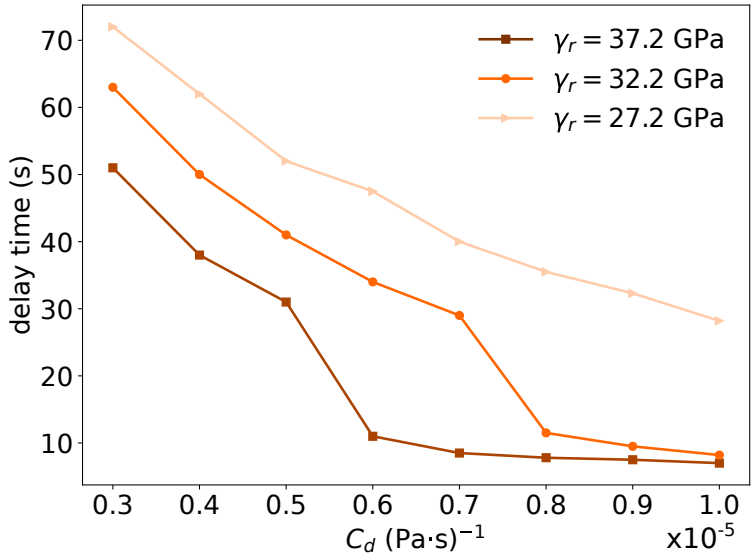

Figure 4.5: Variation of delayed time between the rupturing of the entire fault 1 and the initiation of the dynamic rupture on fault 2 with nonlinear modulus γ_r and damage evolution coefficient C_d in continuum damage breakage (CDB) model in Eq. (4.2). The unchanged parameters are defined in Table 4.2. Each marker represents a delay time derived from one corresponding independent simulation.

We highlight here that the rupture nucleation on the second fault is delayed by around 31 seconds after the first fault was completely ruptured. Such delayed triggering of events has been widely observed in earthquake sequences (Hauksson et al., 1993; Taufiqurrahman et al., 2023; Gabriel et al., 2023). We further investigate how the nonlinear parameters in the CDB model control the delay time in Fig. 4.5. For each nonlinear modulus γ_r, we vary the damage evolution coefficient C_d from 3.0 $\times 10^{-6}$ (Pa·s)$^{-1}$ to 10.0 $\times 10^{-6}$ (Pa·s)$^{-1}$. The trigger delay time when $\gamma_r = 37.2$ GPa increases from 7 to 51 s when we use a smaller damage evolution coefficient C_d. When we further vary the nonlinear modulus γ_r from 37.2 GPa to 27.2 GPa, the trigger delay time is further prolonged from 51 s to 72 s. The trigger delay time may be even longer if we set either γ_r or C_d to a lower value. Further investigation of the possible longer trigger delay time, i.e. a few tens of minutes or even hours, is restricted by the explicit time stepping scheme in the ADER-DG algorithm, which aims at resolving high-resolution wave fields (Dumbser and Käser, 2006; Pelties et al., 2012; Wollherr et al., 2018). To understand the trigger delay on a longer time scale, we may need to solve the CDB model with an implicit time-stepping scheme, such as the symmetric interior penalty discontinuous Galerkin (SIPG) method by Uphoff et al. (2023).

4.5 Conclusions

In this work, we integrate the dynamic rupture simulation with the previous 3D numerical scheme of nonlinear wave propagation. We implement the continuum damage breakage (CDB) model as one realization of the algorithm. We numerically verify the algorithm from three aspects: (1) We show the numerical stability of the algorithm during the rapid transition of the breakage variable from 0 (solid phase) to 1 (granular phase). (2) We show that the localized off-fault damage zones are consistent as we refine the mesh size from 100 m to 25 m around the fault plane. (3) We also show that the energy dissipation during the accumulation of off-fault damage in our numerical simulation quantitatively agrees with the theory of the CDB model.

We show two end members of the off-fault damage distribution with a single vertical strike-slip planar fault setup. In particular, when off-fault damage exceeds the threshold for the solid-to-granular phase transition, we observe localized damage structures extending from the main fault at angles determined by the initial background stress and the internal friction of the rocks. The angles in the numerical simulation also match the theory of the CDB model. Compared with the elastic case, such localized damage structures also generate more high-frequency seismic energy that comes with a rapid transition from the solid to the granular phase.

Despite increased off-fault energy dissipation from damage accumulation, we find that neighboring faults are more easily triggered in the tensile stepover configuration. We show that localized damage zones that extend from one fault can introduce a heterogeneous stress perturbation on its neighboring fault. This stress heterogeneity triggers nucleation on the second fault. The benchmark also demonstrates that this works provides a unique tool that can model how discontinuous fault segments that are separated by a few kilometers can be connected to each other in a fault system (Wesnousky, 2006). The triggering can be delayed depending on the time required for the damage zone to reach the second fault. We find that a smaller damage evolution coefficient C_d or a smaller nonlinear modulus γ_r can prolong the delay time from a few seconds to a few minutes. The delay time can be significantly longer with even lower C_d or γ_r. The current limitation is that the explicit time-stepping algorithm makes it too expensive to simulate damage evolution beyond a few minutes when the finely resolved wave field is not necessary.

Appendices

Appendix 4.A Thermodynamic expressions of the continuum damage breakage model

In this section, we summarize the CDBM proposed by Lyakhovsky et al. (2016) to provide a better understanding of the model in terms of its energy balance. The model starts with the first law of thermodynamics,

$$\dot{u} = \underset{=}{\sigma} : \dot{\underset{=}{\varepsilon}} + \dot{q}, \tag{4.A.1}$$

where $\dot{(\cdot)}$ denotes the time derivative, u is the specific internal energy of the system normalized by volume, w is the external work per unit volume of the system and q is the absorbed heat from the environment per unit volume of the system. At the time scale of elastodynamic processes, the heat transfer and any possible heat sources are assumed to be negligible, i.e. we assume an adiabatic process where $\dot{q} = 0$. In case of only considering mechanical work, it is $\dot{w} = \underset{=}{\sigma} : \dot{\underset{=}{\varepsilon}} = \sigma_{ij}\dot{\varepsilon}_{ij}$ and $\underset{=}{(\cdot)}$ denotes a tensor of rank two.

The expression of the internal energy depends on the choice of state variables that are used to describe the system. For an elastic material, we chose the strain $\underset{=}{\varepsilon}$ and the specific entropy s as state variables. In addition, to incorporate the damage to the material, we include another scalar state variable α. This means $u \equiv u(s, \underset{=}{\varepsilon}, \alpha, B)$.

With the above definitions of state variables, the change of the internal energy in time can be written as

$$\dot{u} = T\dot{s} + \frac{\partial u}{\partial \underset{=}{\varepsilon}} : \dot{\underset{=}{\varepsilon}} + \frac{\partial u}{\partial \alpha}\dot{\alpha} + \frac{\partial u}{\partial B}\dot{B}, \tag{4.A.2}$$

where $T = \dfrac{\partial u}{\partial s} > 0$ is the absolute temperature. If we ignore the coupling between the entropy s and the other state variables, we can define $u = u^s(s) + e(\underset{=}{\varepsilon}, \alpha, B)$, where we define $e(\underset{=}{\varepsilon}, \alpha, B)$ in this work as the mechanical potential energy of rocks.

Different damage models have different ways of defining the internal energy as a function of $\underset{=}{\varepsilon}$ and α. The combination of Eqs. (4.A.1) and (4.A.2), together with the previously defined assumptions of $\dot{q} = 0$ and $\dot{w} = \underset{=}{\sigma} : \dot{\underset{=}{\varepsilon}}$, yields the following results.

$$T\dot{s} = (\underline{\underline{\sigma}} - \frac{\partial e}{\partial \underline{\underline{\varepsilon}}}) : \dot{\underline{\underline{\varepsilon}}} - \frac{\partial e}{\partial \alpha}\dot{\alpha} - \frac{\partial e}{\partial B}\dot{B}. \tag{4.A.3}$$

For a spontaneous process in an adiabatic system, $\mathrm{d}s \geq 0$ for any given $\dot{\underline{\underline{\varepsilon}}}$ and $\dot{\alpha}$, which is known as the Clausius–Duhem inequality (Truesdell, 1952). Assuming $\underline{\underline{\sigma}}$ is independent of $\dot{\underline{\underline{\varepsilon}}}$, we derive:

$$\underline{\underline{\sigma}} = \frac{\partial e}{\partial \underline{\underline{\varepsilon}}}. \tag{4.A.4}$$

We can then derive the energy dissipation rate of the system from Eqs. (4.A.3) and (4.A.4),

$$\dot{\mathscr{D}} = T\dot{s} = -\frac{\partial e}{\partial \alpha}\dot{\alpha} - \frac{\partial e}{\partial B}\dot{B}. \tag{4.A.5}$$

The effective Lamé parameters in Section 4.2 to apply the friction laws on the fault interfaces according to Pelties et al. (2012) are

$$\begin{cases} \lambda^{eff} = (1-B)(\lambda_0 - \alpha\gamma_r\epsilon/\sqrt{I_2}) + B(2a_2 + 3a_3\xi + a_1\epsilon/\sqrt{I_2}) \\ \mu^{eff} = (1-B)(\mu_0 - \alpha\xi_0\gamma_r - 0.5\alpha\gamma_r\xi) + B(a_0 + 0.5a_1\xi - 0.5a_3\xi^3) \end{cases}, \tag{4.A.6}$$

where $\epsilon = (\varepsilon_{xx} + \varepsilon_{yy} + \varepsilon_{zz})/3$.

Appendix 4.B Energy conservation in continuum damage breakage model and dynamic rupturing

The accumulation of damage in rocks is a thermodynamically irreversible process. This comes with an energy partitioning that is different from the elastic case. The loss of potential energy in the rocks not only transforms into frictional energy on the fault and kinetic energy in the bulk material, but dissipates as an entropy increase of the system as well. In this section, we derive the mathematical expression of the dissipated energy and how it is balanced with the change of potential energy, the frictional work on the fault, and the radiated kinetic energy.

We start from the momentum conservation of the system, ignoring the body force, in Eq. (4.B.1).

$$\rho\frac{\partial v_i}{\partial t} = \frac{\partial \sigma_{ij}}{\partial x_j}. \tag{4.B.1}$$

We multiply v_i on both side of Eq. (4.B.1) and integrate it in the entire simulation domain Ω to derive

$$\int_\Omega v_i \rho \frac{\partial v_i}{\partial t} \mathrm{d}V = \int_\Omega v_i \frac{\partial \sigma_{ij}}{\partial x_j} \mathrm{d}V. \tag{4.B.2}$$

We can re-formularize the left-hand-side of Eq. (4.B.2) and apply the Gauss' theorem on the right-hand-side of Eq. (4.B.2). This leads to

$$\int_\Omega \frac{\partial (1/2 \rho v_i v_i)}{\partial t} \mathrm{d}V = \int_\Gamma v_i \sigma_{ij} n_j \mathrm{d}S - \int_\Omega \sigma_{ij} \frac{\partial v_i}{\partial x_j} \mathrm{d}V, \tag{4.B.3}$$

where n_j is the normal vector of the face element Γ, $\Gamma = \Gamma^{fault} \cup \Gamma^{surf}$ consists of the fault interfaces Γ^{fault} and the boundaries of the entire domain Γ^{surf}. Since $\sigma_{ij} = \sigma_{ji}$, we can re-write Eq. (4.B.3) as

$$\int_\Omega \frac{\partial (1/2 \rho v_i v_i)}{\partial t} \mathrm{d}V = \int_\Gamma v_i \sigma_{ij} n_j \mathrm{d}S - \int_\Omega \sigma_{ij} \frac{1}{2} (\frac{\partial v_i}{\partial x_j} + \frac{\partial v_j}{\partial x_i}) \mathrm{d}V. \tag{4.B.4}$$

For infinitesimal deformation, the strain tensor $\dot{\varepsilon}_{ij} = \frac{1}{2}(\frac{\partial v_i}{\partial x_j} + \frac{\partial v_j}{\partial x_i})$. We substitute this into Eq. (4.B.4) and get

$$\int_\Omega \frac{\partial (1/2 \rho v_i v_i)}{\partial t} \mathrm{d}V = \int_\Gamma v_i \sigma_{ij} n_j \mathrm{d}S - \int_\Omega \sigma_{ij} \dot{\varepsilon}_{ij} \mathrm{d}V. \tag{4.B.5}$$

From Eqs. (2.3) and (4.A.4), we can derive

$$T\dot{s} + \frac{\partial e}{\partial \alpha} \dot{\alpha} + \frac{\partial e}{\partial B} \dot{B} = 0. \tag{4.B.6}$$

If we add Eq. (4.B.5) to Eq. (4.B.6), substitute the second term on the right-hand-side of Eq. (4.B.5) with Eq. (4.A.4), and consider the definition of e in Eq. (4.A.2), we derive

$$\begin{aligned} \int_\Gamma v_i \sigma_{ij} n_j \mathrm{d}S &= \int_\Omega \frac{\partial (1/2 \rho v_i v_i)}{\partial t} \mathrm{d}V + \int_\Omega (\frac{\partial e}{\partial \underline{\underline{\varepsilon}}} : \dot{\underline{\underline{\varepsilon}}} + \frac{\partial e}{\partial \alpha} \dot{\alpha} + \frac{\partial e}{\partial B} \dot{B}) \mathrm{d}V + \int_\Omega T\dot{s} \mathrm{d}V \\ &= \int_\Omega \frac{\partial (1/2 \rho v_i v_i)}{\partial t} \mathrm{d}V + \int_\Omega \dot{e} \mathrm{d}V + \int_\Omega T\dot{s} \mathrm{d}V. \end{aligned} \tag{4.B.7}$$

If we define $\dot{W}^f = \int_{\Gamma^{fault}} v_i \sigma_{ij} n_j \mathrm{d}S$ as the power of frictional force on the fault interfaces, $\dot{W}^s = \int_{\Gamma^{surf}} v_i \sigma_{ij} n_j \mathrm{d}S$ as the power of the external work on the domain boundaries, $\dot{K} = \int_\Omega \frac{\partial (1/2 \rho v_i v_i)}{\partial t} \mathrm{d}V$ as the change rate of kinetic energy, $\dot{E} = \int_\Omega \dot{e} \mathrm{d}V$ as the change rate of mechanical potential energy, and $\dot{\mathcal{D}} = \int_\Omega T\dot{s} \mathrm{d}V$ as energy dissipation rate due to irreversibility of the process.

Appendix 4.C Mesh independence of the off-fault damage structure

For the combination of dynamic rupture with nonlinear wave propagation, when the damage reaches solid-granular transition conditions, shear bands start to extend from the fault interface. The angles of the shear bands to the fault agree with the theoretical predictions of the CDB model, as in Fig. 4.2. Here, we also show in Fig. 4.C.1 that the off-fault shear band and damage distribution patterns are mesh-independent when refining off-fault area from 100 m to 25 m. Only the resolution in the localized damage region increases.

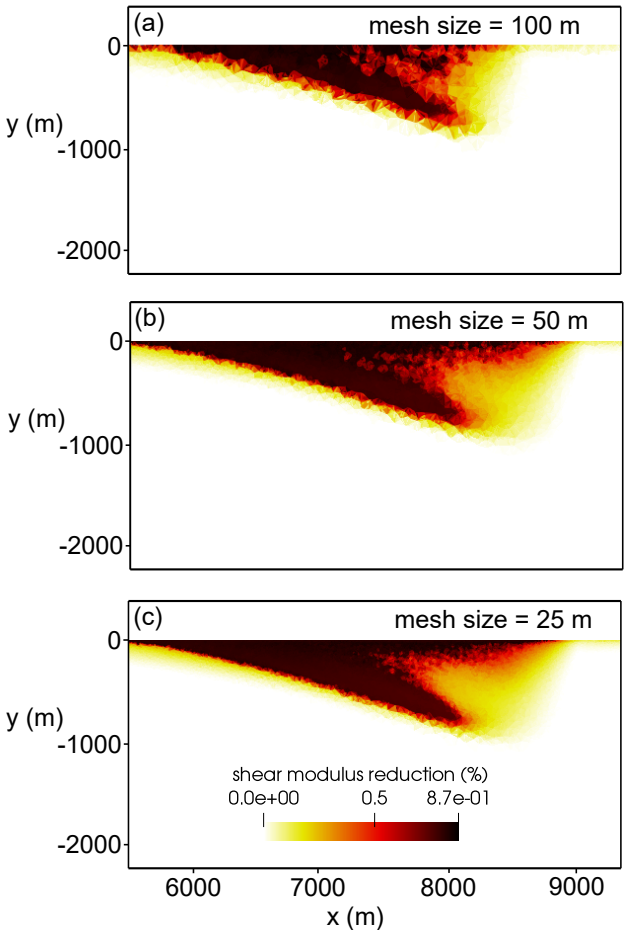

Figure 4.C.1: The spatial distribution of the localized shear modulus reduction, zoomed in on the region within the dashed red rectangle in Fig. 4.2c. The largest tetrahedral element size in (a), (b) and (c) are, respectively, 100 m, 50 m and 25 m.

Such localized damage results in a non-smooth breakage variable distribution inside the damage zone. This also becomes a great challenge for using shape functions of an order higher than 2. The shape function can become highly heterogeneous within the cell and such heterogeneity can enhance the non-smoothness in the results. This can lead to the values of the damage and the breakage variables falling outside of the physical range from 0 (intact rock) to 1 (fully damage rock). We tested that with the Dubiner's basis functions of polynomial degree 1 ($p = 1$, Cockburn et al., 2012; Wollherr et al., 2018), such un-physical

results can be avoided. There are a bunch of methods that can potentially suppress the non-smoothness inside a cell for $p \geq 2$. We may introduce a-priori smoothing algorithms, like introducing artificial viscosity (Hartmann and Houston, 2002; Persson and Peraire, 2006), filtering (Radice and Rezzolla, 2011), WENO- or HWENO-based reconstruction (Qiu and Shu, 2004). We may also detect the oscillatory regions and introduce smoothing locally (Diot et al., 2013; Loubere et al., 2014).

The solid-granular phase transition inside the damage zone also contributes to secondary waves and high-frequency radiation. We show in Fig. 4.C.2 how the high frequency depends on the mesh. Compared to the elastic case (the dashed black curve), the off-fault phase transition generates more energy beyond 0.4 Hz on all three mesh resolutions. The shape of the power spectral density keeps a similar amplitude up to around 5 Hz. Beyond this frequency, a finer mesh resolves a greater energy.

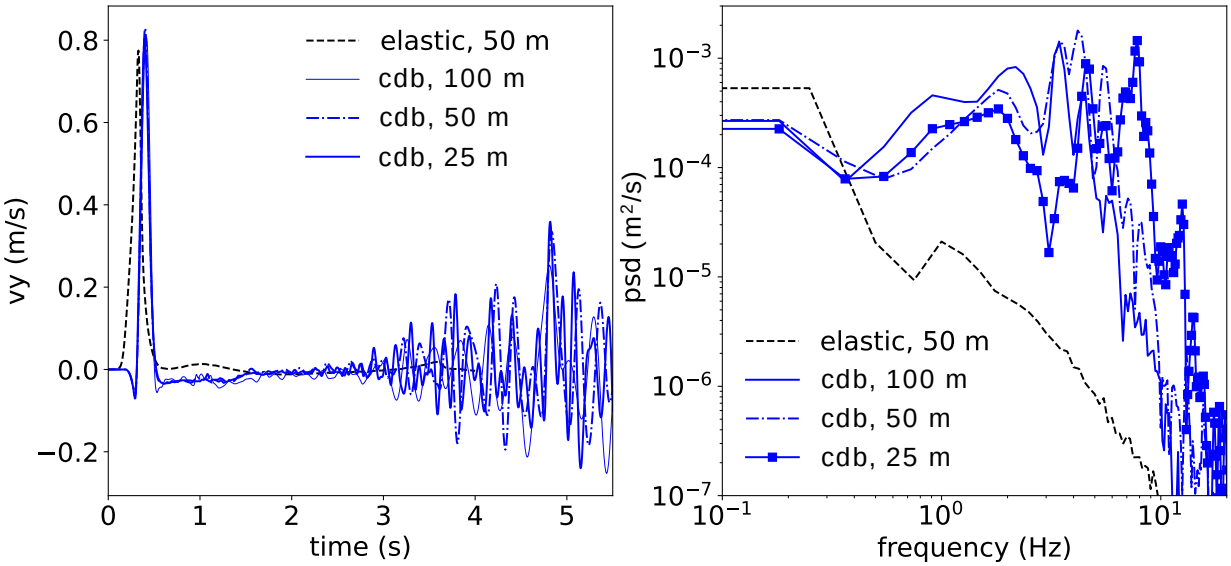

Figure 4.C.2: (a) Particle velocity along y-axis recorded at the red rectangle in Fig. 4.2b. The dashed black curve shows the reference solution when the off-fault material is purely elastic, with a mesh refinement up to 50 m next to the fault plane. We show side-by-side the recorded time series when the off-fault damage in the CDB model is considered with a mesh refinement up to 100 m (the thin solid blue curve), 50 m (the dashed blue curve) and 25 m (the thick solid blue curve). (b) The power spectral density (psd) of the particle velocity along y-axis transformed from the corresponding time series in (a).

Appendix 4.D Supershear transition and cohesive zone width with off-fault damage

In this section, we address the impacts of off-fault damage processes on two important aspects of the dynamic rupture: (1) supershear transition and (2) cohesive zone size.

A rupture front that propagate at an intersonic speed (supershear) can significantly change the directivity of earthquakes. In the supershear, the constructive interference of the waves

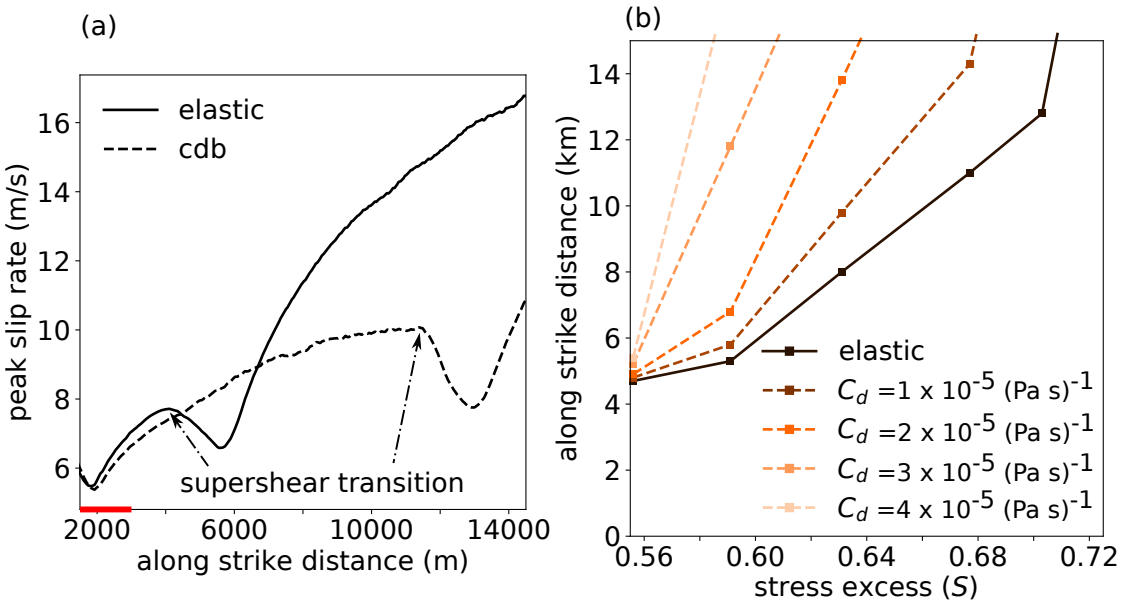

Figure 4.D.1: Variation in the point of supershear transition during the fault rupturing. (a) Changes of peak slip rate in the along strike for both elastic (the solid curve) and CDB (the dashed curve) off-fault material models. The two dash-dotted arrows mark the location where we define as the point of supershear transition. The red line marks region where we nucleate the dynamic rupture (Harris et al., 2018). (b) Variation in the point of supershear transition in the along strike direction with stress excess S. The solid black curve show the variation in elastic case; while the color-coded curves in orange show the variation in CDB model case, with $C_d = 1 \times 10^{-5}$, 2×10^{-5}, 3×10^{-5} and 4×10^{-5} (Pa·s)$^{-1}$. The rest of the parameters are the same as listed in Table 4.1.

radiated from a Mach front results in much stronger ground motions than a wave front that is transported at sub-Rayleigh speeds (Bernard and Baumont, 2005; Dunham and Archuleta, 2005; Bhat et al., 2007). The supershear transition in this work in Section 4.3 results from the daughter crack that nucleates in front of the sub-Rayleigh rupture due to the local dynamic stress peak (Andrews, 1976; Dunham, 2007). We show in Fig. 4.D.1b how the damage coefficient C_d influences the supershear transition. We here define that the supershear transition initiates from the point where the peak slip rate reaches a local maximum as marked with the two dash-dotted arrows in Fig. 4.D.1a according to Gabriel et al. (2012). The red line in Fig. 4.D.1a marks the r_{crit} where we nucleate the dynamic rupture (Harris et al., 2018).

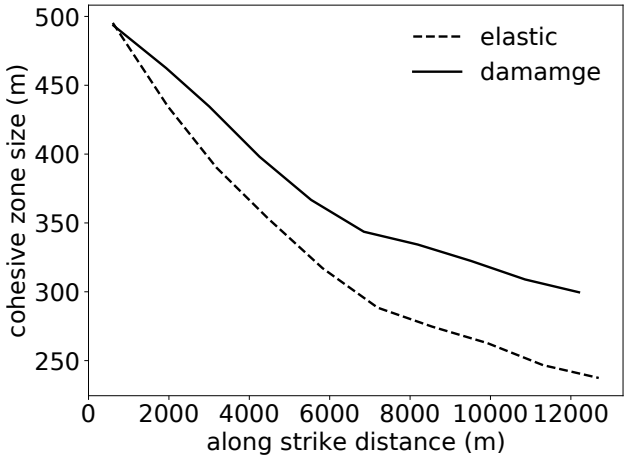

Figure 4.D.2: Variation of the cohesive zone width in the along strike direction for both elastic (the dashed curve) and CDB (the solid curve) model case. In the CDB model case, $C_d = 3 \times 10^{-5}$ $(\text{Pa}\cdot\text{s})^{-1}$ with the rest of the parameters same as those in Table 4.1.

The cohesive zone (also known as breakdown or process zone) is defined as the area behind the rupture front where the shear stress drops from its static to its dynamic value (Day et al., 2005). Within the cohesive zone, the slip rate and the fault traction change significantly. This makes the dimension of the cohesive zone an important length scale to resolve in mesh refinement. We show in Fig. 4.D.2 how the cohesive zone is altered by the off-fault damage.

Appendix 4.E Evolution of damage, traction, and slip rate in the two faults in a step-over setup

We use this section to provide the slip rate and shear traction distribution on the two faults in the step-over set up in Section 4.4 at different times after the nucleation of the dynamic rupture on the first fault. We show in Fig. 4.E.1a-1 to 4.E.1a-4 the distribution of slip rate on the two faults at 4s, 7s, 35 s and 40 s, and in Fig. 4.E.1b-1 to 4.E.1b-4 the distribution of shear traction on the two faults at 4s, 7s, 35 s and 40 s.

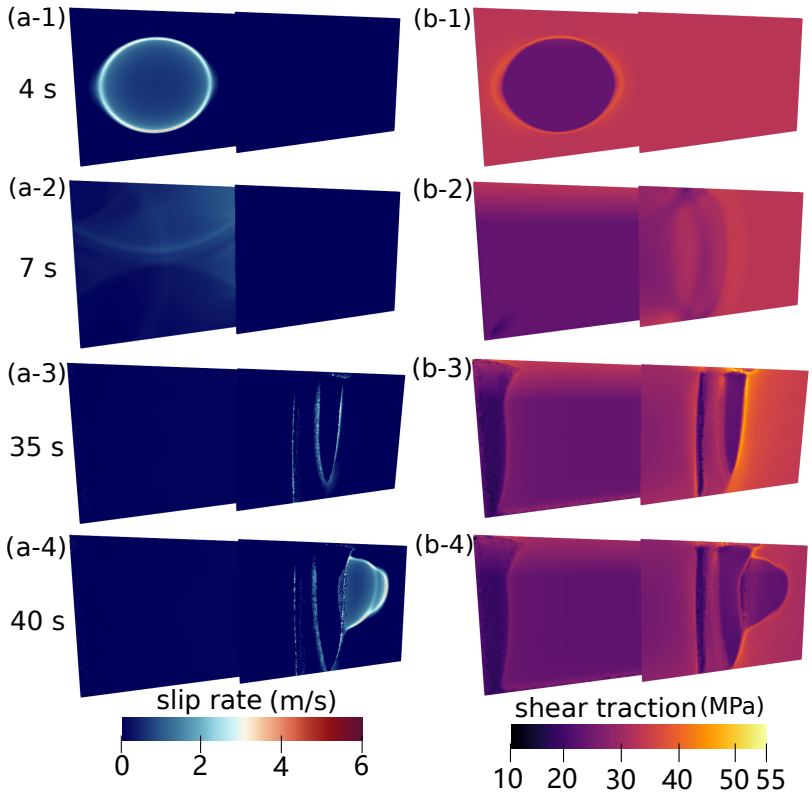

Figure 4.E.1: Slip rate (a-1 to a-4) and shear traction (b-1 to b-4) distribution on the two fault planes at 4, 7, 35, and 40 s for the step-over setup in Fig. 4.4.

Chapter 5

Nonlinear inversion for 3D dynamic rupture simulation - Method

Bayesian inference enables greater scientific insight into simulation models, determining model parameters and meaningful confidence regions from observed data. With hierarchical methods like Multilevel Delayed Acceptance (MLDA) drastically reducing compute cost, sampling Bayesian posteriors for computationally intensive models becomes increasingly feasible. Pushing MLDA towards the strong scaling regime (i.e. high compute resources, short time-to-solution) remains a challenge: Even though MLDA only requires a moderate number of high-accuracy simulation runs, it inherits the sequential chain structure and need for chain burn-in from Markov chain Monte Carlo (MCMC). We present fully asynchronous parallel prefetching for MLDA, adding an axis of scalability complementary to forward model parallelization and parallel chains. A thorough scaling analysis demonstrates that prefetching is advantageous in strong scaling scenarios. We investigate the behavior of prefetching MLDA in small-scale test problems. A large-scale geophysics application, namely parameter identification for non-linear earthquake modelling, highlights interaction with coarse-level quality and model scalability.

5.1 Introduction

Mathematical inverse problems provide a rich framework for gaining insight into a multitude of problems and phenomena in science and technology by combining models and data to infer unknown parameters, such as material properties, reaction rates, or effective potentials (Ghattas and Willcox, 2021; Arridge et al., 2019; Liang et al., 2023; Puel et al., 2022). Observational data is typically noisy and incomplete, while computational models only approximate the true system. Consequently, modern research increasingly focuses on incorporating these uncertainties into inference problems. A common approach to UQ is to formulate an inverse problem in the Bayesian framework (Kaipio and Somersalo, 2005), assigning a posterior probability to unknown parameters based on prior knowledge as well as goodness-of-fit between model prediction and observational data.

An attractive choice for solving Bayesian inverse problems (BIP) are MCMC algorithms (Metropolis et al., 1953; Hastings, 1970; Duane et al., 1987; Homan and Gelman, 2014; Cui et al., 2016), as they impose minimal assumptions on the model. However, this generality comes at the price of requiring large numbers of model evaluations. This cost can easily become excessive, particularly for inverse problems governed by partial differential equations (PDE) that already require High Performance Computing (HPC) resources for a single

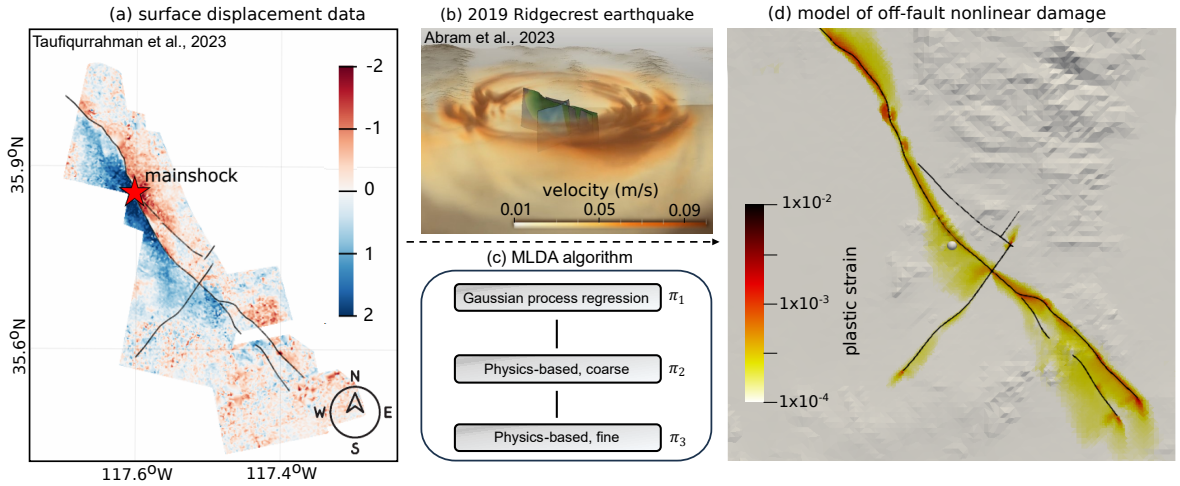

Figure 5.1: Overview of the MLDA algorithm and its target application, the 2019 Ridgecrest earthquake. (a) Surface displacement data during the earthquake Taufiqurrahman et al. (2023). (b) Visualization of the simulated earthquake source and the generated seismic wave field Abram et al. (2019). (c) Structure of the proposed MLDA model hierarchy. (d) Modeled plastic deformation, which is controlled by physical parameters, the target of the inference in this work.

evaluation.

Multilevel Markov chain Monte Carlo (MLMCMC) (Dodwell et al., 2019) exploits a hierarchy of models with varying fidelities, allocating most of the computational effort to less accurate but fast approximate models. MLMCMC thus achieves efficiency gains comparable to Multilevel Monte Carlo (MLMC) (Giles, 2008) in uncertainty propagation. MLMCMC relies on the assumption of independent samples from coarser levels, which serve as proposals for the finer levels. However, in practice, this independence only holds approximately, introducing bias. The more recent MLDA (Lykkegaard et al., 2023), based on delayed-acceptance MCMC (Christen and Fox, 2005), addresses this limitation. Compared to MLMCMC, which has been successfully parallelized and deployed on HPC systems (Seelinger et al., 2021), MLDA introduces stronger data dependencies between levels, and is therefore more challenging to parallelize.

In this work, we introduce a novel parallelization approach for the MLDA algorithm based on prefetching (Strid, 2010; Angelino et al., 2014), the parallel evaluation of possible future Markov Chain states based on a binary decision tree. Prefetching acts as an additional level of parallelism on top of model parallelism and parallel execution of multiple MLDA chains, each of which naturally exhibit diminishing returns.

We discuss the theoretical basis for prefetching in a multilevel context. On an example problem, we investigate performance by comparing prefetching to parallelization with multiple chains. The results indicate that prefetching is in fact needed for optimal parallel efficiency in the strong scaling regime, i.e. where many compute resources are employed to rapidly achieve an inversion result.

Our prefetching MLDA implementation supports the UQ and Modeling Bridge (UM-Bridge)

interface (Seelinger et al., 2023), leading to a modular pipeline that transparently scales to HPC clusters and allows linking to any simulation code. It is available open-source online (Kruse et al., 2024).

Finally, we apply prefetching MLDA to a novel, computationally challenging inverse problem in geoscience. It aims to infer subsurface material parameters in a non-linear seismic model using earthquake data. We use three-dimensional, non-linear dynamic rupture models of the Ridgecrest earthquakes (similar to Taufiqurrahman et al. (2023)), California's biggest earthquakes in more than 20 years which ruptured multiple segments of a complex fault system (Ross et al., 2019). Our inversion aims to explain high-rate global positioning system datasets with earthquake physics. The model is implemented in the earthquake simulation software SeisSol (Heinecke et al., 2014; Uphoff et al., 2017; Krenz et al., 2021), which integrates seamlessly with our computational pipeline. We construct the multilevel model hierarchy by varying the PDE discretization level, and augment it with an adaptive surrogate model based on Gaussian Process (GP) regression (Rasmussen and Williams, 2006) on the coarsest level.

5.2 Asynchronous prefetching MLDA

Bayesian inverse problems define, for some parameter of interest $\theta \in \mathbb{R}^d$, a posterior distribution $\pi_{\text{post}}(\theta|d_{\text{obs}})$, given observations $d_{\text{obs}} \in \mathbb{R}^q$ of the system under consideration. In this work, we consider scenarios where the data is the perturbed output of a PDE model, given a specific parameter set as its input, $d^{\text{obs}} = G(\theta) + \eta$. $\eta \in \mathbb{R}^q$ is the realization of a noise variable with known statistics. This induces a likelihood $l(d_{\text{obs}}|\theta)$ to observe the data, given a parameter candidate. In combination with some prior distribution $\pi_{\text{prior}}(\theta)$, Bayes' theorem yields the posterior as

$$\pi(\theta) \equiv \pi_{\text{post}}(\theta|d_{\text{obs}}) \propto l(d_{\text{obs}}|\theta)\pi_{\text{prior}}(\theta). \tag{5.1}$$

MLDA algorithm MCMC methods generate correlated samples from a target distribution π (in our scenario a Bayesian posterior). Given a sample $\theta_n \in \mathbb{R}^d$, MCMC algorithms generate a new sample θ_{n+1} in a two-step procedure. Firstly, a proposal candidate $\tilde{\theta}_{n+1}$ is drawn from a distribution $q(\cdot|\theta_n)$, which is typically cheap to evaluate. The proposal is then accepted ($\theta_{n+1} = \tilde{\theta}_{n+1}$) or rejected ($\theta_{n+1} = \theta_n$) according to a transition probability $\alpha(\tilde{\theta}_{n+1}|\theta_n)$. Importantly, proposals tend to be cheap to compute, while the transition probability depends on costly target density evaluations $\pi(\tilde{\theta}_{n+1})$ and $\pi(\theta_n)$.

A major drawback of MCMC methods is that they typically require a large number of evaluations of the target density to achieve a sufficient number of effectively uncorrelated samples. Multilevel algorithms may drastically reduce that cost. We employ the MLDA algorithm (Lykkegaard et al., 2023) in this work. The basic idea of MLDA (as for other multilevel methods) is to employ a hierarchy of models with different accuracy-cost tradeoff. We denote this hierarchy as subchain levels $s = 1, 2, \ldots, K$ with corresponding target densities π_s. We presume that densities on lower levels are cheap to compute but coarse approximations of the posterior, whereas evaluations on higher levels are computationally

more expansive, but more exact. We set $\pi = \pi_K$. MLDA generates high-quality proposals on subchain level l by spawning an MCMC chain on subchain level $l-1$ at the current state. The final sample of that coarser-level subchain is then used as a proposal for level l. Applying this recursively across levels results in an increasingly fast rate of decorrelation for samples on finer levels. Through a careful choice of model hierarchy and subchain lengths (see Lykkegaard et al. (2023) for details on convergence rates), MLDA can achieve a significant reduction in overall cost for sampling π.

Prefetching MLDA Like single-level MCMC algorithms, MLDA is inherently sequential. A trivial method of parallelization is the generation of multiple independent chains. However, since each chain requires a burn-in period and mixing, parallel chains scale at diminishing returns. Thus, we additionally employ within-chain parallelization through prefetching (Brockwell, 2006; Strid, 2010; Angelino et al., 2014). The underlying concept of prefetching is to expand possible future states of a MCMC chain $\overline{\theta}_{n+j},\ j = 1, 2, \ldots$ from a given state θ_n in a binary tree, representing all future accept/reject decisions. We refer to this structure as a *Markov tree*. Possible future states can be determined in advance, since proposals are typically cheap. We can then conduct the costly target density evaluations for possible future states in parallel. Now, given a pool of N_p workers, N_p target density evaluations across the Markov tree can be conducted simultaneously. With the obtained results, the Markov chain can potentially be advanced by $N_p > 1$ steps. Since we might precompute density evaluations in branches that the MCMC algorithm ultimately does not take, the efficiency of prefetching depends on a "clever" distribution of computational resources onto the possible future states of the chain.

We now introduce an extension of prefetching for MLDA, including fully asynchronous operations accommodating differing run times across levels. We begin by establishing a formal notation for a Markov tree and its nodes. A general Markov tree consists of a sequence of levels $l \in \mathbb{N}_0^+$, not to be confused with the subchain levels s of the MLDA algorithm. We characterize a node t in layer T_l by a string,

$$t \in T_l \text{ with } T_l \subset \{a, r\}^l, \tag{5.2}$$

indicating the sequence of accepts (a) and rejects (r) leading to the state of that node. We denote the root level as T_0, which only contains the root node t_0. Moving on, we define the concatenation operation to create a descendant or child of a given node,

$$\oplus : T_l \times \{a, r\} \to T_{l+1}. \tag{5.3}$$

Informally, this means that a child node is generated from its parent by appending a letter from $\{a, r\}$ to its defining string. A complete Markov tree is given as the directed acyclic graph resulting from the concatenation of nodes over subsequent layers. Under abuse of notation, we resemble this by the union of layers,

$$T \coloneqq \bigcup_{l \in \mathbb{N}_0^+} T_l. \tag{5.4}$$

An exemplary Markov tree is depicted in Fig. 5.2.

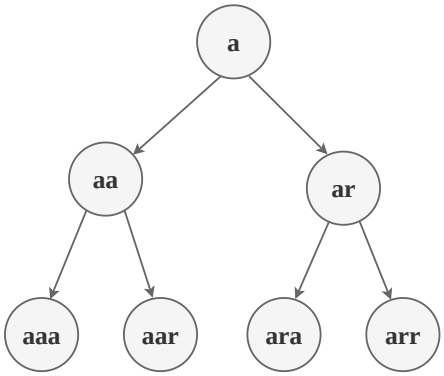

Figure 5.2: Three levels of a Markov decision tree. Nodes are labelled with the sequence of accepts and rejects leading to that node.

For the MLDA algorithm, tree nodes carry two additional quantities, their subchain levels $s(t) \in \{1, 2, \ldots, K\}$ and their indices $i(t) \in \{1, 2, \ldots, I_{s(t)}\}$ within the respective subchain. We define for the root node

$$s(t_0) = K, \quad i(t_0) = 1, \tag{5.5}$$

and for all $t \in T$, $x \in \{a, r\}$ through recursive concatenation

$$s(t \oplus x) = \begin{cases} s(t) & \text{if } s(t) = 1 \text{ and } i(t) < I_0 \\ s(t) + 1 & \text{if } s(t) < K \text{ and } i(t) = I_{s(t)} \\ s(t) - 1 & \text{else,} \end{cases} \tag{5.6}$$

and

$$i(t \oplus x) = \begin{cases} i(t) + 1 & \text{if } s(t) = 1 \text{ and } i(t) < I_0 \\ i(\nu_s(t \oplus x)) + 1 & \text{if } s(t) < K \text{ and } i(t) = I_{s(t)} \\ 1 & \text{else.} \end{cases} \tag{5.7}$$

Here, we have introduced the mapping $\nu_s : T \to T$ from a node to its closest ancestor on the same subchain level, i.e. $s(\nu_s(t)) = s(t)$.

We can now define the states of the nodes in the Markov tree. Assuming that proposals on the coarsest level of the MLDA hierarchy are generated by a distribution $q(\cdot|\cdot)$, we set $\overline{\theta}_{t_0} = \theta_n$ and define subsequent states recursively:

$$\text{If } \; s(t \oplus x) = s(t) = 1 : \quad \overline{\theta}_{t \oplus x} = \begin{cases} \tilde{\theta}_t \sim q(\cdot|\overline{\theta}_t) & \text{if } x = a, \\ \overline{\theta}_t & \text{if } x = r, \end{cases} \tag{5.8a}$$

$$\text{If } \; s(t \oplus x) = s(t) + 1 : \quad \overline{\theta}_{t \oplus x} = \begin{cases} \overline{\theta}_t & \text{if } x = a, \\ \overline{\theta}_{\nu_s(t \oplus x)} & \text{if } x = r, \end{cases} \tag{5.8b}$$

$$\text{If } \; s(t \oplus x) = s(t) - 1 : \quad \overline{\theta}_{t \oplus x} = \overline{\theta}_t. \tag{5.8c}$$

Asynchronous prefetching In our work, we employ asynchronous prefetching, making use of computational resources as soon as they become available. This is absolutely crucial

in MLDA, since model run times may vary extremely across levels: An entire subchain may complete before a previous finer-level node. To this end, we distinguish four computational states for each node in the Markov tree. Nodes in the set $O \subseteq T$ have not been assigned any computational resources yet. Nodes in $W \subseteq T$ are currently running evaluations of the target density. For nodes in $D \subseteq T$, the computation has been completed, and computational resources have been freed. And finally, nodes in $E \subset T$ have been eliminated through MCMC accept/reject decisions.

We make these decisions as soon as the target densities for all relevant nodes have been computed. If an MCMC move from the state θ_t is accepted, we prune $t \oplus r$ and all its children, i.e. we put these nodes into the set E. If the move is rejected, we prune $t \oplus a$ and its subtree. Note that the MLDA algorithm comprises different types of MCMC decisions, each requiring different target densities to be evaluated. For subchains on levels $s = 1, 2, \ldots, K-1$, this facilitates additional within-subchain pruning. On these levels, only the target densities at the first and last subchain index are needed for a subsequent MCMC decision on the next finer level. Consequently, as soon as a succession of three or more nodes in a subchain are uniquely connected, we can make the first node in that sequence the immediate parent of the last node, effectively pruning all intermediates. Given the recursive nature of MLDA's subchains, we would otherwise have to track an extreme amount of subchain nodes before advancing to the next fine-level state.

Next, we devise a strategy for optimally assigning computational resources to nodes in the Markov tree. For this, we assume that we can approximately predict the acceptance probability for a node on subchain level s by a level-dependent estimate $\tilde{\alpha}_s$. Such estimates can be static guesses or adaptive (e.g., depending on the previous behavior of the Markov chain). In addition, we have to take into account that the acceptance probability is either zero or one if the MCMC decision has already been made. We hence define the approximate acceptance rate γ as

$$\gamma(t \oplus a) \coloneqq \begin{cases} \tilde{\alpha}_{s(t \oplus a)} & \text{if } t \oplus a, t \oplus r \notin E, \\ 1 & \text{if } t \oplus r \in E, \\ 0 & \text{if } t \oplus a \in E. \end{cases} \tag{5.9}$$

Moving on, we recursively construct the estimated probability $P_R(t)$ of a node t to be reached by the actual Markov chain. We set $P_R(t_0) = 1$ and extend to other nodes as

$$P_R(\overline{\theta}_{t \oplus x}) = \begin{cases} P_R(\overline{\theta}_t)\gamma(t \oplus a) & \text{if } x = a, \\ P_R(\overline{\theta}_t)(1 - \gamma(t \oplus a)) & \text{if } x = r. \end{cases} \tag{5.10}$$

We can now formulate an optimization problem for finding a node t^* whose target density should be evaluated next, as soon as computational resources become available. This is simply the node $t \in O$ that has maximum probability of being required for the propagation of the Markov chain. The probability of a node being required, in turn, is given by the probability of its immediate ancestor being reached. So we define the mapping $\nu : T \to T$ from a node to its parent, and obtain the next candidate for target density evaluation according to

$$t^* = \operatorname*{argmax}_{t \in O} P_R(\nu(t)). \tag{5.11}$$

Under this choice of optimality condition, the probabilities of child nodes are necessarily lower than those of their parents. Consequentially, the optimal node can always be found in the subtree of layers $l \leq L^*$, where L^* is the first layer for which no target densities have been computed yet.

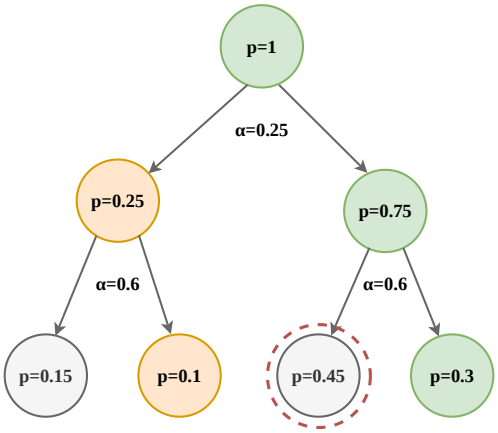

Figure 5.3: Traversal of node probabilities through an exemplary Markov tree. Green color indicates finished posterior evaluation, orange indicates computations in progress. The most likely candidate, selected for the next posterior evaluation, is encircled in red.

Active subtree While considering an infinite tree on a theoretical level, we operate only on an active subtree $T_A \subset T$ in practice, adding and pruning nodes as the algorithm progresses. New node pairs $(t \oplus a, t \oplus r)$ are only added to the active tree if their parent meets one of the following conditions:

(a) t is the root

(b) t is an accept node, meaning that the last letter in its string is an "a", and $t \in D \cup W$

(c) t is a reject node, meaning that the last letter in its string is an "r", and its accept sibling $t_s \in D \cup W$

This ensures that along any possible path, exactly one advance accept/reject decision that still needs target density evaluation is in the active subtree. As soon as computational resources are available, evaluation is started for the current $t^* \in O$. As soon as results of computations are returned and resources freed, available MCMC decisions are performed and subtrees pruned, including within-subchain pruning. Importantly, as soon as there is a unique path between the root node and a fine level child t_N, that child's state is a new sample of the Markov chain. We then discard the entire tree before that sample and make it the new root, i.e. $t_0 \leftarrow t_N$.

Overall, the presented MLDA algorithm iteratively performs a sequence of steps, until the desired number of fine-level samples is reached. These steps can be summarized as follows:

1. Expand the Markov tree, request new posterior evaluations,

2. update the Markov tree with finished jobs,
3. compute available MCMC decisions,
4. prune the Markov tree, and
5. if possible, propagate the Markov chain.

5.3 Scaling MLDA for HPC Simulators via UM-Bridge

Prefetching MLDA applies to a very wide range of inverse problems, since it only requires access to pointwise evaluations of the posterior (and no gradients of the forward model etc.). In order to make our software equally universal, we perform model evaluation calls through UM-Bridge. UM-Bridge is an easy-to-use framework for interacting with simulation codes regardless of programming language or platform, as demonstrated by Seelinger et al. (2025).

It allows our Python implementation of prefetching MLDA to link to any simulation model from simple test problems to highly optimized simulations running on massively parallel HPC architectures. We illustrate the resulting setup in Fig. 5.4.

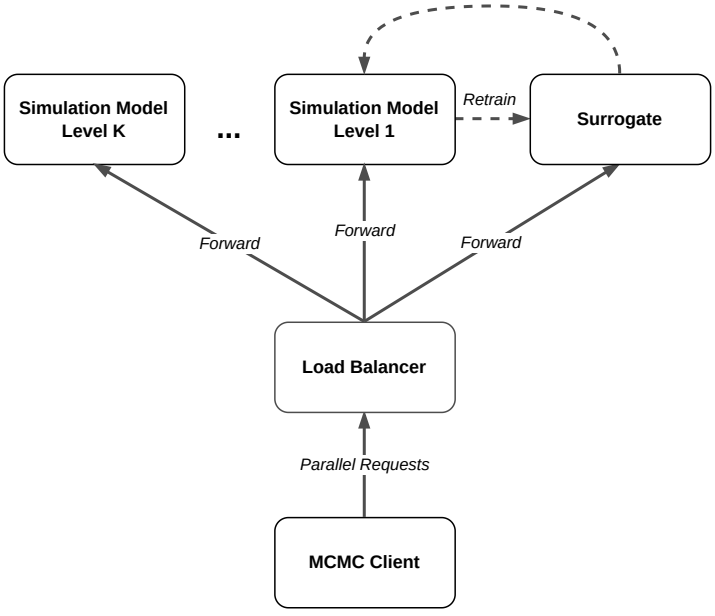

Figure 5.4: Computational setup consisting of UQ client, cluster-side load balancer, adaptive surrogate model and parallel simulation instances.

The prefetching MLDA Python code constitutes the client side in our setup, requesting model evaluations from the cluster via UM-Bridge. The load balancer, typically running on the login node of an HPC cluster, launches simulation model instances as needed and forwards evaluation requests to them.

In total, we employ three levels of parallelism:

- We run multiple independent MLDA samplers and collect their results (which is valid since they sample the same posterior), making use of `multiprocessing`.
- Each sampler performs asynchronous prefetching (Section 5.2) for in-chain parallelism.
- The simulation model itself may be parallelized.

Importantly, since the generic load balancer handles simulation runs on the cluster, Python's `multiprocessing` framework is enough for prefetching MLDA to control parallel simulation runs across thousands of cores. Model parallelism is entirely transparent to the UQ side.

In our geophysics application (Section 5.5), we employ a MLDA model hierarchy that includes a GP surrogate (Rasmussen and Williams, 2006) in addition to numerical simulators. The GP approximates the simulation model on the coarsest simulation level at extremely low cost.

We ensure GP accuracy while restricting training to high-posterior areas through an adaptive procedure: We initially pretrain the surrogate from simulation runs on only a small number of Latin Hypercube points. During the UQ run, we employ the mean prediction as an approximation to the simulator. However, if GP variance exceeds a threshold (indicating high approximation error), we trigger an additional coarse-level simulation for that parameter, updating the GP for higher confidence in that area.

5.4 Application: Bayesian Inference in Seismology

Demonstrating prefetching MLDA in a real-world application, we target a highly relevant inverse problem from computational seismology: Inferring information about earthquake sources from surface recordings only.

5.4.1 Modeling Earthquakes in SeisSol

The forward problem is solved by the earthquake simulation software SeisSol (`www.seissol.org`). The Earth is modeled as a 3D elastic body and the respective elastic wave equation is expressed in first-order formulation,

$$\partial_t u + A\partial_x u + B\partial_y u + C\partial_z u = 0, \tag{5.12}$$

where u is the vector of unknowns (stress and particle velocities). The flux matrices A, B and C contain the material parameters (Lamé parameters and density). This hyperbolic partial differential equation is solved using the Discontinuous Galerkin method with Arbitrary high-order DERivatives time stepping (ADER-DG, Dumbser and Käser, 2006).

SeisSol implements ADER-DG for elastic (Dumbser and Käser, 2006), viscoelastic (Dumbser et al., 2007; Uphoff and Bader, 2016b), anisotropic (de la Puente et al., 2007; Wolf

et al., 2020b) and poroelastic (de la Puente et al., 2008; Wolf et al., 2022) material models. In addition, it features plastic deformation (Wollherr et al., 2018) and the coupling of acoustic and elastic domains (Krenz et al., 2021). A key component of SeisSol are dynamic rupture earthquake sources (Pelties et al., 2012, 2014). For this source type, the non-linear frictional failure along prescribed fault planes is simulated along with the seismic wave fields. The movement of the sliding fault induces wave motion in the surrounding bulk volume. Interaction of frictional failure and wave motion allows researchers to investigate earthquake physics. For example, dynamic models can explain how rupture *jumps* from one fault segment to another one (Taufiqurrahman et al., 2023; Gabriel et al., 2024).

SeisSol has been used on several petascale supercomputers to model earthquake scenarios with several billion degrees of freedom, achieving a significant fraction of the theoretical peak performance (Heinecke et al., 2014; Uphoff et al., 2017; Krenz et al., 2021). On the node level, SeisSol relies on the code generator YATeTo (Uphoff and Bader, 2020), which generates high-performance code by mapping kernel descriptions (in Einstein sum convention) to highly optimized backends for small matrix operations. Through different backends, SeisSol achieves performance portability between different compute architectures including GPUs (Dorozhinskii and Bader, 2021). SeisSol uses a hybrid parallelization approach: On node level, we use either OpenMP (for CPUs) or CUDA/SYCL/ROCm (for GPUs). Between nodes, the mesh is partitioned and communication between ghost and copy cells is done with MPI. Asynchronous communication then hides communication behind computation.

In the Bayesian inverse problem considered (see Section 5.4.2), the results of the forward model depend on several volumetric material parameters, e.g. Lamé parameters λ and μ or plastic cohesion c, encoded in the parameter vector θ. When the UQ sampler requires a forward model evaluation for a parameter θ, a small wrapper script prepares input files for SeisSol. Parallel execution of SeisSol is then triggered. SeisSol produces artificial seismograms, which we compare to real-world recordings in order to form the Bayesian posterior Eq. (5.15).

The wrapper code acts as an UM-Bridge server, making SeisSol easily accessible to the UQ code. Integrating UQ and model in such a way retains full flexibility w.r.t. model complexity (e.g. scattering at material interfaces or at the free surface), while cleanly separating it from the complexity of the UQ workflow.

5.4.2 2019 Ridgecrest, CA, earthquake scenarios

Modern measuring techniques enhance the quality and quantity of data available for characterizing earthquake dynamic rupture processes and include strong-motion and broadband seismometers, high-rate Global Navigation Satellite System (GNSS) instruments and space geodetic datasets (e.g., Gabriel et al., 2023; Hayek et al., 2024).

However, while non-linear inversions of earthquake data for dynamic parameters to construct physically consistent earthquake models have been conducted (Fukuyama and Mikumo, 1993; Peyrat and Olsen, 2004; Gallovič et al., 2019; Schliwa et al., 2024b), the immense computational cost of each forward model restricted these to simplified model setups and

inversions for on-fault parameters only. MLDA addresses the above limitations, drastically reducing the required number of full-complexity, high-resolution forward simulations.

As a demonstrator scenario, we examine linked dynamic rupture simulations of the 2019 M_W6.4 Searles Valley foreshock and the M_W7.1 Ridgecrest mainshock (Taufiqurrahman et al., 2023). This earthquake sequence involves the rupture of a complex fault system comprising four major non-planar segments. To capture off-fault rock deformation, we embed the rupturing faults in elasto-plastic materials using a Drucker-Prager yield criterion (Wollherr et al., 2018). The yielding strength τ_c is defined by two spatially varying material parameters, plastic cohesion c and friction angle ϕ, as

$$\tau_c = c\cos(\phi) - \sigma_m \sin(\phi), \tag{5.13}$$

where $\sigma_m = \sigma_{kk}/3$ is the mean of the stress tensor trace σ_{ij}. These plastic parameters strongly influence earthquake dynamic rupture processes and ground shaking. Following Taufiqurrahman et al. (2023), we define spatially varying rock elastic moduli and prestress fields by combining a 3D community velocity model CVM-S4.26 (Lee et al., 2014) and a 2D community stress model representing the regional state of stress in the Southern California upper crust (Yang and Hauksson, 2013). We also assume spatially varying plastic cohesion $c_0(x, y, z)$ as proportional to the shear modulus of the 3D velocity model. The plastic cohesion is $c = \gamma c_0(x, y, z)$, where γ is a scaling factor to be inverted for using MLDA. The friction angle ϕ is held constant across the domain, for simplicity.

Under the above assumptions, the parameter vector is $\theta = (\gamma, \phi)^T \in \mathbb{R}^2$. Observational data for the inverse problem consists of three-dimensional displacement time series recorded at 10 GNSS stations near the fault system (Melgar et al., 2020). Each station provides surface displacement vectors $\delta_i(t)$, with i representing east-west, north-south or up-down direction, at a sampling rate of 1 Hz. In total, we obtain observations $d^{\text{obs}} \in \mathbb{R}^q$, where $q = 3 \times 10 \times n_t$, and n_t is the number of discrete points in the time series of each displacement component.

We aim to approximate the posterior distribution $\pi(\theta|d^{\text{obs}})$. We employ a uniform prior for all parameters, with the componentwise bounds defining a feasible rectangle Ω_{prior} within the parameter space. Furthermore, we assume that our data corresponds to the output of our forward model $G(\theta)$, perturbed by zero-centered Gaussian noise:

$$d^{\text{obs}} = G(\theta) + \eta, \quad \eta \sim \mathcal{N}(0, C), \; C = \sigma_d^2 I, \tag{5.14}$$

where σ_d^2 is a scalar constant and $I \in \mathbb{R}^{q\times q}$ denotes the identity matrix. In total, we define the Bayesian posterior

$$\pi(\theta|d^{\text{obs}}) = \begin{cases} \frac{1}{Z} \exp\Big(-\frac{1}{2} ||d^{\text{obs}} - G(\theta)||^2_{C^{-1}} \Big), & \text{if } \theta \in \Omega_{\text{prior}}, \\ 0, \quad \text{else}, \end{cases} \tag{5.15}$$

where we have used the matrix-weighted norm $||\cdot||^2_{C^{-1}} = \langle \cdot, C^{-1} \cdot \rangle$. The normalization constant Z only depends on the data and the chosen prior intervals.

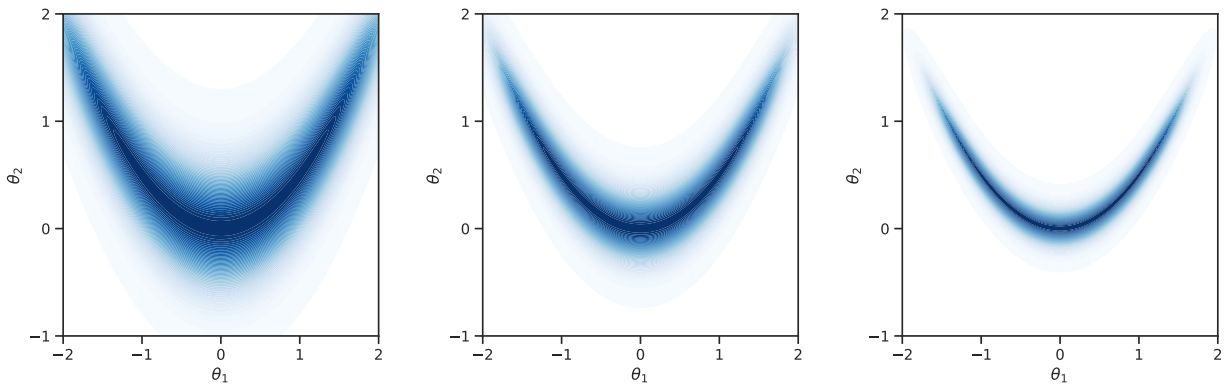

Figure 5.5: Hierarchy of "banana"-shaped posterior densities.

5.5 Results

5.5.1 Artificial Test Case

We first present results for prefetching MLDA based on an artificial hierarchy of 2D posterior densities. We define "banana"-shaped densities, which can be obtained from a simple transformation of a Gaussian density (Kaipio and Somersalo, 2005). Based on a precision coefficient c_i, we write for the parameters $\theta_1, \theta_2 \in \mathbb{R}$ of the i-th member of the density hierarchy

$$\pi_i(\theta_1, \theta_2) \propto \exp\Big[-\tfrac{1}{2} c_i \big(20(\theta_1^2 - 2\theta_2)^2 + 2(\theta_2 - \tfrac{1}{4})^4\big)^2 \Big]. \tag{5.16}$$

We construct a hierarchy of models with precision parameters $c_i = \{0.1, 0.3, 1.0\}$, which is depicted in Fig. 5.5. Since evaluation of these densities is practically instantaneous, we introduce artificial sleep times $t_i = \{0.001s, 3s, 10s\}$ to emulate the workload of more realistic posterior evaluations. The compute time on the coarsest level is still negligible, mimicking a fast surrogate model.

Before evaluating the parallel efficiency of the prefetching algorithm, we demonstrate the potential usefulness of MLDA compared to vanilla MH MCMC (Metropolis et al., 1953), based on our test hierarchy. To this end, we directly draw samples from the fine-level distribution with the MH-MCMC algorithm. We further generate an equal number of samples with the MLDA algorithm, using 30 samples for level one subchains and three samples for level two.

Verifying that our MLDA implementation delivers the expected statistical efficiency, we compare the ACFs and ESSs of the two obtained sample sets (Fig. 5.6). For the MH-MCMC algorithm, samples are highly correlated, initially up to a lag of $\sim$ 40 samples. The autocorrelation is reduced by a factor of more than 10 for the samples obtained with MLDA. Similarly, we observe that the ESS is about a factor 10 higher for the MLDA samples. When implemented efficiently, this means that the utilization of a hierarchy of models can significantly reduce burn-in times and increase the number of effective samples for statistical estimation.

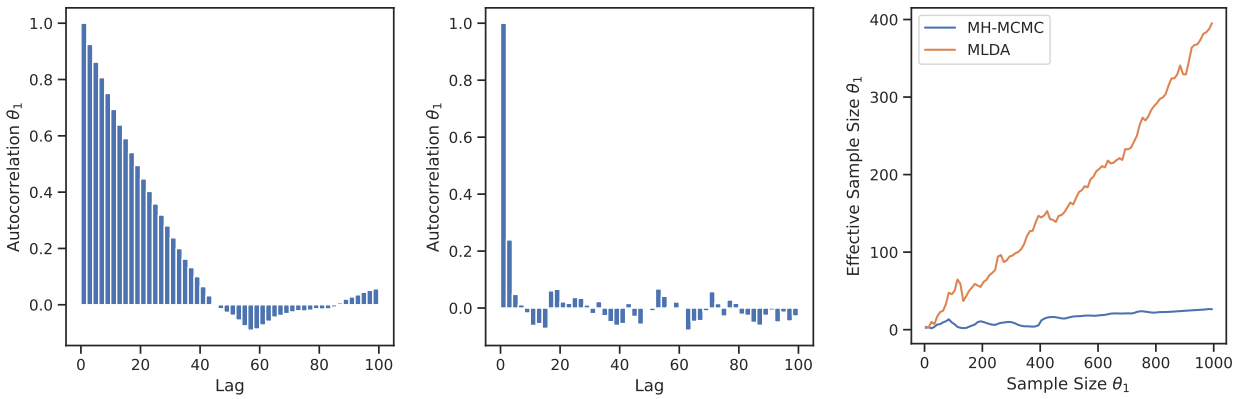

Figure 5.6: ACFs for MH-MCMC (left) and MLDA samples (center). ESS comparison for both algorithms (right).

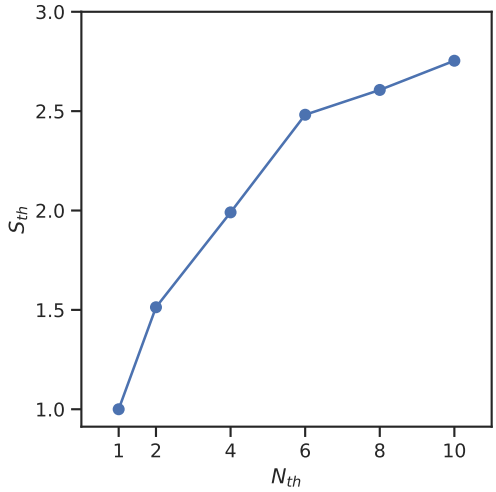

Figure 5.7: Runtime speed-ups for prefetching-based parallelization of MLDA with the banana posterior hierarchy.

Parallel speedup Moving on, we discuss results regarding the core contribution of this work, parallelization through prefetching. We conduct MLDA runs as described above, with parallelization trough prefetching for a varying number of up to 10 parallel threads. To assess parallel efficiency, we inspect the overall speed-up in run times, which is simply given as the ratio of the execution time without pre-fetching, t_1, and that for N_{th} parallel threads, $t_{N_{\text{th}}}$,

$$S_{\text{th}}(N_{\text{th}}) = t_1/t_{N_{\text{th}}}. \tag{5.17}$$

Fig. 5.7 summarizes the speed-up results. In the artificial problem, parallelization through prefetching yields an overall speed-up of about 2.5–3 in the tested range of threads. However, the speed-up reaches a plateau rather quickly, so that we anticipate a single-digit number of threads to be sensible in many cases.

Lastly, we point out that the current implementation of parallelized MLDA leaves some room for improvement. Specifically, ongoing simulation runs are not aborted when they become obsolete through an MCMC decision. Moreover, we employ a rather simplistic acceptance predictor for future states, which does not take into account the random draws

for the realization of the actual Markov Chain.

Optimal parallelization strategy To assess the usefulness of prefetching, we need to compare it to the obvious competing parallelization approach for MCMC, namely running parallel chains. Generating parallel chains is an embarrassingly parallel task, but also exhibits diminishing returns: Burn-in has to be performed for every single chain, implying that an increasing amount of samples has to be discarded when more parallel chains are run. To formalize this, suppose we intend to generate M_{eff} usable samples of a posterior distribution (not to be confused with the ESS presented above). From the total number of samples generated, we have to deduct M_{burn} burn-in samples for every chain. Let $\nu = \frac{M_{\text{eff}}}{M_{\text{burn}}}$ further be the ratio of effective samples to burn-in samples. Given such a fixed ratio ν, the speed-up through N_{ch} parallel chains is

$$S_{\text{ch}}(N_{\text{ch}}) = \frac{N_{\text{ch}}}{1 + \frac{N_{\text{ch}}-1}{\nu+1}}. \tag{5.18}$$

Given the sampling procedure from the banana hierarchy, we choose for our assessment $M_{\text{burn}} = 7$ and $M_{\text{eff}} = \{50, 100, 200, 400\}$. The resulting speed-ups for up to 32 parallel chains are presented in Fig. 5.8 (left). Clearly, parallelization performance deteriorates when burn-in becomes significant compared to the overall number of samples that are computed per chain. This is also apparent from Eq. (5.18). For $\nu \gg N_{\text{ch}}$, we can expect (nearly) perfect speed-up. As we approach $\nu \sim \mathcal{O}(1)$, however, we can observe that also $S_{\text{ch}} \sim \mathcal{O}(1)$, regardless of the number of chains employed.

For the case $M_{\text{eff}} = 50$, we compare the performance gain of parallel chains with that of prefetching. Specifically, we study the relative increase in speed-up $R_S = \Delta S/\Delta N$ for an increase in computational resources ΔN, which is either the number of parallel chains or the number of threads for prefetching. Note that these two quantities are comparable, as they both denote multiples of the computational resources required for a posterior evaluation. The corresponding results are depicted in Fig. 5.8 (right). While speed-up rates for parallel chains are generally higher than those for prefetching, both exhibit diminishing returns. As a result, we have to find an optimal, problem-dependent balance between the two.

To quantify the interplay between N_{ch} and N_{th}, we consider the problem of optimal resource allocation for our artificial problem, under constraints that resemble realistic scenarios. Assume that our posterior evaluation requires one generic unit of computational resources. This might correspond to use-cases where posterior evaluations are obtained from software that is not parallelized or whose parallelization does not scale well. We further consider the scenario that these evaluations are expensive, e.g. for large simulations of physical systems. Thus, we anticipate to obtain only relatively small numbers of samples, and again choose $M_{\text{eff}} = \{50, 100, 200, 400\}$. Further suppose that these samples have to be obtained under severe time constraints, while a large number of resources N_{tot} is available. This might indeed be a typical case for rapid prototyping and risk assessment in R&D projects. For our exposition, we choose $N_{\text{tot}} = \{16, 32, 64, 128\}$. Under these constraints, we intend to find the optimal combination of resources that minimizes evaluation time for the desired sample numbers. Formally, we compute

$$N^*_{\text{ch}}, N^*_{\text{th}} = \underset{N_{\text{ch}}, N_{\text{th}} \in \mathbb{N}_+}{\operatorname{argmax}} \; S_{\text{ch}}(N_{\text{ch}}) S_{\text{th}}(N_{\text{th}}), \quad \text{and } N_{\text{ch}} N_{\text{th}} = N_{\text{tot}}. \tag{5.19}$$

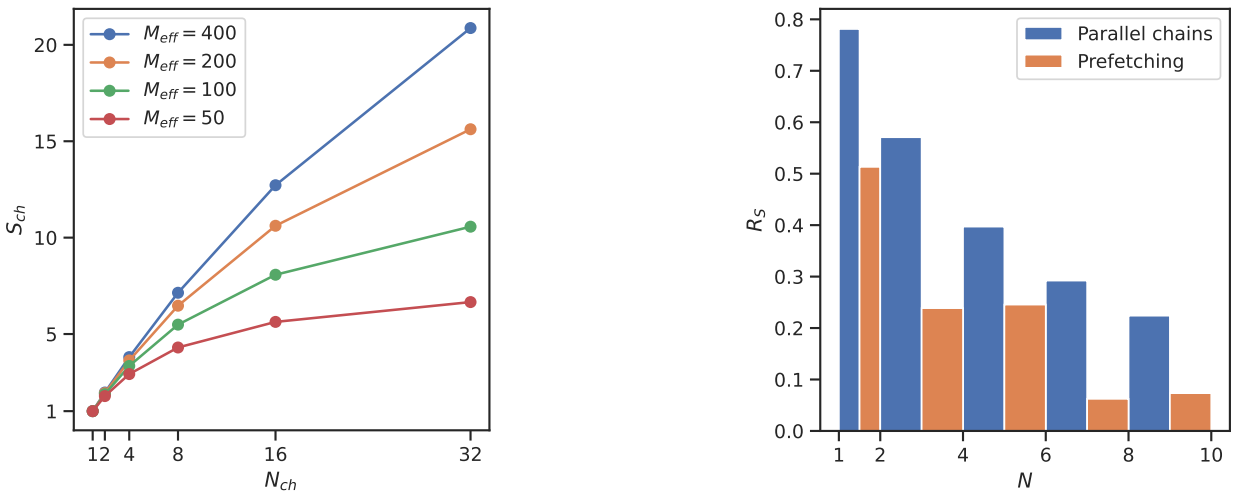

Figure 5.8: Left: Speed-up through employment of parallel chains, for different values of M_{eff} and $M_{\text{burn}} = 7$. Right: Speedup-rates of parallel chains vs. prefetching, for $M_{\text{eff}} = 50$.

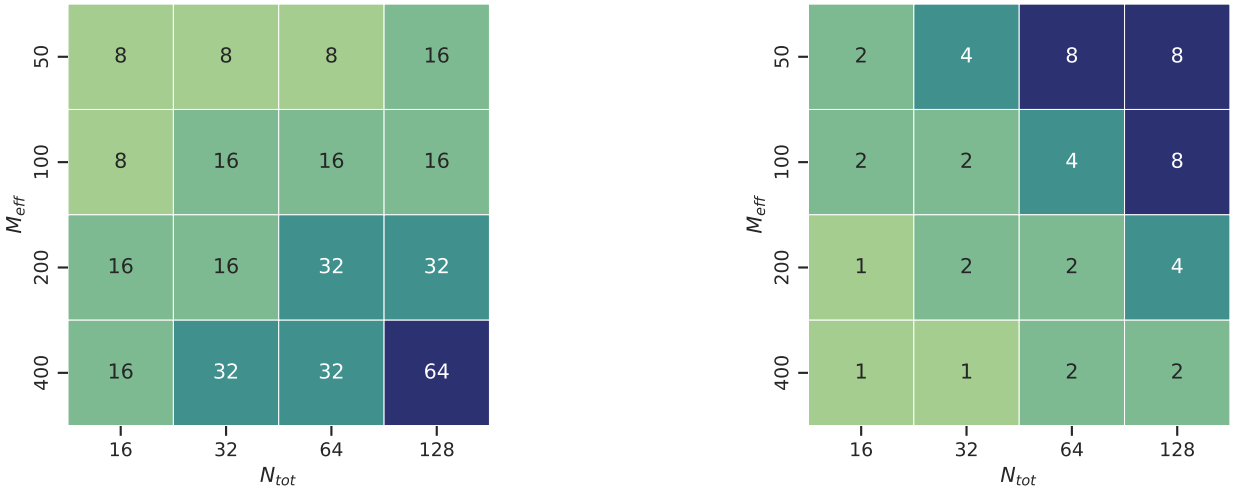

Figure 5.9: Optimal distribution of resources for different combinations of M_{eff} and N_{tot}. Left: Optimal number of parallel chains. Right: Optimal number of threads for prefetching.

This is a simple combinatorial optimization problem, whose results are depicted in Fig. 5.9 for the chosen combinations of M_{eff} and N_{tot}.

The illustrations confirm our qualitative assessment on the interplay of N_{ch} and N_{th}. For relatively large sample numbers M_{eff}, parallel chains are more efficient, although prefetching with a low number of threads might still yield some performance gain. On the other hand, prefetching is particularly effective for low M_{eff}, when burn-in becomes significant more quickly. In this case, up to eight threads can be employed.

To conclude our discussion, we comment on the projected speed-ups $S_{\text{tot}} = S_{\text{ch}} S_{\text{th}}$ for different combinations of resource distribution. Even if prefetching appears to be a favorable choice according to the solution of the above optimization problem, the simpler approach of parallel chains might still be a better option if performance gains are only marginal. Therefore, we evaluate S_{tot} for the case $M_{\text{eff}} = 50$ and varying N_{tot}, for all possible resource combinations $N_{\text{ch}}, N_{\text{th}}$. These speedups are visualized in the bubble plot 5.10.

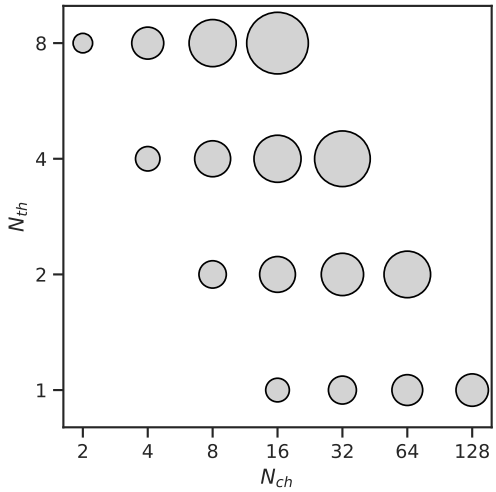

Figure 5.10: Projected Speed-up for different combinations of N_{ch} and N_{th}, for+ $M_{\text{eff}} = 50$. Sizes of the bubbles indicate the speed-up value.

The results indicate that, for given M_{eff}, performance gain through prefetching is highly dependent on the total amount of available resources M_{tot}. If only few resources are available, only few parallel chains can be spawned, whose parallel efficiency is favorable compared to prefetching. In addition, we note that the projected speed-up in this scenario is relatively independent of the chosen resource combination. This is quite different for large N_{tot}. We observe that for $N_{\text{tot}} = 128$, prefetching with up to eight threads is clearly preferable to assigning all resources to parallel chains. Indeed, the potential performance gain through prefetching is almost 100%.

We conclude that prefetching is a viable approach for strong-scaling scenarios, i.e. when high computational resources are employed to compute a limited number of samples in a short time.

5.5.2 Large-Scale Seismology Application

As a real-world use-case, we apply our parallelized MLDA algorithm to the Bayesian inverse problem described in Section 5.4.2. The approach employs a hierarchy of three models with increasing complexity. At the coarsest level, we utilize a surrogate model based on GP regression, trained with data (both pretraining and online) obtained from the next higher level in the model hierarchy. This second, as well as the third and finest level, use full SeisSol simulations on computational meshes with ≈4 million tetrahedral elements. The polynomial order of the basis functions is set to three on the second level, and four on the third level, resulting in roughly double the runtime for the latter. The results of the second level differ by less than 5% difference from those of the third level in most cases. However, the additional accuracy gained by using higher polynomial order is crucial to resolve the coupling between the foreshock and the mainshock in the 2019 Ridgecrest earthquake sequences (Taufiqurrahman et al., 2023). Subchain lengths are set to 30 and two for level one and two, respectively. All following results have been obtained using the Frontera supercomputer (Stanzione et al., 2020). The machine employs Intel Xeon

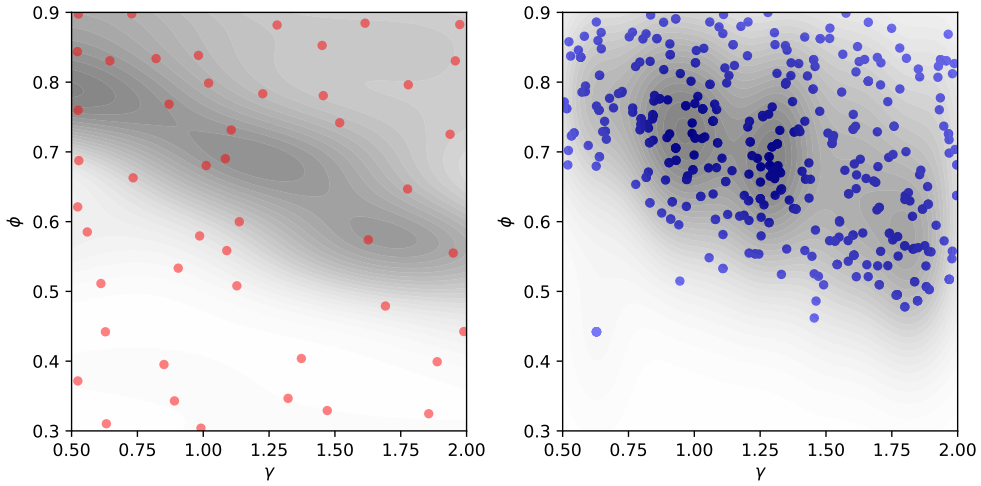

Figure 5.11: Left: Surrogate model estimated probability density of the plastic cohesion γ and the internal friction angle ϕ. Red dots represent training points; Right: Accepted samples and density estimates from the finest MLDA hierarchy level.

Platinum 8280 ("Cascade Lake") processors, each offering 56 cores per node and operating at 2.7 GHz. The total number of available compute nodes is 8368.

The results from the inversion procedure are depicted in Fig. 5.11 (bottom). These include 440 fine-level samples, obtained from two independent chains, together with the density estimate for the two-dimensional posterior. Our main finding is that the plastic cohesion coefficient γ has a near-uniform probability distribution in its parameter space, while the friction coefficient ϕ shows a clear tendency towards higher values. We also observe a slight negative correlation between the two parameters. The GP surrogate posterior density approximation (Fig. 5.11, top) is in good agreement with the fine-level samples, indicating that the surrogate and coarser SeisSol simulations provide a reasonable approximation of the posterior.

We then assess the posterior predictive performance of the inferred parameter set by running fine-level forward simulations for all MCMC samples. We compare the resulting displacement in the east-west direction to the observational data at three GNSS stations, as shown in Fig. 5.12. We observe that the posterior predictive ensemble reproduces the data reasonably well at the first two GNSS stations, with the prediction intervals encompassing the observations. However, the third station (P594) shows a slight discrepancy between the predictive ensemble and the data. We attribute this offset to the simplistic parametrization in our inverse problem, which cannot fully capture all complexities in the high-dimensional data. Nevertheless, the inferred parametrization provides reasonable predictions, including confidence intervals, for the Ridgecrest model.

After discussing the inference results, we now evaluate the performance of our MLDA sampler in context of the geophysics application. As for the artificial setup, we present the ESS and ACF functions of the obtained samples in Fig. 5.13. The results indicate that employing the MLDA algorithm yields similar improvement as for our previous experiment. The ESS reaches about 50% of the total sample size, and burn-in can be estimated as < 10 samples. This again represents an improvement by an order of magnitude compared to

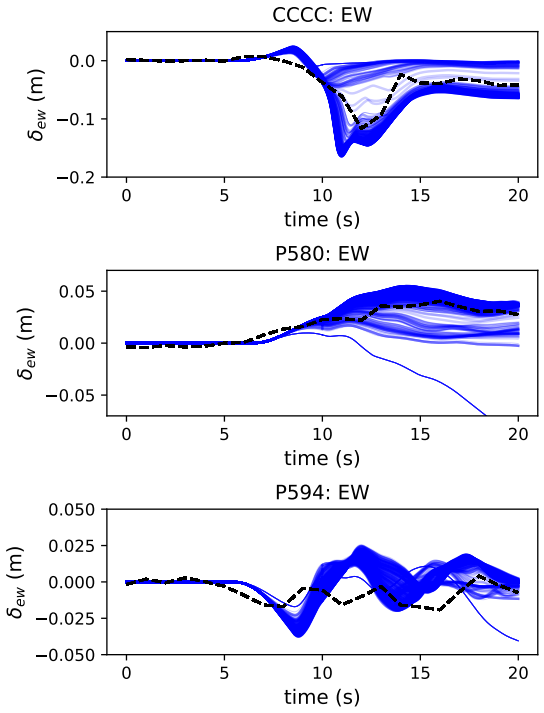

Figure 5.12: Comparison between simulations (blue solid curves) and the observed displacement data δ in the east-west (EW) direction (black dashed curves) from three (CCCC, P580, P594) of the ten GNSS stations.

what can be expected from standard MH-MCMC.

Optimal parallelization strategy Lastly, we assess prefetching for the inversion, compared to other means of parallelization. The procedure is analogous to the analysis of the artificial model hierarchy in Section 5.5.1. We introduce, however, an additional degree of freedom, namely the speed-up $S_{\text{sim}}(N_{\text{sim}})$ of single model evaluations when parallelized on N_{sim} processing units:

$$S_{\text{sim}}(N_{\text{sim}}) = t_1/t_{N_{\text{sim}}}. \tag{5.20}$$

In this concrete setting, processing units correspond to compute nodes. Importantly, S_{sim} is a gross quantity incorporating runtime speed-ups across all levels, weighted by the number of evaluations on each level. Thus, it is specific to the MLDA run configuration. It further implies that we utilize the same number of nodes for the parallelization on levels two and three (surrogate model evaluations are run in serial). The speed-ups for the conducted MLDA run, along with the speed-ups for parallel chains and prefetching threads, are depicted in Fig. 5.14.

We can now formulate an optimization problem for the allocation of computational resources, similar to equation (5.19),

$$\begin{aligned} N^*_{\text{sim}}, N^*_{\text{ch}}, N^*_{\text{th}} = \underset{N_{\text{sim}},N_{\text{ch}},N_{\text{th}}\in\mathbb{N}_+}{\text{argmax}} & S_{\text{sim}}(N_{\text{sim}})S_{\text{ch}}(N_{\text{ch}})S_{\text{th}}(N_{\text{th}}), \\ \text{and } & N_{\text{sim}}N_{\text{ch}}N_{\text{th}} = N_{\text{tot}}. \end{aligned} \tag{5.21}$$

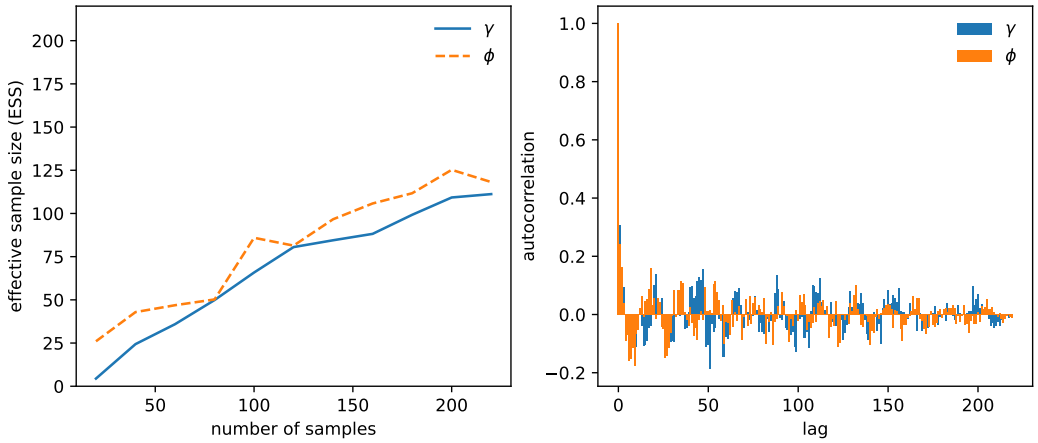

Figure 5.13: Left: Effective sample size over total number of samples in two MLDA chains; Right: Auto-correlation among the samples on the finest level.

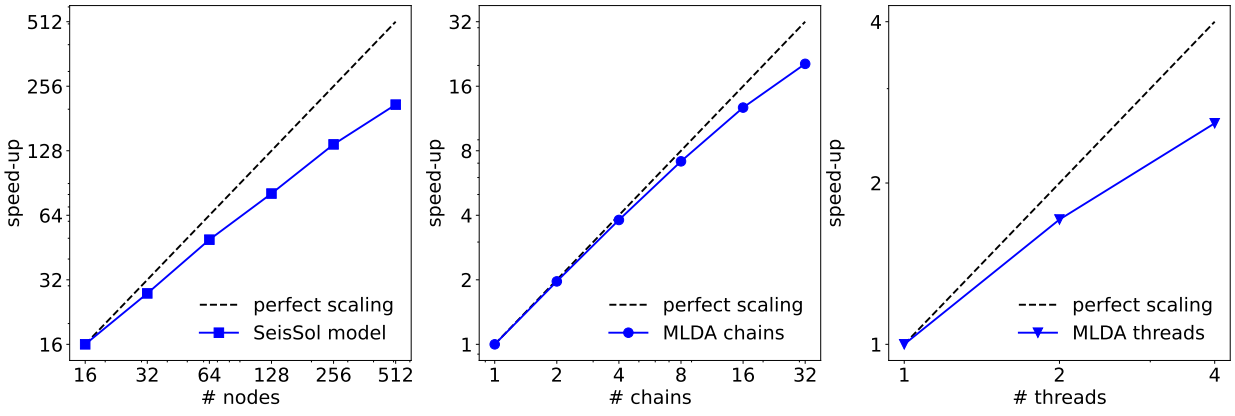

Figure 5.14: Strong scaling for the Ridgecrest model in SeisSol (left), increasing number of MLDA chains (middle), and increasing number of threads used within an MLDA chain (right).

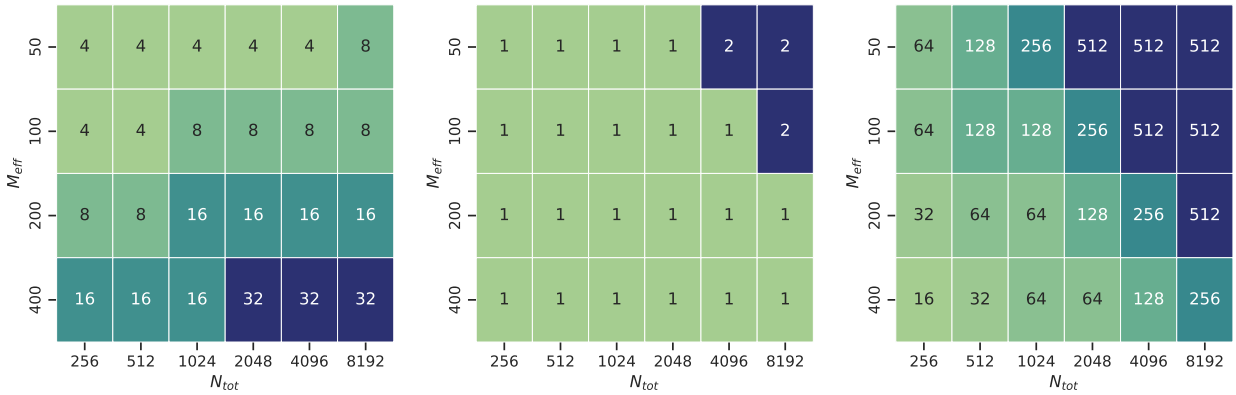

Figure 5.15: Optimal distribution of resources for different combinations of M_{eff} and N_{tot}. Left: Optimal number of parallel chains. Middle: Optimal number of threads for prefetching. Right: Optimal number of nodes for running a single SeisSol simulation.

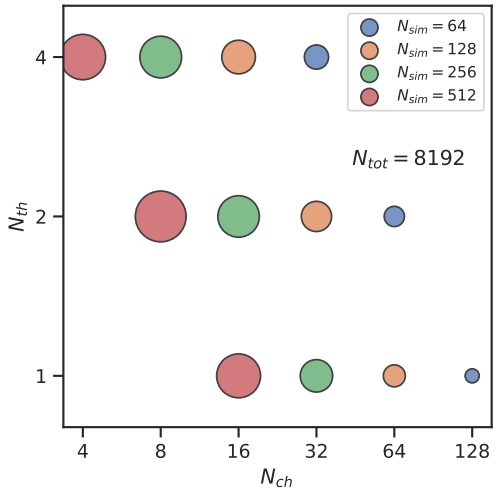

Figure 5.16: Projected Speed-up for different combinations of N_{ch}, N_{th} and N_{sim}, for $M_{\text{eff}} = 50$, and $N_{\text{tot}} = 8192$. Sizes of the bubble indicate the speed-up value, colors indicate different values of N_{sim}.

We investigate distribution of resources for $M_{\text{burn}} = 7$, $M_{\text{eff}} = \{50, 100, 200, 400\}$, and $N_{tot} = \{256, 512, 1024, 2048, 4096, 8192\}$. The maximum amount of available resources corresponds to almost the entire Frontera compute cluster. The results in Fig. 5.15 show that, in contrast to the artificial problem above, prefetching is not as advantageous here. Only for low sample numbers and high computational resources, activating prefetching is optimal. We attribute this to two aspects: (1) SeisSol already scales very well in the given resources, leaving little room for parallelization on the UQ side. (2) The GP surrogate proves extremely effective, leading to highly uncorrelated MLDA samples. This implies that only a very short burn-in phase is necessary, making parallel chains unusually favorable compared to prefetching. We conclude that, although the application has greatly benefited from MLDA and our computational pipeline, it is not an ideal use-case for prefetching.

This is also confirmed by our assessment of the projected speed-ups for $M_{\text{eff}} = 50$ and $N_{\text{tot}} = 8192$, visualized in Fig. 5.16. Although this is a scenario that favors prefetching (small sample size, large amount of resources), we again observe that heavy parallelization

of SeiSol is favored. Distribution of additional resources onto prefetching threads does not yield advantages over parallel chains. In this scenario, parallel chains should be employed, as their implementation is unarguably simpler.

5.6 Conclusion

In this work, we have presented a novel parallelization strategy for the MLDA algorithm via fully asynchronous prefetching. We have introduced the necessary theoretical foundations for prefetching in a multilevel setting. In addition, we have presented a modular computational pipeline that makes our workflow suitable for large-scale applications. We have further introduced the utilization of GP surrogates into the computational model hierarchy.

To assess the viability of the method, we have compared prefetching to the parallel simulation of multiple chains for an example problem. Our findings indicate that prefetching can be a valuable resource for scenarios where the strong scaling behavior of the sampling procedure is relevant. This is typically the case for expensive computational models, large computational resources, but limited time-to-result.

Beyond the example use-case, we have applied our parallelized prefetching algorithm to a large-scale problem in geoscience. Although the parametrization considered is quite simplistic, it demonstrates the viability for Bayesian inference involving large-scale simulations. We envision an extension of the inverse problem setup towards additional parameters, such as friction on the fault planes and off-fault inelastic deformation during seismic events.

While prefetching does not seem to yield significant performance improvements in this particular case, we anticipate it to be valuable in scenarios where the forward model is not as well parallelized as SeisSol. It therefore is a promising addition for the solution of statistical inverse problems in realistic scenarios. Our generic computational pipeline facilitates this transfer, allowing for incorporation of a wide range of computational models.

Chapter 6

Nonlinear inversion for 3D dynamic rupture simulation - Application

This study quantifies uncertainties and correlations among on-fault and off-fault nonlinear physical parameters through Bayesian inversion of the M_W 7.1 2019 Ridgecrest earthquake, constrained by multidisciplinary surface deformation data. We incorporate displacement time series from GNSS, static GPS vector data, and fault-parallel offsets from satellite imagery, employing a multilevel Bayesian inversion algorithm for efficient sampling. The dynamic rupture model adopts strong velocity-weakening rate-and-state friction and Drucker-Prager visco-elasto-plasticity for off-fault deformation. The results reveal a significant correlation between the on-fault rate-and-state friction parameter and the off-fault plasticity parameter, with greater inelastic off-fault deformation compensating for less velocity-weakening behavior. The solution of the probabilistic inverse problem indicates that the mean shallow slip deficit is ∼38.5%, with a standard deviation of ∼26.8%. Preferred models suppress overshooting at the fault's southeastern segment and suggest a gradual decrease in velocity-weakening frictional behavior along the fault. This work demonstrates the feasibility of integrating dynamic rupture simulations hosted in complex fault geometries with Bayesian inversion methods to effectively constrain the properties of earthquake sources.

6.1 Introduction

The M_W 7.1 Ridgecrest earthquake struck California on 5 July 2019 (Shelly, 2020). It is preceded by several foreshocks that are larger than M_W 5.0 (Ross et al., 2019; Taufiqurrahman et al., 2023). The Ridgecrest earthquake sequence is hosted by parts of the Eastern California Shear Zone (ECSZ, DuRoss et al., 2020; Barba-Sevilla et al., 2022), which contains multiple subparallel and conjugate fault structures. Many conjugate faults have not been previously mapped (Brandenberg et al., 2019; Thompson Jobe et al., 2020). Although the M_W 7.1 mainshock occurs in a complicated fault system, it is also recorded with interdisciplinary instruments, e.g. strong motion seismic stations (Hauksson et al., 2020), global navigation satellite system (GNSS) co-seismic displacements (Melgar et al., 2020; Floyd et al., 2020), and fault displacement discontinuities, hereafter referred to as offsets, from optical image correlation (OIC) using satellite images (Antoine et al., 2021).

The extensive and high-quality datasets have significantly enhanced the data-based interpretation of the Ridgecrest earthquake from various perspectives. One notable compilation of this work includes the kinematic inversion of the fault slip distribution using various

methods (Ross et al., 2019; Xu et al., 2020; Qiu et al., 2020b; Goldberg et al., 2020; Wang et al., 2020). After one of the first results of the inversion of the fault slip distribution from Ross et al. (2019), the most recent studies include different high-resolution data, e.g., borehole strain data (Hanagan et al., 2024). Some of the recent high-resolution kinematic fault slip inversion is based on the elastic Green's functions computed from 3D finite element modeling that account for complex fault geometries (Barba-Sevilla et al., 2022; Antoine et al., 2024).

From the kinematically inverted fault slip distribution, different amplitudes of shallow slip deficits (SSD) during the mainshock have been derived. According to Wang et al. (2014) and Milliner et al. (2020), SSD is accommodated either with postseismic and interseismic creep, or by off-fault diffusive deformation due to inelastic deformation. However, in most earthquakes, the former is not large enough to balance the SSD (Fialko et al., 2005; Brooks et al., 2017; Pousse-Beltran et al., 2020; Wang and Bürgmann, 2020).

It is convincing that off-fault inelastic deformation can qualitatively contribute to SSD. But the quantitative calculation of SSD due to off-fault plasticity with physics-based numerical models (dynamic rupture simulations) for the 2019 Ridgecrest earthquake sequences is captured only recently by Taufiqurrahman et al. (2023). Their dynamic rupture model, which moderately matches multidisciplinary data, includes visco-plasto-elastic rheology, heterogeneous 3D velocity model, curvilinear conjugate fault structures, and surface topography. However, the parameter space in dynamic rupture simulations has not been systematically explored. Specifically, the extent of uncertainty in the chosen physical parameters remains unexamined. As a result, the variability in the physically computed SSD and how well it compares to observations remain elusive.

The main challenge for parameter inference lies in computationally expensive dynamic rupture simulations (usually at least hundreds of CPU hours) with complex fault structures and inelastic rock rheology (Wollherr et al., 2018; Ulrich et al., 2019; Gabriel et al., 2023). A systematic exploration of the nonlinear parameter space for uncertainty analysis requires thousands to millions (Gallovič et al., 2019; Schliwa et al., 2024a) of simulations for Markov chain Monte Carlo (MCMC) sampling. With the simplification of the rupture model to planar faults and linear elastic rheology, Schliwa et al. (2024a) significantly compensated for the expensive simulation with GPU-accelerated modeling. Yet a simplified dynamic rupture model is not sufficient to capture the inelastic off-fault deformation for SSD.

Instead of reducing the cost of each simulation, we resort to reducing the number of required simulations, utilizing a multilevel MCMC (ML-MCMC) algorithm that more efficiently explores the parameter space (Giles, 2008; Dodwell et al., 2019). ML-MCMC relies on the assumption of independent samples from coarser levels, which are used as proposals for finer levels. However, in practice, this independence is only approximate, leading to bias. A recent advancement in ML-MCMC, the multilevel delayed acceptance (MLDA) algorithm (Lykkegaard et al., 2023), eliminates this assumption. In addition, further accelerated through prefetching-based parallelization (Christen and Fox, 2005; Angelino et al., 2014), MLDA achieves more than a 10-fold speed-up compared to the single-level MCMC method (Kruse et al., 2025). It also accelerates the sampling based on relatively small models, such as those with a few million elements, by up to four times on HPC architectures with thousands of CPUs (Kruse et al., 2025).

With the prefetching-based MLDA algorithm, we conduct Bayesian inversion of the nonlinear physical parameters in the dynamic rupture model of the M_W 7.1 mainshock in the 2019 Ridgecrest earthquake sequences. The dynamic rupture model accounts for complex fault structure and surface topography, and for nonlinear on-fault friction and off-fault inelastic deformation. We infer the underlying model from a joint dataset that includes real-time (Melgar et al., 2020) and static (Floyd et al., 2020) surface displacement from GNSS, as well as fault-parallel offset from OIC (Antoine et al., 2021). The inversion results shed light on the correlations among the nonlinear parameters. We also, for the first time, derive uncertainties in the fault slip distribution from physics-based dynamic rupture inversion, with a special focus on SSD, for the M_W 7.1 Ridgecrest earthquake.

6.2 Data and Methods

The objective of this work is to quantify the uncertainty and correlation among on-fault and off-fault nonlinear physical parameters that can be constrained by the available data. Surface displacement from GNSS stations and satellite images is widely available data to constrain the rupture process in kinematic source inversion. We use this section to present the near-field surface deformation data that we use. We then elucidate how we employ a parallelized version of the MLDA algorithm (Lykkegaard et al., 2023; Kruse et al., 2025) for efficient probabilistic inference.

6.2.1 Data on surface deformation

The first data set that we incorporate is the fault-parallel offset along the surface fault traces, which is sensitive to the shallow fault slip distribution (Qiu et al., 2020b). The WorldView and Pleiades satellites provide optical images at a ground resolution of 0.5 m. Data processing with image correlation is sensitive to displacement down to 0.05 m (Antoine et al., 2021). We define $\Delta u^{obs}(s)$ as the along-strike variation of the fault-parallel offset, where s is the along-strike distance with an origin defined at the epicenter, as shown with the dashed black axis in Fig. 6.1.

We integrate fault-parallel offsets with near-field surface displacements from GNSS to enrich our data set. Adequately processed recordings of antennas (GNSS stations) that move with the ground during earthquakes can be transformed into real-time point measurements of displacement time series at GNSS stations. We incorporate the processed displacement time series from Melgar et al. (2020) during the 2019 Ridgecrest earthquake, with a sampling rate of 1 Hz. These time series at 10 stations close to the activated fault system are particularly useful for describing the rupture history during the earthquake. For clarity in a later description, we define $u_i^{GT,obs}(t)$ as the recorded time series from a GNSS station. The index i here comprises to degrees of freedom, that is, the direction component j of a given station and the index k of the station itself. The component j includes the north-south (NS), east-west (EW), and upward-downward (UD) directions.

The near-field surface displacement time series are complemented by processed static dis-

placement vector data at 11 more GNSS stations from UNAVCO. The accuracy of the measurement is between 1.5 and 2.1 mm (Floyd et al., 2020). We define $u_i^{GS,obs}$ as the recorded co-seismic static displacement of a GNSS station. Again, the index i comprises two indices, that is, the component j of one station and the station index k. The component j includes the north-south (NS) and east-west (EW) directions.

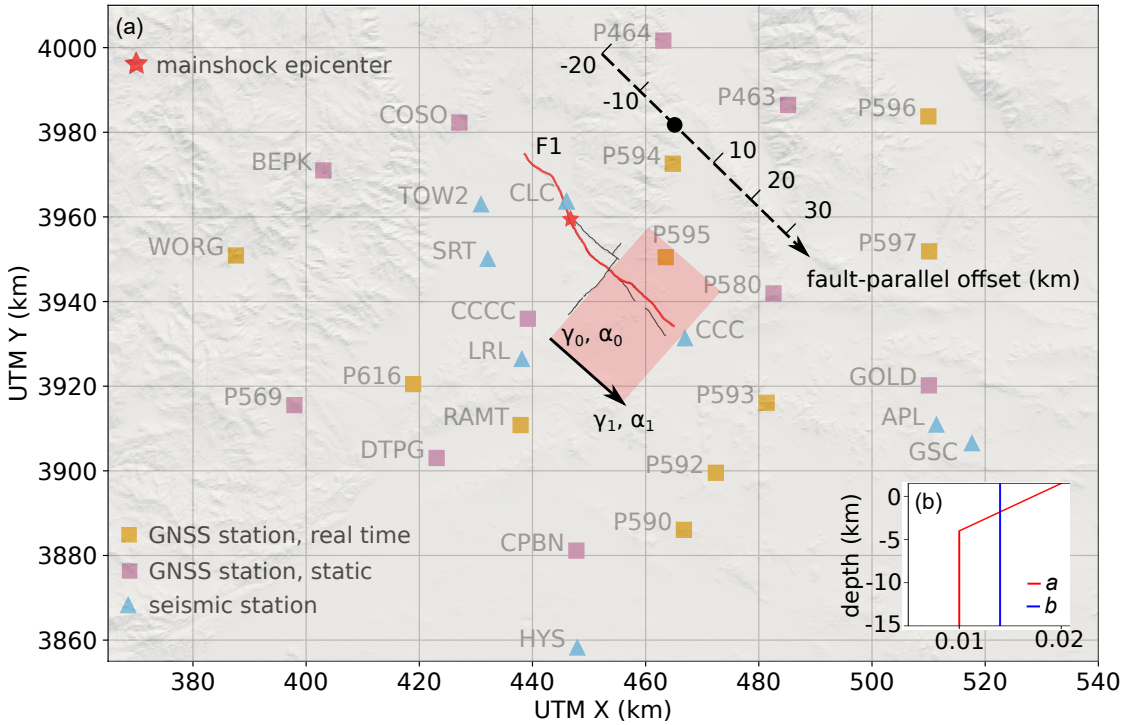

Figure 6.1: (a) Map view of the GNSS and seismic stations that we account for in this work. They are close to the epicenter (the red star) of the M_W 7.1 mainshock and to the fault structure (the solid black curves) that hosts the 2019 Ridgecrest sequence. We mark the fault trace (F1) ruptured by the M_W 7.1 mainshock with a solid red curve. The yellow rectangles denote stations where processed displacement time history are available from Antoine et al. (2021); the purple rectangles are stations where we only use their co-seismic static displacement from Floyd et al. (2020). The blue rectangles are locations of strong-motion seismic stations. We highlight the region where we assume spatial variation of plastic cohesion c and direct-effect parameter a in a red rectangle. Their scaling factor transit, respectively, from γ_0 and α_0 to γ_1 and α_1 along the black arrow. The parameters in the dynamic rupture model follows Taufiqurrahman et al. (2023) and are listed in Table 6.1. We show the coordinate system for the definition of fault-parallel offset with the dashed black axis. Panel (b) reiterates the reference values of the depth dependent direct-effect parameter a and the constant evolution-effect parameter b in Eq. (6.A.5).

Above all, we integrate displacement time series $u_i^{GT,obs}(t)$ from GNSS at 10 stations, fault-parallel offset $\Delta u^{obs}(s)$ from satellite images, and near-field static displacement vectors $u_i^{GS,obs}$ from 11 GNSS stations as data for inversion of nonlinear physical parameters in dynamic rupture simulations.

6.2.2 Model parameters in dynamic rupture modeling of earthquakes

In this section, we define the on-fault and off-fault nonlinear parameters that we attempt to infer with the data in Section 6.2.1. In dynamic rupture modeling of earthquakes, spontaneous rupturing of the fault zone materials is governed by the nonlinear friction law between bulk rock materials on two sides of 2D curved surfaces embedded in 3D space. The friction law that we use here is a strong velocity-weakening rate-and-state (SV-RS, Dunham et al., 2011) friction law, which captures the laboratory-observed significant reduction in co-seismic friction at high slip rates. We provide detailed formulations of the SV-RS friction law in Appendix 6.A.

According to the SV-RS friction, we end up with one friction parameter for this on-fault nonlinear physical process. We need to ensure the accuracy in the quantified uncertainties and correlations among the on-fault and off-fault parameters. But we are restricted by the computationally expensive large-scale dynamic rupture simulation. Therefore, we select a physically important parameter $a-b$ that controls the spontaneity of the dynamic rupture process (Dunham et al., 2011). $a-b$ is also important for reproducing shallow slip behavior in postseismic and interseismic periods (Kaneko and Fialko, 2011). In practice, we fix $b = 0.014$ and vary a to control the value of $a - b$. We adopt the same depth-dependent $a_0(z)$ by Taufiqurrahman et al. (2023) as the reference, where z is the depth axis that points vertically upward. We illustrate their reference model setup in Fig. 6.1b. In the inversion, we scale this reference model with a scaling factor α by defining a depth-varying $a(z)$ as

$$a(z) = \alpha a_0(z). \tag{6.1}$$

The off-fault nonlinear process originates from inelastic deformation of the off-fault materials under large dynamic loading. We adopt the Drucker-Prager visco-elasto-plasticity to model the off-fault inelastic deformation. It defines a yielding strength τ_c beyond which the inelastic deformation starts to accumulate with loading. The yielding strength τ_c of the rocks is defined via two material parameters, plastic cohesion c and bulk friction angle ϕ, as

$$\tau_c = c\cos(\phi) - \sigma_p \sin(\phi), \tag{6.2}$$

where $\sigma_p = \sigma_{kk}/3$ is the mean of the trace of the stress tensor σ_{ij}. The plastic parameters have a strong influence on the fault rupturing processes and near-field ground motions. The fault system is embedded in a geologically heterogeneous region. We define spatially varying rock elastic moduli and the stress field by combining a 3D community velocity model CVM-S4.26 Lee et al. (2014) and a 2D community stress model representing the regional stress state in the upper crust of Southern California Yang and Hauksson (2013). The plastic parameters c and ϕ can also vary in space. For demonstration purposes, we assume a plastic cohesion $c(x, y, z)$ that changes in space (Taufiqurrahman et al., 2023) and is proportional to the shear modulus $\mu(x, y, z)$ according to the 3D community velocity model. Based on that, we define the plastic cohesion in the simulation as

$$c = \gamma_0 \gamma \mu(x, y, z), \tag{6.3}$$

where γ is a scaling factor to be determined, and $\gamma_0 = 10^{-4}$ is the reference value adopted by Taufiqurrahman et al. (2023).

In the reference model from Taufiqurrahman et al. (2023), an overshooting is observed in the southeastern segment of fault F1 according to the surface displacement of GNSS stations and the fault-parallel offset data. To examine whether we can discriminate between on-fault and off-fault nonlinear processes that suppress the overshooting at the southeastern segment of the fault F1, we assume that the on-fault direct-effect parameter α and the off-fault plastic cohesion γ are potentially spatially variable along the fault strike direction, and that such variation can bring the total slip on the fault in dynamic rupture simulations closer to observations. We assume that such variation in a and γ from the northwestern to the southeastern segment of fault F1 in Fig. 6.1a is linear. Their values transit from α_0 to α_1 for the scaling factor of the direct-effect parameter a; while from γ_0 to γ_1 for the scaling factor of plastic cohesion c. We will discuss the validity of this assumption in Section 6.4.1.

6.2.3 Bayesian inversion of large-scale dynamic rupture simulations

To increase the efficiency of the Bayesian inversion, we take advantage of the MLDA algorithm (Dodwell et al., 2019; Lykkegaard et al., 2023), which exploits a hierarchy of models with varying levels of fidelity and allocates most of the computational effort to less accurate but fast approximate models. We start the description of the method from formularizing the Bayesian inverse problem where the algorithm is applied. The data used for constraining the inversion has three different formats. We use a dedicated Section 6.2.3 to describe how the different dataset are assimilated in the Bayesian inversion framework.

Observational data and misfit

As described in Section 6.2.2, we allow for spatial variation of plastic cohesion γ and direct-effect parameter α in the southern part of the fault structure. This brings a higher flexibility in the parameter space. As a result, the epistemic uncertainty in the southern part of the fault is also lower. To account for this effect, we separate the fault-parallel offsets from the satellite images $\Delta u^{obs}(s)$ into $\Delta u^{FN,obs}(s)$ for $s \leq 10$ km, and $\Delta u^{FS,obs}(s)$ elsewhere in the dashed black coordinate system in Fig. 6.1. From our dynamic rupture simulations, we can also derive the accumulated fault slip $\Delta u^{FN}(s)$ and $\Delta u^{FS}(s)$ at the ground surface. We define the L^2 norm of the differences between the data and simulation outputs as 2 independent dimensions, i.e. d^{FN} and d^{FS}, in Bayesian inversion as

$$d^k = \sqrt{\sum_{l=1}^{N_k} (\Delta u^k(s_l) - \Delta u^{k,obs}(s_l))^2}, \; k = FN \text{ or } FS, \tag{6.4}$$

where $N_{FN} = 158$ and $N_{FS} = 101$ are the numbers of discretized along-strike points s_l where the northern- and southern-segment fault-parallel offset values are measured. When

model outputs match the data exactly, the corresponding values for these two dimensions are $d^{FN} = 0$ and $d^{FS} = 0$, which means zero misfit.

Similarly, we can also compute time series for the 3 components of surface displacement vectors at 10 GNSS stations $u_i^{GT}(t)$. We then define the L^2 norm of the differences between the data and simulation outputs as $n_d^{GT} = 3 \times 10$ independent dimensions d_i^{GT} as

$$d_i^{GT} = \sqrt{\sum_{l=1}^{N_{GT}} (u_i^{GT}(t_l) - u_i^{GT,obs}(t_l))^2}, \; i = \; 1, \, 2, \, ..., \, n_d^{GT}, \tag{6.5}$$

where N_{GT} is the number of discretized time points t_l when the displacement vectors are measured. When the model outputs match the data exactly, the corresponding values for these 30 dimensions are $d_i^{GT} = 0$.

The 2 horizontal components of the static surface displacement vectors at 11 GNSS stations are $n_d^{GS} = 2 \times 11$ scalar values. We derive them from dynamic rupture simulations at 60 seconds after the nucleation of the mainshock, as u_j^{GS} and directly define 22 dimensions of output in the inversion d_j^{GS} as

$$d_j^{GS} = u_j^{GS}, \; j = \; 1, \, 2, \, ..., \, n_d^{GS}. \tag{6.6}$$

When the model outputs match the data exactly, the corresponding values are $d_j^{GS} = u_j^{GS,obs}$.

Bayesian problem formulation

The model parameters $\mathbf{m}$ and the experimental observations $\mathbf{d}^{obs}$ are viewed as random variables in $\mathbb{M} \subset \mathbb{R}^{n_m}$ and $\mathbb{D} \subset \mathbb{R}^{n_d}$, where n_m and n_d are the number of model parameters and the number of observed data points. According to Section 6.2.2, $n_m = 4$. Let $G : \mathbb{M} \to \mathbb{D}$ denote the model map taking a parameter set in a model prediction.

We then aim to find the posterior, that is, the conditional distribution of $\mathbf{m}$ for a given observation $\mathbf{d}^{obs}$. We denote the corresponding probability density function (PDF) by $\rho(\mathbf{m}|\mathbf{d}^{obs})$. To directly compute the underlying parameters from the observed data, we would have to apply the inverse of the model map G^{-1}. However, that inverse is not available for our models. Employing Bayes' theorem, we can reformulate the posterior in a way that, as will be detailed below, only involves the forward map G:

$$\rho(\mathbf{m}|\mathbf{d}^{obs}) = \frac{\rho(\mathbf{d}^{obs}|\mathbf{m})\rho(\mathbf{m})}{\rho(\mathbf{d}^{obs})} \propto \rho(\mathbf{d}^{obs}|\mathbf{m})\rho(\mathbf{m}). \tag{6.7}$$

We call $\rho(\mathbf{m})$ the prior density, $\rho(\mathbf{d}^{obs}|\mathbf{m})$ is the likelihood that describes the probability density to measure the observed data when $\mathbf{m}$ is given, and $\rho(\mathbf{d}^{obs}) > 0$ is the unconditional PDF of measuring the observed data, or evidence. Broadly speaking, the posterior consider takes higher values if a parameter is plausible from a-priori knowledge and its corresponding model prediction is close to the observed data.

In practice, $\rho(\mathbf{d}^{obs})$ is prohibitively expensive to evaluate. MCMC methods circumvent this issue, in that they only require evaluations of the un-normalized density.

The prior encodes expert knowledge about what parameters might be generally plausible, not considering our specific observation. Taking into account physical constraints, we define an upper and a lower bound for the prior range of each value, as $\mathbb{M} = \{\mathbf{m} \in \mathbb{R}^{n_m} | lb_i \leq m_i \leq ub_i, i = 1, 2, \ldots, n_m\}$. lb_i and ub_i are the assumed lower and upper bounds of each model parameter, as listed in Table 6.1. With the above two constraints and based on the maximum entropy principle of designing the prior (Good, 1963), the data is assumed to be uniformly distributed in $\mathbb{M}$.

Table 6.1: Summary of all model parameters considered in the dynamic rupture modeling, with α_0 and α_1 being the scaling factors of the direct-effect parameter a in Fig. 6.1b, L the characteristic slip distance, γ_0 and γ_1 the scaling factors for plastic cohesion, and ϕ the bulk friction angle. The on-fault friction parameters that do not vary in the inversion are V_0, f_0, V_W, f_W, V_init and b in Eq. (6.A.2) to Eq. (6.A.6).

	Param.	Values	Units	Param.	Values	Units
off-fault	γ_0	[0.1, 2.0]	1	γ_1	[0.1, 2.0]	1
	ϕ	0.7	arc			
on-fault	α_0	[0.4,1.4]	1	α_1	[0.4,1.4]	1
	L	0.2	m			
	b	0.014	1	V_{init}	1.0×10^{-16}	m/s
	f_0	0.6	1	V_0	1.0×10^{-6}	m/s
	f_W	0.1	1	V_W	1.0×10^{-1}	m/s

We assume a zero-centered, additive Gaussian noise model for the observed data. It follows that the likelihood $\rho(\mathbf{d}^{obs}|\mathbf{m})$ is given as

$$\rho(\mathbf{d}^{obs}|\mathbf{m}) \propto \exp\Big(-\frac{1}{2}(\mathbf{d}^{obs} - G(\mathbf{m}))^T \mathbf{C}^{-1} (\mathbf{d}^{obs} - G(\mathbf{m}))\Big). \tag{6.8}$$

The covariance matrix $\mathbf{C} \in \mathbb{R}^{n_d \times n_d}$ encapsulates the statistics of the noise, reflecting our understanding of measurement precision and the epistemic uncertainties inherent in model assumptions. Given the modest dimensionality of our model space $\dim(\mathbb{M}) = 4$, we assume that the components of the covariance matrix exceed their respective measurement accuracies for the fault-parallel offset and the processed displacement data from the GNSS stations.

As described in Section 6.2.2, we allow for a larger variation in the model space of the southeastern segment of fault F1. We assume that this can reduce epistemic uncertainty in the southeastern segment of fault F1. Consequently, we distinguish between the standard deviations for point-wise measurements of the fault-parallel offset, assigning $\sigma^{FS} = 1.2$ m to the southeastern segment and $\sigma^{FN} = 1.7$ m to the northwestern segment, to reflect the differentiated uncertainties between the segments. We set the standard deviation σ_i^{GT} of the processed GNSS time series (GT) based on their comparison with the reference model. For point measurement at each time point, we set σ_i^{GT} between 5 and 15 cm, depending on how well the reference model matches the observations. We set σ_j^{GS} for each component of the horizontal static displacement of GNSS stations at 6 mm, which is around 3 $\times$ the

precision of the data (Floyd et al., 2020). We additionally assume that all observations are statistically independent and set $\mathbf{C} = \mathrm{diag}(\sigma^{FN,2}, \sigma^{FS,2}, \sigma_i^{GT,2}, \sigma_j^{GS,2})$, where $i = 1, \ldots, n_d^{GT}$ and $j = 1, \ldots, n_d^{GS}$.

From Eq. (6.7) and Eq. (6.8), it is clear that the posterior density $\rho(\mathbf{m}|\mathbf{d}^{obs})$ can be computed point-wise up to an unknown constant factor. Then every sample requires an evaluation of the model map $G(\mathbf{m})$, i.e., one dynamic rupture simulation. Since each simulation can be computationally expensive, we employ the following MLDA algorithm to make sure the sampled simulation can represent the posterior as effectively as possible.

6.2.4 MLDA accelerated with prefetching

MCMC is a crucial algorithm for sampling the posterior probability distribution in Bayesian inversion. But a major drawback of MCMC methods is that they typically require a large number of evaluations of the target density π to achieve a sufficient number of effectively uncorrelated samples. To reduce the number of costly evaluations, we employ the MLDA algorithm proposed by Lykkegaard et al. (2023), which is further accelerated with the prefetching technique (Kruse et al., 2025). The basic idea of MLDA is to employ a hierarchy of models with different accuracy-cost trade-offs. We denote this hierarchy as levels $l = 1, 2, \ldots, L$ with the corresponding target densities π_l. We assume that densities at low levels are inexpensive to compute, while those at higher levels converge to $\pi_L \approx \pi$. MLDA generates high-quality proposals at level l by spawning a sub-chain on a lower level $l-1$ for the current state. The final state of that sub-chain is then used as a proposal for the level l. Applying this recursively across levels results in an increasingly faster rate of decorrelation for samples on finer levels. Through a careful choice of the model hierarchy (see Lykkegaard et al. (2023) for details on convergence rates), MLDA can achieve a significant reduction in the total cost for sampling π.

In practice, we employ a three-level ($L = 3$) implementation of the MLDA algorithm. We use a Gaussian process regression (GPR, Schulz et al., 2018) surrogate model at the coarsest level ($l = 1$). We train the surrogate model with data from the model on $l = 2$, so that it can provide estimates for the likelihood in Eq. (6.8) with a given set of model parameters $\mathbf{m}$. The surrogate model acts as a guide for the sampling process, proposing mostly decorrelated samples at the finer levels ($l = 2, 3$). Both models at levels $l = 2$ and $l = 3$ use full SeisSol simulations on computational meshes with approximately 4 million tetrahedral elements. The polynomial degree of the basis functions in SeisSol is set to two on level $l = 2$ and three on level $l = 3$, resulting in roughly double the runtime for the latter. Between each sample on level $l = 3$, we explore 2 samples from level $l = 2$, between which we obtain another 40 samples from level $l = 1$. This can decrease autocorrelation between the samples up to 90% at the finest level ($l = 3$), allowing for posterior estimation with a drastically reduced number of samples (Kruse et al., 2025).

6.3 Results

In this section, we present the results of the Bayesian inference for the parameters of interest, namely the off-fault plastic cohesion (γ_0, γ_1) and the on-fault direct-effect parameter in SV-RS friction (α_0, α_1). All simulations have been run on the Frontera supercomputer (Stanzione et al., 2020). The machine employs Intel Xeon Platinum 8280 ("Cascade Lake") processors, each offering 56 cores per node and operating at 2.7 GHz. The total number of available compute nodes is 8368. We have utilized approximately half of the machine (4097 nodes) for 12 hours. Following a previous benchmark (Kruse et al., 2025), we optimize the configuration of the MLDA level hierarchy to maximize the number of effecitve samples. With 32 MLDA chains, 2 prefetching threads, and SeisSol parallelization on 64 nodes, we have obtained 640 samples in total on the finest level.

6.3.1 Posterior distribution of on- and off-fault parameters

To more effectively estimate the Bayesian posterior in Eq. (6.7), we exclude samples that belong to the "burn-in" phase (Kruse et al., 2025). Statistically, only the samples that are accepted after the "burn-in" phase can represent the posterior probabilistic distribution $\rho(\mathbf{m}|\mathbf{d}^{obs})$ of the parameter space.

Excluding burn-in samples, we show the 1D and 2D marginal distributions of off-fault plastic cohesion (γ_0, γ_1) and the on-fault direct-effect parameter in SV-RS friction (α_0, α_1) on the upper diagonal of Fig. 6.2. The highest probability in the 1D marginal distribution of γ_0 and γ_1 is, respectively, around 0.9 and 0.5. According to Eq. (6.3), they correspond to 9.0 $\times 10^{-5}\mu(x, y, z)$ for the background off-fault plastic cohesion and 5.0 $\times 10^{-5}\mu(x, y, z)$ for the plastic cohesion around the southeast of the faults in Fig. 6.1. For the on-fault direct-effect parameter, the highest probability in the 1D marginal distribution of α_0 and α_1 is around 1.2 and 1.0. This corresponds to a linear transition from $a - b = -0.002$ in the northwest part of fault F1 to $a - b = -0.004$ in the southeast part of fault F1. We will discuss the spatial variation of the plastic cohesion and the direct-effect parameter in Section 6.2.1. Among the 2D marginal distribution of different pairs of parameters, we find a clear positive correlation between γ_0 and α_0. Physically, this means the effect of smaller off-fault inelastic deformation (larger α_0) can be at least partially compensated by less velocity-weakening on-fault friction (larger γ_0).

For comparison, we also show the pre-trained surrogate model at level $l = 1$ of the MLDA model hierarchy on the lower diagonal of Fig. 6.2. We find that the pre-trained model captures most features in the Bayesian posterior in terms of the parameter range with high probability, as well as the correlation between γ_0 and α_0. It misses a high-probability region marked with the blue rectangle in Fig. 6.2b. But it also demonstrates that the MLDA algorithm can still retrieve proper Bayesian posterior when models at a lower level contain inaccurate information.

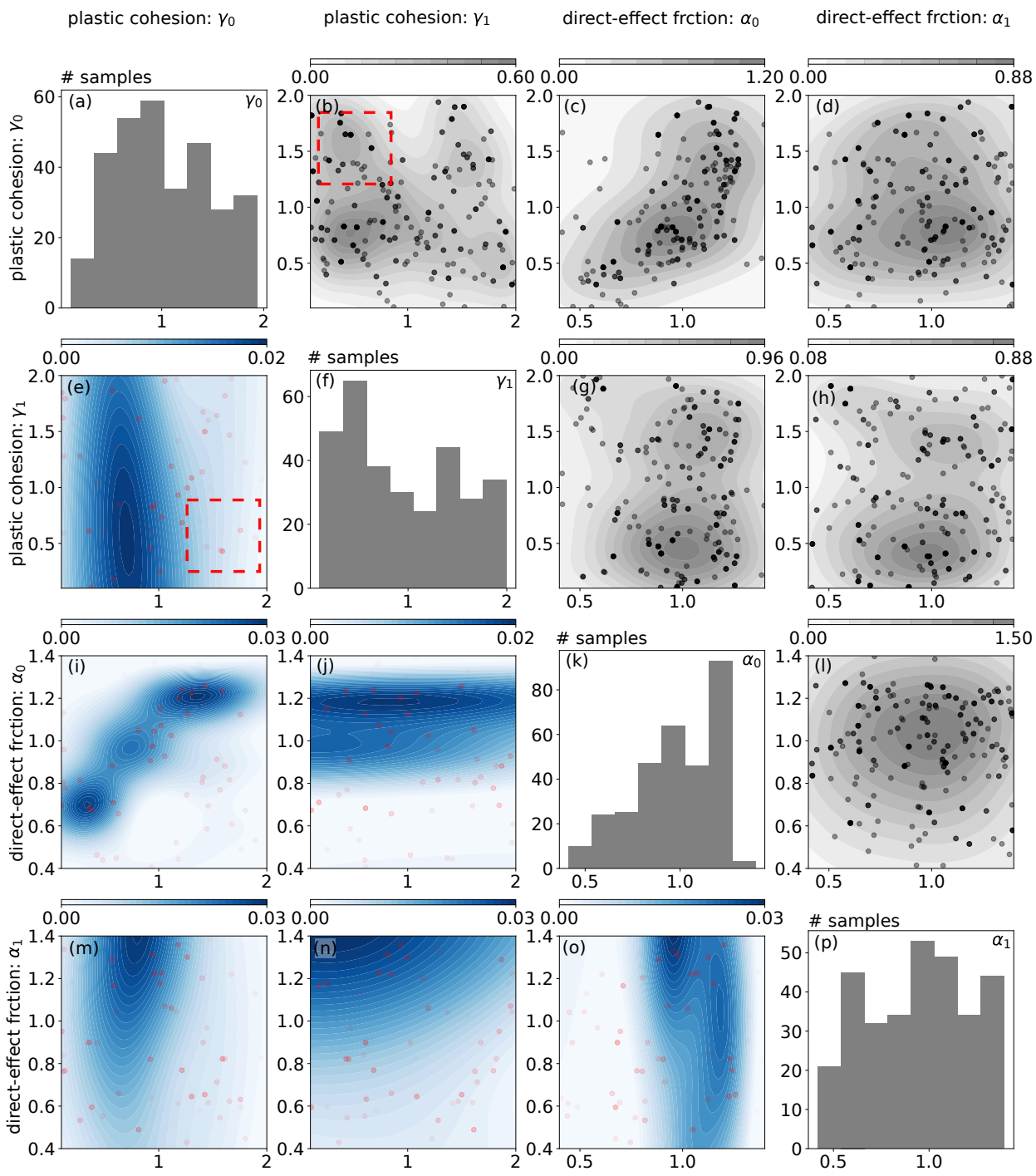

Figure 6.2: Panels of the Bayesian likelihood $\rho(\mathbf{d}^{obs}|\mathbf{m})$ from the pretrained surrogate model and Bayesian posterior $\rho(\mathbf{m}|\mathbf{d}^{obs})$ from MLDA inversion. The panels on the diagonal from top to bottom are 1D marginal posterior probabilistic distribution of off-fault plastic cohesion (γ_0, γ_1) and on-fault direct-effect parameter in SV-RS friction (α_0, α_1). The panels on the upper triangle are the 2D marginal Bayesian posterior of each parameter pair from MLDA inversion. The black dots are all the accepted samples excluding the burn-in phase. The density of the dots is color-coded in gray, which is proportional to $\rho(\mathbf{m}|\mathbf{d}^{obs})$. The panels on the lower diagonal are the 2D marginal Bayesian likelihood, color-coded in blue. The red dots are the 52 samples used for pretraining the surrogate model. The more transparent dots correspond to lower $\rho(\mathbf{d}^{obs}|\mathbf{m})$.

6.3.2 Models with high posterior probability

After an overview of the complete ensemble of sample parameters, here we focus on the subset of samples with relatively high posterior probability. In Figs. 6.3a and 6.3b, we show samples with a posterior probability density $\rho(\mathbf{m}|\mathbf{d}^{obs})$ greater than 0.25 ρ_{max} (blue and red dots) and 0.5 ρ_{max} (yellow rectangles), where ρ_{max} is the maximum $\rho(\mathbf{m}|\mathbf{d}^{obs})$ among all the accepted samples in MLDA. We can still observe the positive correlation between γ_0 and α_0. We plot the corresponding model output of the fault-parallel offset along the surface fault trace (blue and red curves), together with the data (the dashed black curve) from Antoine et al. (2021). We find a subset of models where the fault slips do not reach the surface in the south-eastern part of the fault (between 12 km and 30 km). Provided their relatively good match with the data at the north-western part of the fault (between -10 km and 10 km) from the epicenter, their data misfits are not prominently larger than the misfits from the models where the south-eastern surface fault trace is ruptured. We mark the former subset of models in red (hereafter referred to as group 2); while the latter subset in blue (hereafter referred to as group 1) in Fig. 6.3.

We further select a subset of samples with posterior probability density larger than 0.5 ρ_{max} (yellow rectangles) in Fig. 6.3a and 6.3b. All samples in this subset belong to group 1 (blue dots). This indicates that the models where south-eastern part of the fault is ruptured at the surface are preferred. Among this subset of samples, the mean values of off-fault plastic cohesion are 0.6 for γ_0 and 0.6 for γ_1; whereas the mean values of on-fault direct-effect parameter are 0.8 for α_0 and 1.1 for α_1. At the same time, the correlation between γ_0 and α_0 is still preserved in this subset.

In addition to fault-parallel offset, we also utilize both static and real-time surface displacement from GNSS in the inversion. We show the static displacement at 21 stations in Fig. 6.4a, together with 40 s of the three-component displacement time series at 10 stations in Fig. 6.4b. We continue showing the model output from group 1 (red arrows and curves in Fig. 6.4) and group 2 (blue arrows and curves in Fig. 6.4), corresponding to samples with posterior probability density larger than $0.25\rho_{max}$. The blue and red circles in Fig. 6.4a delineate the uncertainties in the static displacement, respectively, in group 1 and group 2. The radius of the circle is equal to two times the standard deviation of the subset of models. The static displacement data fall inside the circles at 14 out of the 20 stations for group 1, whereas this value is only 6 for group 2. This also means that the surface static displacement data prefer the models in group 1 to those in group 2. But such a preference is no longer as obvious from real-time displacement time series at the 10 GNSS stations (Melgar et al., 2020).

6.3.3 Uncertainties in shallow slip deficit

With the ensemble of accepted models in MLDA, we can single out a best-fit model that has the highest Bayesian posterior probability density. We show the total fault slip on fault F1 in Fig. 6.5a. We mark a small segment of the fault where the rupture does not reach the surface. Such an unruptured fault surface has also been captured in previous kinematic fault slip inversion results from the 2019 Ridgecrest mainshock (Barba-Sevilla et al., 2022;

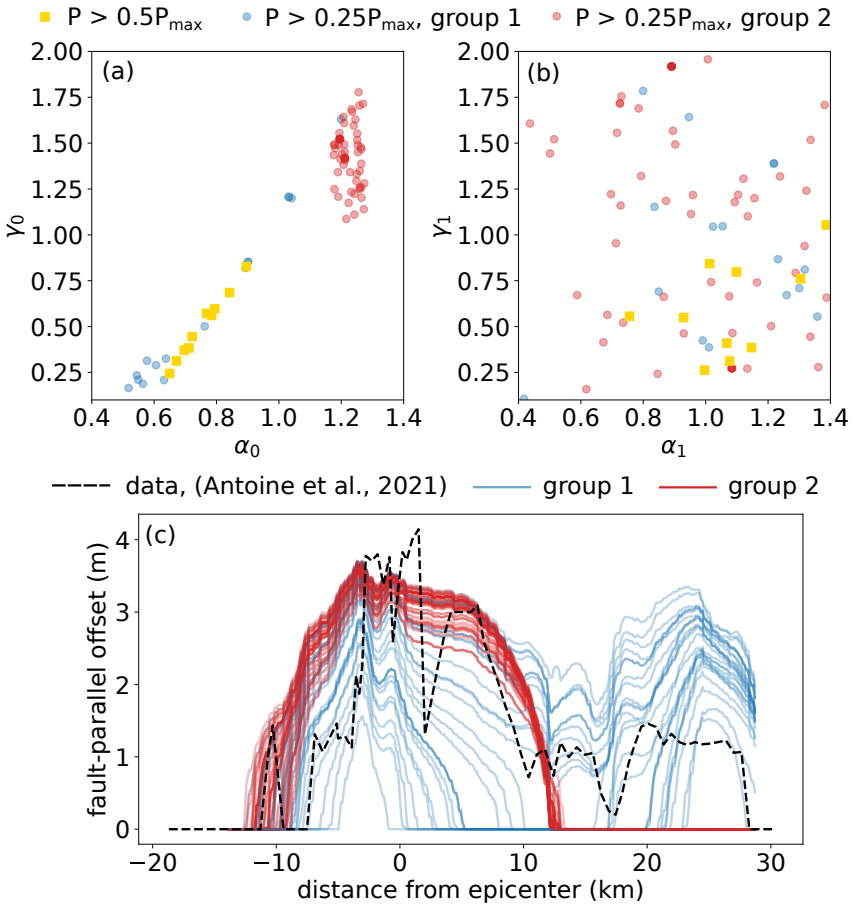

Figure 6.3: Accepted models in MLDA with high posterior probability density. We separately show the 2D marginal distributions for the pair of parameters (γ_0, α_0) in panel (a) and (γ_1,α_1) in panel (b). We plot the models with posterior probability density $\rho(\mathbf{m}|\mathbf{d}^{obs})$ larger than $0.25\rho_{max}$ in two groups (group 1 in blue dots and group 1 in red dots); and the models with $\rho(\mathbf{m}|\mathbf{d}^{obs})$ larger than $0.5\rho_{max}$ in yellow dots. ρ_{max} is the maximum $\rho(\mathbf{m}|\mathbf{d}^{obs})$ among all the accepted models in MLDA. We also plot the fault-parallel offset results from group 1 (in blue curves) and group 2 (in red curves) in panel (c). Meanwhile, we show the fault-parallel offset data from Antoine et al. (2021) in the dashed black curve.

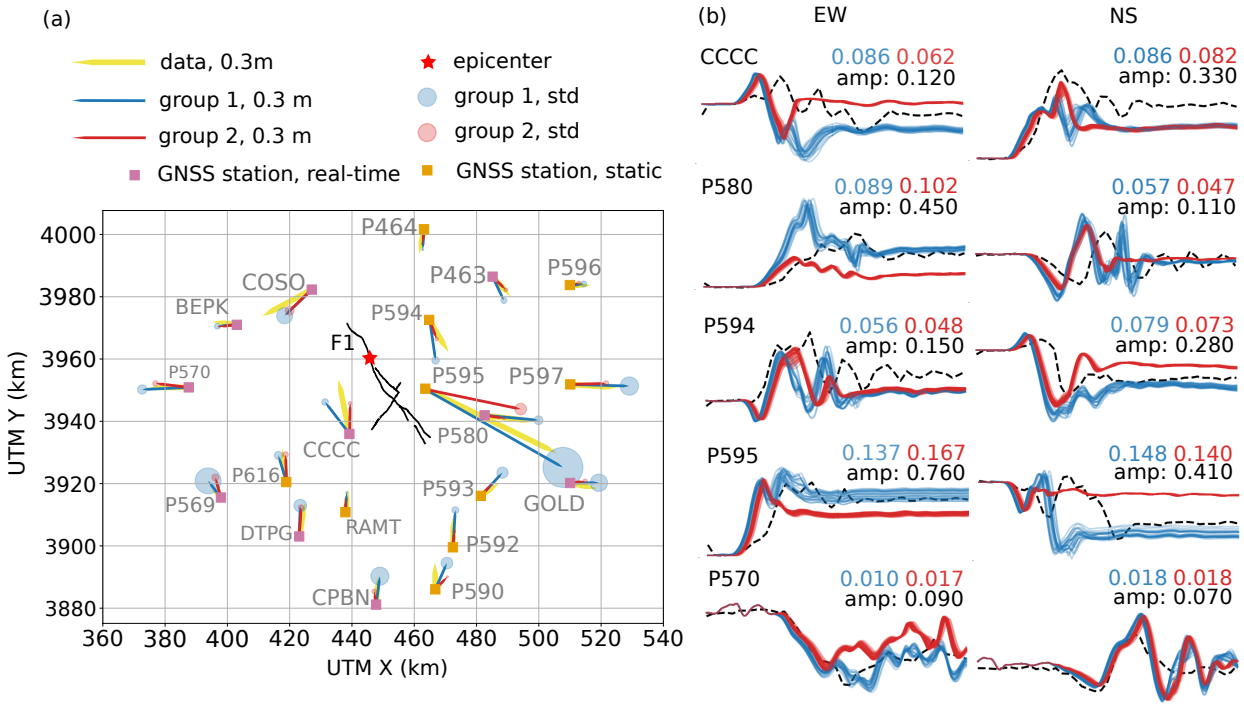

Figure 6.4: Comparison of the model output from group 1 and group 2 with static and real-time surface displacement measurements at GNSS stations. (a) Co-seismic horizontal static displacements at 21 GNSS stations. The stations where we only use the static displacement data are shown in orange rectangles, while the stations where real-time displacement measurements are available are marked with pink rectangles. The mean values of displacement output from models in group 1 and group 2 are, respectively, in blue and red arrows. The radii of the blue and the red circles equal two times the standard deviation values in each group of models. The yellow arrows denote static displacement data from Floyd et al. (2020). (b) 40 s of real-time displacement time series at 5 of the 10 pink stations in (a). The left and the right column are, respectively, east-west (EW) and north-south (NS) components. The blue and red curves are simulation results from models in, respectively, group 1 and group 2. The black dashed curves are from the processed GNSS data by Melgar et al. (2020). We compute the average data misfits between the data and, respectively, the results from group 1 (the blue numbers) and those from group 2 (the red numbers). The black numbers mark the peak amplitudes of the time series in each sub-panel of (b).

Hanagan et al., 2024; Antoine et al., 2024).

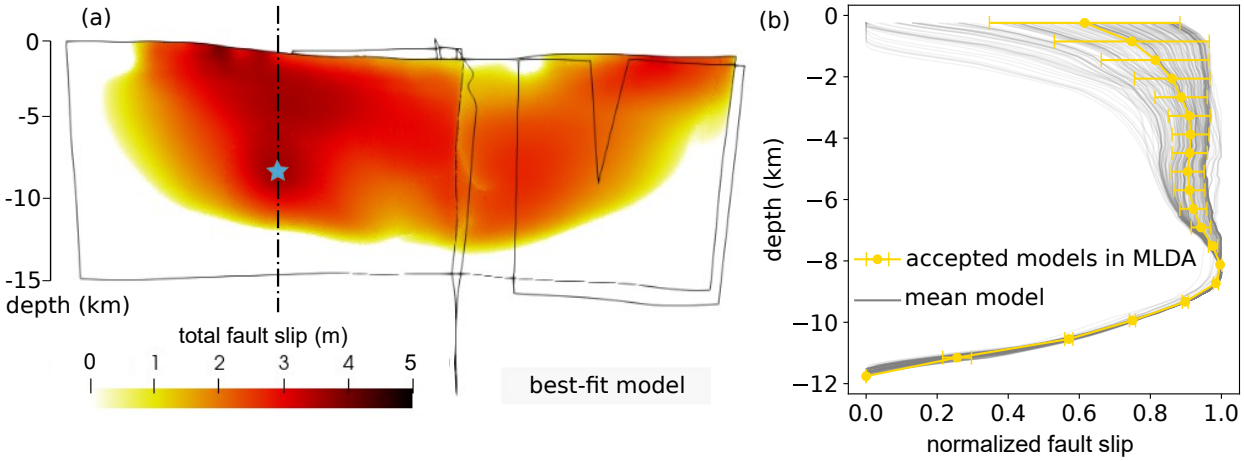

Figure 6.5: (a) The fault slip distribution of the best-fit model from the MLDA inversion. The blue star marks the center of earthquake nucleation in dynamic rupture simulations. (b) Fault slip variation along the intersection A-A' in (a). Results from all the accepted models are shown in gray curves. The yellow curve plots the mean fault slip among all the accepted models, with the error bars marking the depth-dependent fault slip standard deviation.

A more unique estimation of the model output from the Bayesian inversion with MLDA and physics-based dynamic rupture simulations is that we can now statistically evaluate SSD from all the accepted models in the inversion. We show the fault slip distribution along a vertical intersection (A-A') on the fault that goes through the earthquake nucleation center. We plot the fault slip along A-A' from all the accepted models with the gray curves in Fig. 6.5b. We find that while the rupture does not reach the surface in a few models, the normalized fault slip at the surface is between 0.4 and 0.9 in most models. We compute the mean output of all accepted models and plot it in the yellow curve in Fig. 6.5b. The lengths of the error bars mark the standard deviation of all accepted models. The mean value of SSD in the inversion is approximately 38.5%, with a standard deviation of 26.8%. We also observe a trend that the slip uncertainty increases towards shallower depths. We will discuss the inverted SSD in this work and compare it with previous results in Section 6.4.2.

6.4 Discussion

In this section, we further analyze the results from Section 6.3. Bayesian inversion with the MLDA algorithm in this work provides us with a unique opportunity to explore statistics in the nonlinear parameter space of physics-based dynamic rupture simulations. We start from an analysis of the preferred model parameters from the inversion. The ensemble of accepted models used for estimating the Bayesian posterior in parameter space is also useful for statistically evaluating the fault slip distribution that are constrained by both data and physical principles. In this regard, SSD is of special interest due to its close correlation with the off-fault (inelastic) diffuse deformation (Xu et al., 2016). We will discuss the SSD from our dynamic rupture inversion in comparison with the previous results from the kinematic

fault slip inversion. In the end of this section, we will discuss the two groups of models that both have relatively high probability density ($> 0.25\rho_{max}$). This sheds light on the merits and limitations of the inversion method that we employed in this work.

6.4.1 Off-fault plasticity and on-fault friction

Both off-fault plastic cohesion c in Eq. (6.2) and on-fault $a - b$ values in the SW-RS friction law in Eq. (6.A.2) are important to determine the fault slip distribution and the off-fault deformation. The former controls the energy dissipation through off-fault inelastic deformation, competing with the energy loss from frictional heating in consuming the total energy released from the earthquake (Dunham et al., 2011; Gabriel et al., 2013; Nielsen et al., 2016). On the other hand, $a - b$ influences the amount of energy dissipation from a given fault slip and determines whether the rupture process is spontaneous (velocity weakening) or not (Dunham et al., 2011). The Bayesian inversion with the MLDA algorithm provides a unique opportunity to investigate whether (and how) it is possible to discriminate the effects of c and $a - b$ on the on- and off-fault deformation with surface displacement measurement.

From the inversion results in Fig. 6.2, we can also observe the correlation between c and $a - b$. Less energy dissipation through off-fault inelastic deformation (larger γ_0) needs to be compensated for by less prominent velocity-weakening (larger α_0) in on-fault friction. Compared with the model parameters manually chosen by Taufiqurrahman et al. (2023), that is, $c = 1.0 \times 10^{-4}\mu(x, y, z)$, the results from all the accepted samples (Figs. 6.2a and 6.2f) and from the high-probability subset of samples (yellow rectangles in Fig. 6.3) prefer a lower plastic cohesion. Among the high-probability subset of samples, the mean values of γ_0 and γ_1 are, respectively, 0.58 and 0.61. They correspond to $c = 5.8 \times 10^{-5}\mu(x, y, z)$ and $c = 6.1 \times 10^{-5}\mu(x, y, z)$. A lower plastic cohesion helps suppress the amplitudes of surface displacement close to the fault and allows a better match with observations at GNSS stations, e.g., P464, P580, and P616, in Fig. 6.4a.

In terms of $a - b$ value for on-fault friction, results from all the accepted samples (Fig. 6.2k and 6.2p) and from high-probability subset of samples (yellow rectangles in Fig. 6.3) show a different trend in terms of how $a - b$ varies from the northwestern part (α_0) to the southeastern (α_1) part of fault F1. In Fig. 6.2, most samples distribute around 1.2 for α_0; while around 1.0 for α_1. This corresponds to a decrease of $a - b$ from -0.002 to -0.004 from northwest to southeast, indicating a more prominent velocity-weakening friction behavior in the southeast segment of fault F1. However, based on the high-probability subset of samples (yellow rectangles) in Fig. 6.3, most samples distribute around 0.8 for α_0; while around 1.1 for α_1. We can find an explanation for this disagreement from the subset of samples in group 2 (the red dots) in Fig. 6.3a. Almost all ($> 95\%$) of the samples where α_0 centers around 1.2 come from group 2, where the fault rupture does not reach the surface between 12 and 30 km. We also find that samples from group 2 do not show up in models with even higher probability density (the yellow dots) in Fig. 6.3a. This indicates that the samples from group 2 biased the distribution in Fig. 6.2k. We therefore propose that the inversion results prefer an increase of $a - b$ from around -0.006 to -0.003 from the northwest to the southeast. This corresponds to a less prominent velocity-weakening frictional behavior on the southeastern segment of the fault F1. A geological observation that may support such

transition is the less continuous surface fault trace outcrop from observations before the 2019 Ridgecrest earthquake around the south-eastern segment of the fault F1 (Thompson Jobe et al., 2020). This indicates a less mature fault zone (Dolan and Haravitch, 2014; Manighetti et al., 2021), which might result in less prominent velocity-weakening on-fault friction (Ikari et al., 2011).

6.4.2 Uncertainties in shallow slip deficit

In this work, we for the first time present SSD from physics-based dynamic rupture simulations systematically constrained from multidisciplinary surface displacement data. We used this opportunity to quantitatively compare with SSD derived from kinematic fault slip inversion, constrained by different types of observation, and using different inversion methods (Wang et al., 2020).

With lower plastic cohesion values (γ_0 and γ_1) and less prominent velocity-weakening fault friction (larger α_1) in the south-eastern part of the fault, the fault slip values are generally smaller in the best-fit model in this work, as shown in Fig. 6.5a, compared to the reference model by Taufiqurrahman et al. (2023). Meanwhile, lower plastic cohesion results in larger diffused off-fault deformation (Roten et al., 2017), and thus larger SSD. The SSD in the reference model is around 20%. From the ensemble of accepted models in the MLDA algorithm in this work, the mean value of SSD is 38.5%, i.e. Fig. 6.5b. In a most recent estimate of the SSD from kinematic fault slip inversion by Antoine et al. (2024), the shallow slip deficit is around 36%. Earlier estimations of this value vary from 2% to 45%, indicating a large uncertainty in the estimation of SSD (Wang et al., 2020; Jin et al., 2022). The uncertainty in the estimated SSD in Fig. 6.5b is also comparably large, with a standard deviation of 26.8%.

With a ten-fold acceleration in Bayesian inversion with prefetching MLDA (Kruse et al., 2025), we show the practicality of solving low-dimensional inverse problems for regional-scale earthquakes with complex geometry and inelastic off-fault deformation, such as the M_W 7.1 Ridgecrest earthquake, 2019. However, the dimension of parameter space is still limited by computationally expensive dynamic rupture simulations. The low dimension of parameter space that we explore in this work increases the epistemic uncertainties and prevents us from matching the observations to their measurement accuracies. Potential methods for further accelerating the inversion process are emerging on the horizon. They include deep-learning-based surrogate models (Yang et al., 2023) to handle high-dimensional input for lower-level model in MLDA, adjoint dynamic rupture simulations from Stiernström et al. (2024), which provides parametric gradient information for inversion, and fused simulation that enables execution of ensembles of dynamic rupture simulations at the same time, which can provide additional speed-up (Breuer et al., 2017; Heinecke et al., 2019).

6.5 Conclusions

This study presents the application of a novel MLDA algorithm for Bayesian inversion, partition uncertainty, and correlation among nonlinear parameters in physics-based dynamic rupture simulations. Through an integration of multidisciplinary surface deformation data, we reveal a strong correlation between on-fault friction (direct-effect parameter, a) and off-fault plastic cohesion (c). The results demonstrate that lower plastic cohesion compensates for reduced velocity-weakening friction, highlighting the interplay between these processes in controlling fault slip distribution and off-fault deformation.

The estimated shallow slip deficit (SSD) is 38.5%, with a standard deviation of 26.8%. Such range of SSD are comparable with results from previous kinematic fault slip inversion studies. We highlight that the SSD values in this work are supported by dynamic rupture simulations that account for off-fault inelastic deformation. This supports the hypothesis that off-fault inelastic deformation can quantitatively explain the observed SSD in the M_W 7.1 2019 Ridgecrest earthquake. Additionally, preferred models from our inversion suggest a gradual decrease in velocity-weakening behavior along the fault, suppressing overshooting at the southeastern segment. This finding is consistent with the geological observations of less mature fault zones in this region.

The combination of MLDA and dynamic rupture simulations provides a powerful framework for quantifying earthquake mechanics, despite current limitations in measurement accuracy and parameter space dimensionality. Future advancements, such as AI-based surrogate models and adjoint dynamic rupture simulations, hold promise for improving efficiency and resolution in large-scale inversions. Overall, this work establishes a foundation for more precise and comprehensive investigations of the earthquake source properties with direct constraints from quantitative field observations.

Appendices

Appendix 6.A SV-RS friction law in dynamic rupture modeling of earthquakes

We use this section to clarify the nonlinear parameters in the SV-RS friction law in Section 6.2.2. In this friction law, the frictional fault strength τ_s (the upper bound of the shear traction τ on a fault surface) is proportional to the local normal traction σ_n, which is

$$\tau_s = f(V, \Psi)\sigma_n, \tag{6.A.1}$$

where $f(V, W)$ is known as the friction coefficient. It is a function of the slip rate V and the state variable Ψ. In SV-RS friction, it is defined as

$$f(V, \Psi) = a \sinh^{-1}(\frac{V}{2V_0} \exp(\frac{\Psi}{a})), \tag{6.A.2}$$

where a is the direct-effect parameter and V_0 is the reference slip rate, at which the friction coefficient takes a reference value f_0. The state variable Ψ evolves to its steady-state value Ψ_{ss} depending on the slip rate V and a characteristic slip distance L in Eq. (6.A.3).

$$\frac{\mathrm{d}\Psi}{\mathrm{d}t} = -\frac{V}{L}(\Psi - \Psi_{ss}(V)), \tag{6.A.3}$$

where $\Psi_{ss}(V)$ is written as

$$\Psi_{ss}(V) = a \ln(\frac{2V_0}{V} \sinh(\frac{f_{ss}(V)}{a})), \tag{6.A.4}$$

corresponding to a steady-state friction coefficient f_{ss}. At steady state, the low-velocity friction coefficient f_{LV} is defined as

$$f_{LV}(V, \Psi) = f_0 - (b - a) \ln \frac{V}{V_0}, \tag{6.A.5}$$

where b is the evolution-effect parameter that determines how the friction evolves with the state variable Ψ from the instantaneous direct effect a. To account for the friction reduction at high slip rates, SV-RS friction further defines a fully weakened friction coefficient f_W at a weakened slip rate V_W. Combining f_{LV}, f_W and V_W, f_{ss} can be defined as

$$f_{ss}(V) = f_W + \frac{f_{LV}(V) - f_W}{(1 + (V/V_W)^8)^{1/8}}. \tag{6.A.6}$$

Appendix 6.B Real-time displacement at the GNSS stations not presented in Fig. 6.4b

In Fig. 6.B.1, we provide the comparison between the output of the accepted models in MLDA and the real-time displacement recordings at 10 GNSS stations, supplementary to Fig. 6.4b.

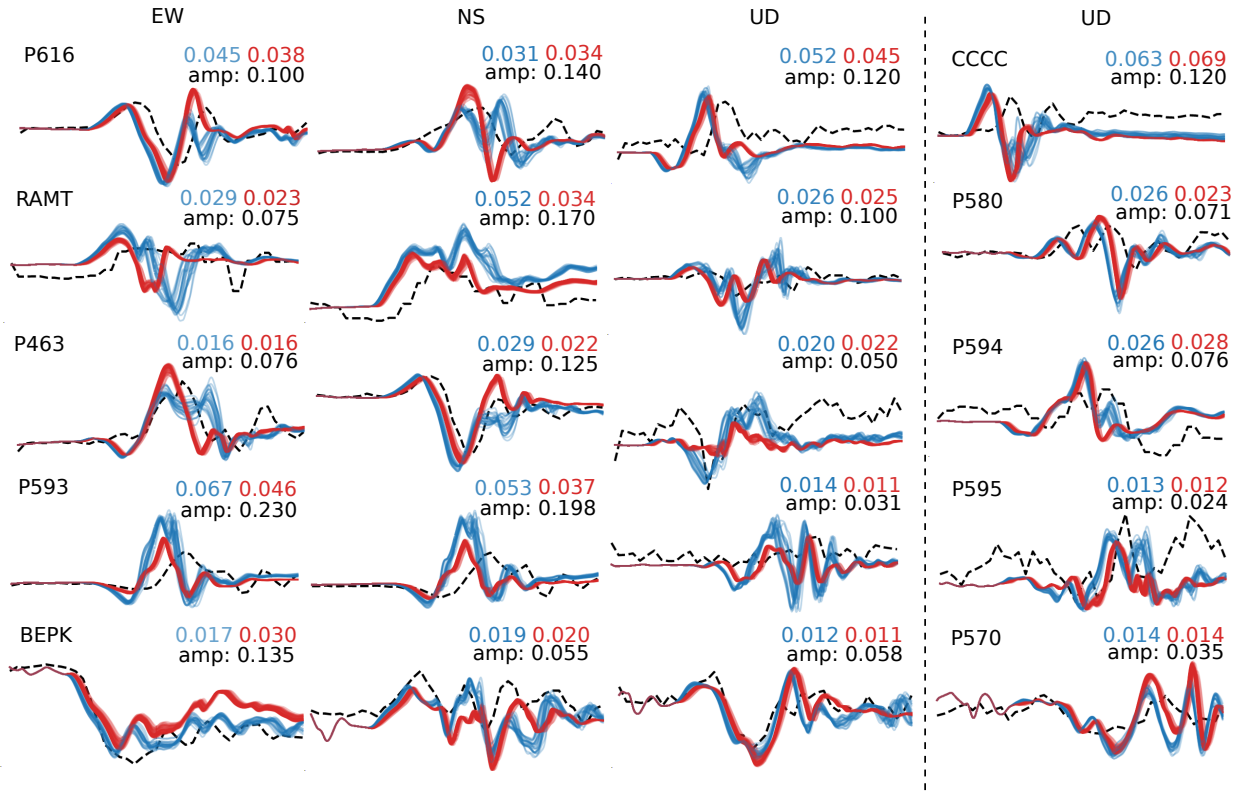

Figure 6.B.1: Supplementary results of Fig. 6.4b. The first three columns from the left are 40 s of real-time displacement time series at the remaining 5 of the 10 pink stations that are not presented in Fig. 6.4b. From left to right, they show, respectively, east-west (EW), north-south (NS), and upward-downward (UD) components. The blue and red curves are simulation results from models in, respectively, group 1 and group 2. The black dashed curves are from the processed GNSS data by Melgar et al. (2020). Meanwhile, the upward-downward (UD) components of the 5 stations in Fig. 6.4b are shown in the right most column of this figure.

Chapter 7

Concluding remarks

7.1 Summary

In this dissertation, I advance nonlinear rock models and constrain their parameters from laboratory experiments, develop a nonlinear discontinuous Galerkin (DG) algorithm that incorporates these models into wave propagation and dynamic rupture simulations, and integrate the efficient Bayesian inversion algorithm MLDA with supercomputing infrastructures. The eventual goal for which this dissertation is intended is to pave the way towards constraining nonlinear rock model parameters from earthquake observations so that it is eventually possible to compare these values with measurements from laboratory experiments.

I start from exploring the applicability of two models explaining the observed non-classical nonlinear behaviors in rocks, comparing an internal variable model (IVM) and a continuum damage model (CDM). The IVM is based on the work of Berjamin et al. (2017), while the CDM is adapted from Lyakhovsky et al. (1997a). The results indicate that both models provide a quantitative match with laboratory observations, supporting their effectiveness in capturing the co-seismic wave speed changes in rocks. But they have different merits and deficiencies. CDM is derived from a more physical assumption, but it also has more parameters to be constrained; whereas IVM has fewer parameters and can be easier constrained, but is also more phenomenological (still based on laws of thermodynamics).

Based on the above understandings of the nonlinear rock models, I move on to develop a scalable software for numerical modeling of regional-scale 3D seismic wave propagation, extending from the in-house maintained software SeisSol. The extended solver can now account for geometric complexities of the surface topography and heterogeneous geological structures. I evaluate the parallel performance of our implementation on Frontera and find that both weak and strong scaling remain close to linear up to 20 nodes per million elements, allowing efficient simulations on meshes with up to 100 million elements and scalability up to 2048 nodes. With an implementation of the experimentally constrained nonlinear model IVM, I apply the extended solver to the 2015 M_w 7.8 Gorkha earthquake in the Kathmandu Valley, incorporating a free surface with topography, a sedimentary basin with low wave speeds and complex bathymetry, a layered geological structure, and a finite source model that accounts for rupture directivity effects. The simulation results show that co-seismic wave speed reductions depend on the fault slip distribution near the source and are modulated by basin depths tens of kilometers away from the fault. Additionally, co-seismic wave speed changes enhance low-frequency components in soft sedimentary layers, affecting ground motions, which is relevant for seismic hazard assessment.

As a next step, I further integrated the nonlinear DG algorithm for wave propagation with 3D dynamic rupture simulations. The numerical framework proposed in this work is flexible with different nonlinear models. With another nonlinear rock model, the continuum damage breakage model (Lyakhovsky et al., 2016), which is well suited for fault zone nonlinearity, I investigate the impact of off-fault co-seismic moduli reduction on the earthquake source mechanism and earthquake interaction. The results show that localized damage zones that extend from one fault can introduce a heterogeneous stress perturbation on its neighboring fault. This stress heterogeneity triggers nucleation on the second fault. This part of the dissertation demonstrates that the tool developed in this work is unique in modeling how discontinuous fault segments that are separated by a few kilometers can be connected to each other during earthquakes (Wesnousky, 2006).

With the extended solver developed in this work, we are equipped with the tool to model nonlinear earthquake-related observations in the field. Along the path towards a comparison between the constrained nonlinear rock model parameters from earthquake observations and these values from laboratory experiments, I integrated the SeisSol simulations with an efficient and scalable Bayesian inversion algorithm, the prefetching-based multilevel delayed acceptance Markov chain Monte Carlo (MLDA-MCMC) algorithm, on supercomputers. Tests on the integrated inversion framework indicate that the prefetching technique with MLDA-MCMC can be a valuable tool for scenarios where the strong scaling behavior of the sampling procedure is relevant. This is typically the case for expensive computational models, large computational resources, and limited time-to-result.

I end this dissertation with an application of the inversion algorithm to data from the 2019 M_w 7.1 Ridgecrest earthquake to investigate the interaction between nonlinear on-fault friction and off-fault inelastic deformation. Through an integration of multidisciplinary surface deformation data, the inversion results demonstrate that a lower plastic cohesion compensates for the reduced velocity-weakening friction, highlighting the interplay between these processes in controlling fault slip distribution and off-fault deformation. The inversion also provides an estimated shallow slip deficit (SSD) of 38.5%, with a standard deviation of 26.8%. The uniqueness of this work lies in the fact that inverted SSD values are supported by high-resolution dynamic rupture simulations that account for off-fault inelastic deformation.

7.2 Outlook

This work contains four emerging ingredients in earthquake physics: better nonlinear mechanical models for rocks and soils, an extended numerical solver for nonlinear wave propagation and dynamic rupture, a generic framework for Bayesian inversion of rupture dynamics with complex geometry and nonlinear parameters, and their geophysical applications to regional-scale earthquakes. This dissertation provides a tool for evaluating the effects of different nonlinear models on ground motions and earthquake source mechanisms. It can be used for investigation of mechanisms and observations in actual earthquakes (as in Chapter 3), for theoretical study of the first-order influence of the nonlinear models (as in Chapter 4), and for constraining the nonlinear on-fault and off-fault parameters in earthquakes hosted by fault structures with complex geometry and nonlinear physical mechanisms (as

in Chapter 6). In this section, I list some practical extensions of this dissertation.

Explain high-frequency seismic energy radiated from the fault structures that host regional-scale earthquakes: This work provides unique foundations for studying more observations in earthquakes with nonlinear models. One example can be to investigate whether the co-seismic off-fault moduli reduction can explain the high-frequency ground motions between 0.5 and 5 Hz during the 2016 M_w 6.2 Amatrice, Italy, earthquake, which cannot be explained with fault roughness and surface topography (Taufiqurrahman et al., 2022). The results in Chapter 4 show the co-seismic off-fault moduli reduction can introduce significantly enhanced high-frequency seismic radiation from 0.4 Hz and up to 10 Hz. This range covers the gap in the previous study very well. Therefore, the co-seismic off-fault moduli reduction may be a promising candidate to fill this gap.

More realistic ground motion simulation for soft sediments in 3D: Aside from the better characterization of earthquake sources, the extension of SeisSol in this work also enables a better characterization of ground motions above soft sediments. In Chapter 3, I investigate the effect of co-seismic wave speed reduction on ground motions within the Kathmandu sedimentary basin. While the results already show that such reductions in wave speed can reproduce low-frequency enhancement, the nonlinear model IVM used in Chapter 3 does not yet include the accumulation of inelastic strain. For the extension in this direction, I already have some preliminary work that combine inelastic strain (using a single-mechanism Maxwell visco-elastic model) with time-dependent degradation of moduli in non-classical nonlinearity in Fig. 1.1. This model extends from the model in Eq. (3.1). I formulate the combined model as:

$$\begin{cases} \dfrac{\partial \varepsilon_{ij}}{\partial t} + \dfrac{\partial \varepsilon_{ij}^{p}}{\partial t} &= \dfrac{1}{2}\left(\dfrac{\partial v_i}{\partial x_j} + \dfrac{\partial v_j}{\partial x_i}\right) \\ \rho \dfrac{\partial v_i}{\partial t} &= \dfrac{\partial \sigma_{ij}(\underline{\underline{\varepsilon}}, \alpha)}{\partial x_j} \\ \dfrac{\partial \alpha}{\partial t} &= r_{\alpha}(\underline{\underline{\varepsilon}}, \alpha) \\ \dfrac{\partial \varepsilon_{ij}^{p}}{\partial t} &= \dfrac{1}{\eta}\tau_{ij} \end{cases}, \tag{7.1}$$

where the additional variables to Eq. (3.1) are the inelastic strain tensor ε_{ij}^{p}, the deviatoric stress tensor $\tau_{ij} = \sigma_{ij} - 1/3\sigma_{kk}$, and the viscous coefficient η. I show in Fig. 7.1 that this simple combination of visco-elasticity and IVM can reproduce the stress-strain curves measured on a soil sample under cyclic loading (Weaver, 2019). The implementation of this combined model is also available in the SeisSol repository (https://github.com/SeisSol/SeisSol) under the branch ‘‘`damaged-material-nonlinear-drPlasB`’’.

Further improvement in the accuracy and performance of the nonlinear DG algorithm: Aside from the geophysical application, there is also plenty of room for improvement on the solver side for the nonlinear extension of SeisSol. Here, I briefly summarize the following three major points:

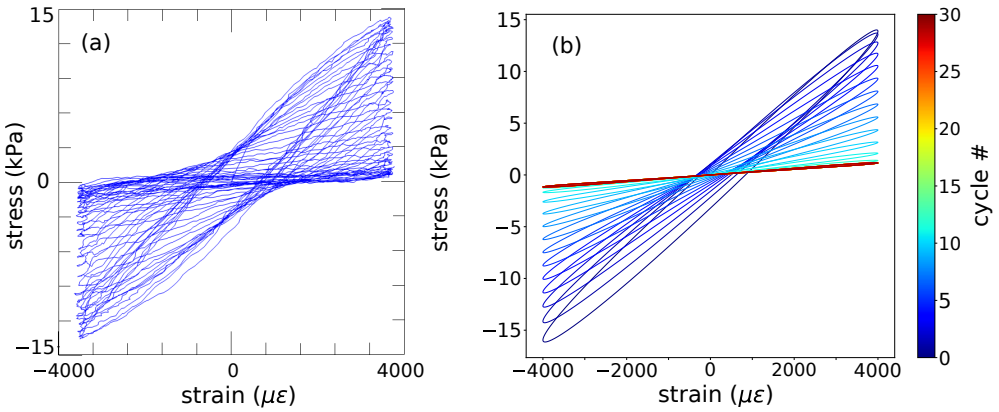

Figure 7.1: Comparison between the stress-strain curves from (a) laboratory experiments on soil samples from Weaver (2019) and (b) the model that combines inelastic strain with IVM in Eq. (7.1). The soil sample is subjected to dynamic cyclic loading. With the increase in the number of loading cycle, which is the color code of panel (b), the angle between the hysteresis curve and x-axis drops.

- As discussed in Chapter 3, some node-level performance optimization is required to enhance hardware performance for the newly implemented space-time integration (matrix-matrix multiplication) function.

- Another promising point of improvement is to enable the local-time-stepping (LTS) for the nonlinear implementation in this work. The currently version only supports a uniform time step size in all the elements of a mesh. This is a significant bottleneck for the simulation domain with complex geometry or significant local mesh refinement for higher resolution. While LTS has limited room for improvement in hardware performance, it can increase the speed by more than 10 times in terms of the time to solution (Breuer and Heinecke, 2022).

- The third point is related to the convergence order of the current nonlinear DG algorithm in this work. As shown in Chapter 3, with a linearized Cauchy-Kovalevskaya procedure in the prediction step of time integration, the algorithm only has a first-order convergence rate independent of the polynomial degrees of the basis functions in space. As discussed by Käser et al. (2008), a high-order convergence rate can also reduce the time-to-solution. A potentially promising extension of our work is the incorporation of a discrete Picard iteration scheme (Lindelöf, 1894; Youssef and El-Arabawy, 2007; Dumbser et al., 2008; Gassner et al., 2011; Reinarz et al., 2020) to replace the linearized Cauchy-Kovalevskaya procedure. This approach has been shown to help preserve high-order convergence up to 7 in ADER-DG solvers (Dumbser et al., 2008).

Further acceleration of the Bayesian inversion with dynamic rupture simulations: Chapters 5 and 6 introduce the multi-level delayed acceptance (MLDA) Markov chain Monte Carlo (MCMC) algorithm (Dodwell et al., 2019), which significantly enhances the efficiency of Bayesian inversion. However, the number of parameters that can be inverted is still limited by: (1) the current Gaussian process regression surrogate model lacks generalization across different earthquake sources and gives insufficiently good estimation

in high-dimensional parameter space; (2) each forward simulation has a high computational cost; and (3) the curse of dimensionality in gradient-blind MCMC (Fichtner et al., 2019). A promising avenue for addressing these limitations is the integration of deep learning (DL) architectures to develop surrogate models that improve computational efficiency while generalizing effectively across diverse earthquake scenarios. By combining the MLDA algorithm with DL-based surrogate models and adjoint 3D dynamic rupture simulations (Stiernström et al., 2024), it is possible to further accelerate Bayesian inversion while improving accuracy and scalability. Future research can focus on refining these techniques to expand the applicability of high-dimensional seismic inversion in large-scale earthquake modeling.

Bibliography

Abram, G., Gabriel, A., Samsel, F., Schliwa, N., Wang, Y., Cunningham, S., 2019. Conversing faults: The 2019 ridgecrest earthquake, in: Proceedings of the International Conference for High Performance Computing, Networking, Storage, and Analysis (SC23), Texas Advanced Computing Center, University of Texas; University of California, San Diego; Ludwig-Maxmilians-Universität München. p. 1. URL: https://sc23.supercomputing.org/proceedings/sci_viz/sci_viz_pages/svs102.html.

Aleshin, V., Van Den Abeele, K., 2007. Microcontact-based theory for acoustics in microdamaged materials. Journal of the Mechanics and Physics of Solids 55, 366–390.

Andrews, D., 1976. Rupture velocity of plane strain shear cracks. Journal of Geophysical Research 81, 5679–5687.

Andrews, D.J., 2005. Rupture dynamics with energy loss outside the slip zone. Journal of Geophysical Research: Solid Earth 110. doi:https://doi.org/10.1029/2004JB003191.

Angelino, E., Kohler, E., Waterland, A., Seltzer, M., Adams, R.P., 2014. Accelerating mcmc via parallel predictive prefetching, in: Proceedings of the Thirtieth Conference on Uncertainty in Artificial Intelligence, AUAI Press, Arlington, Virginia, USA. p. 22–31.

Antoine, S.L., Klinger, Y., Delorme, A., Wang, K., Bürgmann, R., Gold, R.D., 2021. Diffuse deformation and surface faulting distribution from submetric image correlation along the 2019 ridgecrest, california, ruptures. Bulletin of the Seismological Society of America 111, 2275–2302.

Antoine, S.L., Klinger, Y., Wang, K., Bürgmann, R., 2024. Coseismic shallow slip deficit accounted for by diffuse off-fault deformation. Geophysical Research Letters 51, e2024GL110798.

Arridge, S., Maass, P., Öktem, O., Schönlieb, C.B., 2019. Solving inverse problems using data-driven models. Acta Numerica 28, 1–174. URL: https://www.cambridge.org/core/product/identifier/S0962492919000059/type/journal_article, doi:10.1017/S0962492919000059.

Arrowsmith, S.J., Trugman, D.T., MacCarthy, J., Bergen, K.J., Lumley, D., Magnani, M.B., 2022. Big data seismology. Reviews of Geophysics 60, e2021RG000769.

Barall, M., 2009. A grid-doubling finite-element technique for calculating dynamic three-dimensional spontaneous rupture on an earthquake fault. Geophysical Journal International 178, 845–859.

Barba-Sevilla, M., Glasscoe, M.T., Parker, J., Lyzenga, G.A., Willis, M.J., Tiampo, K.F., 2022. High-resolution finite fault slip inversion of the 2019 ridgecrest earthquake using 3d finite element modeling. Journal of Geophysical Research: Solid Earth 127, e2022JB024404.

Ben-Zion, Y., Beroza, G.C., Bohnhoff, M., Gabriel, A.A., Mai, P.M., 2022. A grand challenge international infrastructure for earthquake science.

Ben-Zion, Y., Sammis, C.G., 2003. Characterization of fault zones. Pure and applied geophysics 160, 677–715.

Ben-Zion, Y., Zhang, S., Meng, X., 2024. Isotropic high-frequency radiation in near-fault seismic data. Geophysical Research Letters 51, e2024GL110303.

Beresnev, I.A., Wen, K.L., 1998. Nonlinear site response–a reality? Bulletin of the Seismological Society of America 86, 1964–1978.

Berjamin, H., Favrie, N., Lombard, B., Chiavassa, G., 2017. Nonlinear waves in solids with slow dynamics: an internal-variable model. Proceedings of the Royal Society A: Mathematical, Physical and Engineering Sciences 473, 20170024.

Berjamin, H., Lombard, B., Chiavassa, G., Favrie, N., 2019. Plane-strain waves in nonlinear elastic solids with softening. Wave Motion 89, 65–78.

Bernard, P., Baumont, D., 2005. Shear mach wave characterization for kinematic fault rupture models with constant supershear rupture velocity. Geophysical Journal International 162, 431–447.

Bhat, H.S., Dmowska, R., King, G.C., Klinger, Y., Rice, J.R., 2007. Off-fault damage patterns due to supershear ruptures with application to the 2001 mw 8.1 kokoxili (kunlun) tibet earthquake. Journal of Geophysical Research: Solid Earth 112.

Bizzarri, A., Cocco, M., 2006. A thermal pressurization model for the spontaneous dynamic rupture propagation on a three-dimensional fault: 1. methodological approach. Journal of Geophysical Research: Solid Earth 111.

Boatwright, J., Boore, D.M., 1982. Analysis of the ground accelerations radiated by the 1980 Livermore Valley earthquakes for directivity and dynamic source characteristics. Bulletin of the Seismological Society of America 72, 1843–1865.

Bohara, P., Ghimire, S., 2015. Analysis of shallow seismic waves to determine geo-technical characterization of major earthquake affected sites of kathmandu valley, in: Proceedings of IOE Graduate Conference, pp. 63–68.

Bokelmann, G.H., Harjes, H.P., 2000. Evidence for temporal variation of seismic velocity within the upper continental crust. Journal of Geophysical Research: Solid Earth 105, 23879–23894.

Bonilla, L.F., Ben-Zion, Y., 2021. Detailed space–time variations of the seismic response of the shallow crust to small earthquakes from analysis of dense array data. Geophysical Journal International 225, 298–310.

Bonilla, L.F., Guéguen, P., Ben-Zion, Y., 2019. Monitoring coseismic temporal changes of shallow material during strong ground motion with interferometry and autocorrelation. Bulletin of the Seismological Society of America 109, 187–198.

Bonilla, L.F., Steidl, J.H., Gariel, J.C., Archuleta, R.J., 2002. Borehole response studies at the garner valley downhole array, southern california. Bulletin of the Seismological Society of America 92, 3165–3179.

Bonilla, L.F., Tsuda, K., Pulido, N., Régnier, J., Laurendeau, A., 2011. Nonlinear site response evidence of k-net and kik-net records from the 2011 off the pacific coast of tohoku earthquake. Earth, planets and space 63, 785–789.

Borst, R.d., Remmers, J.J., Needleman, A., Abellan, M.A., 2004. Discrete vs smeared crack models for concrete fracture: bridging the gap. International journal for numerical and analytical methods in geomechanics 28, 583–607.

Bouchon, M., 1997. The state of stress on some faults of the san andreas system as inferred from near-field strong motion data. Journal of Geophysical Research: Solid Earth 102, 11731–11744.

Brandenberg, S.J., Wang, P., Nweke, C.C., Hudson, K., Mazzoni, S., Bozorgnia, Y., Hudnut, K.W., Davis, C.A., Ahdi, S.K., Zareian, F., et al., 2019. Preliminary report on engineering and geological effects of the July 2019 Ridgecrest earthquake sequence. Technical Report. Geotechnical Extreme Event Reconnaissance Association.

Brenguier, F., Campillo, M., Hadziioannou, C., Shapiro, N.M., Nadeau, R.M., Larose, E., 2008a. Postseismic relaxation along the San Andreas fault at Parkfield from continuous seismological observations. Science 321, 1478–1481.

Brenguier, F., Campillo, M., Takeda, T., Aoki, Y., Shapiro, N., Briand, X., Emoto, K., Miyake, H., 2014. Mapping pressurized volcanic fluids from induced crustal seismic velocity drops. Science 345, 80–82.

Brenguier, F., Shapiro, N.M., Campillo, M., Ferrazzini, V., Duputel, Z., Coutant, O., Nercessian, A., 2008b. Towards forecasting volcanic eruptions using seismic noise. Nature Geoscience 1, 126–130.

Brennan, B., Smylie, D., 1981. Linear viscoelasticity and dispersion in seismic wave propagation. Reviews of Geophysics 19, 233–246.

Breuer, A., Heinecke, A., 2022. Next-generation local time stepping for the ader-dg finite element method, in: 2022 IEEE international parallel and distributed processing symposium (IPDPS), IEEE. pp. 402–413.

Breuer, A., Heinecke, A., Bader, M., 2016. Petascale local time stepping for the ader-dg finite element method, in: 2016 IEEE international parallel and distributed processing symposium (IPDPS), IEEE. pp. 854–863.

Breuer, A., Heinecke, A., Cui, Y., 2017. EDGE: Extreme scale fused seismic simulations with the discontinuous Galerkin method, in: International Conference on High Performance Computing, Springer. pp. 41–60.

Brockwell, A.E., 2006. Parallel Markov chain Monte Carlo simulation by pre-fetching. Journal of Computational and Graphical Statistics 15, 246–261. URL: https://doi.org/10.1198/106186006X100579, doi:10.1198/106186006X100579.

Brodsky, E.E., Mori, J.J., Anderson, L., Chester, F.M., Conin, M., Dunham, E.M., Eguchi, N., Fulton, P.M., Hino, R., Hirose, T., et al., 2020. The state of stress on the fault before, during, and after a major earthquake. Annual Review of Earth and Planetary Sciences 48, 49–74.

Brooks, B.A., Minson, S.E., Glennie, C.L., Nevitt, J.M., Dawson, T., Rubin, R., Ericksen, T.L., Lockner, D., Hudnut, K., Langenheim, V., et al., 2017. Buried shallow fault slip from the south Napa earthquake revealed by near-field geodesy. Science Advances 3, e1700525.

Browning, J., Meredith, P.G., Stuart, C., Healy, D., Harland, S., Mitchell, T.M., 2017. Acoustic characterization of crack damage evolution in sandstone deformed under conventional and true triaxial loading. Journal of Geophysical Research: Solid Earth 122, 4395–4412.

Budiansky, B., O'connell, R.J., 1976. Elastic moduli of a cracked solid. International journal of Solids and structures 12, 81–97.

Butcher, J., 2007. Runge-Kutta methods. Scholarpedia 2, 3147.

Byerlee, J., 1978. Friction of rocks. Rock friction and earthquake prediction , 615–626.

Carcione, J.M., Kosloff, D., Kosloff, R., 1988. Wave propagation simulation in a linear viscoelastic medium. Geophysical Journal International 95, 597–611.

Carrington, L., Komatitsch, D., Laurenzano, M., Tikir, M.M., Michéa, D., Le Goff, N., Snavely, A., Tromp, J., 2008. High-frequency simulations of global seismic wave propagation using SPECFEM3D_GLOBE on 62k processors, in: SC'08: Proceedings of the 2008 ACM/IEEE Conference on Supercomputing, IEEE. pp. 1–11.

Castellaro, S., Musinu, G., 2023. Resonance versus shape of sedimentary basins. Bulletin of the Seismological Society of America 113, 745–761.

Castro, G., 1975. Liquefaction and cyclic mobility of saturated sands. Journal of the geotechnical engineering division 101, 551–569.

Castro, R.R., Ben-Zion, Y., 2013. Potential signatures of damage-related radiation from aftershocks of the 4 April 2010 (mw 7.2) El Mayor–Cucapah earthquake, Baja California, México. Bulletin of the Seismological Society of America 103, 1130–1140.

Castro-Cruz, D., Regnier, J., Bertrand, E., Courboulex, F., 2020. A new parameter to empirically describe and predict the non-linear seismic response of sites derived from the analysis of Kik-Net database. Soil Dynamics and Earthquake Engineering 128, 105833.

Causse, M., Dalguer, L., Mai, P.M., 2014. Variability of dynamic source parameters inferred from kinematic models of past earthquakes. Geophysical Journal International 196, 1754–1769.

Chaboche, J.L., 1988. Continuum damage mechanics: Part i—general concepts. Journal of Applied Mechanics .

Chaboche, J.L., 1992. Damage induced anisotropy: on the difficulties associated with the active/passive unilateral condition. International Journal of Damage Mechanics 1, 148–171.

Chapman, C., 2004. Fundamentals of seismic wave propagation. Cambridge university press.

Chapman, M., Godbee, R., 2012. Modeling geometrical spreading and the relative amplitudes of vertical and horizontal high-frequency ground motions in eastern North America. Bulletin of the Seismological Society of America 102, 1957–1975.

Chester, F.M., Evans, J.P., Biegel, R.L., 1993. Internal structure and weakening mechanisms of the san andreas fault. Journal of Geophysical Research: Solid Earth 98, 771–786.

Christen, J., Fox, C., 2005. Markov chain monte carlo using an approximation. Journal of Computational and Graphical Statistics 14, 795–810. doi:10.1198/106186005X76983.

Cockburn, B., Karniadakis, G.E., Shu, C.W., 2012. Discontinuous Galerkin methods: theory, computation and applications. volume 11. Springer Science & Business Media.

Cockburn, B., Shu, C.W., 1989. TVB Runge-Kutta local projection discontinuous Galerkin finite element method for conservation laws. II. General framework. Mathematics of computation 52, 411–435.

Cui, T., Law, K.J., Marzouk, Y.M., 2016. Dimension-independent likelihood-informed MCMC. Journal of Computational Physics 304, 109 – 137. URL: http://www.sciencedirect.com/science/article/pii/S0021999115006701, doi:https://doi.org/10.1016/j.jcp.2015.10.008.

Cui, Y., Olsen, K.B., Jordan, T.H., Lee, K., Zhou, J., Small, P., Roten, D., Ely, G., Panda, D.K., Chourasia, A., et al., 2010. Scalable earthquake simulation on petascale supercomputers, in: SC'10: Proceedings of the 2010 ACM/IEEE International Conference for High Performance Computing, Networking, Storage and Analysis, IEEE. pp. 1–20.

Darabi, M.K., Al-Rub, R.K.A., Little, D.N., 2012. A continuum damage mechanics framework for modeling micro-damage healing. International Journal of Solids and Structures 49, 492–513.

Darendeli, M.B., 2001. Development of a new family of normalized modulus reduction and material damping curves. The university of Texas at Austin.

Das, S., Aki, K., 1977. Fault plane with barriers: A versatile earthquake model. Journal of geophysical research 82, 5658–5670.

Day, S.M., Dalguer, L.A., Lapusta, N., Liu, Y., 2005. Comparison of finite difference and boundary integral solutions to three-dimensional spontaneous rupture. Journal of Geophysical Research: Solid Earth 110.

de la Puente, J., Dumbser, M., Käser, M., Igel, H., 2008. Discontinuous Galerkin methods for wave propagation in poroelastic media. Geophysics 73, T77–T97. doi:10.1190/1.2965027.

de la Puente, J., Käser, M., Dumbser, M., Igel, H., 2007. An arbitrary high-order discontinuous Galerkin method for elastic waves on unstructured meshes - IV. Anisotropy. Geophysical Journal International 169, 1210–1228. doi:10.1111/j.1365-246X.2007.03381.x.

Delsanto, P.P., Scalerandi, M., 2003. Modeling nonclassical nonlinearity, conditioning, and slow dynamics effects in mesoscopic elastic materials. Physical Review B 68, 064107.

Desmorat, R., 2016. Anisotropic damage modeling of concrete materials. International Journal of Damage Mechanics 25, 818–852.

Dieterich, J.H., 1979. Modeling of rock friction: 1. experimental results and constitutive equations. Journal of Geophysical Research: Solid Earth 84, 2161–2168.

Diot, S., Loubère, R., Clain, S., 2013. The multidimensional optimal order detection method in the three-dimensional case: very high-order finite volume method for hyperbolic systems. International Journal for Numerical Methods in Fluids 73, 362–392.

Dodwell, T., Ketelsen, C., Scheichl, R., Teckentrup, A., 2019. Multilevel Markov chain Monte Carlo. SIAM Review 61, 509–545. doi:10.1137/19M126966X.

Dolan, J.F., Haravitch, B.D., 2014. How well do surface slip measurements track slip at depth in large strike-slip earthquakes? The importance of fault structural maturity in controlling on-fault slip versus off-fault surface deformation. Earth and Planetary Science Letters 388, 38–47.

Dorozhinskii, R., Bader, M., 2021. SeisSol on Distributed Multi-GPU Systems: CUDA Code Generation for the Modal Discontinuous Galerkin Method, in: The International Conference on High Performance Computing in Asia-Pacific Region, Association for Computing Machinery, New York, NY, USA. pp. 69–82. doi:10.1145/3432261.3436753.

Duane, S., Kennedy, A., Pendleton, B.J., Roweth, D., 1987. Hybrid Monte Carlo. Physics Letters B 195, 216 – 222. URL: http://www.sciencedirect.com/science/article/pii/037026938791197X, doi:https://doi.org/10.1016/0370-2693(87)91197-X.

Dumbser, M., Balsara, D.S., Toro, E.F., Munz, C.D., 2008. A unified framework for the construction of one-step finite volume and discontinuous Galerkin schemes on unstructured meshes. Journal of Computational Physics 227, 8209–8253.

Dumbser, M., Käser, M., 2006. An arbitrary high-order discontinuous Galerkin method for elastic waves on unstructured meshes - II. The three-dimensional isotropic case. Geophysical Journal International 167, 319–336. doi:10.1111/j.1365-246X.2006.03120.x.

Dumbser, M., Käser, M., Toro, E.F., 2007. An arbitrary high-order Discontinuous Galerkin method for elastic waves on unstructured meshes – V. Local time stepping and p-adaptivity. Geophysical Journal International 171, 695–717. doi:10.1111/j.1365-246X.2007.03427.x.

Dunham, E.M., 2007. Conditions governing the occurrence of supershear ruptures under slip-weakening friction. Journal of Geophysical Research: Solid Earth 112.

Dunham, E.M., Archuleta, R.J., 2005. Near-source ground motion from steady state dynamic rupture pulses. Geophysical Research Letters 32.

Dunham, E.M., Belanger, D., Cong, L., Kozdon, J.E., 2011. Earthquake ruptures with strongly rate-weakening friction and off-fault plasticity, part 2: Nonplanar faults. Bulletin of the Seismological Society of America 101, 2308–2322.

DuRoss, C.B., Gold, R.D., Dawson, T.E., Scharer, K.M., Kendrick, K.J., Akciz, S.O., Angster, S.J., Bachhuber, J., Bacon, S., Bennett, S.E., et al., 2020. Surface displacement distributions for the July 2019 Ridgecrest, California, earthquake ruptures. Bulletin of the Seismological Society of America 110, 1400–1418.

Egorov, A., Correa, J., Bóna, A., Pevzner, R., Tertyshnikov, K., Glubokovskikh, S., Puzyrev, V., Gurevich, B., 2018. Elastic full-waveform inversion of vertical seismic profile data acquired with distributed acoustic sensors. Geophysics 83, R273–R281.

Einav, I., 2007a. Breakage mechanics—part i: theory. Journal of the Mechanics and Physics of Solids 55, 1274–1297.

Einav, I., 2007b. Breakage mechanics—part ii: Modelling granular materials. Journal of the Mechanics and Physics of Solids 55, 1298–1320.

Esmaeilzadeh, A., Motazedian, D., Hunter, J., 2019. 3D nonlinear ground-motion simulation using a physics-based method for the Kinburn basin. Bulletin of the Seismological Society of America 109, 1282–1311.

Fan, W., Shearer, P.M., 2015. Detailed rupture imaging of the 25 April 2015 Nepal earthquake using teleseismic P waves. Geophysical Research Letters 42, 5744–5752.

Favrie, N., Lombard, B., Payan, C., 2015. Fast and slow dynamics in a nonlinear elastic bar excited by longitudinal vibrations. Wave Motion 56, 221–238. URL: https://www.sciencedirect.com/science/article/pii/S0165212515000311, doi:https://doi.org/10.1016/j.wavemoti.2015.02.014.

Fei, F., Mia, M.S., Elbanna, A.E., Choo, J., 2023. A phase-field model for quasi-dynamic nucleation, growth, and propagation of rate-and-state faults. International Journal for Numerical and Analytical Methods in Geomechanics 47, 187–211.

Feng, X., Fehler, M., Brown, S., Szabo, T.L., Burns, D., 2018. Short-period nonlinear viscoelastic memory of rocks revealed by copropagating longitudinal acoustic waves. Journal of Geophysical Research: Solid Earth 123, 3993–4006.

Fialko, Y., Sandwell, D., Simons, M., Rosen, P., 2005. Three-dimensional deformation caused by the Bam, Iran, earthquake and the origin of shallow slip deficit. Nature 435, 295–299.

Fichtner, A., Trampert, J., Cupillard, P., Saygin, E., Taymaz, T., Capdeville, Y., Villasenor, A., 2013. Multiscale full waveform inversion. Geophysical Journal International 194, 534–556.

Fichtner, A., Walter, F., Paitz, P., Klaasen, S., Bowden, D.C., Noe, S., Müller, N., Husmann, D., Morel, J., 2025. An illustrated guide to: Distributed and integrated fibre-optic sensing in seismology. Earthquake Science 38, 67–77.

Fichtner, A., Zunino, A., Gebraad, L., 2019. Hamiltonian Monte Carlo solution of tomographic inverse problems. Geophysical Journal International 216, 1344–1363.

Finzi, Y., Langer, S., 2012. Damage in step-overs may enable large cascading earthquakes. Geophysical Research Letters 39.

Floyd, M., Funning, G., Fialko, Y., Terry, R., Herring, T., 2020. Survey and continuous GNSS in the vicinity of the July 2019 Ridgecrest earthquakes. Seismological Research Letters 91, 2047–2054.

Fukuyama, E., Mikumo, T., 1993. Dynamic rupture analysis: Inversion for the source process of the 1990 Izu-Oshima, Japan, earthquake (M = 6.5). Journal of Geophysical Research: Solid Earth 98.

Gabriel, A.A., Ampuero, J.P., Dalguer, L., Mai, P.M., 2012. The transition of dynamic rupture styles in elastic media under velocity-weakening friction. Journal of Geophysical Research: Solid Earth 117.

Gabriel, A.A., Ampuero, J.P., Dalguer, L., Mai, P.M., 2013. Source properties of dynamic rupture pulses with off-fault plasticity. Journal of Geophysical Research: Solid Earth 118, 4117–4126.

Gabriel, A.A., Garagash, D.I., Palgunadi, K.H., Mai, P.M., 2024. Fault size–dependent fracture energy explains multiscale seismicity and cascading earthquakes. Science 385, eadj9587.

Gabriel, A.A., Li, D., Chiocchetti, S., Tavelli, M., Peshkov, I., Romenski, E., Dumbser, M., 2021. A unified first-order hyperbolic model for nonlinear dynamic rupture processes in diffuse fracture zones. Philosophical Transactions of the Royal Society A 379, 20200130.

Gabriel, A.A., Ulrich, T., Marchandon, M., Biemiller, J., Rekoske, J., 2023. 3D dynamic rupture modeling of the 6 February 2023, Kahramanmaraş, Turkey M_W 7.8 and 7.7 earthquake doublet using early observations. The Seismic Record 3, 342–356.

Gajst, H., 2020. Deformation Bands Damage Localization Processes and Damage Rheoloy. Ph.D. thesis. Tel Aviv University.

Gallovič, F., Valentová, L., 2020. Earthquake stress drops from dynamic rupture simulations constrained by observed ground motions. Geophysical Research Letters 47, e2019GL085880.

Gallovič, F., Valentová, L., Ampuero, J.P., Gabriel, A.A., 2019. Bayesian dynamic finite-fault inversion: 2. Application to the 2016 Mw 6.2 Amatrice, Italy, earthquake. Journal of Geophysical Research: Solid Earth 124, 6970–6988.

Gao, K., Euser, B.J., Rougier, E., Guyer, R.A., Lei, Z., Knight, E.E., Carmeliet, J., Johnson, P.A., 2018. Modeling of stick-slip behavior in sheared granular fault gouge using the combined finite-discrete element method. Journal of Geophysical Research: Solid Earth 123, 5774–5792.

Gassenmeier, M., Sens-Schönfelder, C., Eulenfeld, T., Bartsch, M., Victor, P., Tilmann, F., Korn, M., 2016. Field observations of seismic velocity changes caused by shaking-induced damage and healing due to mesoscopic nonlinearity. Geophysical Journal International 204, 1490–1502.

Gassner, G., Dumbser, M., Hindenlang, F., Munz, C.D., 2011. Explicit one-step time discretizations for discontinuous Galerkin and finite volume schemes based on local predictors. Journal of Computational Physics 230, 4232–4247.

Gebraad, L., Boehm, C., Fichtner, A., 2020. Bayesian elastic full-waveform inversion using Hamiltonian Monte Carlo. Journal of Geophysical Research: Solid Earth 125, e2019JB018428.

Geubelle, P.H., Rice, J.R., 1995. A spectral method for three-dimensional elastodynamic fracture problems. Journal of the Mechanics and Physics of Solids 43, 1791–1824.

Ghattas, O., Willcox, K., 2021. Learning physics-based models from data: perspectives from inverse problems and model reduction. Acta Numerica 30, 445–554. URL: https://www.cambridge.org/core/product/identifier/S0962492921000064/type/journal_article, doi:10.1017/S0962492921000064.

Giles, M.B., 2008. Multilevel Monte Carlo path simulation. Oper. Res. 56, 607–617. URL: https://doi.org/10.1287/opre.1070.0496, doi:10.1287/opre.1070.0496.

van Ginkel, J., Ruigrok, E., Wentinck, R., Herber, R., 2022. Amplification behaviour of compressional waves in unconsolidated sediments. Frontiers in Earth Science 10, 812658.

Godunov, S.K., Bohachevsky, I., 1959. Finite difference method for numerical computation of discontinuous solutions of the equations of fluid dynamics. Matematičeskij sbornik 47, 271–306.

Goldberg, D.E., Melgar, D., Sahakian, V., Thomas, A., Xu, X., Crowell, B., Geng, J., 2020. Complex rupture of an immature fault zone: A simultaneous kinematic model of the 2019 ridgecrest, ca earthquakes. Geophysical Research Letters 47, e2019GL086382.

Good, I.J., 1963. Maximum entropy for hypothesis formulation, especially for multidimensional contingency tables. The Annals of Mathematical Statistics 34, 911–934.

Graves, R.W., 1996. Simulating seismic wave propagation in 3D elastic media using staggered-grid finite differences. Bulletin of the Seismological Society of America 86, 1091–1106.

Guyer, R.A., Johnson, P.A., 1999. Nonlinear mesoscopic elasticity: Evidence for a new class of materials. Physics today 52, 30–36.

Haario, H., Saksman, E., Tamminen, J., 2001. An adaptive Metropolis algorithm. Bernoulli 7. doi:10.2307/3318737.

Hamiel, Y., Katz, O., Lyakhovsky, V., Reches, Z., Fialko, Y., 2006. Stable and unstable damage evolution in rocks with implications to fracturing of granite. Geophysical Journal International 167, 1005–1016.

Hamiel, Y., Lyakhovsky, V., Ben-Zion, Y., 2011. The elastic strain energy of damaged solids with applications to non-linear deformation of crystalline rocks. Pure and Applied Geophysics 168, 2199–2210.

Hamiel, Y., Lyakhovsky, V., Stanchits, S., Dresen, G., Ben-Zion, Y., 2009. Brittle deformation and damage-induced seismic wave anisotropy in rocks. Geophysical Journal International 178, 901–909.

Hanagan, C., Bennett, R., Barbour, A., Hughes, A.N., 2024. Afterslip and creep in the rate-dependent framework: Joint inversion of borehole strain and GNSS displacements for the Mw 7.1 Ridgecrest earthquake. Journal of Geophysical Research: Solid Earth 129, e2024JB028908.

Hanks, T.C., 1982. f max. Bulletin of the seismological Society of America 72, 1867–1879.

Hanks, T.C., McGuire, R.K., 1981. The character of high-frequency strong ground motion. Bulletin of the Seismological Society of America 71, 2071–2095.

Harris, R.A., Barall, M., Aagaard, B., Ma, S., Roten, D., Olsen, K., Duan, B., Liu, D., Luo, B., Bai, K., Ampuero, J., Kaneko, Y., Gabriel, A., Duru, K., Ulrich, T., Wollherr, S., Shi, Z., Dunham, E., Bydlon, S., Zhang, Z., Chen, X., Somala, S.N., Pelties, C., Tago, J., Cruz-Atienza, V.M., Kozdon, J., Daub, E., Aslam, K., Kase, Y., Withers, K., Dalguer, L., 2018. A suite of exercises for verifying dynamic earthquake rupture codes. Seismological Research Letters 89, 1146–1162.

Harris, R.A., Barall, M., Archuleta, R., Dunham, E., Aagaard, B., Ampuero, J.P., Bhat, H., Cruz-Atienza, V., Dalguer, L., Dawson, P., et al., 2009. The SCEC/USGS dynamic earthquake rupture code verification exercise. Seismological Research Letters 80, 119–126.

Hartmann, R., Houston, P., 2002. Adaptive discontinuous Galerkin finite element methods for the compressible Euler equations. Journal of Computational Physics 183, 508–532.

Hartzell, S., Meremonte, M., Ramírez-Guzmán, L., McNamara, D., 2014. Ground motion in the presence of complex topography: Earthquake and ambient noise sources. Bulletin of the Seismological Society of America 104, 451–466.

Hastings, W.K., 1970. Monte Carlo sampling methods using Markov chains and their applications. Biometrika 57, 97–109.

Hauksson, E., Jones, L.M., Hutton, K., Eberhart-Phillips, D., 1993. The 1992 Landers earthquake sequence: Seismological observations. Journal of Geophysical Research: Solid Earth 98, 19835–19858.

Hauksson, E., Yoon, C., Yu, E., Andrews, J.R., Alvarez, M., Bhadha, R., Thomas, V., 2020. Caltech/USGS Southern California Seismic Network (SCSN) and Southern California Earthquake Data Center (SCEDC): Data availability for the 2019 Ridgecrest sequence. Seismological Research Letters 91, 1961–1970.

Hayek, J.N., Marchandon, M., Li, D., Pousse-Beltran, L., Hollingsworth, J., Li, T., Gabriel, A.A., 2024. Non-typical supershear rupture: Fault heterogeneity and segmentation govern unilateral supershear and cascading multi-fault rupture in the 2021 7.4 Maduo earthquake. Geophysical Research Letters 51, e2024GL110128. URL: https://agupubs.onlinelibrary.wiley.com/doi/abs/10.1029/2024GL110128, doi:https://doi.org/10.1029/2024GL110128, arXiv:https://agupubs.onlinelibrary.wiley.com/doi/pdf/10.1029/2024GL110128. e2024GL110128 2024GL110128.

Hayek, J.N., May, D.A., Pranger, C., Gabriel, A.A., 2023. A diffuse interface method for earthquake rupture dynamics based on a phase-field model. Journal of Geophysical Research: Solid Earth 128, e2023JB027143.

Heinecke, A., Breuer, A., Cui, Y., 2019. Tensor-optimized hardware accelerates fused discontinuous Galerkin simulations. Parallel Computing 89, 102550.

Heinecke, A., Breuer, A., Rettenberger, S., Bader, M., Gabriel, A., Pelties, C., Bode, A., Barth, W., Liao, X., Vaidyanathan, K., Smelyanskiy, M., Dubey, P., 2014. Petascale High Order Dynamic Rupture Earthquake Simulations on Heterogeneous Supercomputers, in: SC14: Proceedings of the International Conference for High Performance Computing, Networking, Storage and Analysis, pp. 3–14. doi:10.1109/SC.2014.6.

Herrera, M.T., Ampuero, J.P., Crempien, J.G., 2024. A proxy implementation of thermal pressurization for earthquake cycle modelling on rate-and-state faults. Geophysical Journal International 237, 1432–1441.

Hesthaven, J.S., Warburton, T., 2007. Nodal discontinuous Galerkin methods: algorithms, analysis, and applications. Springer Science & Business Media.

Homan, M.D., Gelman, A., 2014. The no-u-turn sampler: adaptively setting path lengths in hamiltonian monte carlo. J. Mach. Learn. Res. 15, 1593–1623.

Hughes, D.S., Kelly, J., 1953. Second-order elastic deformation of solids. Physical review 92, 1145.

Iaffaldano, G., Bunge, H.P., 2009. Relating rapid plate-motion variations to plate-boundary forces in global coupled models of the mantle/lithosphere system: Effects of topography and friction. Tectonophysics 474, 393–404.

Iai, S., Matsunaga, Y., Kameoka, T., 1990. Strain space plasticity model for cyclic mobility. Report of the Port and harbour Research Institute 29.

Idini, B., Ampuero, J.P., 2020. Fault-zone damage promotes pulse-like rupture and back-propagating fronts via quasi-static effects. Geophysical Research Letters 47, e2020GL090736.

Igel, H., Mora, P., Riollet, B., 1995. Anisotropic wave propagation through finite-difference grids. Geophysics 60, 1203–1216.

Ikari, M.J., Marone, C., Saffer, D.M., 2011. On the relation between fault strength and frictional stability. Geology 39, 83–86.

Illien, L., Sens-Schönfelder, C., Andermann, C., Marc, O., Cook, K.L., Adhikari, L.B., Hovius, N., 2022. Seismic velocity recovery in the subsurface: transient damage and groundwater drainage following the 2015 Gorkha earthquake, Nepal. Journal of Geophysical Research: Solid Earth 127, e2021JB023402.

IPOC, 2006. IPOC Seismic Network, GFZ German Research Centre for Geosciences, Institut des Sciences de l'Univers-Centre National de la Recherche CNRS-INSU. doi:10.14470/PK615318.

Iwan, W.D., 1967. On a class of models for the yielding behavior of continuous and composite systems. Journal of Applied Mechanics 34, 612–617.

Jacob, N.I., Israelachvili, N., 1992. Intermolecular and surface forces. San Diego: Academic .

Jiao, J., Li, Z., Li, L., Li, G., Lu, X., 2025. Nondestructive evaluation of adhesive joints using nonlinear non-collinear wave mixing technique. Journal of Nondestructive Evaluation 44, 1–15.

Jin, J., Rivière, J., Ohara, Y., Shokouhi, P., 2018. Dynamic acousto-elastic response of single fatigue cracks with different microstructural features: An experimental investigation. Journal of Applied Physics 124, 075303.

Jin, Z., Fialko, Y., Zubovich, A., Schöne, T., 2022. Lithospheric deformation due to the 2015 M7.2 Sarez (Pamir) earthquake constrained by 5 years of space geodetic observations. Journal of Geophysical Research: Solid Earth 127, e2021JB022461.

Johnson, P., Sutin, A., 2005. Slow dynamics and anomalous nonlinear fast dynamics in diverse solids. The Journal of the Acoustical Society of America 117, 124–130.

Johnson, P.A., Rasolofosaon, P.N., 1993. Nonlinear elasticity and stress-induced anisotropy in rocks: reflections on experimental results, in: SEG Technical Program Expanded Abstracts 1993. Society of Exploration Geophysicists, pp. 792–795.

Johnson, S.E., Song, W.J., Vel, S.S., Song, B.R., Gerbi, C.C., 2021. Energy partitioning, dynamic fragmentation, and off-fault damage in the earthquake source volume. Journal of Geophysical Research: Solid Earth 126, e2021JB022616.

Kachanov, L., 1958. On creep rupture time. Izv. Acad. Nauk SSSR, Otd. Techn. Nauk 8, 26–31.

Kachanov, L., 1986. Introduction to continuum damage mechanics. volume 10. Springer Science & Business Media.

Kaipio, J., Somersalo, E., 2005. Statistical and computational inverse problems. volume 160 of *Applied mathematical sciences*. Springer.

Kanamori, H., Rivera, L., 2006. Energy partitioning during an earthquake. Geophysical Monograph Series 170, 3–13.

Kaneko, Y., Fialko, Y., 2011. Shallow slip deficit due to large strike-slip earthquakes in dynamic rupture simulations with elasto-plastic off-fault response. Geophysical Journal International 186, 1389–1403.

Käser, M., Dumbser, M., De La Puente, J., Igel, H., 2007. An arbitrary high-order discontinuous Galerkin method for elastic waves on unstructured meshes—III. Viscoelastic attenuation. Geophysical Journal International 168, 224–242.

Käser, M., Hermann, V., Puente, J.d.l., 2008. Quantitative accuracy analysis of the discontinuous Galerkin method for seismic wave propagation. Geophysical Journal International 173, 990–999.

King, G., 1986. Speculations on the geometry of the initiation and termination processes of earthquake rupture and its relation to morphology and geological structure. Pure and applied geophysics 124, 567–585.

Kirk, S.S., Williamson, D.M., 2012. Structure and thermal properties of porous geological materials, in: AIP Conference Proceedings, American Institute of Physics. pp. 867–870.

Kojima, K., Takewaki, I., 2016. Closed-form critical earthquake response of elastic–plastic structures on compliant ground under near-fault ground motions. Frontiers in Built Environment 2, 1.

Komatitsch, D., Tromp, J., 1999. Introduction to the spectral-element method for three-dimensional seismic wave propagation. Geophysical Journal International 139, 806–822.

Komatitsch, D., Vilotte, J.P., 1998. The spectral element method: An efficient tool to simulate the seismic response of 2D and 3D geological structures. Bulletin of the Seismological Society of America 88, 368–392.

Kovalevskaja, S.V., 1874. Zur Theorie der partiellen Differentialgleichungen.

Kozdon, J.E., Dunham, E.M., Nordström, J., 2013. Simulation of dynamic earthquake ruptures in complex geometries using high-order finite difference methods. Journal of Scientific Computing 55, 92–124.

Kramer, S.L., Stewart, J.P., 2024. Geotechnical earthquake engineering. CRC Press.

Krenz, L., Uphoff, C., Ulrich, T., Gabriel, A.A., Abrahams, L.S., Dunham, E.M., Bader, M., 2021. 3D acoustic-elastic coupling with gravity: The dynamics of the 2018 Palu, Sulawesi earthquake and tsunami, in: Proceedings of the International Conference for High Performance Computing, Networking, Storage and Analysis, Association for Computing Machinery, New York, NY, USA. pp. 1–14. doi:10.1145/3458817.3476173.

Kruse, M., Niu, Z., Wolf, S., Lykkegaard, M., Bader, M., Gabriel, A.A., Seelinger, L., 2024. Scalable bayesian inference of large simulations via asynchronous prefetching multilevel delayed acceptance. URL: https://doi.org/10.5281/zenodo.14315615, doi:10.5281/zenodo.14315615.

Kruse, M., Niu, Z., Wolf, S., Lykkegaard, M.B., Bader, M., Gabriel, A.A., Seelinger, L., 2025. Scalable bayesian inference of large simulations via asynchronous prefetching multilevel delayed acceptance. arXiv .

Kumagai, H., Saito, T., O'Brien, G., Yamashina, T., 2011. Characterization of scattered seismic wavefields simulated in heterogeneous media with topography. Journal of Geophysical Research: Solid Earth 116.

Kumar, R., Carroll, C., Hartikainen, A., Martin, O., 2019. Arviz a unified library for exploratory analysis of bayesian models in python. Journal of Open Source Software 4, 1143. URL: https://doi.org/10.21105/joss.01143, doi:10.21105/joss.01143.

Kurzon, I., Lyakhovsky, V., Sagy, A., Ben-Zion, Y., 2022. Radiated seismic energy and source damage evolution from the analysis of simulated dynamic rupture and far-field seismograms. Geophysical Journal International 231, 1705–1726.

Landau, L.D., Lifšic, E.M., Lifshitz, E.M., Kosevich, A.M., Pitaevskii, L.P., 1986. Theory of elasticity: volume 7. volume 7. Elsevier.

Lapusta, N., Liu, Y., 2009. Three-dimensional boundary integral modeling of spontaneous earthquake sequences and aseismic slip. Journal of Geophysical Research: Solid Earth 114.

Lapusta, N., Rice, J.R., Ben-Zion, Y., Zheng, G., 2000. Elastodynamic analysis for slow tectonic loading with spontaneous rupture episodes on faults with rate-and state-dependent friction. Journal of Geophysical Research: Solid Earth 105, 23765–23789.

Lax, P.D., 2005. Weak solutions of nonlinear hyperbolic equations and their numerical computation, in: Selected Papers Volume I. Springer, pp. 198–232.

Lebedev, A., Ostrovsky, L., 2014. A unified model of hysteresis and long-time relaxation in heterogeneous materials. Acoustical Physics 60, 555–561.

Lee, E.J., Chen, P., Jordan, T.H., Maechling, P.B., Denolle, M.A., Beroza, G.C., 2014. Full-3-D tomography for crustal structure in southern California based on the scattering-integral and the adjoint-wavefield methods. Journal of Geophysical Research: Solid Earth 119, 6421–6451.

Lee, S.J., Komatitsch, D., Huang, B.S., Tromp, J., 2009. Effects of topography on seismic-wave propagation: An example from northern Taiwan. Bulletin of the Seismological Society of America 99, 314–325.

Lemaitre, J., Desmorat, R., 2006. Engineering damage mechanics: ductile, creep, fatigue and brittle failures. Springer Science & Business Media.

LeVeque, R.J., 2002. Finite volume methods for hyperbolic problems. volume 31. Cambridge university press.

Li, G., Ben-Zion, Y., 2023. Daily and seasonal variations of shallow seismic velocities in southern California from joint analysis of H/V ratios and autocorrelations of seismic waveforms. Journal of Geophysical Research: Solid Earth 128, e2022JB025682.

Liang, B., Tan, J., Lozenski, L., Hormuth, D.A., Yankeelov, T.E., Villa, U., Faghihi, D., 2023. Bayesian inference of tissue heterogeneity for individualized prediction of glioma growth. IEEE Transactions on Medical Imaging 42, 2865–2875. URL: https://doi.org/10.1109/TMI.2023.3267349. publisher: IEEE.

Lieou, C.K., Daub, E.G., Ecke, R.E., Johnson, P.A., 2017. Slow dynamics and strength recovery in unconsolidated granular earth materials: A mechanistic theory. Journal of Geophysical Research: Solid Earth 122, 7573–7583.

Lindelöf, E., 1894. Sur l'application de la méthode des approximations successives aux équations différentielles ordinaires du premier ordre. Comptes rendus hebdomadaires des séances de l'Académie des sciences 116, 454–457.

Liu, Z., Duan, B., 2014. Dynamics of parallel strike-slip faults with pore fluid pressure change and off-fault damage. Bulletin of the Seismological Society of America 104, 780–792.

Lott, M., Remillieux, M.C., Garnier, V., Le Bas, P.Y., Ulrich, T., Payan, C., 2017. Nonlinear elasticity in rocks: A comprehensive three-dimensional description. Physical Review Materials 1, 023603.

Loubere, R., Dumbser, M., Diot, S., 2014. A new family of high order unstructured mood and ader finite volume schemes for multidimensional systems of hyperbolic conservation laws. Communications in Computational Physics 16, 718–763.

Lowrie, W., Fichtner, A., 2020. Fundamentals of geophysics. Cambridge university press.

Lu, Y., Ben-Zion, Y., 2022. Regional seismic velocity changes following the 2019 Mw 7.1 Ridgecrest, California earthquake from autocorrelations and P/S converted waves. Geophysical Journal International 228, 620–630.

Lyakhovsky, V., Ben-Zion, Y., 2014. A continuum damage–breakage faulting model and solid-granular transitions. Pure and Applied Geophysics 171, 3099–3123.

Lyakhovsky, V., Ben-Zion, Y., Agnon, A., 1997a. Distributed damage, faulting, and friction. Journal of Geophysical Research: Solid Earth 102, 27635–27649.

Lyakhovsky, V., Ben-Zion, Y., Ilchev, A., Mendecki, A., 2016. Dynamic rupture in a damage-breakage rheology model. Geophysical Journal International 206, 1126–1143.

Lyakhovsky, V., Panteleev, I., Shalev, E., Browning, J., Mitchell, T.M., Healy, D., Meredith, P.G., 2022. A new anisotropic poroelasticity model to describe damage accumulation during cyclic triaxial loading of rock. Geophysical Journal International 230, 179–201.

Lyakhovsky, V., Reches, Z., Weinberger, R., Scott, T.E., 1997b. Non-linear elastic behaviour of damaged rocks. Geophysical Journal International 130, 157–166.

Lyakhovsky, V., Sagy, A., Kurzon, I., 2023. Simulated rupture dynamics and radiated energy on heterogeneously damaged faults. Journal of Geophysical Research: Solid Earth 128, e2022JB025559.

Lykkegaard, M.B., Dodwell, T.J., Fox, C., Mingas, G., Scheichl, R., 2023. Multilevel delayed acceptance MCMC. SIAM/ASA Journal on Uncertainty Quantification 11, 1–30. URL: https://doi.org/10.1137/22M1476770, doi:10.1137/22M1476770, arXiv:https://doi.org/10.1137/22M1476770.

Ma, S., 2008. A physical model for widespread near-surface and fault zone damage induced by earthquakes. Geochemistry, Geophysics, Geosystems 9.

Ma, X., Hertrich, M., Amann, F., Bröker, K., Gholizadeh Doonechaly, N., Gischig, V., Hochreutener, R., Kästli, P., Krietsch, H., Marti, M., et al., 2022. Multi-disciplinary characterizations of the bedrettolab–a new underground geoscience research facility. Solid Earth 13, 301–322.

Madariaga, R., 1976. Dynamics of an expanding circular fault. Bulletin of the Seismological Society of America 66, 639–666.

Madariaga, R., 1977. High-frequency radiation from crack (stress drop) models of earthquake faulting. Geophysical Journal International 51, 625–651.

Maggi, A., Jackson, J., Mckenzie, D., Priestley, K., 2000. Earthquake focal depths, effective elastic thickness, and the strength of the continental lithosphere. Geology 28, 495–498.

Manighetti, I., Mercier, A., De Barros, L., 2021. Fault trace corrugation and segmentation as a measure of fault structural maturity. Geophysical Research Letters 48, e2021GL095372.

Manogharan, P., Wood, C., Marone, C., Elsworth, D., Rivière, J., Shokouhi, P., 2021. Nonlinear elastodynamic behavior of intact and fractured rock under in-situ stress and saturation conditions. Journal of the Mechanics and Physics of Solids 153, 104491.

Manogharan, P., Wood, C., Marone, C., Elsworth, D., Rivière, J., Shokouhi, P., 2022. Experimental investigation of elastodynamic nonlinear response of dry intact, fractured and saturated rock. Rock Mechanics and Rock Engineering 55, 2665–2678.

Marra, G., Clivati, C., Luckett, R., Tampellini, A., Kronjäger, J., Wright, L., Mura, A., Levi, F., Robinson, S., Xuereb, A., et al., 2018. Ultrastable laser interferometry for earthquake detection with terrestrial and submarine cables. Science 361, 486–490.

Marty, M., de Kruijf, M., Adriaens, J., Alfeld, C., Bauer, S., Contavalli, C., Dalton, M., Dukkipati, N., Evans, W.C., Gribble, S., et al., 2019a. Snap: A microkernel approach to host networking, in: Proceedings of the 27th ACM Symposium on Operating Systems Principles, pp. 399–413.

Marty, S., Passelègue, F., Aubry, J., Bhat, H., Schubnel, A., Madariaga, R., 2019b. Origin of high-frequency radiation during laboratory earthquakes. Geophysical Research Letters 46, 3755–3763.

Matlack, K.H., Kim, J.Y., Jacobs, L.J., Qu, J., 2015. Review of second harmonic generation measurement techniques for material state determination in metals. Journal of Nondestructive Evaluation 34, 273.

Mayergoyz, I., 1985. Hysteresis models from the mathematical and control theory points of view. Journal of Applied Physics 57, 3803–3805.

McBeck, J., Ben-Zion, Y., Renard, F., 2022. Predicting fault reactivation and macroscopic failure in discrete element method simulations of restraining and releasing step overs. Earth and Planetary Science Letters 593, 117667.

McCall, K., 1994. Theoretical study of nonlinear elastic wave propagation. Journal of Geophysical Research: Solid Earth 99, 2591–2600.

McCall, K., Guyer, R., 1996. A new theoretical paradigm to describe hysteresis, discrete memory and nonlinear elastic wave propagation in rock. Nonlinear processes in geophysics 3, 89–101.

McNamara, D.E., Yeck, W.L., Barnhart, W.D., Schulte-Pelkum, V., Bergman, E., Adhikari, L., Dixit, A., Hough, S., Benz, H.M., Earle, P.S., 2017. Source modeling of the 2015 Mw 7.8 Nepal (Gorkha) earthquake sequence: Implications for geodynamics and earthquake hazards. Tectonophysics 714, 21–30.

Melgar, D., Melbourne, T.I., Crowell, B.W., Geng, J., Szeliga, W., Scrivner, C., Santillan, M., Goldberg, D.E., 2020. Real-time high-rate GNSS displacements: Performance demonstration during the 2019 Ridgecrest, California, earthquakes. Seismological Research Letters 91, 1943–1951.

Mellors, R.J., Pitarka, A., Matzel, E., Magana-Zook, S., Knapp, D., Walter, W.R., Chen, T., Snelson, C.M., Abbott, R.E., 2018. The source physics experiments large N array. Seismological Research Letters 89, 1618–1628.

Metropolis, N., Rosenbluth, A.W., Rosenbluth, M.N., Teller, A.H., Teller, E., 1953. Equation of state calculations by fast computing machines. The Journal of Chemical Physics 21, 1087–1092. doi:10.1063/1.1699114.

Meurer, T., Qu, J., Jacobs, L., 2002. Wave propagation in nonlinear and hysteretic media—-a numerical study. International Journal of Solids and Structures 39, 5585–5614.

Mia, M.S., 2024. Spatiotemporal evolution of seismic and aseismic frictional sliding with bulk plasticity. Ph.D. thesis. University of Illinois at Urbana-Champaign.

Mia, M.S., Abdelmeguid, M., Harris, R.A., Elbanna, A.E., 2024. Rupture jumping and seismic complexity in models of earthquake cycles for fault stepovers with off-fault plasticity. Bulletin of the Seismological Society of America 114, 1466–1480.

Mikumo, T., Hirahara, K., Miyatake, T., 1987. Dynamical fault rupture processes in heterogeneous media. Tectonophysics 144, 19–36.

Milliner, C., Bürgmann, R., Inbal, A., Wang, T., Liang, C., 2020. Resolving the kinematics and moment release of early afterslip within the first hours following the 2016 Mw 7.1 Kumamoto earthquake: Implications for the shallow slip deficit and frictional behavior of aseismic creep. Journal of Geophysical Research: Solid Earth 125, e2019JB018928.

Mitchell, T., Faulkner, D., 2009. The nature and origin of off-fault damage surrounding strike-slip fault zones with a wide range of displacements: A field study from the atacama fault system, northern chile. Journal of Structural Geology 31, 802–816.

Moczo, P., Bard, P.Y., 1993. Wave diffraction, amplification and differential motion near strong lateral discontinuities. Bulletin of the Seismological Society of America 83, 85–106.

Molina-Ormazabal, D., Ampuero, J.P., Tassara, A., 2023. Diverse slip behaviour of velocity-weakening fault barriers. Nature Geoscience 16, 1200–1207.

Molnar, P., 2020. The brittle-plastic transition, earthquakes, temperatures, and strain rates. Journal of Geophysical Research: Solid Earth 125, e2019JB019335.

Morad, D., Sagy, A., Tal, Y., Hatzor, Y.H., 2022. Fault roughness controls sliding instability. Earth and Planetary Science Letters 579, 117365.

Morgan, W.J., 1968. Rises, trenches, great faults, and crustal blocks. Journal of Geophysical Research 73, 1959–1982.

Mosconi, F., Tinti, E., Casarotti, E., Gabriel, A.A., Rinaldi, A.P., Dal Zilio, L., Cocco, M., 2024. Modeling the 3D dynamic rupture of microearthquakes induced by fluid injection. Authorea Preprints .

Munjiza, A., 1992. Discrete elements in transient dynamics of fractured media. Ph.D. thesis. University College of Swansea.

Munjiza, A.A., 2004. The combined finite-discrete element method. John Wiley & Sons.

Murnaghan, F.D., 1937. Finite deformations of an elastic solid. American Journal of Mathematics 59, 235–260.

Narayan, J.P., Sahar, D., 2014. Three-dimensional viscoelastic finite-difference code and modelling of basement focusing effects on ground motion characteristics. Computational Geosciences 18, 1023–1047.

Nielsen, S., Spagnuolo, E., Violay, M., Smith, S., Di Toro, G., Bistacchi, A., 2016. G: Fracture energy, friction and dissipation in earthquakes. Journal of seismology 20, 1187–1205.

Niu, F., Silver, P.G., Nadeau, R.M., McEvilly, T.V., 2003. Migration of seismic scatterers associated with the 1993 parkfield aseismic transient event. Nature 426, 544–548.

Niu, Z., Gabriel, A.A., Sebastian, W., Vladimir, L., Ulrich, T., Heiner, I., 2025. Data for reproducing "A discontinuous Galerkin method for simulating 3D seismic wave propagation in nonlinear rock models: Verification and application to the 2015 M_w 7.8 Gorkha earthquake" [Software]. URL: https://doi.org/10.5281/zenodo.14712559, doi:10.5281/zenodo.14712559.

Niu, Z., Gabriel, A.A., Seelinger, L., Igel, H., 2024. Modeling and quantifying parameter uncertainty of co-seismic non-classical nonlinearity in rocks. Journal of Geophysical Research: Solid Earth 129, e2023JB027149.

Nur, A., 1971. Effects of stress on velocity anisotropy in rocks with cracks. Journal of Geophysical Research 76, 2022–2034.

Nur, A., Simmons, G., 1969. Stress-induced velocity anisotropy in rock: An experimental study. Journal of Geophysical Research 74, 6667–6674.

Oglesby, D.D., Archuleta, R.J., Nielsen, S.B., 1998. Earthquakes on dipping faults: The effects of broken symmetry. Science 280, 1055–1059.

Okada, Y., Kasahara, K., Hori, S., Obara, K., Sekiguchi, S., Fujiwara, H., Yamamoto, A., 2004. Recent progress of seismic observation networks in Japan—Hi-net, F-net, K-NET and KiK-net. Earth, Planets and Space 56, xv–xxviii.

Okubo, K., Bhat, H.S., Rougier, E., Marty, S., Schubnel, A., Lei, Z., Knight, E.E., Klinger, Y., 2019. Dynamics, radiation, and overall energy budget of earthquake rupture with coseismic off-fault damage. Journal of Geophysical Research: Solid Earth 124, 11771–11801.

Okubo, K., Rougier, E., Lei, Z., Bhat, H.S., 2020. Modeling earthquakes with off-fault damage using the combined finite-discrete element method. Computational particle mechanics 7, 1057–1072.

Okuwaki, R., Yagi, Y., 2018. Role of geometric barriers in irregular-rupture evolution during the 2008 Wenchuan earthquake. Geophysical Journal International 212, 1657–1664.

Olsen, K., Day, S., Bradley, C., 2003. Estimation of q for long-period (> 2 sec) waves in the Los Angeles basin. Bulletin of the Seismological Society of America 93, 627–638.

Olsen, K.B., Day, S.M., Cui, Y., 2008. Earthquake ground motion modeling using a staggered-grid finite-difference method. Bulletin of the Seismological Society of America 98, 1009–1020.

Operto, S., Miniussi, A., Brossier, R., Combe, L., Métivier, L., Monteiller, V., Ribodetti, A., Virieux, J., 2015. Efficient 3-D frequency-domain mono-parameter full-waveform inversion of ocean-bottom cable data: application to Valhall in the visco-acoustic vertical transverse isotropic approximation. Geophysical Journal International 202, 1362–1391.

Oral, E., Ayoubi, P., Ampuero, J.P., Asimaki, D., Bonilla, L.F., 2022. Kathmandu basin as a local modulator of seismic waves: 2-d modelling of non-linear site response under obliquely incident waves. Geophysical Journal International 231, 1996–2008.

Oral, E., Gélis, C., Bonilla, L.F., 2019. 2-D P-SV and SH spectral element modelling of seismic wave propagation in non-linear media with pore-pressure effects. Geophysical Journal International 217, 1353–1365.

Oth, A., Bindi, D., Parolai, S., Di Giacomo, D., 2011. Spectral analysis of K-NET and KiK-net data in Japan, Part II: On attenuation characteristics, source spectra, and site response of borehole and surface stations. Bulletin of the Seismological Society of America 101, 667–687.

Oucif, C., Mauludin, L.M., 2018. Continuum damage-healing and super healing mechanics in brittle materials: A state-of-the-art review. Applied Sciences 8, 2350.

Palgunadi, K.H., Gabriel, A.A., Garagash, D.I., Ulrich, T., Mai, P.M., 2024a. Rupture dynamics of cascading earthquakes in a multiscale fracture network. Journal of Geophysical Research: Solid Earth 129, e2023JB027578.

Palgunadi, K.H., Gabriel, A.A., Garagash, D.I., Ulrich, T., Schliwa, N., Mai, P.M., 2024b. Ground motion characteristics of cascading earthquakes in a multiscale fracture network. arXiv preprint arXiv:2412.15416 .

Panteleev, I., Lyakhovsky, V., Browning, J., Meredith, P.G., Healy, D., Mitchell, T.M., 2021. Non-linear anisotropic damage rheology model: Theory and experimental verification. European Journal of Mechanics-A/Solids 85, 104085.

Panteleev, I., Lyakhovsky, V., Shalev, E., 2024. Azimuthal pore pressure response to teleseismic waves: effects of damage and stress anisotropy. Geophysical Journal International , ggae081.

Pao, Y.H., Gamer, U., 1985. Acoustoelastic waves in orthotropic media. The Journal of the Acoustical Society of America 77, 806–812.

Parker, T., Shatalin, S., Farhadiroushan, M., 2014. Distributed acoustic sensing–a new tool for seismic applications. first break 32.

Parno, M., Davis, A., Seelinger, L., 2021. Muq: The mit uncertainty quantification library. Journal of Open Source Software 6, 3076.

Passelègue, F.X., Schubnel, A., Nielsen, S., Bhat, H.S., Deldicque, D., Madariaga, R., 2016. Dynamic rupture processes inferred from laboratory microearthquakes. Journal of Geophysical Research: Solid Earth 121, 4343–4365.

Pecorari, C., 2004. Adhesion and nonlinear scattering by rough surfaces in contact: Beyond the phenomenology of the Preisach–Mayergoyz framework. The Journal of the Acoustical Society of America 116, 1938–1947.

Pecorari, C., Solodov, I., 2006. Nonclassical nonlinear dynamics of solid surfaces in partial contact for NDE applications, in: Universality of Nonclassical Nonlinearity: Applications to Non-Destructive Evaluations and Ultrasonic. Springer, pp. 309–326.

Pelties, C., Gabriel, A.A., Ampuero, J.P., 2014. Verification of an ADER-DG method for complex dynamic rupture problems. Geoscientific Model Development 7, 847–866. doi:10.5194/gmd-7-847-2014.

Pelties, C., De la Puente, J., Ampuero, J.P., Brietzke, G.B., Käser, M., 2012. Three-dimensional dynamic rupture simulation with a high-order discontinuous Galerkin method on unstructured tetrahedral meshes. Journal of Geophysical Research: Solid Earth 117.

Persson, P.O., Peraire, J., 2006. Sub-cell shock capturing for discontinuous Galerkin methods, in: 44th AIAA aerospace sciences meeting and exhibit, p. 112.

Peyrat, S., Olsen, K., 2004. Nonlinear dynamic rupture inversion of the 2000 Western Tottori, Japan, earthquake. Geophysical research letters 31.

Plessix, R.E., Perkins, C., 2010. Thematic set: Full waveform inversion of a deep water ocean bottom seismometer dataset. First Break 28.

Poupinet, G., Ellsworth, W., Frechet, J., 1984. Monitoring velocity variations in the crust using earthquake doublets: An application to the Calaveras fault, California. Journal of Geophysical Research: Solid Earth 89, 5719–5731.

Poursartip, B., Fathi, A., Kallivokas, L.F., 2017. Seismic wave amplification by topographic features: A parametric study. Soil Dynamics and Earthquake Engineering 92, 503–527.

Pousse-Beltran, L., Nissen, E., Bergman, E.A., Cambaz, M.D., Gaudreau, É., Karasözen, E., Tan, F., 2020. The 2020 Mw 6.8 Elazığ (Turkey) earthquake reveals rupture behavior of the East Anatolian Fault. Geophysical Research Letters 47, e2020GL088136.

Power, W., Tullis, T., Brown, S., Boitnott, G., Scholz, C., 1987. Roughness of natural fault surfaces. Geophysical Research Letters 14, 29–32.

Powrie, W., 2018. Soil mechanics: concepts and applications. CRC Press.

Pranger, C., Sanan, P., May, D.A., Le Pourhiet, L., Gabriel, A.A., 2022. Rate and state friction as a spatially regularized transient viscous flow law. Journal of Geophysical Research: Solid Earth 127, e2021JB023511.

Preisach, F., 1935. Über die magnetische nachwirkung. Zeitschrift für physik 94, 277–302.

Premus, J., Gallovič, F., Ampuero, J.P., 2022. Bridging time scales of faulting: From coseismic to postseismic slip of the m w 6.0 2014 south napa, california earthquake. Science advances 8, eabq2536.

Premus, J., Gallovič, F., Hanyk, L., Gabriel, A.A., 2020. FD3D_TSN: a fast and simple code for dynamic rupture simulations with GPU acceleration. Seismological Research Letters 91, 2881–2889.

Preuss, S., Ampuero, J.P., Gerya, T., van Dinther, Y., 2020. Characteristics of earthquake ruptures and dynamic off-fault deformation on propagating faults. Solid Earth 11, 1333–1360.

Preuss, S., Herrendörfer, R., Gerya, T., Ampuero, J.P., van Dinther, Y., 2019. Seismic and aseismic fault growth lead to different fault orientations. Journal of Geophysical Research: Solid Earth 124, 8867–8889.

Puel, S., Khattatov, E., Villa, U., Liu, D., Ghattas, O., Becker, T.W., 2022. A mixed, unified forward/inverse framework for earthquake problems: fault implementation and coseismic slip estimate. Geophysical Journal International 230, 733–758. URL: https://doi.org/10.1093/gji/ggac050. oxford University Press.

de la Puente, J., Ampuero, J.P., Käser, M., 2009. Dynamic rupture modeling on unstructured meshes using a discontinuous Galerkin method. Journal of Geophysical Research: Solid Earth 114.

Qin, L., Ben-Zion, Y., Bonilla, L.F., Steidl, J.H., 2020. Imaging and monitoring temporal changes of shallow seismic velocities at the Garner Valley near Anza, California, following the M7.2 2010 El Mayor-Cucapah earthquake. Journal of Geophysical Research: Solid Earth 125, e2019JB018070.

Qiu, H., Hillers, G., Ben-Zion, Y., 2020a. Temporal changes of seismic velocities in the San Jacinto Fault zone associated with the 2016 Mw 5.2 Borrego Springs earthquake. Geophysical Journal International 220, 1536–1554.

Qiu, J., Shu, C.W., 2004. Hermite WENO schemes and their application as limiters for Runge–Kutta discontinuous Galerkin method: one-dimensional case. Journal of Computational Physics 193, 115–135.

Qiu, Q., Barbot, S., Wang, T., Wei, S., 2020b. Slip complementarity and triggering between the foreshock, mainshock, and afterslip of the 2019 Ridgecrest rupture sequence. Bulletin of the Seismological Society of America 110, 1701–1715.

Radice, D., Rezzolla, L., 2011. Discontinuous galerkin methods for general-relativistic hydrodynamics: Formulation and application to spherically symmetric spacetimes. Physical Review D 84, 024010.

Rajaure, S., Asimaki, D., Thompson, E.M., Hough, S., Martin, S., Ampuero, J., Dhital, M., Inbal, A., Takai, N., Shigefuji, M., et al., 2017. Characterizing the Kathmandu Valley sediment response through strong motion recordings of the 2015 Gorkha earthquake sequence. Tectonophysics 714, 146–157.

Rasmussen, C.E., Williams, C.K.I., 2006. Gaussian processes for machine learning. Adaptive computation and machine learning, MIT Press.

Reinarz, A., Charrier, D.E., Bader, M., Bovard, L., Dumbser, M., Duru, K., Fambri, F., Gabriel, A.A., Gallard, J.M., Köppel, S., et al., 2020. Exahype: an engine for parallel dynamically adaptive simulations of wave problems. Computer Physics Communications 254, 107251.

Remillieux, M.C., Ulrich, T., Goodman, H.E., Ten Cate, J.A., 2017. Propagation of a finite-amplitude elastic pulse in a bar of Berea sandstone: A detailed look at the mechanisms of classical nonlinearity, hysteresis, and nonequilibrium dynamics. Journal of Geophysical Research: Solid Earth 122, 8892–8909.

Renaud, G., Le Bas, P.Y., Johnson, P., 2012. Revealing highly complex elastic nonlinear (anelastic) behavior of earth materials applying a new probe: Dynamic acoustoelastic testing. Journal of Geophysical Research: Solid Earth 117.

Resnyansky, A., Romensky, E., Bourne, N., 2003. Constitutive modeling of fracture waves. Journal of applied physics 93, 1537–1545.

Rice, J.R., 1980. The mechanics of earthquake rupture. Physics of the Earth and Planetary Interiors 21, 227–234.

Rice, J.R., 1985. Constitutive relations for fault slip and earthquake instabilities. Instabilities in continuous media , 443–475.

Rice, J.R., Sammis, C.G., Parsons, R., 2005. Off-fault secondary failure induced by a dynamic slip pulse. Bulletin of the Seismological Society of America 95, 109–134.

Ripperger, J., Ampuero, J.P., Mai, P., Giardini, D., 2007. Earthquake source characteristics from dynamic rupture with constrained stochastic fault stress. Journal of Geophysical Research: Solid Earth 112.

Rivière, J., Pimienta, L., Scuderi, M., Candela, T., Shokouhi, P., Fortin, J., Schubnel, A., Marone, C., Johnson, P.A., 2016. Frequency, pressure, and strain dependence of nonlinear elasticity in Berea sandstone. Geophysical Research Letters 43, 3226–3236.

Rivière, J., Renaud, G., Guyer, R., Johnson, P., 2013. Pump and probe waves in dynamic acousto-elasticity: Comprehensive description and comparison with nonlinear elastic theories. Journal of applied physics 114, 054905.

Rivière, J., Shokouhi, P., Guyer, R.A., Johnson, P.A., 2015. A set of measures for the systematic classification of the nonlinear elastic behavior of disparate rocks. Journal of Geophysical Research: Solid Earth 120, 1587–1604.

Robbiano, F., Orellana, L.F., Violay, M., 2024. Physical and mechanical characterization of veined rocks: Implications to a porphyry model. Technical Report. Copernicus Meetings.

Rockwell, T.K., Ben-Zion, Y., 2007. High localization of primary slip zones in large earthquakes from paleoseismic trenches: Observations and implications for earthquake physics. Journal of Geophysical Research: Solid Earth 112.

Romenski, E., Resnyansky, A., Toro, E., 2007. Conservative hyperbolic formulation for compressible two-phase flow with different phase pressures and temperatures. Quarterly of applied mathematics 65, 259–279.

Romenski, E., Toro, E., 2004. Compressible two-phase flows: two-pressure models and numerical methods. Comput. Fluid Dyn. J 13, 403–416.

Ross, Z.E., Idini, B., Jia, Z., Stephenson, O.L., Zhong, M., Wang, X., Zhan, Z., Simons, M., Fielding, E.J., Yun, S.H., et al., 2019. Hierarchical interlocked orthogonal faulting in the 2019 ridgecrest earthquake sequence. Science 366, 346–351.

Roten, D., Fäh, D., Bonilla, L.F., 2013. High-frequency ground motion amplification during the 2011 Tohoku earthquake explained by soil dilatancy. Geophysical Journal International 193, 898–904.

Roten, D., Olsen, K., Day, S., 2017. Off-fault deformations and shallow slip deficit from dynamic rupture simulations with fault zone plasticity. Geophysical Research Letters 44, 7733–7742.

Roten, D., Olsen, K., Day, S., Cui, Y., Fäh, D., 2014. Expected seismic shaking in Los Angeles reduced by San Andreas fault zone plasticity. Geophysical Research Letters 41, 2769–2777.

Roten, D., Olsen, K., Pechmann, J., 2012. 3D simulations of M 7 earthquakes on the Wasatch fault, Utah, Part II: Broadband (0–10 Hz) ground motions and nonlinear soil behavior. Bulletin of the Seismological Society of America 102, 2008–2030.

Roten, D., Olsen, K.B., Day, S., Cui, Y., 2018. Implementation of Iwan-type plasticity model in awp-odc, in: Poster Presentation at 2018 SCEC Annual Meeting, p. 1.

Roten, D., Olsen, K.B., Day, S.M., Cui, Y., 2016. High-frequency nonlinear simulations of southern San Andreas earthquake scenarios. Poster Presentation at 2016 SCEC Annual Meeting.

Roten, D., Yeh, T.Y., Olsen, K.B., Day, S.M., Cui, Y., 2023. Implementation of Iwan-type nonlinear rheology in a 3D high-order staggered-grid finite-difference method. Bulletin of the Seismological Society of America 113, 2275–2291.

Rubin, A.M., Ampuero, J.P., 2005. Earthquake nucleation on (aging) rate and state faults. Journal of Geophysical Research: Solid Earth 110.

Sambridge, M., 1999. Geophysical inversion with a neighbourhood algorithm—i. searching a parameter space. Geophysical journal international 138, 479–494.

Sammis, C.G., Rosakis, A.J., Bhat, H.S., 2010. Effects of off-fault damage on earthquake rupture propagation: experimental studies. Mechanics, structure and evolution of fault zones , 1629–1648.

Schaff, D.P., Beroza, G.C., 2004. Coseismic and postseismic velocity changes measured by repeating earthquakes. Journal of Geophysical Research: Solid Earth 109.

Schliwa, N., Gabriel, A.A., Premus, J., Gallovič, F., 2024a. The linked complexity of coseismic and postseismic faulting revealed by seismo-geodetic dynamic inversion of the 2004 Parkfield earthquake. Journal of Geophysical Research: Solid Earth 129, e2024JB029410.

Schliwa, N., Gabriel, A.A., Premus, J., Gallovič, F., 2024b. The linked complexity of coseismic and postseismic faulting revealed by seismo-geodetic dynamic inversion of the 2004 parkfield earthquake. Journal of Geophysical Research: Solid Earth 129, e2024JB029410. URL: https://doi.org/10.1029/2024JB029410.

Scholz, C.H., 2019. The mechanics of earthquakes and faulting. Cambridge university press.

Schulz, E., Speekenbrink, M., Krause, A., 2018. A tutorial on gaussian process regression: Modelling, exploring, and exploiting functions. Journal of mathematical psychology 85, 1–16.

Seed, H., Romo, M., Sun, J., Jaime, A., Lysmer, J., 1989. Influence of site conditions on the ground motion during the Mexican earthquake of September 19, 1985. Earthquake Spectra 5, 687–729.

Seelinger, L., Cheng-Seelinger, V., Davis, A., Parno, M., Reinarz, A., 2023. Um-bridge: Uncertainty quantification and modeling bridge. Journal of Open Source Software 8, 4748. URL: https://doi.org/10.21105/joss.04748, doi:10.21105/joss.04748.

Seelinger, L., Reinarz, A., Lykkegaard, M.B., Akers, R., Alghamdi, A.M., Aristoff, D., Bangerth, W., Bénézech, J., Diez, M., Frey, K., Jakeman, J.D., Jørgensen, J.S., Kim, K.T., Kent, B.M., Martinelli, M., Parno, M., Pellegrini, R., Petra, N., Riis, N.A., Rosenfeld, K., Serani, A., Tamellini, L., Villa, U., Dodwell, T.J., Scheichl, R., 2025. Democratizing uncertainty quantification. Journal of Computational Physics 521, 113542. URL: https://www.sciencedirect.com/science/article/pii/S0021999124007903, doi:https://doi.org/10.1016/j.jcp.2024.113542.

Seelinger, L., Reinarz, A., Rannabauer, L., Bader, M., Bastian, P., Scheichl, R., 2021. High performance uncertainty quantification with parallelized multilevel markov chain monte

carlo, in: Proceedings of the International Conference for High Performance Computing, Networking, Storage and Analysis (SC21), Association for Computing Machinery. pp. 1–15. URL: https://doi.org/10.1145/3458817.3476150, doi:10.1145/3458817.3476150.

Semblat, J.F., Kham, M., Parara, E., Bard, P.Y., Pitilakis, K., Makra, K., Raptakis, D., 2005. Seismic wave amplification: Basin geometry vs soil layering. Soil dynamics and earthquake engineering 25, 529–538.

Sens-Schönfelder, C., Snieder, R., Li, X., 2019. A model for nonlinear elasticity in rocks based on friction of internal interfaces and contact aging. Geophysical Journal International 216, 319–331.

Sens-Schönfelder, C., Wegler, U., 2006. Passive image interferometry and seasonal variations of seismic velocities at Merapi Volcano, Indonesia. Geophysical research letters 33.

Seylabi, E., Restrepo, D., Taborda, R., Asimaki, D., 2021. Deterministic ground motion simulations with shallow crust nonlinearity at Garner Valley in Southern California. Earthquake Engineering & Structural Dynamics 50, 43–59.

Shah, A., Ribakov, Y., 2009. Non-linear ultrasonic evaluation of damaged concrete based on higher order harmonic generation. Materials & design 30, 4095–4102.

Sharma, M., 2010. Wave propagation in a pre-stressed anisotropic generalized thermoelastic medium. Earth, planets and space 62, 381–390.

Shelly, D.R., 2020. A high-resolution seismic catalog for the initial 2019 Ridgecrest earthquake sequence: Foreshocks, aftershocks, and faulting complexity. Seismological Research Letters 91, 1971–1978.

Shi, Z., Day, S.M., 2013. Rupture dynamics and ground motion from 3-D rough-fault simulations. Journal of Geophysical Research: Solid Earth 118, 1122–1141.

Shokouhi, P., Rivière, J., Guyer, R.A., Johnson, P.A., 2017. Slow dynamics of consolidated granular systems: Multi-scale relaxation. Applied Physics Letters 111, 251604.

Sibson, R., 1977. Fault rocks and fault mechanisms. Journal of the Geological Society 133, 191–213.

Snieder, R., Sens-Schönfelder, C., Wu, R., 2017. The time dependence of rock healing as a universal relaxation process, a tutorial. Geophysical Journal International 208, 1–9.

Stähler, S.C., Sigloch, K., Hosseini, K., Crawford, W.C., Barruol, G., Schmidt-Aursch, M.C., Tsekhmistrenko, M., Scholz, J.R., Mazzullo, A., Deen, M., 2016. Performance report of the RHUM-RUM ocean bottom seismometer network around la réunion, western indian ocean. Advances in Geosciences 41, 43–63.

Stanzione, D., West, J., Evans, R.T., Minyard, T., Ghattas, O., Panda, D.K., 2020. Frontera: The evolution of leadership computing at the national science foundation, in: Practice and Experience in Advanced Research Computing 2020: Catch the Wave, Association for Computing Machinery. pp. 106–111. URL: https://doi.org/10.1145/3311790.3396656, doi:10.1145/3311790.3396656.

Stiernström, V., Almquist, M., Dunham, E.M., 2024. Adjoint-based inversion for stress and frictional parameters in earthquake modeling. Journal of Computational Physics 519, 113447.

Strid, I., 2010. Efficient parallelisation of Metropolis–Hastings algorithms using a prefetching approach. Computational Statistics & Data Analysis 54, 2814–2835. URL: https://www.sciencedirect.com/science/article/pii/S0167947309004320, doi:https://doi.org/10.1016/j.csda.2009.11.019. the Fifth Special Issue on Computational Econometrics.

Taborda, R., Roten, D., 2015. Physics-based ground-motion simulation. Encyclopedia of Earthquake Engineering, Springer-Verlag, Berlin Heidelberg .

Takai, N., Shigefuji, M., Rajaure, S., Bijukchhen, S., Ichiyanagi, M., Dhital, M.R., Sasatani, T., 2016. Strong ground motion in the Kathmandu Valley during the 2015 Gorkha, Nepal, earthquake. Earth, Planets and Space 68, 1–8.

Takanami, T., Kitagawa, G., Obara, K., 2003. Hi-net: High sensitivity seismograph network, Japan. Methods and Applications of Signal Processing in Seismic Network Operations , 79–88.

Taufiqurrahman, T., Gabriel, A.A., Li, D., Ulrich, T., Li, B., Carena, S., Verdecchia, A., Gallovič, F., 2023. Dynamics, interactions and delays of the 2019 Ridgecrest rupture sequence. Nature 618, 308–315.

Taufiqurrahman, T., Gabriel, A.A., Ulrich, T., Valentova, L., Gallovič, F., 2022. Broadband dynamic rupture modeling with fractal fault roughness, frictional heterogeneity, viscoelasticity and topography: The 2016 Mw 6.2 Amatrice, Italy earthquake. Geophysical Research Letters 49, e2022GL098872.

Tavelli, M., Chiocchetti, S., Romenski, E., Gabriel, A.A., Dumbser, M., 2020. Space-time adaptive ader discontinuous Galerkin schemes for nonlinear hyperelasticity with material failure. Journal of computational physics 422, 109758.

Ten Cate, J.A., Shankland, T.J., 1996. Slow dynamics in the nonlinear elastic response of berea sandstone. Geophysical Research Letters 23, 3019–3022.

TenCate, J.A., 2011. Slow dynamics of earth materials: An experimental overview. Pure and Applied Geophysics 168, 2211–2219.

Terzaghi, K., Peck, R.B., Mesri, G., 1996. Soil mechanics in engineering practice. John wiley & sons.

Thomas, M.Y., Bhat, H.S., 2018. Dynamic evolution of off-fault medium during an earthquake: a micromechanics based model. Geophysical Journal International 214, 1267–1280. URL: https://doi.org/10.1093/gji/ggy129, doi:10.1093/gji/ggy129, arXiv:https://academic.oup.com/gji/article-pdf/214/2/1267/25081307/ggy129.pdf.

Thomée, V., 2007. Galerkin finite element methods for parabolic problems. volume 25. Springer Science & Business Media.

Thompson Jobe, J.A., Philibosian, B., Chupik, C., Dawson, T., K. Bennett, S.E., Gold, R., DuRoss, C., Ladinsky, T., Kendrick, K., Haddon, E., et al., 2020. Evidence of previous faulting along the 2019 Ridgecrest, California, earthquake ruptures. Bulletin of the Seismological Society of America 110, 1427–1456.

Tinti, E., Spudich, P., Cocco, M., 2005. Earthquake fracture energy inferred from kinematic rupture models on extended faults. Journal of Geophysical Research: Solid Earth 110.

Titarev, V.A., Toro, E.F., 2002. ADER: Arbitrary high order Godunov approach. Journal of Scientific Computing 17, 609–618.

Toro, E.F., Millington, R., Nejad, L., 2001. Towards very high order Godunov schemes, in: Godunov methods: theory and applications, Springer. pp. 907–940.

Truesdell, C., 1952. The mechanical foundations of elasticity and fluid dynamics. Journal of Rational Mechanics and Analysis 1, 125–300.

Twardzik, C., Das, S., Madariaga, R., 2014. Inversion for the physical parameters that control the source dynamics of the 2004 parkfield earthquake. Journal of Geophysical Research: Solid Earth 119, 7010–7027.

Ulrich, T., Gabriel, A.A., Ampuero, J.P., Xu, W., 2019. Dynamic viability of the 2016 mw 7.8 kaikōura earthquake cascade on weak crustal faults. Nature Communications 10, 1213. URL: https://www.nature.com/articles/s41467-019-09125-w, doi:10.1038/s41467-019-09125-w.

Uphoff, C., 2020. Flexible model extension and optimisation for earthquake simulations at extreme scales. Ph.D. thesis. Technische Universität München.

Uphoff, C., Bader, M., 2016a. Generating high performance matrix kernels for earthquake simulations with viscoelastic attenuation, in: 2016 international conference on high performance computing & simulation (HPCS), IEEE. pp. 908–916.

Uphoff, C., Bader, M., 2016b. Generating high performance matrix kernels for earthquake simulations with viscoelastic attenuation, in: 2016 International Conference on High Performance Computing Simulation (HPCS), pp. 908–916. doi:10.1109/HPCSim.2016.7568431.

Uphoff, C., Bader, M., 2020. Yet Another Tensor Toolbox for Discontinuous Galerkin Methods and Other Applications. ACM Transactions on Mathematical Software 46, 34:1–34:40. doi:10.1145/3406835.

Uphoff, C., Krenz, L., Ulrich, T., Wolf, S., Schneller, D., Kurapati, V., Knoll, A., Li, D., Dorozhinskii, R., Heinecke, A., Wollherr, S., Bohn, M., Schliwa, N., Brietzke, G., Taufiqurrahman, T., Anger, S., Rettenberger, S., Simonis, F., Gabriel, A., Pauw, V., Breuer, A., Kutschera, F., Hendrawan Palgunadi, K., Rannabauer, L., van de Wiel, L., Li, B., Chamberlain, C., Yun, J., Rekoske, J., G, Y., Bader, M., 2024. SeisSol. URL: https://doi.org/10.5281/zenodo.14051105, doi:10.5281/zenodo.14051105.

Uphoff, C., May, D.A., Gabriel, A.A., 2023. A discontinuous Galerkin method for sequences of earthquakes and aseismic slip on multiple faults using unstructured curvilinear grids. Geophysical Journal International 233, 586–626.

Uphoff, C., Rettenberger, S., Bader, M., Madden, E.H., Ulrich, T., Wollherr, S., Gabriel, A.A., 2017. Extreme Scale Multi-physics Simulations of the Tsunamigenic 2004 Sumatra Megathrust Earthquake, in: Proceedings of the International Conference for High Performance Computing, Networking, Storage and Analysis, ACM, New York, NY, USA. pp. 21:1–21:16. doi:10.1145/3126908.3126948.

Vakhnenko, O.O., Vakhnenko, V.O., Shankland, T.J., 2005. Soft-ratchet modeling of endpoint memory in the nonlinear resonant response of sedimentary rocks. Physical Review B 71, 174103.

Vakhnenko, O.O., Vakhnenko, V.O., Shankland, T.J., Ten Cate, J.A., 2004. Strain-induced kinetics of intergrain defects as the mechanism of slow dynamics in the nonlinear resonant response of humid sandstone bars. Physical review E 70, 015602.

Van Den Abeele, K.A., Carmeliet, J., Ten Cate, J.A., Johnson, P.A., 2000. Nonlinear elastic wave spectroscopy (news) techniques to discern material damage, part ii: Single-mode nonlinear resonance acoustic spectroscopy. Journal of Research in Nondestructive Evaluation 12, 31–42.

Vardanega, P.J., Bolton, M.D., 2013. Stiffness of clays and silts: Normalizing shear modulus and shear strain. Journal of Geotechnical and Geoenvironmental Engineering 139, 1575–1589.

Vehtari, A., Gelman, A., Simpson, D., Carpenter, B., Bürkner, P.C., 2021. Rank-normalization, folding, and localization: An improved $\hat{R}$ for assessing convergence of MCMC (with discussion). Bayesian analysis 16, 667–718.

Virieux, J., 1986. P-SV wave propagation in heterogeneous media: Velocity-stress finite-difference method. Geophysics 51, 889–901.

Virieux, J., Operto, S., 2009. An overview of full-waveform inversion in exploration geophysics. Geophysics 74, WCC1–WCC26.

Vucetic, M., Mortezaie, A., 2015. Cyclic secant shear modulus versus pore water pressure in sands at small cyclic strains. Soil Dynamics and Earthquake Engineering 70, 60–72. URL: https://www.sciencedirect.com/science/article/pii/S0267726114002796, doi:https://doi.org/10.1016/j.soildyn.2014.12.001.

Vyas, J.C., Gabriel, A.A., Ulrich, T., Mai, P.M., Ampuero, J.P., 2023. How does thermal pressurization of pore fluids affect 3D strike-slip earthquake dynamics and ground motions? Bulletin of the Seismological Society of America 113, 1992–2008.

Wang, K., Bürgmann, R., 2020. Probing fault frictional properties during afterslip updip and downdip of the 2017 mw 7.3 sarpol-e zahab earthquake with space geodesy. Journal of Geophysical Research: Solid Earth 125, e2020JB020319.

Wang, K., Dreger, D.S., Tinti, E., Bürgmann, R., Taira, T., 2020. Rupture process of the 2019 Ridgecrest, California Mw 6.4 foreshock and Mw 7.1 earthquake constrained by seismic and geodetic data. Bulletin of the Seismological Society of America 110, 1603–1626.

Wang, L., Hainzl, S., Zöller, G., 2014. Assessment of stress coupling among the inter-, co-and post-seismic phases related to the 2004 M6 Parkfield earthquake. Geophysical Journal International 197, 1858–1868.

Wang, S.Y., Zhuang, H.Y., Zhang, H., He, H.J., Jiang, W.P., Yao, E.L., Ruan, B., Wu, Y.X., Miao, Y., 2021. Near-surface softening and healing in eastern honshu associated with the 2011 magnitude-9 Tohoku-Oki earthquake. Nature communications 12, 1–10.

Weaver, T., 2019. Dynamic Response of Soil under Multidirectional Loading. Office of Nuclear Regulatory Research. URL: https://www.nrc.gov/docs/ML1917/ML19178A191.pdf.

Wei, S., Chen, M., Wang, X., Graves, R., Lindsey, E., Wang, T., Karakaş, Ç., Helmberger, D., 2018. The 2015 Gorkha (Nepal) earthquake sequence: I. source modeling and deterministic 3D ground shaking. Tectonophysics 722, 447–461.

Wesnousky, S.G., 2006. Predicting the endpoints of earthquake ruptures. Nature 444, 358–360.

White, R.S., 1988. The earth's crust and lithosphere. Journal of Petrology , 1–10.

Wilcox, L.C., Stadler, G., Burstedde, C., Ghattas, O., 2010. A high-order discontinuous Galerkin method for wave propagation through coupled elastic–acoustic media. Journal of computational Physics 229, 9373–9396.

Wolf, S., Gabriel, A.A., Bader, M., 2020a. Optimization and local time stepping of an ader-dg scheme for fully anisotropic wave propagation in complex geometries, in: International Conference on Computational Science, Springer. pp. 32–45.

Wolf, S., Gabriel, A.A., Bader, M., 2020b. Optimization and Local Time Stepping of an ADER-DG Scheme for Fully Anisotropic Wave Propagation in Complex Geometries, in: Krzhizhanovskaya, V.V., Závodszky, G., Lees, M.H., Dongarra, J.J., Sloot, P.M.A., Brissos, S., Teixeira, J. (Eds.), Computational Science – ICCS 2020, Springer International Publishing, Cham. pp. 32–45. doi:10.1007/978-3-030-50420-5_3.

Wolf, S., Gabriel, A.A., Galis, M., Moczo, P., Gregor, D., Bader, M., 2024. 3D wave propagation and earthquake dynamic rupture simulations in complex poroelastic media. EarthArXiv .

Wolf, S., Galis, M., Uphoff, C., Gabriel, A.A., Moczo, P., Gregor, D., Bader, M., 2022. An efficient ADER-DG local time stepping scheme for 3D HPC simulation of seismic waves in poroelastic media. Journal of Computational Physics 455, 1–29. doi:10.1016/j.jcp.2021.110886.

Wollherr, S., Gabriel, A.A., Mai, P.M., 2019. Landers 1992 "reloaded": Integrative dynamic earthquake rupture modeling. Journal of Geophysical Research: Solid Earth 124, 6666–6702.

Wollherr, S., Gabriel, A.A., Uphoff, C., 2018. Off-fault plasticity in three-dimensional dynamic rupture simulations using a modal discontinuous Galerkin method on unstructured meshes: implementation, verification and application. Geophysical Journal International 214, 1556–1584.

Xu, S., Ben-Zion, Y., Ampuero, J.P., Lyakhovsky, V., 2015. Dynamic ruptures on a frictional interface with off-fault brittle damage: feedback mechanisms and effects on slip and near-fault motion. Pure and Applied Geophysics 172, 1243–1267.

Xu, X., Sandwell, D.T., Ward, L.A., Milliner, C.W., Smith-Konter, B.R., Fang, P., Bock, Y., 2020. Surface deformation associated with fractures near the 2019 ridgecrest earthquake sequence. Science 370, 605–608.

Xu, X., Tong, X., Sandwell, D.T., Milliner, C.W., Dolan, J.F., Hollingsworth, J., Leprince, S., Ayoub, F., 2016. Refining the shallow slip deficit. Geophysical Journal International 204, 1867–1886.

Yamaoka, K., Kunitomo, T., Miyakawa, K., Kobayashi, K., Kumazawa, M., 2001. A trial for monitoring temporal variation of seismic velocity using an across system. Island Arc 10, 336–347.

Yamashita, T., 2000. Generation of microcracks by dynamic shear rupture and its effects on rupture growth and elastic wave radiation. Geophysical Journal International 143, 395–406.

Yang, K., Cai, P., Zhang, Z., Hou, Q., Zheng, R., Hao, B., 2024. Effects of soil–structure interaction on the seismic response of RC frame–shear wall building structures under far-field long-period ground motions. Buildings 14, 3796. URL: https://www.mdpi.com/2075-5309/14/12/3796, doi:10.3390/buildings14123796.

Yang, W., Hauksson, E., 2013. The tectonic crustal stress field and style of faulting along the Pacific North America Plate boundary in Southern California. Geophysical Journal International 194, 100–117.

Yang, Y., Gao, A.F., Azizzadenesheli, K., Clayton, R.W., Ross, Z.E., 2023. Rapid seismic waveform modeling and inversion with neural operators. IEEE Transactions on Geoscience and Remote Sensing 61, 1–12.

Yen, M.H., Türker, E., Ulrich, T., Marchandon, M., Gabriel, A.A., Cotton, F., 2025. An analysis of directivity pulses using empirical data and dynamic rupture simulations of the 2023 Kahramanmaras earthquake doublet. Earthquake Spectra , 87552930241305012.

Youssef, I.K., El-Arabawy, H., 2007. Picard iteration algorithm combined with Gauss–Seidel technique for initial value problems. Applied Mathematics and computation 190, 345–355.

Zhan, Z., 2020. Distributed acoustic sensing turns fiber-optic cables into sensitive seismic antennas. Seismological Research Letters 91, 1–15.

Zhang, W., Cai, Y., 2010. Continuum damage mechanics and numerical applications. Springer Science & Business Media.

Zhang, X., Lomas, A., Zhou, M., Zheng, Y., Curtis, A., 2023. 3-D Bayesian variational full waveform inversion. Geophysical Journal International 234, 546–561.

Zoback, M., Zoback, M., Watts, A., Schubert, G., 2007. Lithosphere stress and deformation. Treatise on geophysics , 253–273.